Investigating BWR Stability with a New Linear Frequency-Domain Method and Detailed 3D Neutronics

A Dissertation Submitted to the

SWISS FEDERAL INSTITUTE OF TECHNOLOGY
ZURICH

for the Degree of

Doctor of Technical Sciences

presented by

PHILIPP HÄNGGI

Dipl. Phys. ETH
born December 19, 1968
Citizen of Rickenbach (SO), Switzerland

accepted on the recommendation of

Prof. Dr. G. Yadigaroglu, examiner
Prof. Dr. J. Blomstrand, co-examiner
PD Dr. J. Halin, co-examiner

2001

Dipl. Phys. ETH Philipp Hänggi:
Investigating BWR Stability with a
New Linear Frequency-Domain Method
and Detailed 3D Neutronics

This work has been submitted to the Swiss Federal Institute of Technology Zürich to obtain the degree 'doctor of technical sciences'. All necessary requirements were met and the title had been granted.

Abstract

Using frequency-domain methods, sparse matrix techniques and advanced numerical algorithms a new computer program MATSTAB has been developed to predict the core stability characteristics of a boiling water nuclear reactor. The code uses the same thermal-hydraulic model as the transient code RAMONA-3B and the same neutronic model as the online steady-state core simulator POLCA. This includes three-dimensional neutronics and an individual representation of each fuel assembly (no lumping).

The very large set of equations is linearized and leads to a generalized eigenvalue problem which is solved iteratively using a combination of Newton's method and sub-space decomposition. The tailor-made algorithm calculates the first few dominating eigenvalues (decay ratios) and their left and right eigenvectors. MATSTAB not only predicts global, but also regional oscillations. A comparison between the decay ratios of the two oscillation types allows to judge which mode will occur.

Using MATSTAB and the interface to the online steady-state core simulator POLCA, it is possible to predict the stability of the reactor core in its present state. A calculation with full spatial resolution (all fuel assemblies, 25 axial nodes) is performed within a few minutes on a standard personal computer.

The eigenvalues and eigenvectors may not only be used to calculate the decay ratio and oscillation frequency, but also to analyze the stability behavior of the coupled neutronic/thermal-hydraulic system. A new method is introduced which allows to calculate and display the contribution to (in)stability of any part of the reactor model (fuel assembly, neutronics, thermal-hydraulics, riser, pumps, etc.). It is also possible to display the contribution to (in)stability of any physical quantity (power-density distribution, void, pumps etc.). This allows to enter a new territory and possibly to gain new insights into the mechanisms behind instabilities. This new method is not yet explored in depth, but some simple judgments were already used to optimize the core design and control rod sequence with respect to stability during start up procedures in Forsmark.

The results of the code have been successfully validated against numerous stability measurements from the Forsmark, Oskarshamn (both in Sweden) and Leibstadt (Switzerland) plants. The predictions show good agreement with the measured data for all global oscillations in all the plants. The regional oscillations in Cycle seven of Leibstadt were clearly predicted by MATSTAB, but the specific values for the decay ratios were underestimated in a systematic way.

Zusammenfassung

Um die Kernstabilität eines Siedewasserreaktors vorherzusagen, wurde unter Einbezug von Frequenz-Raum-Methoden, schwach besetzten Matrizen und fortgeschrittenen numerischen Algorithmen das Computer Programm MATSTAB entwickelt. Das Programm benutzt die gleichen thermodynamischen Modelle wie das Transienten-Programm RAMONA-3B und das gleiche Neutronik-Modell wie der Online-Kernsimulator POLCA. Dies beinhaltet eine dreidimensionale Neutronik und eine explizite Modellierung jedes Brennelementes (keine Gruppenbildung).

Das sehr grosse Gleichungssystem wird linearisiert und führt zu einem verallgemeinerten Eigenwertproblem, das unter Verwendung der Newton-Methode und der Zerlegung in Unterräume iterative gelöst wird. Der eigens entwickelte Algorithmus berechnet die dominierenden Eigenwerte und deren zugeordnete linke und rechte Eigenvektoren. Dadurch ist MATSTAB in der Lage, nicht nur die globalen, sondern auch die regionalen Schwingungen vorherzusagen. Ein Vergleich der Dämpfungskonstanten (DR) der beiden Schwingungstypen erlaubt es zudem abzuschätzen welcher Schwingungstyp auftreten wird.

Verwendet man das in MATSTAB eingebaute Interface zum Online-Kernsimulator POLCA, kann man die aktuelle Kernstabilität berechnen. Ein Rechenlauf mit voller räumlicher Auflösung (alle Brennelemente, 25 axiale Knoten) dauert auf einem Standard Personal-Computer nur wenige Minuten.

Die Eigenwerte und Eigenvektoren dienen nicht nur zur Berechnung der Dämpfungskonstanten und der Frequenz der Schwingungen, sondern können auch zur Analyse des Stabilitätsverhaltens des gekoppelten Schwingungssystems (Thermohydraulik/Neutronik) herangezogen werden. Eine neue Methode wird eingeführt, die es erlaubt, den Beitrag von jedem Modellteil (Brennelement, Neutronik, Thermohydraulik, Pumpen usw.) zur (In)stabilität abzuschätzen und grafisch darzustellen. Es ist zusätzlich möglich, den Beitrag einzelner physikalischer Grössen (Leistungsdichte, Dampfblasen Anteil, Brennstofftemperatur usw.) zur (In)stabilität zu berechnen. Dadurch wird ein neues Forschungsfeld erschlossen, das möglicherweise zu neuen Erkenntnissen über den Mechanismus hinter den Instabilitäten führt. Die neuen Methoden sind derzeit noch nicht in voller Tiefe umgesetzt, aber erste einfache Ansätze wurden angewandt. Die Resultate sind in Forsmark eingesetzt worden, um die Kernbeladung und die Kontrollstab-Sequenz während des Anfahrens zu optimieren.

Die Resultate von MATSTAB wurden erfolgreich anhand zahlreicher Messungen in Forsmark, Oskarsham (beide Schweden) und Leibstadt (Schweiz) überprüft. Die Vorhersagen zeigten in allen Kernkraftwerken gute Übereinstimmung, mit den gemessenen Daten für globale Schwingungen. Die regionalen Schwingungen, die im siebten Zyklus in Leibstadt aufgetreten sind, wurden qualitativ zwar eindeutig vorhergesagt, quantitativ jedoch auf systematische Art und Weise unterschätzt.

Contents

List of Tables

Chapter 1

Introduction

Contents

1.1   Motivation

In 2000, 438 Nuclear Power Plants (NPPs) produced 2'468 TWh of electric power, covering 16% of the worldwide and 42% of the West European electricity consumption. Even though many different reactor designs exist, 80% of all reactors are of two basic types. The pressurized water reactors (PWRs) are leading in numbers with 258 operating plants, followed by the boiling water reactors (BWRs) with 90 plants in operation. Naturally, both designs have their advantages and disadvantages.

The local power generation in the core of a nuclear reactor is directly related to the neutron flux, which itself is a function of the reactivity. In BWRs, the reactivity depends strongly on the core void fraction. Thus when a void fraction oscillation is established in a BWR, the power oscillates according to the neutronic feedback. This feedback mechanism which is shown in Figure 1.1 in a simplified manner (see also Figure 3.1 on page 24 in Chapter 3 for full detail) may under certain conditions lead to poorly damped or even limit-cycle power oscillations. Their frequency lies around 0.5 Hz (about twice the transport time of the coolant through the core). Amplitudes from nearly 0% to more than 100% in power have been observed. The oscillations are mostly global, i.e. "in-phase".
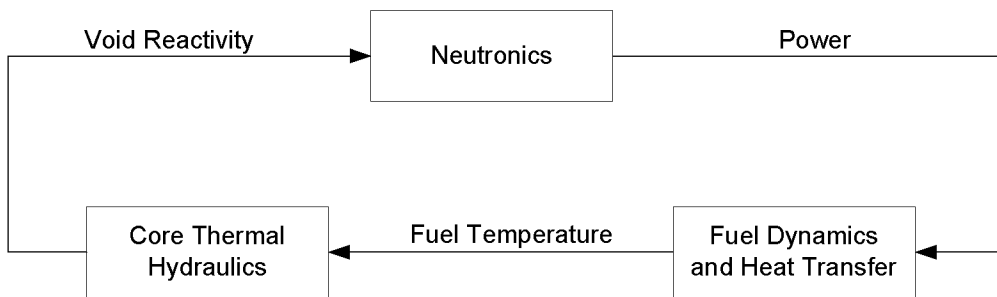
Figure 1.1: Simplified Neutronic/Thermal-Hydraulic Feedback System in a BWR

Higher mode power oscillations are also possible; these divide the core into two regions oscillating in opposite directions at constant overall power. These regional oscillations are cumbersome for the operators since their detection is not directly possible with standard instruments that display only core-average data. Even more complex modes of instability have also been observed.

In addition to the regional oscillations, also local oscillations are possible. Under certain conditions it is possible, that one or a few fuel channels are oscillating independent of the core. The two phase flow inside a channel allows density wave oscillations without the presence of a neutronic feedback ([8] and many others). This effect may dominate the neutronic/thermal-hydraulic feedback loop in rare occasions. For example, in 1997 a badly seated fuel assembly caused local oscillations in Forsmark [4].

During the early years of BWR technology, there was considerable concern about the possible effect of coupled neutronic/thermal-hydraulic instabilities. However, after various in

depth experiments and analyses, it became clear that BWRs could be designed such that instabilities would not occur under normal operating conditions.

In addition, the BWR stability issue is no major industry safety problem from a technical point of view. Given appropriate instrumentation, power oscillations are easy to detect and there exist simple, as well as effective, counter measures. A scram will normally solve the problem, even though other less drastic measures will normally suffice. Furthermore, normal operating points in power and core flow tend to be very stable. Stability problems may only arise during start up or during transients which significantly shift the operating point towards low core flow and high power. Therefore, the operating instructions for BWRs contain clear rules on how to avoid operating points (regions) that may produce power-void oscillations. Figure 1.2 shows a power-flow map for the Leibstadt NPP. The lower right side of the plot marks the allowed operating region, the gray regime may only be entered if special measures are taken and finally, the black regime is forbidden due to stability concerns.
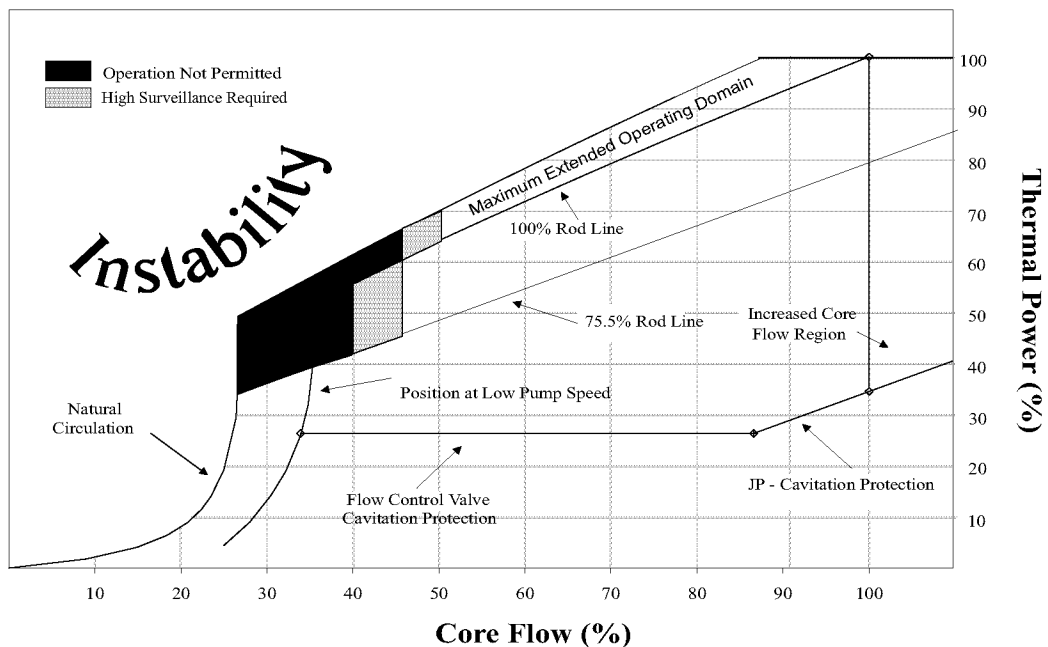
Figure 1.2: Instability Region in the Power-Flow Map

The numerous modifications in "reactor size", reactor power, fuel design, power density, discharge burnup and loading strategies changed the core stability behavior of the BWR reactor to a significant extent. In comparison to the situation in the seventies, the region of the power-flow map which has to be avoided grew to a respectable size. Several plants, e.g. Caorso and La Salle (see Table 1.1), accidentally entered the less stable region and actually experienced power-void oscillations.

Since, for economic reasons, the trend towards smaller-diameter fuel rods and different loading strategies will persist, the stability problem has to be taken care of. It is, therefore, important to understand the underlying mechanism of power-void instability as thoroughly as possible, as well as to be able to detect and predict power oscillations with the aim to sup-

Date	Plant	Country, Manufact.	Event (as described by the operator)
30.06.82	Caorso	IT, AMN	Core instability during plant start up
01.10.83	Caorso	IT, AMN	Core instability during special tests
17.10.84	S. Maria de Garona	ES, GE	Power oscillations during operation
23.02.87	TVO 1	Fe, ABB	Power oscillations during plant start up
09.03.88	La Salle 2	US, GE	Core instability with scram caused by neutron flux oscillation
29.10.88	Vermont Yankee	US, GE	Power oscillations
26.10.89	Ringhals 1	SE, GE	Instability during power ascent after refueling
08.01.89	Oskarshamn	SE, ABB	Power oscillations
29.01.91	Cofrentes	ES, GE	Power oscillations due to inadvertent entry in the reactor power-core flow map instability zone "B"
03.07.91	Isar 1	DE, KWU	Scram due to power oscillations
15.08.92	WNP	US, GE	Power oscillations
09.07.93	Perry	US, GE	Entry into a region of core instability
17.07.96	Forsmark 1	SE, ABB	Local oscillations due to a bad seated fuel assembly
08.02.98	Oskarshamn 3	SE, ABB	Power oscillations due to a bad combination of core design and control-rod pattern during start up
25.02.99	Oskarshamn 2	SE, ABB	Power oscillations after a turbine trip with pump runback

Table 1.1: Events with Core Instabilities

press them, or at least to mitigate them, should they occur. The instability events mentioned in Table 1.1 and the open questions led to numerous new investigations and reports and fostered the development of more sophisticated computational tools.

1.2   Previous Work

Over the past several years, many mathematical models and computer codes have been developed, and tests have been carried out, to investigate density-wave and power-void instabilities in BWRs. In the theoretical work done so far, stability analyses have usually been carried out by evaluating the decay ratios and oscillation frequencies and studying the effect of certain parameters on BWR core stability. Numerical simulations have been done to study the time evolution of certain phase variables. The results of some of these stability analyses and numerical simulations have been compared with test results or data collected from actual BWR instability incidents, and the overall agreement has been reasonably good. This

overall good agreement between the computational and mathematical analyses, and the experimental tests and the actual operational BWR incidents, has led to a better understanding of the instability phenomenon.

1.2.1   Selected Papers

The broad literature on BWR-stability covers a wide range of subjects. Reviews of most aspects of nuclear coupled stability may be found in [22], [57], [67].

Apart from some very interesting but limited approaches addressing the issue from an analytical point of view, e.g. the analysis of March-Leuba [54], most investigations involve measurements and/or extensive numerical simulations. Hence, a wide variety of codes (see Table 1.2) have been developed to predict and/or analyze the BWR-stability phenomena.

March-Leuba et al. [54] developed a phenomenological model to simulate the "qualitative" behavior of BWRs. They also developed a detailed nodalized (numerically discretized) physical model to simulate the dynamic behavior of the Vermont Yankee BWR over a broad operating range by varying the power and flow [55]. Their analysis led to the conclusion that for a wide range of oscillation amplitudes, no significant effect on the integrity of the fuel is expected. However, in order to keep their model simple, they assumed that the coolant enters the core at saturation enthalpy (not as sub-cooled liquid), i.e. that the boiling boundary always is at the bottom of the core channels.

Belblidia et al. [5] adopted a nodal approach to describe the neutron kinetics of a BWR core. They subdivide the core into radial zones and develop nodal kinetics equations by introducing inter-nodal coupling. Using this model they showed that the point kinetics model representation of BWR neutron kinetics yields conservative results, but that for better assessment of BWR core stability, radial coupling effects should be included. However, Karve [39] showed, that the point kinetics model representation may yield dramatically nonconservative results by failing to capture the important effect of the first harmonic mode, which may lead to regional power oscillations in a BWR. Only a three-dimensional neutronic model or a modal kinetic representation will predict those oscillations.

Peng et al. [78] developed a linear frequency-domain computer code NUFREQ-NP for BWR stability analysis under conditions of either forced or natural circulation. That code is based on a one-dimensional drift flux model for the two-phase flow, a simplified 3-D neutronic model and takes into account sub-cooled boiling, arbitrary nonuniform axial and radial power shapes, distributed local losses, detailed fuel assembly dynamics, and system pressure perturbation. The results were compared with experimental data from Peach Bottom-2 stability tests and showed good agreement.

Bergdahl et al. [7] conducted a series of noise measurements at Forsmark-1 and 2 to investigate the oscillations at low-flow/high-power operating conditions during reactor start-up. The LPRM signals in the measurements on Forsmark-1 indicated that these oscillations, which occurred at 0.5 Hz, were generally in phase throughout the core. However, the oscillations varied in strength in different radial positions of the core. Furthermore, the upper

LPRM signals were influenced by the lower ones in the same probe due to void transport upwards in the core. They also noted that the decay ratio (DR) ranged above 0.7, instead of the value of 0.6 predicted by a large computer code.

Valtonen [106] validated the RAMONA-3B three-dimensional BWR transient analysis code, and the TRAB one-dimensional BWR transient analysis code, using data from an oscillation incident that occurred at the TVO I BWR. It was shown, that both regional and global oscillations are possible in BWRs operating in the low-flow/high-power region of the power-flow map. Sensitivities to the inlet orifice of the core, the fuel gap conductance, the axial power distribution and the fuel type were studied. It was shown that decreasing the fuel gas gap conductance, which leads to increasing the time constant of the fuel heat transfer, has a destabilizing effect.

Rizwan-Uddin and Dorning [102] studied the effects of unheated riser sections that are added to enhance natural circulation in the next generation of BWRs. They found that, for a fixed flow rate, the addition of the riser sections makes the system less stable. They also showed that the feedback recirculation loop plays an important role in reactor stability, and if omitted from the model, can lead to nonconservative conclusions.

Wulff et al. [115] simulated the instability that occurred at the LaSalle-2 power plant (and several other BWR transients), using the Brookhaven National Laboratory Engineering Plant Analyzer (EPA) in order to determine the causes that led to the observed magnitudes of power, flow and temperature oscillations. They found it to be a powerful tool for scoping calculations and for supporting accident management. Although very valuable in many contexts, production codes such as EPA are not very useful for thorough stability analyses or extensive parameter studies in general, because of their complexity and long computer running times.

To study the mechanisms for regional instability, March-Leuba and Blakeman [57] developed a model by modifying the LAPUR code. They studied the effect of the first harmonic neutron kinetics mode on the regional instability. They showed that it has a very important influence on this instability and that because of its effect, there is a region in the power-flow map where an regional instability mode is likely, even though the core-wide mode is stable.

Munoz-Cobo et al. [65] extended the phenomenological model developed by March-Leuba [57] to study both global and regional instability. They replaced the point kinetics equations in [57] by modal kinetics equations which they developed based on λ-modes. Using this model, they showed that global oscillations only appear when the first harmonic mode does not have enough thermal-hydraulic feedback to overcome the eigenvalue separation. Further, they showed that self-sustained regional oscillations could arise due to the different thermal-hydraulic properties of the reactor planar halves, if the modal reactivities have appropriate feedback gains.

Van der Hagen et al. [112] developed methods for obtaining the stability characteristics of global and regional oscillations separately from neutron noise signals. The methods were applied for the Ringhals 1 measurements in 1990, where the decay ratio of the regional oscillation was higher than the decay ratio of the global oscillation but could not be seen,

because the signal amplitude of the global mode was much higher than the signal amplitude of the local mode.

1.2.2 Different Types of Computer Codes

Table 1.2 lists the common computer codes for stability calculations available in 1997 [22]. In more recent years, some of the codes were further developed. For example, RAMONA-5 was released, which runs significantly faster than RAMONA-3B and contains better thermal-dynamic models. Despite all improvements in several codes, no code similar to MATSTAB has been developed. The combination of frequency domain, three dimensional neutronics and eigenvalue/eigenvector analysis is still unique.

Time Domain

The computer codes which calculate transients operate in the time domain (TD) [15], [76],[98],[114]. These codes numerically integrate the differential equations that describe the physical development of the system in time. As TD codes allow a very detailed description of the physical structures/mechanisms in the reactor core, a three-dimensional description of the power shape is possible with advanced codes and proved to be indispensable for precise calculations.

The TD approach requires no major simplifications. It allows the equations to be addressed step by step and therefore uses no significant amount of computer memory. However, as TD codes cover the complete dynamic range of practical relevance, including non-linear behavior such as limit-cycle oscillations, the time needed to calculate a large number of minute time steps is extensive, for a full three-dimensional neutronic description.

Frequency Domain

Although instability is a highly non-linear phenomenon, a significant amount of information (e.g. the stability criteria of the reactor core for a specified operating point) may nevertheless be determined from the set of linearized system equations. It goes without saying, that dealing with stability only using linear equations is much faster than simulations using the full set of differential equations. The frequency-domain (FD) approach [70], [79], [119] takes full advantage of this fact and analyses the linearized form of the TD equations in the frequency domain.

Another advantage of the FD approach is its capability of describing an oscillation with one single complex number (eigenvalue), instead of the many points representing a trajectory in the time domain. Finally, FD methods are not plagued by the numerical stability difficulties present in the TD solutions. However, a significant drawback, besides the loss of information due to linearization, is that many equations have to be addressed simultaneously, wherefore a much larger amount of computer memory is required. Nevertheless, the immense trade-off

Common codes operating in the time domain						
	Thermal-Hydraulics			**Neutronics**	**Owner /**	**Reference**
Name	**Channels**	**Model**	**eq.**	**Dimension**	**User**	
RAMONA-3B	all	D-F NE	4	3	ScandPower A/S	[114]
RELAP5	a few	2 fluid	6	point kin.	INEL, NRC	[15]
RETRAN-3D	4	slip EQ	5	1	EPRI	[76]
TRACG	a few	2 fluid	6	3	GE	[98]

Common codes in the frequency domain						
	Thermal-Hydraulics			**Neutronics**	**Owner /**	**Reference**
Name	**Channels**	**Model**	**eq.**	**Dimension**	**User**	
NUFREQ NP	a few	D-F EQ	3-4	3 simplified	RPI (USA)	[79]
LAPUR5	1-7	slip EQ		point kin.	ORNL/NRC	[70]
STAIF	10	D-F NE	5	1	SIEMENS	[119]
FABLE	24	slip EQ		point kin.	GE	[22]
ODYSY	a few	D-F NE	5	1	GE	[22]
MATSTAB	All	D-F NE	4	3	FORSMARK AB	[32]

eq.	number of conservation equations for thermal hydraulics
D-F	drift-flux description of mixture
NE	thermal non-equilibrium between phases
Slip	non-equal gas and liquid velocities
EQ	thermal equilibrium between phases

Table 1.2: Common Stability Codes in 1998

in speed and the fact that FD results translate easily into stability criteria offer overriding advantages, particularly, if only the onset of instability, and not its development in time, is of interest.

1.3   The Scope of this Work

The advances in fuel design which raised the stability questions again, also posed new challenges to the existing codes and the detail of the models involved. From the point of view of a core physicist, it is necessary to have a detailed model, a fast code and results that are both easy to visualize and to interpret. The TD codes satisfy the need for accuracy and a high level of detail, but they lack in speed and produce results which do not relate directly to stability-relevant information. By contrast, FD codes produce quick results which are easy to use but do not necessarily reach the required level of detail and accuracy.

With these problems in mind, Dr. Thomas Smed and his co-worker Pär Lansåker at the Forsmark site in Sweden started the MATSTAB (MATrix STABility) project. Recognizing the potential of this work, Dr. H.-U. Zwicky and C. G. Wiktor from the Leibstadt NPP in Switzerland financed this Ph. D. thesis to support the ongoing efforts and to build up some more expertise at the Leibstadt site. The development of MATSTAB provided not only an in depth knowledge of modeling a BWR reactor, but also the opportunity to gain a deeper understanding of the physical phenomena taking place inside the reactor.

The primary objectives for developing MATSTAB and using a new method for calculating and predicting the onset of instability in BWRs were to achieve short execution times (without loss of prediction accuracy) and to provide the capability of predicting core-wide as well as regional oscillations.

Short execution times are achieved by evaluating the core and system dynamics in the frequency domain. This implies that only the *small* deviations around steady state operating conditions are considered, for which the dynamic behavior of the power-void-feedback mechanism is sufficiently linear to be correctly described by a system of linear equations. This approach is widely accepted for studies that are restricted to operating points below the stability limit where the amplitude of the oscillations is limited. One also observes, that when determining stability criteria from noise measurements of power reactors, linear concepts give the best results (e.g. ARMA models, see section 6.1.1 and [47]).

Accuracy is achieved by the detail of the model. The models used in the well known and widely accepted transient code RAMONA-3B were linearized and adapted to the frequency domain for this work.

The ability to detect *global as well as regional oscillations* was achieved with a less common FD approach. No Laplace transformation of the equations are applied. The resulting large sparse system matrix is addressed directly to profit from the information (e.g. global/regional) contained in the eigenvectors. It is the nature of this FD approach that leads to new ways of visualizing and analyzing the BWR stability and constitutes the novel aspects of this work.

In conclusion it was possible

- to "linearize Ramona"

- to predict successfully decay ratios for Forsmark, Leibstadt and Oskarshamn

- to predict regional oscillations for Leibstadt

- to show the influence of different components of the reactor system on stability

To be able to create a tool like MATSTAB, it was necessary to combine expertise from very different fields such as thermal-hydraulics, neutronics, control theory, advanced numerical methods, sparse matrix techniques and, last but not least, some good programming.

The Norwegian based company Studsvik Scandpower contributed the source code of RAMONA-3B to support the cooperation between the two power plants and the Nuclear Engineering Laboratory (LKT) of the Swiss Federal Institute of Technology (ETH).

Finally, it remains to be said that MATSTAB is programmed in the script language of the high performance computing platform MATLAB (MATrix LABoratory) [59] and is called MATSTAB (MATrix STABility). The code is owned by the Forsmark Kraftgrupp AB, which is entirely open minded with respect to new research programs.

Chapter 2

The Concept Behind MATSTAB

Contents

2.1 The Central Equations

MATSTAB combines well known methods from different fields in a new manner.

- Sets of linearized equations

- Sparse matrix techniques

- Frequency domain calculations (eigenvalues\eigenvectors)

The linearization of the equations reduces the computational workload while giving access to many sophisticated methods of linear systems.

The sparse matrix techniques overcome the huge memory and time demands of an algorithm that solves up to half a million equations simultaneously ($\approx$200MB instead of $\approx$10GB).

The frequency domain representation allows to calculate eigenvalues and eigenvectors which contain much more information than a time series from a time domain approach. Therefore not only more information is gained, but the results can also be visualized in a very interesting way.

The combination of these methods makes it feasible to model a nuclear reactor in detail. Each of the roughly 650 fuel assemblies is represented with 25 axial nodes. Each node contains up to 20 equations, hence creating a system with roughly $650 * 25 * 20 = 325'000$ equations in the core alone.

2.1.1 Linearization

The dynamic behavior of boiling water reactors can be assumed to be linear for small deviations around steady operating conditions. This makes it possible to study stability of BWRs using locally linearized equations. The reactor is described with an appropriate form of the governing equations as well as the equations needed to close the system. The n_x state variables which are described by differential equations are represented by the vector $\mathbf{x}$ while the n_u variables described by algebraic equations are represented by the vector $\mathbf{u}$. To be consistent with the model description of RAMONA [114], the time is denoted with τ. The continuous-time dynamical system consists, therefore, of a set of n_x first-order differential equations of the form

$$\frac{d}{d\tau}\mathbf{x}\left(\tau\right) = \mathbf{f}\left(\mathbf{x}\left(\tau\right),\mathbf{u}\left(\tau\right)\right) \tag{2.1}$$

and n_u algebraic equations of the form

$$\mathbf{g}(\mathbf{x}(\tau),\mathbf{u}(\tau)) = \mathbf{0} \tag{2.2}$$

where

$$\mathbf{x}(\tau) = \begin{pmatrix} x_1(\tau) \\ \vdots \\ x_{n_x}(\tau) \end{pmatrix} \quad \text{and} \quad \mathbf{u}(\tau) = \begin{pmatrix} u_1(\tau) \\ \vdots \\ u_{n_u}(\tau) \end{pmatrix} \tag{2.3}$$

Examples of variables of the type $x_i(\tau)$ are mixture energy, steam mass and fuel temperature. Examples of variables of the type $u_i(\tau)$ are mixture volumetric flux, slip and power generation rate. Table 2.1 shows a complete list of the state variables/equations. A detailed description about the state variables is given in the next chapter and in Appendix A.

Symbol	Variable	Algebraic	Differential	Remarks
Thermal-Hydraulics				
P	Pressure		1	
$u_m\rho_m$	Mixture Energy		1	
m_g	Steam Mass		1	
j_m	Mixture Volumetric Flux	1		
S	Slip	1		
w_g	Phasic Velocity	1		
W_g, W_l	Mass Flow Rate	2		
Γ_v	Vapor Generation Rate	1		
q'_w	Linear Heat Generation Rate	1		
t_l	Liquid Temperature	1		
t_w	Wall Temperature	1		
Neutronics / Power Generation				
φ_1	Fast Flux	1		
φ_2	Thermal Flux	(1)		integrated into φ_1
C_d	Precursors	(6)		integrated into φ_1
q''''	Power Generation Rate	1		
Thermal Conduction				
t_f	Fuel Temperature		4	
t_c	Cladding Temperature		2	
Total		11	9	

Table 2.1: Differential and Algebraic Equations used in MATSTAB

The equations 2.1 and 2.2 build together the set of equations which has to be linearized.

$$\left| \begin{array}{rcl} \frac{d}{d\tau}\mathbf{x}(\tau) & = & \mathbf{f}(\mathbf{x}(\tau),\mathbf{u}(\tau)) \\ \mathbf{0} & = & \mathbf{g}(\mathbf{x}(\tau),\mathbf{u}(\tau)) \end{array} \right| \tag{2.4}$$

$\mathbf{x}(\tau)$ in (2.4) can be substituted by $\mathbf{x}(\tau) = \mathbf{x}_0 + \Delta\mathbf{x}(\tau)$, where $\mathbf{x}_0$ is the steady state value and $\Delta\mathbf{x}$ is a small perturbation around $\mathbf{x}_0$. Similarly $\mathbf{u}(\tau) = \mathbf{u}_0 + \Delta\mathbf{u}(\tau)$. The Taylor-series of $\mathbf{f}(\mathbf{x},\mathbf{u})$ and $\mathbf{g}(\mathbf{x},\mathbf{u})$ yield

$$\frac{d}{d\tau}\mathbf{x}_0 + \frac{d}{d\tau}\Delta\mathbf{x} = \mathbf{f}_0 + \frac{\partial\mathbf{f}(\mathbf{x},\mathbf{u})}{\partial\mathbf{x}}\Delta\mathbf{x} + \frac{\partial\mathbf{f}(\mathbf{x},\mathbf{u})}{\partial\mathbf{u}}\Delta\mathbf{u} + O\left(\Delta\mathbf{x}^2,\Delta\mathbf{u}^2,\Delta\mathbf{x}\Delta\mathbf{u}\right) \tag{2.5}$$

$$\mathbf{0} = \mathbf{g}_0 + \frac{\partial\mathbf{g}(\mathbf{x},\mathbf{u})}{\partial\mathbf{x}}\Delta\mathbf{x} + \frac{\partial\mathbf{g}(\mathbf{x},\mathbf{u})}{\partial\mathbf{u}}\Delta\mathbf{u} + O\left(\Delta\mathbf{x}^2,\Delta\mathbf{u}^2,\Delta\mathbf{x}\Delta\mathbf{u}\right) \tag{2.6}$$

Neglecting second and higher order terms and using the fact that $\mathbf{f}_0 = \mathbf{f}(\mathbf{x}_0(\tau),\mathbf{u}_0(\tau)) = 0$ for the steady state under investigation leaves us - for the differential equations - with

$$\frac{d}{d\tau}\Delta\mathbf{x} \quad = \quad \frac{\partial\mathbf{f}(\mathbf{x},\mathbf{u})}{\partial\mathbf{x}}\Delta\mathbf{x} + \frac{\partial\mathbf{f}(\mathbf{x},\mathbf{u})}{\partial\mathbf{u}}\Delta\mathbf{u}$$

$$\equiv \quad \mathbf{A}\Delta\mathbf{x} + \mathbf{B}\Delta\mathbf{u} \tag{2.7}$$

where

$$\mathbf{A} = [a_{ij}] = \left[\frac{\partial f_i}{\partial x_j}\right], \quad \mathbf{B} = [b_{ij}] = \left[\frac{\partial f_i}{\partial u_j}\right] \tag{2.8}$$

and for the algebraic equations with

$$\mathbf{0} \quad = \quad \frac{\partial\mathbf{g}(\mathbf{x},\mathbf{u})}{\partial\mathbf{x}}\Delta\mathbf{x} + \frac{\partial\mathbf{g}(\mathbf{x},\mathbf{u})}{\partial\mathbf{u}}\Delta\mathbf{u}$$

$$\equiv \quad \mathbf{C}\Delta\mathbf{x} + \mathbf{D}\Delta\mathbf{u} \tag{2.9}$$

where

$$\mathbf{C} = [c_{ij}] = \left[\frac{\partial g_i}{\partial x_j}\right], \quad \mathbf{D} = [d_{ij}] = \left[\frac{\partial g_i}{\partial u_j}\right] \tag{2.10}$$

Solving 2.9 for $\Delta\mathbf{u}$ yields

$$\Delta\mathbf{u} = -\mathbf{D}^{-1}\mathbf{C}\Delta\mathbf{x} \tag{2.11}$$

and inserting the result into 2.7

$$\frac{d}{d\tau}\Delta\mathbf{x} = \left(\mathbf{A} - \mathbf{B}\mathbf{D}^{-1}\mathbf{C}\right)\Delta\mathbf{x} \tag{2.12}$$

is obtained. This reduces the system 2.4 to n_x equations. After introducing the system matrix $\mathbf{A}_s = \left(\mathbf{A} - \mathbf{B}\mathbf{D}^{-1}\mathbf{C}\right)$, equation 2.12 becomes the set of differential equations which is the center of MATSTAB

$$\frac{d}{d\tau}\Delta\mathbf{x} = \mathbf{A}_s\Delta\mathbf{x} \tag{2.13}$$

From an analytical point of view, equation 2.13 is a compact, linearized reformulation of the original equation set 2.4. However, from a practical point of view, a new problem occurs. Even though the matrices $\mathbf{A}$, $\mathbf{B}$, $\mathbf{C}$ and $\mathbf{D}$ are very sparse, the matrix $\mathbf{D}^{-1}$ is not (see Figures 4.4, 4.5 and 4.6). For fast execution, the sparsity of the matrix $\mathbf{A}_s$ is in general much more important than its size. Therefore MATSTAB does not apply equation 2.13 in an explicit but rather in an implicit manner. The specific algorithms used to solve equation 2.12 are outlined in Chapter 4. The main idea for overcoming the loss of sparsity - and hence the numerical problem - is to distinguish between state variables that are only coupled to a few neighboring nodes and state variables that are either coupled with all six neighboring nodes (e.g. neutron flux) or many hydraulic channels (e.g. mass flux).

2.1.2 Sparse Matrix Techniques

The idea behind sparse matrix techniques is very simple. Instead of storing a huge n by n matrix element for element and, therefore, using memory space for n^2, elements, one stores only the k nonzero elements and their position. For a full matrix where $k = n^2$ this scheme would use up to 3 times more memory, but for a sparse matrix where n is large and k is much closer to n than to n^2, the latter method is far more efficient.

This way to store a matrix is only useful, if basic linear operations like $\mathbf{C} = \mathbf{A} * \mathbf{B}$ and basic linear problems like $\mathbf{Ax} = \mathbf{b}$ can be calculated directly within the sparse format. The libraries with these 'sparse functions/algorithms' and their use is what is called sparse matrix technique. The programming environment MATLAB which was used to create MATSTAB provides a large and efficient base of functions and algorithms for 'sparse problems'.

2.1.3 Eigenvalues and Eigenvectors

Since the matrix $\mathbf{A}_s$ in 2.13 represents differential and algebraic equations, the standard eigenvalue equation

$$\mathbf{A}_s\mathbf{e}_i = \lambda_i\mathbf{e}_i \qquad (2.14)$$

does not apply. Instead the generalized eigenvalue equation must be used [30]:

$$\mathbf{A}_s\mathbf{e}_i = \lambda_i\mathbf{B}\mathbf{e}_i \qquad (2.15)$$

where $\mathbf{B}$ is a diagonal but singular [nxn] matrix of the form

$$
\mathbf{B} = \begin{bmatrix}
1 & 0 & \cdots & & & 0 \\
0 & \ddots & & & & \\
 & & 1 & & & \\
\vdots & & & 0 & & \vdots \\
 & & & & \ddots & \\
0 & & \cdots & & & 0
\end{bmatrix}
\left.\begin{array}{c} \\ \\ \\ \end{array}\right\} \text{Part referring to differential equations}
\left.\begin{array}{c} \\ \\ \\ \end{array}\right\} \text{Part referring to algebraic equations}
$$

Similar to the right eigenvectors $\mathbf{e}_i$ in 2.15, there are left eigenvectors $\mathbf{f}_i$ for $\mathbf{A}_s$

$$\mathbf{f}_i^T\mathbf{A}_s = \lambda_i\mathbf{f}_i^T\mathbf{B} \qquad (2.16)$$

The matrices containing all left and right eigenvectors

$$\mathbf{E} = [\mathbf{e_i}\ldots\mathbf{e_n}] \ , \quad \mathbf{F} = [\mathbf{f_i}\ldots\mathbf{f_n}] \qquad (2.17)$$

are related as follows

$$\mathbf{EF} = \mathbf{I} \qquad (2.18)$$

The matrices $\mathbf{E}$ and $\mathbf{F}$ have one more interesting property.

$$\mathbf{F}\mathbf{A}_s\mathbf{E} = \Lambda = \begin{bmatrix} \lambda_1 & & 0 \\ & \ddots & \\ 0 & & \lambda_n \end{bmatrix} \tag{2.19}$$

This allows to rewrite equation 2.13 by multiplying with $\mathbf{F}$ from the left and inserting the unity matrix $\mathbf{E}\mathbf{F}$,

$$\mathbf{F}\frac{d}{d\tau}\Delta\mathbf{x}(\tau) = \mathbf{F}\mathbf{A}_s\mathbf{E}\mathbf{F}\Delta\mathbf{x}(\tau) \tag{2.20}$$

to obtain

$$\frac{d}{d\tau}\left(\mathbf{F}\Delta\mathbf{x}(\tau)\right) = \Lambda\left(\mathbf{F}\Delta\mathbf{x}(\tau)\right). \tag{2.21}$$

Solving the differential equation above for $\mathbf{F}\Delta\mathbf{x}(\tau)$ leads to

$$\mathbf{F}\Delta\mathbf{x}(\tau) = e^{\Lambda\tau}\mathbf{F}\Delta\mathbf{x}(0) \tag{2.22}$$

or, after multiplying with $\mathbf{E}$ from the left

$$\Delta\mathbf{x}(\tau) = \mathbf{E}e^{\Lambda\tau}\mathbf{F}\Delta\mathbf{x}(0) \tag{2.23}$$

Stating the implicit sums in the matrix notation, equation 2.23 becomes

$$\Delta\mathbf{x}(\tau) = \sum_{i=1}^{n}\mathbf{e_i}e^{\lambda_i\tau}\mathbf{f_i}^T\Delta\mathbf{x}(0) \equiv \sum_{i=1}^{n}\Delta\mathbf{x}_i(\tau). \tag{2.24}$$

The last equation defines the vector $\Delta\mathbf{x}_i(\tau)$. Note the difference between the vector $\Delta\mathbf{x}_i(\tau)$ in equation 2.24 and the scalar x_i in equation 2.3. The vector $\Delta\mathbf{x}_i(\tau)$ is the contribution of the ith mode to all states at time τ, while the scalar $x_i(\tau)$ is the value of the ith component of the state vector $\mathbf{x}(\tau)$ at time τ. Let us study the mode

$$\Delta\mathbf{x}_i(\tau) = \mathbf{e}_i e^{\lambda_i\tau}[\mathbf{f}_i^T\Delta\mathbf{x}_i(0)] \tag{2.25}$$

The following interpretation of the eigenvectors and eigenvalues can be made.

Since both $e^{\lambda_i\tau}$ and $\mathbf{f}_i^T\Delta\mathbf{x}(0)$ are complex numbers, the shape of the mode $\Delta\mathbf{x}_i(\tau)$ is entirely defined by $\mathbf{e}_i$. Therefore, the *right eigenvector* $\mathbf{e}_i$ describes the relative magnitude and phase of the participating states.

On the other hand, the *left eigenvector* $\mathbf{f}_i$ determines how the mode is excited by the initial condition. Note that if $\Delta\mathbf{x}_i(0) = k_i\,\mathbf{e}_i$ for some scalar k_i, then only the i-th mode is excited, since according to equation 2.18, $\mathbf{f}_i^T\mathbf{e}_j$ equals one for $i = j$ and zero for all other cases.

The dominating *eigenvalue* governs the time domain evolution of the mode, in particular if $\lambda_i = \sigma_i + j\omega_i$ with $j = \sqrt{-1}$ then $\Delta\mathbf{x}_i(\tau) = \mathbf{k}_i e^{\sigma_i\tau}(\cos\omega_i\tau + j\sin\omega_i\tau)$.

The *stability* is described by the decay ratio (DR), which is the ratio of two consecutive maxima of the impulse response of the oscillating variable (Figure 2.1).
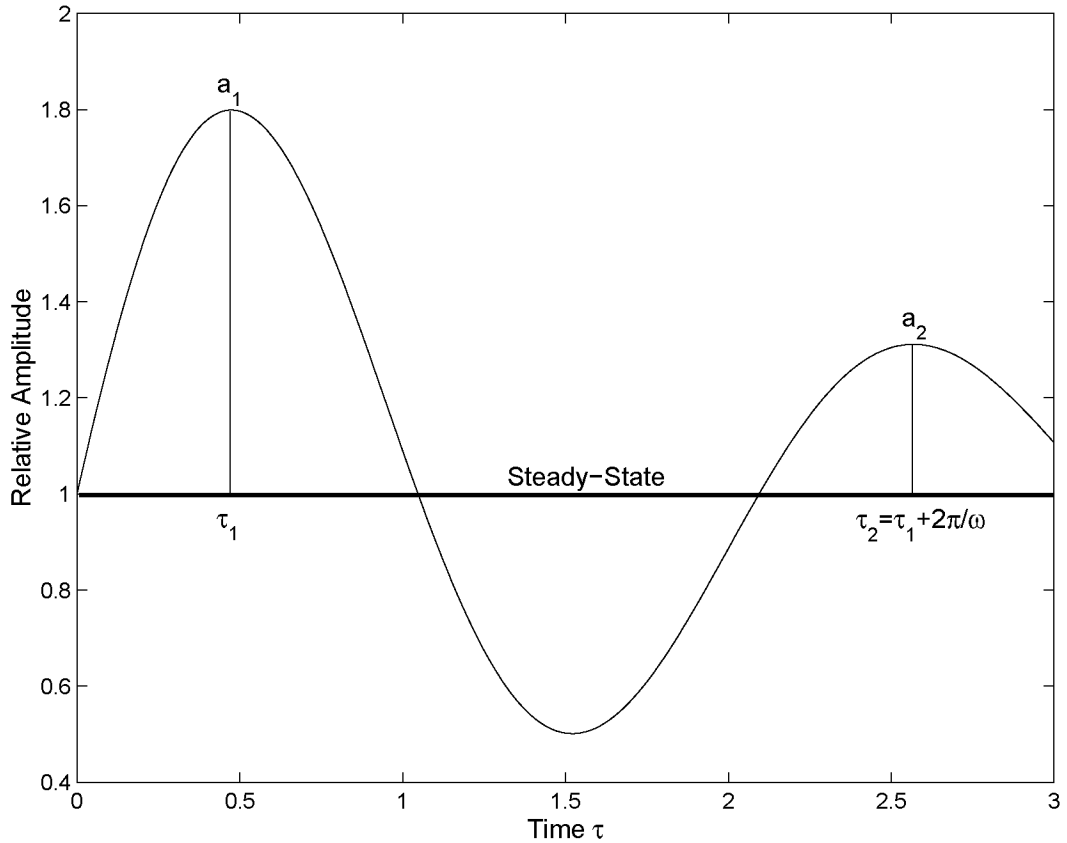
Figure 2.1: Definition of the Decay Ratio (DR)

$$DR = \frac{a_2}{a_1} = \frac{ke^{\sigma \tau_2}(\cos(\omega \tau_2) + j\sin(\omega \tau_2))}{ke^{\sigma \tau_1}(\cos(\omega \tau_1) + j\sin(\omega \tau_1))} \qquad (2.26)$$

The times τ_1 and τ_2 are defined by the local maxima. Therefore the cosine of $\omega \tau_1$ and $\omega \tau_2$ equals one. The sine of $\omega \tau_1$ and $\omega \tau_2$ equals zero respectively.

$$DR = \frac{ke^{\sigma \tau_2}(1 + j0)}{ke^{\sigma \tau_1}(1 + j0)} = \frac{ke^{\sigma \tau_2}}{ke^{\sigma \tau_1}} \qquad (2.27)$$

$$= e^{\sigma(\tau_2 - \tau_1)} \qquad (2.28)$$

$$= e^{2\pi \frac{\sigma}{\omega}} \qquad (2.29)$$

The dominating eigenvalue and its two associated eigenvectors (left and right) are the main computational results of MATSTAB. They are the basis of all further investigations. Chapter 5 shows ways to visualize and interpret the results in a much more complete manner than just displaying decay ratios.

2.2   The Structure of MATSTAB

MATSTAB is a family of modules and functions written in the high-performance computing environment MATLAB [59]. The five parts of MATSTAB are (Figure 2.2):

- INPUT:
  The collection and processing of the steady state plant data

- PROBLEM:
  The calculation of the system matrix $\mathbf{A_s}$

- SOLUTION:
  The calculation of the dominating eigenvalue and eigenvectors

- SOLUTION+:
  The calculation of additional (regional) eigenvalues and eigenvectors

- VISUALIZATION
  Visualization and analysis of the calculated properties

These parts themselves contain numerous modules which have a well defined interface for handing over the data. The high degree of modularization makes it possible to replace or extend existing models without restructuring larger parts of the code.

2.2.1   Input Data

To get reliable calculation results, it is essential to have input data which describes the actual plant state sufficiently accurate. Most of the codes used today use extensive input desks which are normally generated by a time consuming and tedious manual procedure.

Some of this workload was reduced with the introduction of a conversion tool developed by Vattenfall [43]. This program uses data files from the online steady state core simulator which are used to calculate and oversee thermal margins and are therefore running in almost every nuclear power plant. These so called distribution and master files [51] contain all relevant dynamic data.

The master file contains the information about the reactor/fuel geometry and the reactor model. The file stays the same for at least one cycle. The distribution file contains the data calculated by the simulator and is therefore different for every operating point. In contrast to manual and semiautomatic procedures, MATSTAB is able to access distribution and master files directly and automatically. This import function is very much hardware independent, i.e. it is possible to read any (binary) distribution file on any common (DEC, SUN, HP, SGI, LINUX, WINDOWS NT, WINDOWS 9x) operating system and platform. The only input which needs to be generated by the user, are some geometric data (downcomer, steam dome, pumps etc.) of the ex-core system, which is plant, but not time dependent. These data are
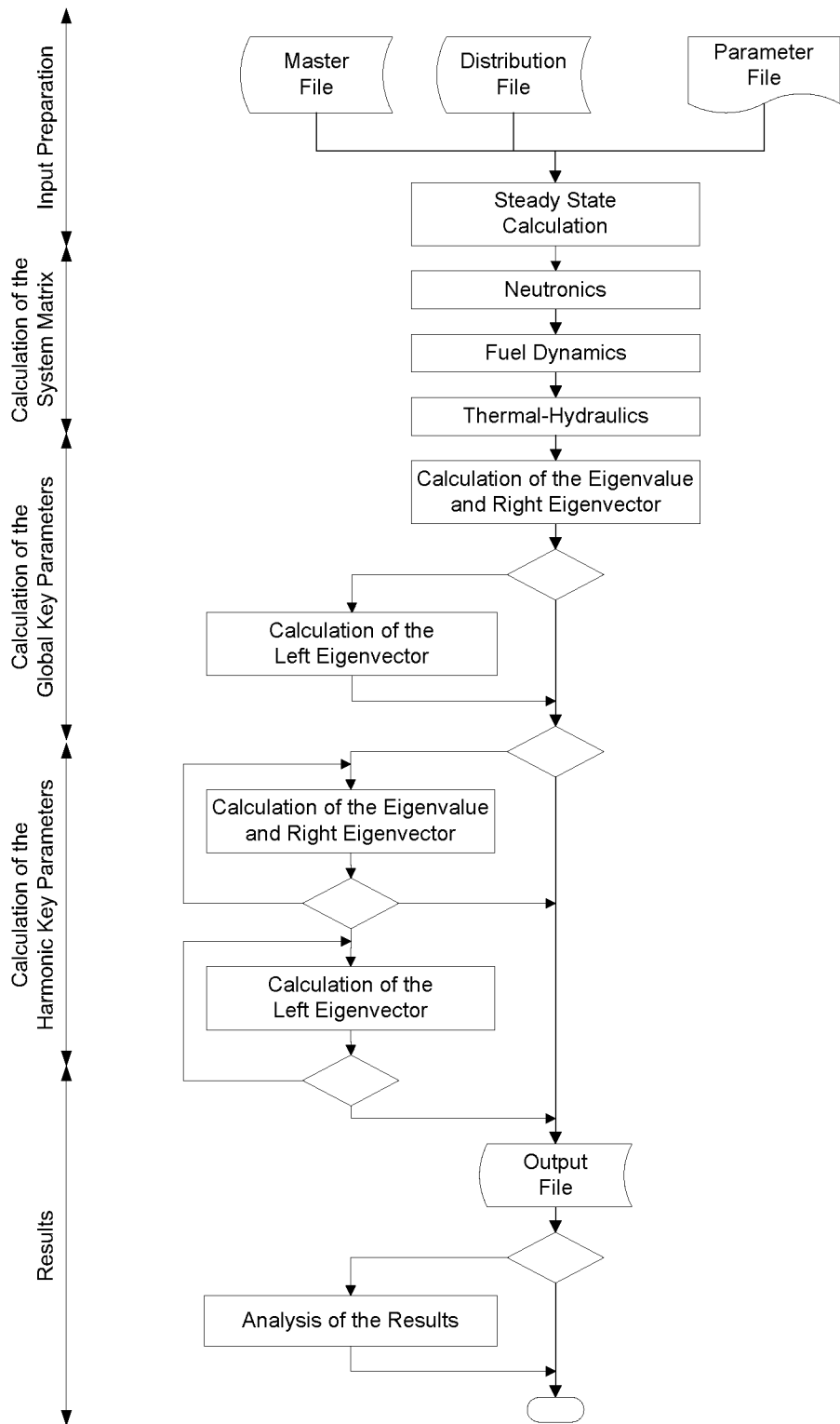
Figure 2.2: Structure of MATSTAB

supplied as a standard input file. In fact, this input file is a small subset of the RAMONA input file. To maintain some "backward" compatibility with RAMONA, it is possible, though not recommended, to use a normal RAMONA input desk combined with a RAMONA steady state calculation instead of the distribution and master files [92].

The input data from the online core simulator are self consistent, but from a simpler set of equations than the MATSTAB model. Therefore, it is not possible to use the distributions directly. To overcome this problem, the online steady state data is used as an input for a MATSTAB steady state module, generating the distributions which satisfy the set of equations used by MATSTAB.

2.2.2 Constructing the System Matrix A_s

The system matrix A_s introduced in 2.13 is composed of the sub-matrices A, B, C and D defined in 2.7 and 2.9. The linearized form of the $n_x + n_u$ equations is evaluated with the steady state values x_0 and u_0 (defined in 2.5, 2.6) to obtain the matrix coefficients a_{ij}, b_{ij}, c_{ij} and d_{ij} in 2.10, 2.8. For example, the algebraic equation for the void fraction is a function of the steam mass in a cell and the pressure.

$$\alpha = \alpha(m_g, P) = \frac{m_g}{\rho_g(P)V} \tag{2.30}$$

With the help of 2.10, this can be written as

$$\begin{aligned}
\Delta \alpha &= c_{\alpha m_g} \Delta m_g + c_{\alpha P} \Delta P \\
&= \frac{\partial \alpha}{\partial m_g} \Delta m_g + \frac{\partial \alpha}{\partial P} \Delta P \\
&= \frac{1}{\rho_g(P)V} \Delta m_g - \frac{m_g}{\rho_g^2(P)V} \frac{\partial \rho_g}{\partial P} \Delta P
\end{aligned} \tag{2.31}$$

The equation 2.31 which is valid for each node in the core, just with a different set of m_g, ρ_g and V, is actually programmed as a vector equation. $\Delta \alpha, \Delta m_g, \Delta P$ and ΔV are vectors of size 25 times the number of fuel assemblies.

After calculating A, B, C and D, the rows and columns in the matrix A_s are scaled to eliminate numerical problems due to the large absolute difference between the coefficients in the neutronics section and the values in the thermal hydraulic section.

It remains to be said, that the matrix A_s does not only contain all the equations describing the physics in the core, but also all the equations describing the ex-core system. On the one hand, the thermal hydraulic equations that are valid in the core extend naturally to the outer part of the reactor, on the other hand, some equations are needed in addition, for example; pump equations, system pressure and the flow distribution model.

A detailed description of the model and all equations used follows in the next Chapter. A detailed description of the structure of the matrix A_s is given in Appendix A.

2.2.3 Eigenvalue Calculation

The eigenvalues and their eigenvectors are the main output of MATSTAB. Therefore, the implemented calculation methods and their reliability are crucial for valid results. The generalized eigenvalue problem

$$\mathbf{A}_s \mathbf{e} = \lambda \mathbf{B} \mathbf{e} \qquad (2.15)$$

has a well known direct solution method [30]. However, the direct method contains steps which are not feasible for very large systems (e.g. 200'000x200'000) from a practical point of view (days of calculation time instead of minutes).

Fortunately, it is not necessary to calculate all eigenvalues and eigenvectors. MATSTAB uses iterative methods, which directly calculate the few dominant eigenvalues and their corresponding eigenvectors. This solution can be extended to the regional modes with the construction of a good starting guess, as will be described in Section 4.7.

As eigenvalue problems are very common in many engineering applications, there are a wide variety of codes available that work with iterative methods. Even though these codes are very sophisticated and advanced, as for example the functions available in MATLAB, they are not able to solve the specific system created by MATSTAB within reasonable time (minutes).

The method used in MATSTAB is not new, it is basically Newton's method, but it is extended and combined with subspace methods to take full advantage of the known and fixed structure of $\mathbf{A}_s$.

The detailed description of the methods follows in Chapter 4.

2.2.4 Visualization

The final numerical result, the eigenvalue/decay ratio, is interesting but does not give the complete picture. The real advantage of the frequency domain approach is not the faster execution time, but the additional information present in the eigenvectors.

Because the eigenvectors can be scaled in any way, the interesting aspect is their shape.

The right eigenvector describes the relative phase and magnitude of the participating states, the left eigenvector determines how the mode is exited by the initial conditions 2.25.

MATSTAB uses a modern graphical user interface to visualize the stabilizing and destabilizing regions in a core as well as the shape of the oscillations.

Chapter 5 is fully dedicated to the new possibilities and insights derived from this information.

Chapter 3

The Model

Contents

3.1   Choosing the RAMONA Model

Modeling BWR dynamics requires the simulation of the thermal-hydraulics and the neutronics as well as their mutual interactions. This involves the setting up and the solution of the partial differential equations describing the basic phenomenon. The interaction during instabilities in BWRs is shown in Figure 3.1.
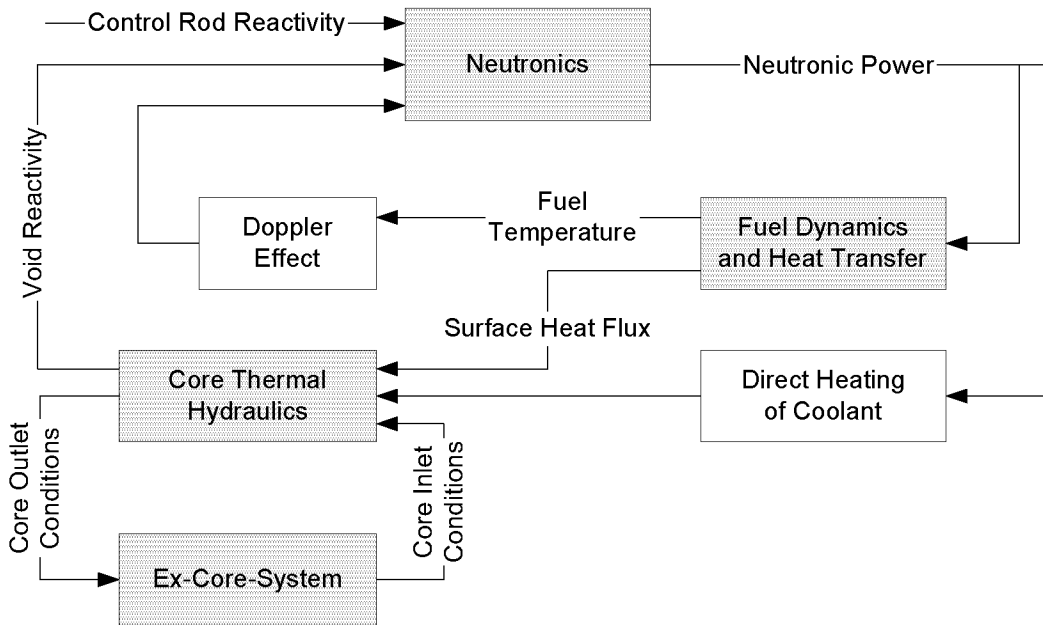
Figure 3.1: Neutronic/Thermal-Hydraulic Feedback System in a BWR

Four main interaction blocks can be noted:

- Core thermal hydraulics, which affects power production by fission and is often the trigger for instability mechanisms.

- Neutron kinetics, which is directly responsible for the power variation, as a consequence of the external and the feedback reactivity perturbations.

- Fuel dynamics and heat transfer, which act as a filter of power perturbations and introduce time delays between power production and coolant flow heating.

- Ex-core-systems which impose the boundary conditions to the core channels, thus influencing their stability.

As mentioned before, the physical model of MATSTAB was taken from RAMONA-3B. Naturally, MATSTAB does not contain all the features and details implemented in RAMONA

since the scope of transients to be analyzed is condensed from a wide variety to one only. Especially changes that happen in time, like the opening or closing of valves or the movement of control rods, are not meant to be modeled in MATSTAB.

To start with, it was not yet perfectly clear how good the new approach, was and to what detail one would be forced to go when using linear equations. Therefore, the RAMONA model was transferred in a one to one scope.

This means that not only the proven and established principles were mined out, but also some past sins as well as unnecessary burdens found their way into MATSTAB (e.g. a too detailed model for the fuel temperatures and some thermal hydraulic properties or different numbering schemes in the neutronic and thermal hydraulic part of the core).

Since MATSTAB was just a 1-D model at its very beginning, this overkill had no significant influence on the computational effort needed. Actually, the ability to compare the results of the two codes in a very direct manner was an intended and welcome benefit.

After everything went smooth in 1-D, MATSTAB was extended to handle 3-D neutronics and one thermal hydraulic channel per fuel assembly. The resulting explosion in demand for CPU power, and most important, system memory, made it necessary to simplify some of the equations. It goes without saying, that the simplifications were judged against their physical impact.

The following section presents some comments on the BWR reactor types implemented and an overview over the nodalization scheme, in order to give an impression of the scale and detail of the model. The subsequent sections address the major changes introduced by MATSTAB to the RAMONA-3B model. The complete model implemented in MATSTAB can be found in Appendix A.

For the sake of convenience, Appendix A is written like a normal chapter in its own right with detailed derivations. It can therefore be read as a whole, without flipping back and forth between Appendix A and Chapter 3. Consequently, all changes discussed below will also be found in Appendix A.

3.1.1 Nodalization Scheme

As mentioned before, MATSTAB was and still is developed at the Forsmark site in Sweden. The three Forsmark reactors were supplied by ABB. The Leibstadt NPP situated in Switzerland, which was integrated in the project later on, is a BWR6 supplied by GE. As far as modeling is concerned, the plants differ mainly in their pump types; internal pumps are used in Forsmark and jet pumps in Leibstadt (Figure 3.2).

Both pump types are part of the MATSTAB/RAMONA model. The other differences are mainly in their geometrical data which are supplied by the user in the file `parameter.inp`. Besides these differences in construction, the specification of the fuel, such as heat transfer coefficients and pressure drops over spacers, are also supplied as an input by the user.

1. Vent and head spray
2. Steam dryer lifting lug
3. Steam dryer assembly
4. Steam outlet
5. Core spray inlet
6. Steam separator assembly
7. Feedwater inlet
8. Feedwater sparger
9. Low-pressure coolant injection inlet
10. Core spray line
11. Core spray sparger
12. Top guide
13. Jet pump assembly
14. Core shroud
15. Fuel assemblies
16. Control blade
17. Core plate
18. Recirculation water inlet
19. Recirculation water outlet
20. Vessel support skirt
21. Shield wall
22. Control rod drives
23. Control rod drive hydraulic lines
24. In-core flux monitor

Figure 3.2: The Leibstadt BWR6 Reactor
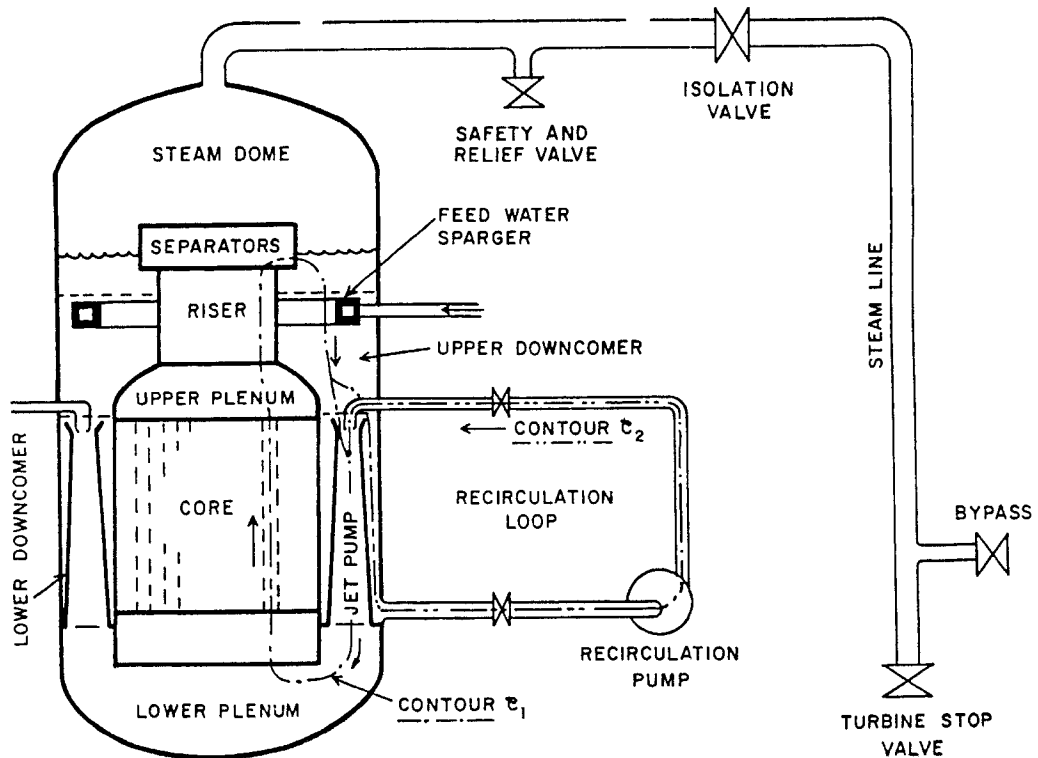
Figure 3.3: Schematic View of the Leibstadt Reactor

This allows MATSTAB to model a wide range of different boiling water reactors. A more schematic view of the reactor is shown in Figure 3.3.

The complete model is divided into 8 regions (downcomer 1&2, lower plena 1&2, core, bypass, riser, steam dome), each of which has an individual and variable number of nodes. In addition to these physical nodes, most sections also have a non physical entry-node containing the boundary conditions. The number of nodes in each section, as well as several parameters for each node, may be chosen by the user, see Figure 3.4.

The nodes are numbered counter-clockwise, beginning in the downcomer 1 and ending in the steam dome. Each core plane is subdivided into channels that coincide with the fuel assemblies. Within a plane, the numbering begins with channel 1 and ends with the bypass. The values in Figure 3.4 may be changed by the user. However, they should reflect the physical reality and remain the same for all cases. Only a major plant upgrade would introduce a change.

The only numbers which have to be adjusted annually are the parameters for the fuel, i.e. at the beginning of a cycle, when a new fuel type is introduced, its parameters have to be added to the parameter file.
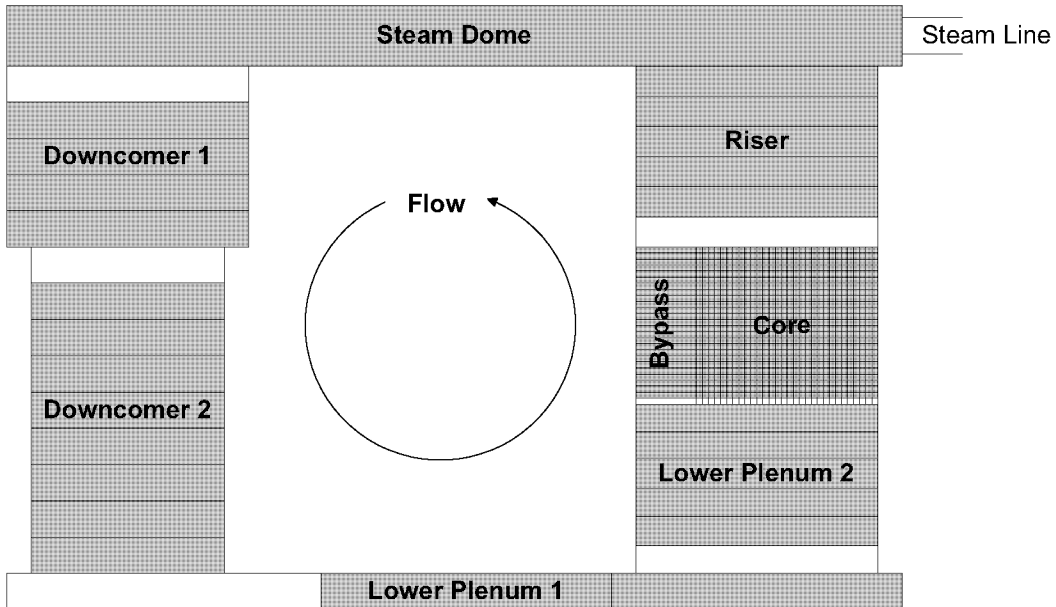
	Axial Nodes	Flow Area $[m^2]$	Height $[m]$	Hydraulic diameter $[m]$
Leibstadt				
Downcomer 1	6	10.330	5.073	1.160
Downcomer 2	6	0.720	4.384	0.128
Lower Plenum 1	2	9.260	6.000	6.100
Lower Plenum 2	3	10.510	1.790	0.300
Core Channel	25	Fuel type dependent		
Bypass		7.420		0.030
Riser	5	8.040	4.375	0.168
Steam Dome		20.960	8.460	5.170
Forsmark 1				
Downcomer 1	4	21.990	3.160	1.440
Downcomer 2	8	12.530	7.640	1.440
Lower Plenum 1	2	10.250	0.930	0.216
Lower Plenum 2	5	10.250	4.220	0.216
Core Channel	25	Fuel type dependent		
Bypass Channel		1.818		0.025
Riser	5	8.500	2.900	0.246
Steam Dome		25.540	8.540	10.000

Figure 3.4: Nodalization Scheme of the Leibstadt and Forsmark Reactors

3.1.2   Inconsistencies with the POLCA Model

In the beginning, MATSTAB was designed to use a steady state calculation of RAMONA as the starting point for its own calculations. The various data vectors (also called distributions) saved by RAMONA, such as cross sections, neutron fluxes, temperatures etc., could easily be loaded into MATSTAB, since the equations and parameters used were identical. This method was very convenient when comparing results. However, once trust in MATSTAB calculations was established, it was much simpler to use the distributions calculated from the online core simulator POLCA [1]. This simulator is used to overview various safety relevant numbers (e.g. thermal margins) and calculates the most recent state of the reactor core at least every half hour.

These distribution files are a natural starting point for all extended reactor calculations. As a matter of fact, also the input of RAMONA calculations is based on the very same files. Therefore, it is not only convenient but also logical to omit the RAMONA calculations in-between.

Unfortunately, the POLCA model differs somewhat from the neutronic model used in RA-MONA, as it is optimized to reflect the current state of the reactor and not to investigate future transients. Since MATSTAB only needs a good steady state, use of either model is possible. In fact, the POLCA model is even more suitable, since its degree of sophistication is better adapted for steady state calculations.

The first attempt to use steady state data from POLCA distribution files as a base for MAT-STAB calculations failed miserably. It took an in depth investigation to understand what went wrong, because the comparison between POLCA and RAMONA distributions showed good agreement.

The explanation, as far as we understand the problem today, lies in some non-obvious inconsistency of the data. Even though both sets of distributions fit their own equations well, there is a small discrepancy with respect to the equation of the other model. For example, the cross sections are only known to a certain precision. The same small error is reflected in a neutron flux calculation based on these cross sections. Now, if this neutron flux is inserted in the equations of the other model which differs in the calculation for boundary terms, one could readily argue that it also fits these equations assuming different cross sections. The new cross sections differ, however, more from the reality than their uncertainty allows. This leads to wrong results. The resulting error was that large, that the temperatures for the fuel zones were wrong by up to 100 degrees. Since all countermeasures to make the data consistent were in vain, the POLCA model was eventually coded into MATSTAB. Now the model used in MATSTAB is consistent with the steady state data used as input. The above explanation is also confirmed by the fact that the currently ongoing implementation of the POLCA 7 model [3] shows the same problems (POLCA 7 is a major update to POLCA 4 and uses a more detailed TH model as well as a two group neutronic model).

Since also the POLCA 4 model used in MATSTAB differs from the original POLCA 4 model by the simplifications introduced below, a few power-void iterations are executed to definitely adapt the input data to the model changes introduced in MATSTAB.

3.2   Neutron Kinetics and Power Generation

The original neutronic model from RAMONA or POLCA with eight differential equations per node (two energy groups and six delayed neutron groups) would represented a heavy computational burden. Especially the spatial coupling, which relates most of the roughly 9'000 nodes in a half-core case to its six neighbors, represented an obstacle which is expensive in computer time to overcome. Therefore, MATSTAB uses a slightly simplified neutronic model.

3.2.1   Fast and Thermal Neutron Flux

MATSTAB is based on a $1\frac{1}{2}$ energy group model (neglecting the divergence term of the thermal flux) with a simplified representation of the six delayed neutron groups. The power generation in the reactor core is calculated with full three-dimensional kinetics. Each individual fuel assembly is modeled separately and is subdivided into 25 axial nodes. For each fuel assembly, the burnup, the control rod history, the thermal parameters and the geometry e.g. spacers are given as an input. The operating point dependent data as nuclear cross-sections as well as many of the thermal hydraulic parameters are described as function of temperature, pressure and void etc.

The major changes with respect to POLCA are the use of the prompt jump approximation and a simplification of the precursor equation as shown below. For the complete derivation of all following equations see Appendix A. For convenience, the equations below are numbered the same way as in the Appendix.

The time derivative of the fast and the thermal flux are both set to zero, which means that the left hand side of A.14 and A.15 are set to zero.

$$\frac{1}{V_1}\frac{d\overline{\varphi}_{1n}}{d\tau} = -\sum_{m=1}^{6}\frac{1}{h_{nm}}\mathbf{J}_{1,nm} - (\Sigma_{a1}+\Sigma_r)\overline{\varphi}_{1n} + (1-\beta)\left(\nu_1\Sigma_{f1}\overline{\varphi}_{1n}+\nu_2\Sigma_{f2}\overline{\varphi}_{2n}\right)$$
$$+ \sum_{d}\lambda_d\overline{C}_d = 0 \tag{A.14}$$

$$\frac{1}{V_2}\frac{d\overline{\varphi}_{2n}}{d\tau} = -\sum_{m=1}^{6}\frac{1}{h_{nm}}\mathbf{J}_{2,nm} - \Sigma_{a2}\overline{\varphi}_{2n} + \Sigma_r\overline{\varphi}_{1n} = 0 \tag{A.15}$$

The prompt jump approximation is valid, if the life time of a neutron is much smaller than the studied phenomena. Physically it is an immediate adaption of the neutron flux to perturbations.

3.2.2 Delayed Neutrons

The life time of the precursors

$$\frac{d\overline{C}_{dn}}{d\tau} = \beta_d \left(\nu_1 \Sigma_{f1} \overline{\varphi}_{1n} + \nu_2 \Sigma_{f2} \overline{\varphi}_{2n}\right) - \lambda_d \overline{C}_{dn} \quad , \quad \begin{array}{l} d = 1, \ldots, 6 \\ n = nodenumber \end{array} \qquad (A.16)$$

is much closer to the time a density wave needs to pass the reactor than the neutron life time and, therefore, significant. The time derivative of the precursors may therefore not be set to zero. Nevertheless, it is possible to simplify equation A.16 without much loss in accuracy.

Equation 2.25 describes the time dependence of a state variable. For the variable $\overline{C}_d n(\tau)$ it reads as follows

$$\overline{C}_{dn}(\tau) = \overline{c}_{dn} e^{\lambda \tau} \qquad (A.28)$$

where $\overline{c}_{dn}$ is a scalar and not time dependent. Equation A.16 may now be written as follows.

$$\frac{d\overline{c}_{dn} e^{\lambda \tau}}{d\tau} = \beta_d (\nu_1 \Sigma_{f1} \overline{\varphi}_{1n} + \nu_2 \Sigma_{f2} \overline{\varphi}_{2n}) - \lambda_d \overline{C}_{dn} \qquad (A.29)$$

It is now possible to carry out the derivation with respect to time. This transforms the differential equation into an algebraic equation.

$$\lambda \overline{C}_{dn} = \beta_d (\nu_1 \Sigma_{f1} \overline{\varphi}_{1n} + \nu_2 \Sigma_{f2} \overline{\varphi}_{2n}) - \lambda_d \overline{C}_{dn} \qquad (A.30)$$

Solving for $\overline{C}_{dn}$ yields

$$\overline{C}_{dn} = \frac{\beta_d}{\lambda - \lambda_d} (\nu_1 \Sigma_{f1} \overline{\varphi}_{1n} + \nu_2 \Sigma_{f2} \overline{\varphi}_{2n}) \qquad (A.31)$$

$\overline{C}_{dn}$ is depending on λ which is unknown. Therefore, the starting guess of λ is used to calculate $\overline{C}_{dn}$. This simplification is good enough, as long as the starting guess for λ is reasonable. The draw back is however, that λ is complex and therefore the matrix **A** becomes complex too. It remains to mention that this simplification is used for the POLCA model as well as for the RAMONA model. Inserting A.31 into A.26 yields

$$0 = -\left[\sum_{m=1}^{6} \mathbf{X}_{1,nm} + \Sigma_{a1} + \Sigma_r\right] \overline{\varphi}_{1n} + \sum_{m=1}^{6} \mathbf{Y}_{1,nm} \overline{\varphi}_{1m} + \tilde{\beta}(\nu_1 \Sigma_{f1} \overline{\varphi}_{1n} + \nu_2 \Sigma_{f2} \overline{\varphi}_{2n}) \qquad (A.32)$$

where

$$\tilde{\beta} = 1 - \beta + \sum_d \frac{\beta_d \lambda_d}{\lambda + \lambda_d} \qquad (A.33)$$

Solving A.27 for $\overline{\varphi}_{2n}$ yields

$$\overline{\varphi}_{2n} = \frac{\left[\Sigma_r - \sum_{m=1}^{6} \mathbf{X}_{2,nm}\right]}{\Sigma_{a2}} \overline{\varphi}_{1n} + \frac{\sum_{m=1}^{6} \mathbf{Y}_{2,nm}}{\Sigma_{a2}} \overline{\varphi}_{1m}. \qquad (A.34)$$

Inserting the solution into A.32 leads to

$$
0 = - \left[\sum_{m=1}^{6} \mathbf{X}_{1,nm} + \Sigma_{a1} + \Sigma_r - \tilde{\beta}\nu_1\Sigma_{f1} - \tilde{\beta}\nu_2\Sigma_{f2} \frac{\left[\Sigma_r - \sum_{m=1}^{6}\mathbf{X}_{2,nm}\right]}{\Sigma_{a2}} \right] \bar{\varphi}_{1n}
$$
$$
+ \left[\sum_{m=1}^{6} \mathbf{Y}_{1,nm} + \tilde{\beta}\nu_2\Sigma_{f2} \frac{\sum_{m=1}^{6}\mathbf{Y}_{2,nm}}{\Sigma_{a2}} \right] \bar{\varphi}_{1m}
$$

(A.35)

The algebraic equation A.35 which is the center of the neutronics in MATSTAB contains all information of the original eight differential equations besides the small differences introduced by the simplifications mentioned above.

3.3 Thermal Conduction

Associated with each neutronic node is an average fuel pin for which the thermal energy source and heat conduction are calculated. The calculated average fuel temperature feeds back into the neutronics (Doppler effect) and the calculated heat flux from the cladding surface enters the hydraulics calculations.

The thermal energy storage and conduction in the fuel pins, consisting of the fuel pellets, of the gas gap between pellet and cladding and of the fuel cladding is modeled with the following assumptions.

- Fuel and cladding are rigid, retaining their cylindrical geometries. Possible variations in time of the gas gap width can be taken into account by a temperature dependent gap conductance.

- The volumetric heat generation q_f''' is uniformly distributed over the fuel pellet cross section. Gamma heat generation in the gas gap and the cladding is ignored.

- Axial and azimuthal conduction is negligible

- The thermal properties like heat capacity, conductivity etc. can be represented with the correlations stated below.

3.4 Thermal-Hydraulics

The thermal-hydraulics model of RAMONA and hence of MATSTAB is a four-equation, non-homogeneous, non-equilibrium one-dimensional two-phase flow model with constitutive equations for thermodynamic state variables. Thermal non-equilibrium between the phases is accounted for by allowing the liquid in a two-phase mixture to depart from saturated conditions, while the vapor is assumed to be at saturation. Hydrodynamic non-equilibrium, i.e. un-equal velocities of the two phases, is introduced via a slip correlation.

3.5 Summary

MATSTAB uses a four-equation, non-homogeneous, non-equilibrium, one-dimensional, two-phase flow model for the thermal-hydraulics. The neutronic model is based on a $1\frac{1}{2}$ energy group approach with six delayed neutron groups. The power generation in the reactor core is calculated with full three-dimensional kinetics. Each individual fuel assembly is modeled separately and is subdivided into 25 axial nodes.

The fast and the thermal neutron flux are represented with algebraic equations. The precursors are also represented with algebraic equations, but using a more sophisticated approach. These simplifications are based on physical judgment and showed no significant influence on the calculation results.

Chapter 4

Calculation of the Key Parameters

Contents

4.1 The Numerical Problem

The key values in MATSTAB are the eigenvalue λ and the eigenvector $\mathbf{e}_i$ in 2.25. In order to calculate λ and $\mathbf{e}_i$ one must solve the generalized eigenvalue problem 2.15. Using the standard nomenclature from linear algebra textbooks [30], 2.15 can be written as follows.

$$\mathbf{Ae} = \lambda\mathbf{Be} \tag{4.1}$$

$$\mathbf{A} \in C^{nxn}, \quad \mathbf{B} = \begin{bmatrix} 1 & 0 & & \cdots & & 0 \\ 0 & \ddots & & & & \\ & & 1 & & & \\ \vdots & & & 0 & & \vdots \\ & & & & \ddots & \\ 0 & & \cdots & & & 0 \end{bmatrix}$$

As stated earlier, the analytical solution for 4.1 is well known and can be derived with various decomposition methods [30]. However, the computational effort for large matrices grows with n^2 and becomes very soon infeasible.

In the case where only one or a few eigenvalue/eigenvector pairs are needed, iterative methods are a practical and fast solution. There are numerous efficient algorithms available for reasonable sized systems e.g. [30], [100], [90], [23], [53] and many others. Some robust and general methods are also directly available as FORTRAN programs or modules like ARPACK [50], NSPCG [69] and others.

However, to solve 2.25 an algorithm must fulfill the following requirements in a efficient way.

- Handle a *non-symmetric* matrix $\mathbf{A}$

- Handle the *generalized* eigenvalue problem

- Handle a *very large* matrix $\mathbf{A}$

- Handle a *complex* matrix $\mathbf{A}$

- Be applicable for a *sparse* matrix $\mathbf{A}$

This list is ordered in decreasing difficulty and rules out most of the published algorithms. From the remaining possibilities, the LANCZOS method [20],[75] and the ARNOLDI iteration [37],[89] are the most promising. Nevertheless, these state-of-the-art methods were too general to solve 2.15 efficiently. MATSTAB therefore uses a tailored subspace method that takes full advantage of the known and fixed structure of $\mathbf{A}$, combined with an extended version of Newton's method. Subspace methods and Newton's method are not new in this field, see [80] and [30]. However, their combination does not appear in the literature.

Basically the matrix **A** is divided into suitable sub-matrices $\mathbf{A}_i$ that form a set of linear sets of equations. The sub-matrices are chosen in a way that it becomes easier to solve the resulting set of equations. Unfortunately, it is not possible to decouple the subsets completely and therefore an outer iteration over the sub-solutions is necessary. The details of this approach are described in the six sections of this chapter. The first two sections introduce the standard numerical methods and their modification for MATSTAB while the later four sections describe the algorithms specifically designed for MATSTAB. Please note, that in a section dealing with numerical methods, **A** stands for any matrix while speaking about MATSTAB, **A** stands for the main matrix in the linearized BWR stability problem.

Structure of this chapter:

1. Solving $\mathbf{Ax} = \mathbf{b}$ for a very large **A**

2. Solving $\mathbf{Ax} = \lambda\mathbf{Bx}$ for specific λ's

3. Partitioning into subspaces

4. The MATSTAB algorithm for the global mode

5. Calculating the left eigenvector

6. The MATSTAB algorithm for the regional mode

4.2 Solving Ax = b for a Very Large Matrix A

Whatever algorithm is used to solve a large eigenvalue problem, one must be able to solve efficiently matrix equations of the form

$$\mathbf{Ax} = \mathbf{b} \tag{4.2}$$

The straightforward approach would be to invert **A**, but the algorithms to invert a matrix are computational very expensive and only recommendable if the explicit answer for $\mathbf{A}^{-1}$ is needed. To solve 4.2 for **x**, $\mathbf{A}^{-1}$ is of no interest. Depending on the size and structure of the matrix, MATSTAB uses either Gaussian elimination to solve equation sets with an easy structure, the **LU** decomposition for a moderate structured or the iterative conjugate-gradient method for a difficult structured equation set 4.2.

4.2.1 LU - Decomposition

Any square matrix **A** can be decomposed into a lower and upper triangular matrix.

$$\mathbf{A} = \mathbf{LU} \tag{4.3}$$

$$
\mathbf{L} = \begin{bmatrix} 1 & 0 & 0 & \ldots & 0 \\ * & 1 & 0 & & \vdots \\ * & \ddots & \ddots & \ddots & 0 \\ \vdots & & * & 1 & 0 \\ * & \ldots & * & * & 1 \end{bmatrix} \qquad \mathbf{U} = \begin{bmatrix} * & * & \ldots & * & * \\ 0 & * & & & \vdots \\ 0 & \ddots & \ddots & & * \\ \vdots & & 0 & * & * \\ 0 & \ldots & 0 & 0 & * \end{bmatrix} \qquad * \in C
$$

Where $\mathbf{L}$ is the lower triangular matrix and $\mathbf{U}$ is the upper triangular matrix. The equation

$$
\mathbf{Ax} = \mathbf{LUx} = \mathbf{b} \tag{4.4}
$$

can thus be solved with

$$
\mathbf{x} = \mathbf{U}^{-1}\mathbf{L}^{-1}\mathbf{b} \tag{4.5}
$$

Because of the structure of $\mathbf{L}$ and $\mathbf{U}$, equation 4.4 is very efficiently solvable with backward substitution. It is not necessary to calculate $\mathbf{L}^{-1}$ or $\mathbf{U}^{-1}$. The major computational work lies in the decomposition 4.3.

To emphasize the fact that $\mathbf{L}^{-1}$ and $\mathbf{U}^{-1}$ are not calculated, 4.5 is written as

$$
\mathbf{x} = \mathbf{U}\backslash(\mathbf{L}\backslash\mathbf{b}) \tag{4.6}
$$

or

$$
\mathbf{x} = \mathbf{A} \underset{LU}{\backslash} \mathbf{b} \tag{4.7}
$$

To illustrate the problems of the $\mathbf{LU}$ decomposition, the real matrices encountered in MAT-STAB are discussed. Figure 4.1 shows the structure of the matrix $\mathbf{A}_{tu}$

$$
\mathbf{A}_{tu} = \begin{bmatrix} \mathbf{u}_{t,1}^T & \mathbf{0} \\ \mathbf{A}_t - \lambda_k \mathbf{B}_t & -\mathbf{B}_t \mathbf{e}_{t,k} \end{bmatrix}
$$

which is used in step 2 of algorithm 4.6. The blank part of the matrix represents zero elements and the remaining part represents non-zero elements. The large *black triangle* is not as densely filled with numbers as it looks. In fact the dots should form a grid with two black dots every 50 points, but the resolution of the Figure suppresses the 48 white points in between.

Figures 4.2 and 4.3 show the $\mathbf{L}$ and $\mathbf{U}$ factors of $\mathbf{A}_{tu}$. The number of non-zero values in $\mathbf{L}$ and $\mathbf{U}$ is approximately 3 times higher than the number of non-zeros in $\mathbf{A}_{tu}$. Hence, the construction of this sub-matrix succeeded and the sparsity is in this case preserved.

Although the $\mathbf{LU}$ decomposition is much faster than the true inversion of $\mathbf{A}_{tu}$, some drawbacks remain. A very large $\mathbf{A}$ is normally, and especially in our case, truly sparse. Less than 0.1% of all entries in $\mathbf{A}_{tu}$ are different from zero. The algorithms take profit of this property and conduct no calculations for the "zero" parts of the resulting matrix. Unfortunately, the $\mathbf{L}$ and $\mathbf{U}$ factors of a sparse matrix are not necessarily sparse too. This fact increases extensively the computing time, and more crucial, the memory requirements of $\mathbf{L}$ and $\mathbf{U}$.
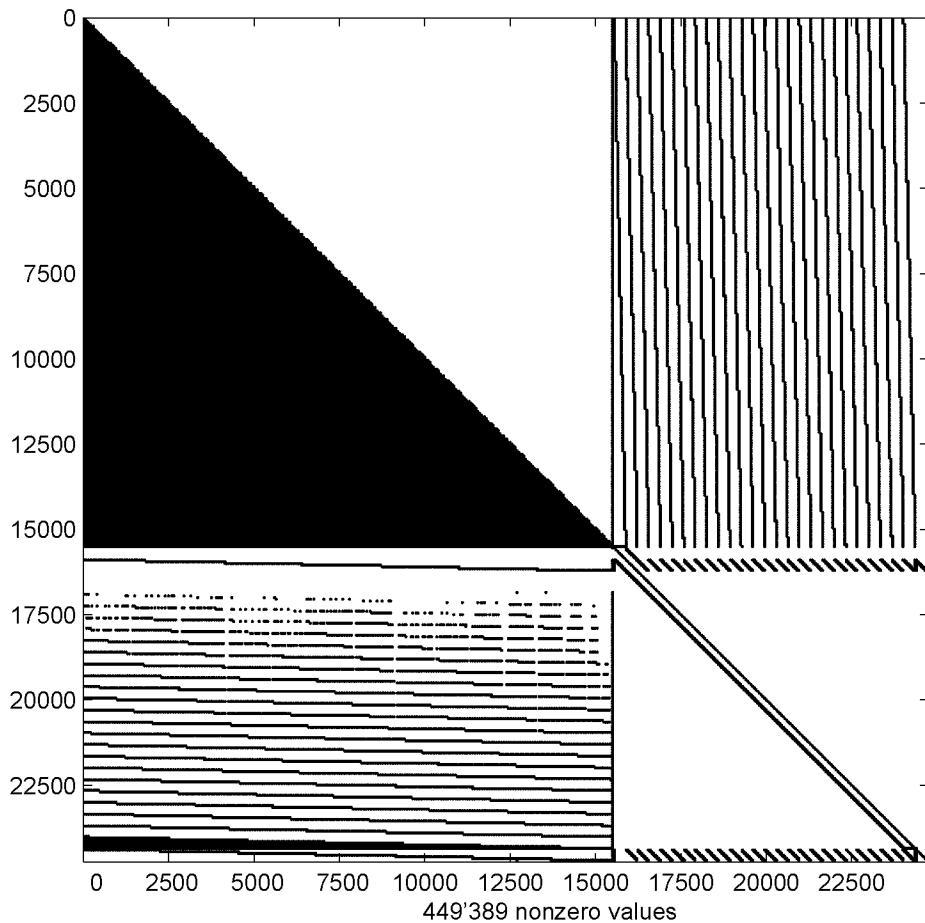
Figure 4.1: Structure of the Matrix $\mathbf{A}_{tu}$ Used in Step 2 of Algorithm 4.6

The requirements for a decomposition of some matrices appearing in MATSTAB are prohibitively high. Figures 4.4, 4.5 and 4.6 show the **LU** decomposition of the matrix $\mathbf{A}_n$, the neutronic part of the matrix **A**. Even though the matrix $\mathbf{A}_n$ is relatively small, and the structure of the matrix is more appropriate for an efficient numerical treatment than the structure of $\mathbf{A}_{tu}$, the loss of sparsity is very significant. The non-zeros and, therefore, the memory requirements are multiplied by a factor of 330. So the **LU** decomposition of $\mathbf{A}_n$ takes 250MB of RAM and nearly an hour of computing time. The reason for the different behavior of $\mathbf{A}_{tu}$ and $\mathbf{A}_n$ lies in the physical structure of the underling equations. The thermal hydraulics properties described in $\mathbf{A}_{tu}$ are in most cases only coupled to the up- and downstream neighbors. The neutronic properties of $\mathbf{A}_n$ on the opposite, are coupled with all six spatial neighbors. It is this interconnection with many other nodes, that makes the decomposition of $\mathbf{A}_n$ computationally expensive. To overcome this technical bottle neck, MATSTAB uses the iterative conjugate gradient method explained in the next section to solve equations of this type.
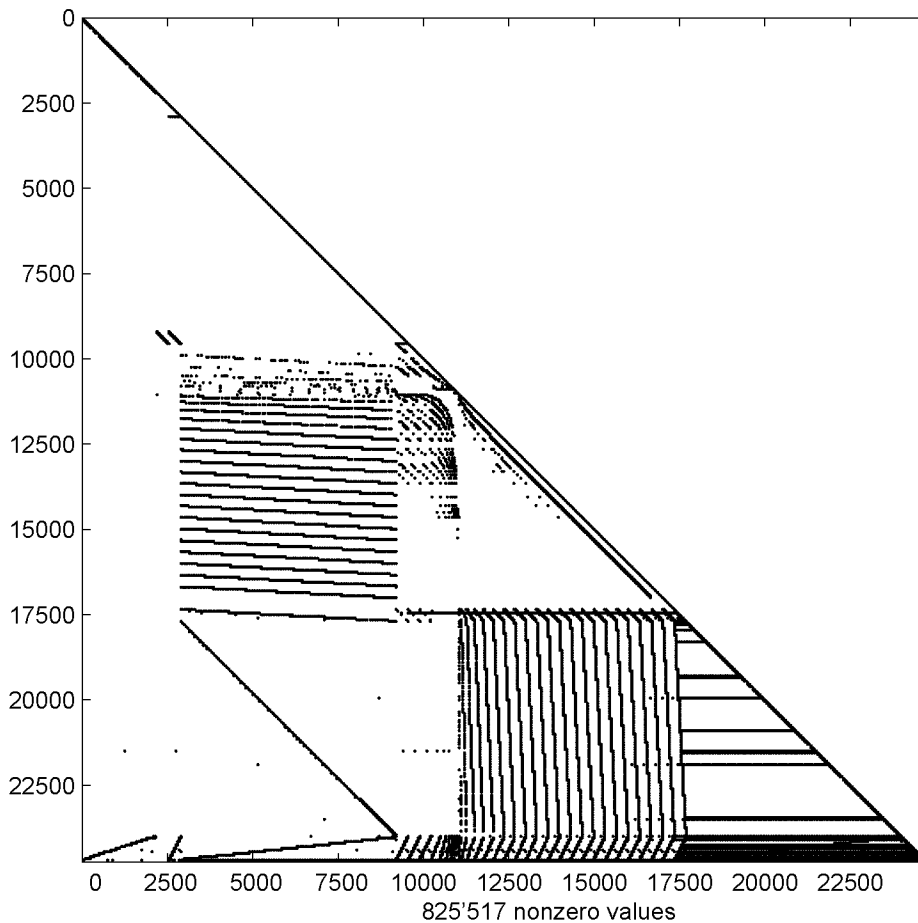
Figure 4.2: Lower Triangular Part of $\mathbf{A}_{tu}$

4.2.2 Conjugate Gradient Method

The method of conjugate gradients (CG) can be found in most numerical linear algebra textbooks [31], [90]. There are several slightly different versions that converge with different speed depending on the structure of $\mathbf{A}$. For the sake of completeness, we state the basic ideas behind conjugate gradients and the algorithm implemented in MATSTAB.

Assuming $\mathbf{A}$ is positive definite, for the functional

$$F(\mathbf{x}) \equiv \frac{1}{2}\mathbf{x}^T \mathbf{A}\mathbf{x} - \mathbf{x}^T \mathbf{b} \qquad (4.8)$$

with its gradient

$$\nabla F(\mathbf{x}) = \mathbf{A}\mathbf{x} - \mathbf{b} \qquad (4.9)$$

the minimization problem $\nabla F(\mathbf{x}) = 0$ is equivalent to solving $\mathbf{A}\mathbf{x} = \mathbf{b}$. In the following, the minimization of F with respect to a particular direction $\mathbf{p}$ plays a central role. Optimization
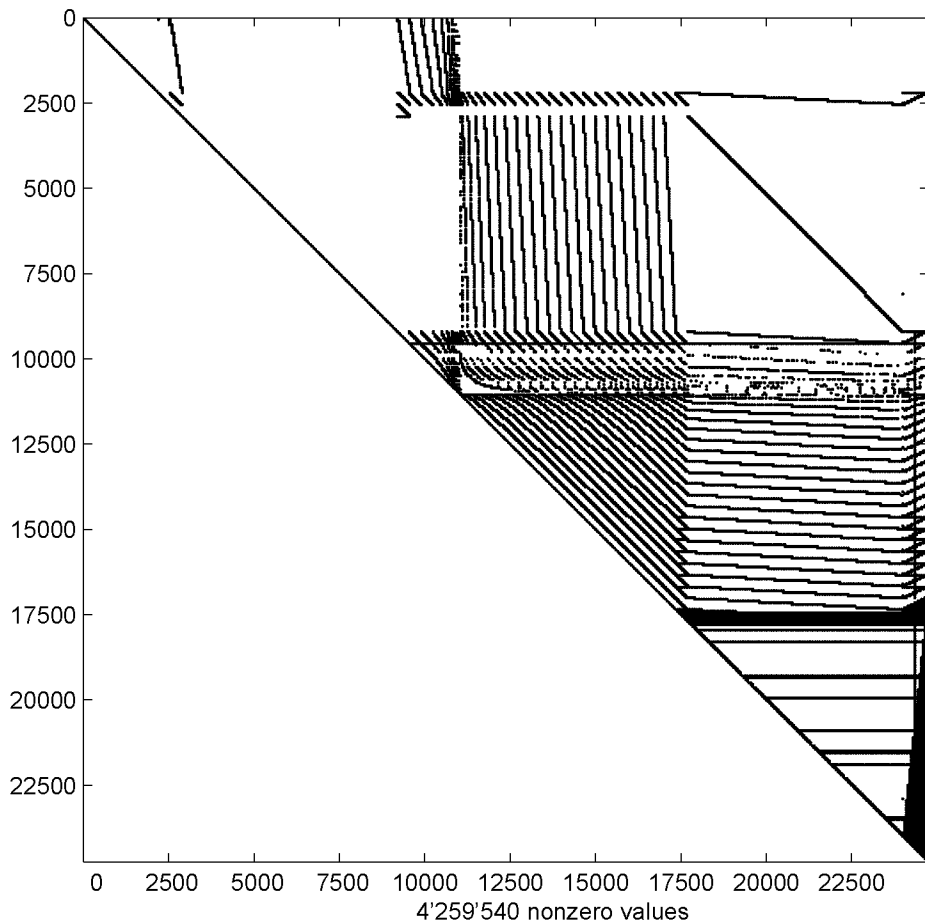
Figure 4.3: Upper Triangular Part of $\mathbf{A}_{tu}$

over all $\mathbf{x} \in \Re^n$ is replaced by the one-dimensional minimization problem

$$\nabla f(\alpha) \equiv \nabla F(\mathbf{x} + \alpha \mathbf{p}) = 0 \qquad (4.10)$$

After solving 4.10 the optimal α is found to be

$$\alpha_{opt}(\mathbf{x}, \mathbf{p}) = \frac{||\mathbf{r}_m||_2^2}{\mathbf{p}^T \mathbf{A} \mathbf{p}} \qquad (4.11)$$

where $\mathbf{r}_m = \mathbf{b} - \mathbf{A}\mathbf{x}_m$. In each iteration of the CG method, the vector $\mathbf{x}_m$ is now optimized in a new direction $\mathbf{p}_{m+1}$. The optimal choice for $\mathbf{p}_{m+1}$ is not obvious, but a detailed analysis e.g. [30] shows

$$\mathbf{p}_{m+1} = \mathbf{r}_m + \frac{||\mathbf{r}_m||_2^2}{||\mathbf{r}_{m+1}||_2^2} \mathbf{p}_m \qquad (4.12)$$

Hence MATSTAB uses the following algorithm for solving $\mathbf{A}\mathbf{x} = \mathbf{b}$.
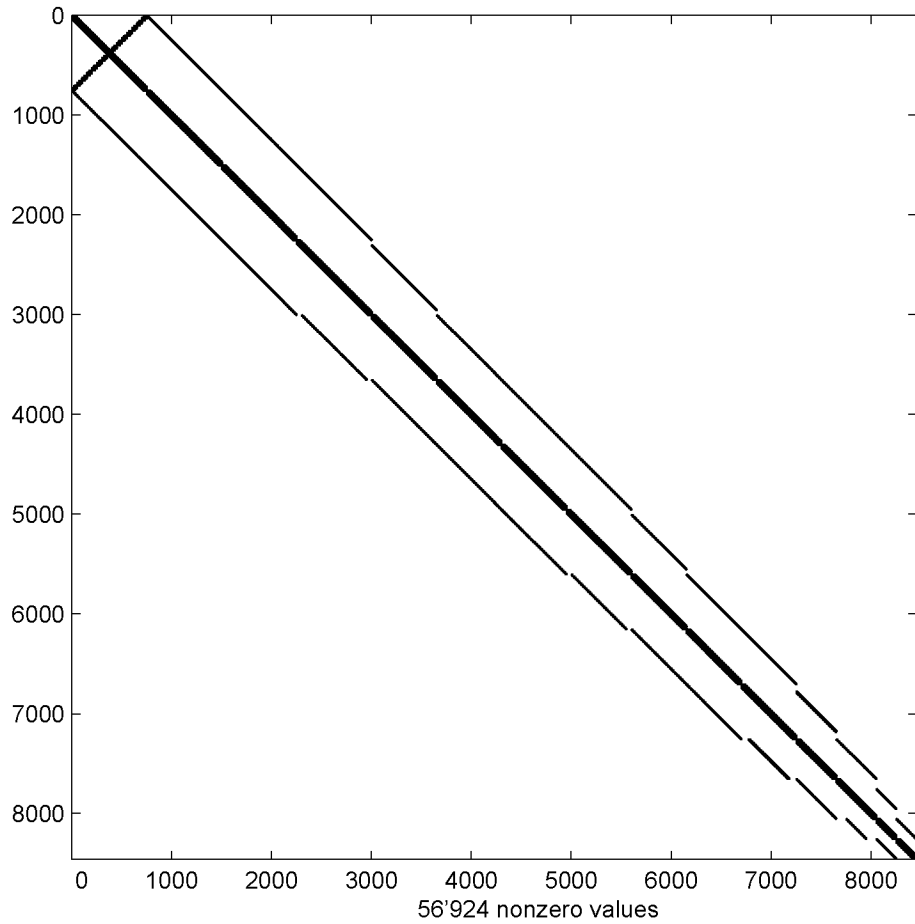
Figure 4.4: Structure of the Matrix $\mathbf{A}_n$

Algorithm 4.1: Conjugate Gradients

1. $\mathbf{p}_0 = \mathbf{0}$
   $\mathbf{x}_0 = $ any starting guess
   $\mathbf{r}_0 = \mathbf{b} - \mathbf{A}\mathbf{x}_0$

2. $\mathbf{p}_{m+1} = \mathbf{r}_m + \frac{||\mathbf{r}_m||_2^2}{||\mathbf{r}_{m+1}||_2^2} \mathbf{p}_m$

3. $\alpha_{opt} = \frac{||\mathbf{r}_m||_2^2}{\mathbf{p}_{m+1}^T \mathbf{A}\mathbf{p}_{m+1}}$

4. $\mathbf{x}_{m+1} = \mathbf{x}_m + \alpha_{opt}\mathbf{p}_{m+1}$

5. $\mathbf{r}_{m+1} = \mathbf{b} - \mathbf{A}\mathbf{x}_{m+1} = \mathbf{b} - \mathbf{A}\mathbf{x}_m - \alpha_{opt}\mathbf{p}_{m+1} = \mathbf{r}_m - \alpha_{opt}\mathbf{p}_{m+1}$

6. If $||\mathbf{r}_{m+1}||_2^2 > tol$ goto step 2

Figure 4.5: Lower Triangular Part of the Matrix $\mathbf{A}_n$

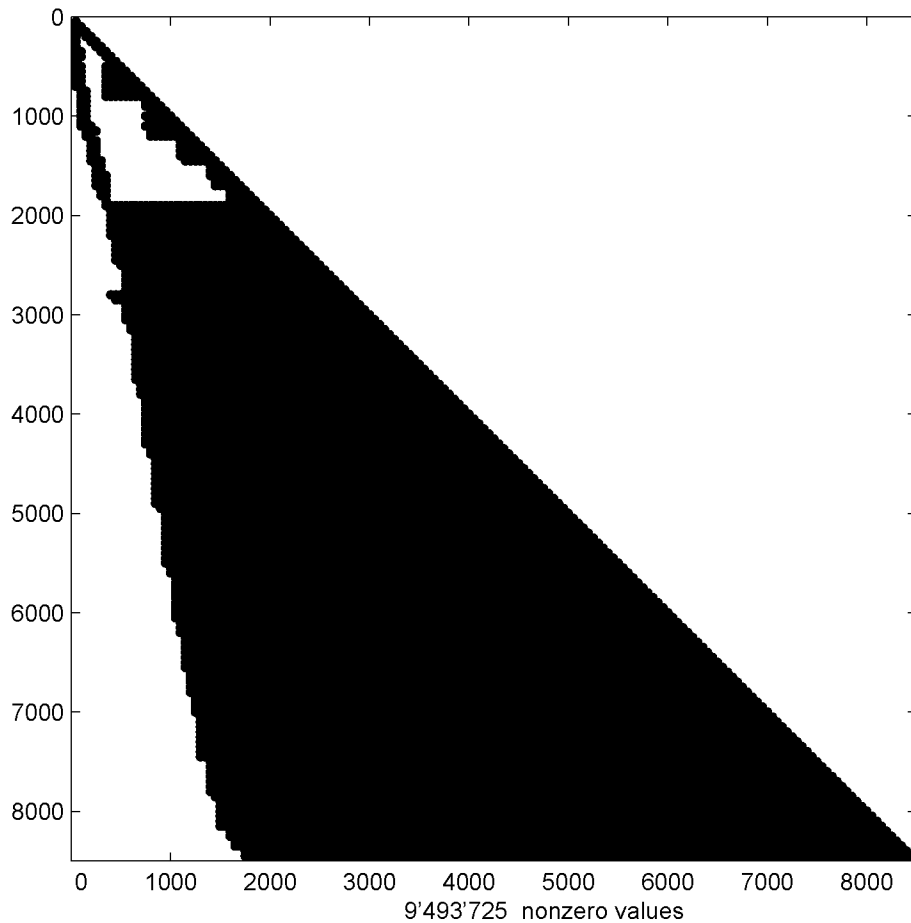## 4.3 The Calculation of a Specific Eigenvalue/Eigenvector

From a physical point of view, only the few dominant eigenvalues are of interest. Since the computation time for the eigenvalue/eigenvector is significant, not to say crucial, MATSTAB uses methods which calculate only the dominant eigenvalues. These eigenvalues can be singled out because from equation 2.27 follows that a high decay ratio is equivalent with a large real part of the eigenvalue, therefore the eigenvalue with the largest real part is dominating. The following paragraphs give a stepwise approach to the calculation of selected eigenvalues. These methods are by no means new, but they are necessary to understand the final algorithm 4.6.

The mechanism behind calculating one single eigenvalue/eigenvector pair $\lambda/\mathbf{e}$ for

$$\mathbf{A}\mathbf{e} = \lambda\mathbf{e} \tag{4.13}$$

can be best understood in the power method.
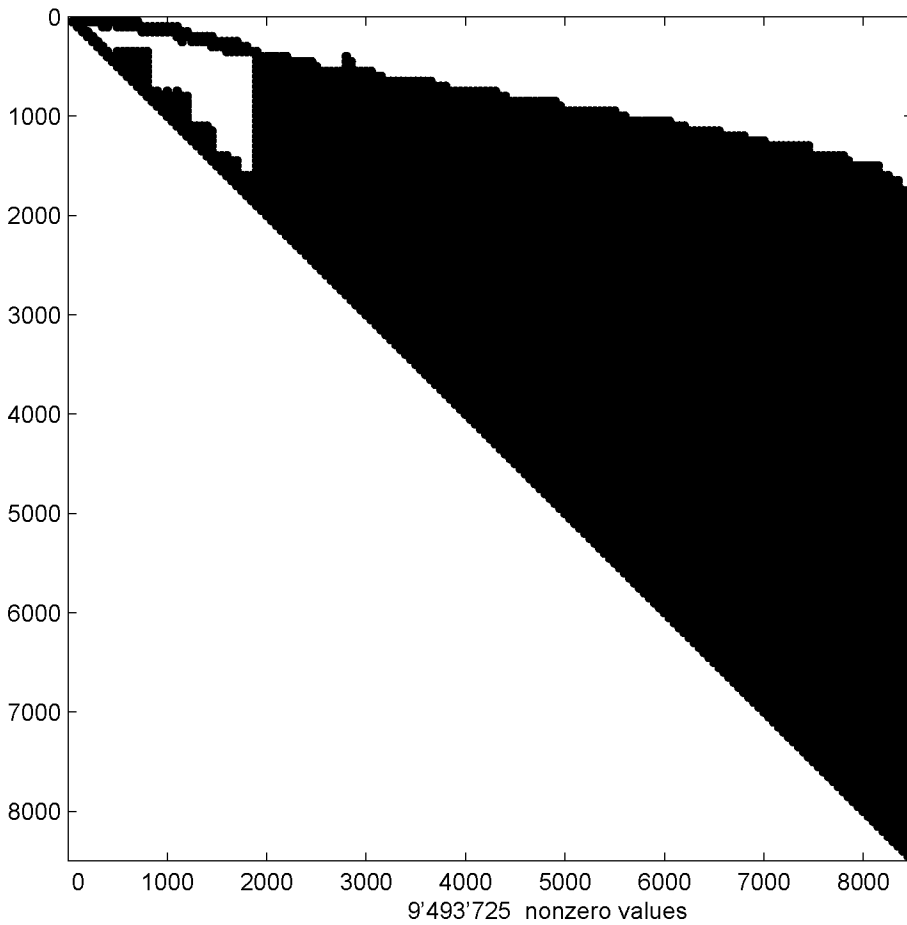
Figure 4.6: Upper Triangular Part of the Matrix $\mathbf{A}_n$

4.3.1   Power Method

The *largest* (in magnitude) eigenvalue and its right eigenvector for the matrix $\mathbf{A} \in \mathbf{C}^{n \times n}$ are found with the iteration:

Algorithm 4.2: Power Method

1. $\mathbf{e}_0$ any starting guess

2. $\mathbf{e}_{k+1} = \mathbf{A}\mathbf{e}_k$

3. $\lambda_{k+1} = \frac{\mathbf{e}_{k+1}^T \mathbf{A}\mathbf{e}_{k+1}}{\mathbf{e}_{k+1}^T \mathbf{e}_{k+1}}$

4. If $\|\mathbf{A}\mathbf{e}_{k+1} - \lambda_{k+1}\mathbf{e}_{k+1}\| > tol$ goto step 2

In order to understand why this iteration works, assume that $\mathbf{A}$ has distinct eigenvalues, with $|_1\lambda| < \cdots < |_i\lambda| < \cdots < |_n\lambda|$. Since $\mathbf{A}$ then has a full set of eigenvectors, $_1\mathbf{e}, _2\mathbf{e}, \ldots, _n\mathbf{e}$ forming a base, the start vector can be written as

$$\mathbf{e}_0 = \sum_{i=1}^{n} {}_ic_i\mathbf{e} \tag{4.14}$$

The vector $\mathbf{e}_k$, resulting after k iterations can be written as,

$$\mathbf{e}_k = \mathbf{A}^k\mathbf{e}_0 = \sum_{i=1}^{n} {}_ic_i\lambda^k{}_i\mathbf{e} \tag{4.15}$$

Clearly, $\mathbf{e}_k$ will be more and more dominated by $_n\mathbf{e}$. The convergence of the power method is linear, with a convergence rate proportional to $\frac{_{n-1}\lambda}{_n\lambda}$. The computational effort for this algorithm is very small, since the only matrix operations involved are multiplications. However, the eigenvalues with the largest absolute value are not of any interest from a physical point of view. The algorithm has therefore to be modified to calculate the eigenvalues with the desired properties (e.g. smallest real part).

4.3.2 Inverse Iteration

The next simple step is the modification of algorithm 4.2 for the calculation of the *smallest* (in magnitude) eigenvalue.

```
Algorithm 4.3: Inverse Iteration
```

1. $\mathbf{e}_0$ = any starting guess

2. $\mathbf{A}\mathbf{e}_{k+1} = \mathbf{e}_k$

3. $\lambda_{k+1} = \frac{\mathbf{e}_{k+1}^T\mathbf{A}\mathbf{e}_{k+1}}{\mathbf{e}_{k+1}^T\mathbf{e}_{k+1}}$

4. If $||\mathbf{A}\mathbf{e}_{k+1} - \lambda_{k+1}\mathbf{e}_{k+1}|| > tol$ goto step 2

The major computation here is to solve $\mathbf{A}\mathbf{e}_{k+1} = \mathbf{e}_k$ for $\mathbf{e}_{k+1}$ each iteration. This is somewhat expensive, but doable with either an $\mathbf{LU}$ decomposition or the conjugate gradient method. Inverse iteration is the power method applied to $\mathbf{A}^{-1}$, and consequently the convergence of the inverse iteration is linear with convergence rate proportional to $\frac{_1\lambda}{_2\lambda}$.

4.3.3   Inverse Iteration with Shift

If more than one, or a special, eigenvalue is needed, a spectral transformation is necessary.

`Algorithm 4.4: Inverse Iteration with shift`

1. $\mathbf{e}_0$ = any starting guess
   λ_0 = any starting guess

2. $(\mathbf{A} - \lambda_k \mathbf{I})\mathbf{e}_{k+1} = \mathbf{e}_k$

3. $\lambda_{k+1} = \frac{\mathbf{e}_{k+1}^T \mathbf{A}\mathbf{e}_{k+1}}{\mathbf{e}_{k+1}^T \mathbf{e}_{k+1}} = \lambda_k + \frac{\mathbf{e}_{k+1}^T \mathbf{e}_k}{\|\mathbf{e}_{k+1}\|^2}$

4. If $\|\mathbf{A}\mathbf{e}_{k+1} - \lambda_{k+1}\mathbf{e}_{k+1}\| > tol$ got to step 2

Note that it is not necessary to update λ_k in $(\mathbf{A} - \lambda_k \mathbf{I})$ each iteration. In general, the convergence will be faster if one does, but on the other hand without updating λ_k, the **LU** decomposition of $(\mathbf{A} - \lambda_k \mathbf{I})$ from the previous iteration can be used again. The convergence is cubic for the symmetric case.

4.3.4   Newton's Method

Due to the limited machine precision, the algorithm 4.4 has significant error bounds for a very large **A**. Therefore a combination with Newton's method is introduced [80].

The quality of an approximate solution $\mathbf{x}_k$ of $\mathbf{f}(\mathbf{x}) = \mathbf{0}$ may be improved by the update

$$\mathbf{x}_{k+1} = \mathbf{x}_k - \nabla \mathbf{f}(\mathbf{x}_k)^{-1} \mathbf{f}(\mathbf{x}_k) \tag{4.16}$$

Because the magnitude of an eigenvector is not defined, one equation has to be added to 4.13 to define a unique function f for the eigenvalue problem, e.g.

$$\mathbf{u}_1^T \mathbf{e} = \mathbf{e}(1) = 1 \quad \mathbf{u}_1^T = [1, 0, \dots, 0] \tag{4.17}$$

The function f therefore is defined as follows.

$$\mathbf{f}(\lambda, \mathbf{e}) = \mathbf{0} \quad \Leftrightarrow \quad \begin{vmatrix} \mathbf{u}_1^T \mathbf{e} - 1 & = & 0 \\ (\mathbf{A} - \lambda \mathbf{I})\mathbf{e} & = & \mathbf{0} \end{vmatrix} \tag{4.18}$$

The Newton update

$$\begin{bmatrix} \mathbf{e}_{k+1} \\ \lambda_{k+1} \end{bmatrix} = \begin{bmatrix} \mathbf{e}_k \\ \lambda_k \end{bmatrix} - \nabla \mathbf{f}(\lambda_k, \mathbf{e}_k)^{-1} \mathbf{f}(\lambda_k, \mathbf{e}_k) \tag{4.19}$$

for the inverse iteration with shift becomes

$$\begin{bmatrix} \mathbf{e}_{k+1} \\ \lambda_{k+1} \end{bmatrix} = \begin{bmatrix} \mathbf{e}_k \\ \lambda_k \end{bmatrix} - \begin{bmatrix} \mathbf{u}_1^T & 0 \\ \mathbf{A} - \lambda_k \mathbf{I} & -\mathbf{e}_k \end{bmatrix} \setminus \begin{bmatrix} \mathbf{u}_1^T \mathbf{e}_k - 1 \\ (\mathbf{A} - \lambda_k \mathbf{I})\mathbf{e}_k \end{bmatrix} \tag{4.20}$$

The meaning of the backslash used above is explained in the comment to equation 4.6.

$$\begin{bmatrix} \mathbf{u}_1^T & 0 \\ \mathbf{A} - \lambda_k \mathbf{I} & -\mathbf{e}_k \end{bmatrix} \begin{bmatrix} \mathbf{e}_{k+1} - \mathbf{e}_k \\ \lambda_{k+1} - \lambda_k \end{bmatrix} = - \begin{bmatrix} 0 \\ (\mathbf{A} - \lambda_k \mathbf{I}) \mathbf{e}_k \end{bmatrix} \tag{4.21}$$

Equation 4.21 can be extended naturally for the generalized eigenvalue problem

$$\mathbf{A}\mathbf{e} = \lambda \mathbf{B}\mathbf{e} \tag{4.22}$$

$$f(\lambda, \mathbf{e}) = 0 \quad \Leftrightarrow \quad \begin{vmatrix} \mathbf{u}_1^T \mathbf{e} - 1 & = & 0 \\ (\mathbf{A} - \lambda \mathbf{B})\mathbf{e} & = & 0 \end{vmatrix} \tag{4.23}$$

$$\begin{bmatrix} \mathbf{u}_1^T & 0 \\ \mathbf{A} - \lambda_k \mathbf{B} & -\mathbf{B}\mathbf{e}_k \end{bmatrix} \begin{bmatrix} \mathbf{e}_{k+1} - \mathbf{e}_k \\ \lambda_{k+1} - \lambda_k \end{bmatrix} = - \begin{bmatrix} 0 \\ (\mathbf{A} - \lambda_k \mathbf{B})\mathbf{e}_k \end{bmatrix} \tag{4.24}$$

The iteration process for 4.24 becomes now:

`Algorithm 4.5: Generalized Newton's Method`

1. $\mathbf{e}_0$ any starting guess
   λ_0 any starting guess

2. $\begin{bmatrix} \Delta \mathbf{e}_{k+1} \\ \Delta \lambda_{k+1} \end{bmatrix} = \begin{bmatrix} \mathbf{e}_{k+1} - \mathbf{e}_k \\ \lambda_{k+1} - \lambda_k \end{bmatrix} = \begin{bmatrix} \mathbf{u}_1^T & 0 \\ \mathbf{A} - \lambda_k \mathbf{B} & -\mathbf{B}_t \mathbf{e}_k \end{bmatrix} \Big\backslash \begin{bmatrix} \mathbf{u}_1^T \mathbf{e}_k - 1 \\ (\mathbf{A} - \lambda_k \mathbf{B})\mathbf{e}_k \end{bmatrix}$

3. $\mathbf{e}_{k+1} = \mathbf{e}_k + \Delta \mathbf{e}$

4. $\lambda_{k+1} = \lambda_k + \Delta \lambda$

5. If $||\Delta \mathbf{e}|| > tol$ goto step 2

4.4 Partitioning Into Subspaces

The direct implementation of algorithm 4.5 fails due to the sheer size of $\mathbf{A}$ (see Figure 4.7) in MATSTAB. Step 2 of 4.24 is not feasible in reasonable time. Therefore the matrix $\mathbf{A}$ is divided into suitable sub-matrices.

The matrices $\mathbf{A}$, $\mathbf{B}$ and the vector $\mathbf{e}$ are split up as follows.

$$\mathbf{A} = \begin{bmatrix} \mathbf{A}_t & \mathbf{A}_{tj} & \mathbf{0} & \mathbf{A}_{tq} & \mathbf{A}_{tf} \\ \mathbf{A}_{jt} & \mathbf{A}_j & \mathbf{0} & \mathbf{0} & \mathbf{A}_{jf} \\ \mathbf{A}_{NT} & \mathbf{0} & \mathbf{A}_N & \mathbf{0} & \mathbf{0} \\ \mathbf{A}_{qt} & \mathbf{0} & \mathbf{A}_{qn} & -\mathbf{I} & \mathbf{0} \\ \mathbf{A}_{ft} & \mathbf{A}_{fj} & \mathbf{0} & \mathbf{A}_{fq} & \mathbf{A}_f \end{bmatrix} \tag{4.25}$$
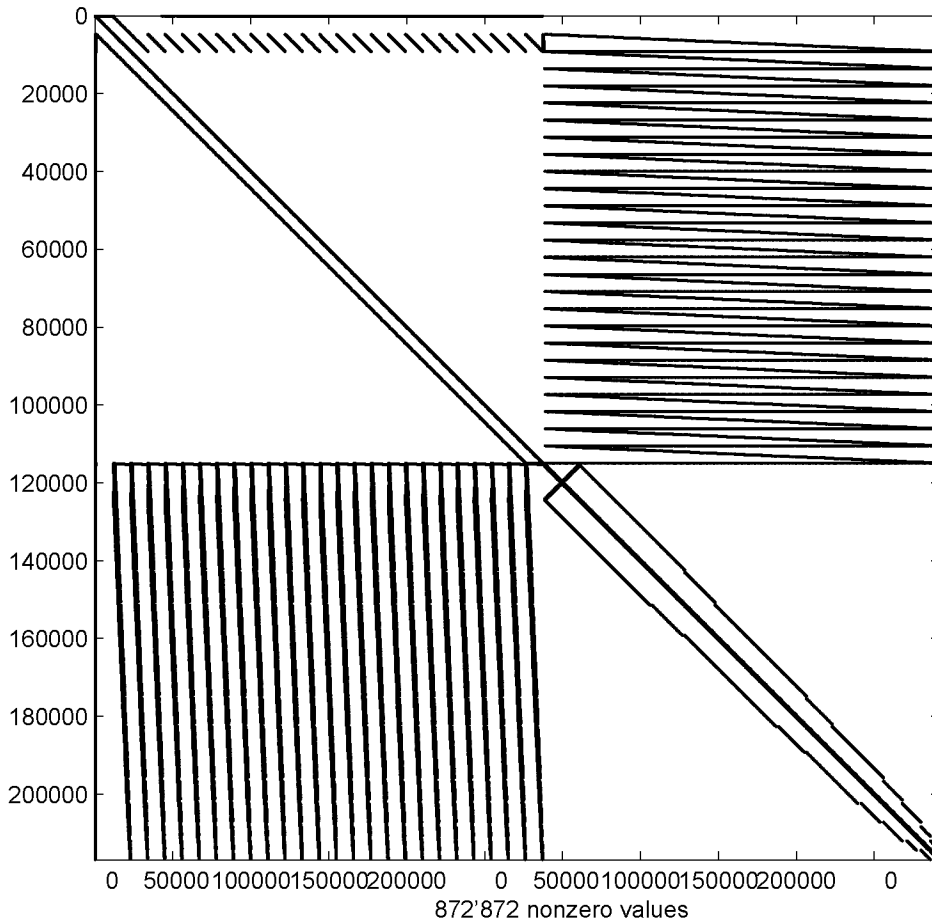
Figure 4.7: The Structure of the Matrix $\mathbf{A}$

$$\mathbf{B} = \begin{bmatrix} \mathbf{B}_t & 0 & 0 & 0 & 0 \\ 0 & \mathbf{B}_j & 0 & 0 & 0 \\ 0 & 0 & 0 & 0 & 0 \\ 0 & 0 & 0 & 0 & 0 \\ 0 & 0 & 0 & 0 & \mathbf{B}_f \end{bmatrix} \qquad \mathbf{e} = \begin{bmatrix} \mathbf{e}_t \\ \mathbf{e}_j \\ \mathbf{e}_n \\ \mathbf{e}_q \\ \mathbf{e}_f \end{bmatrix} \qquad (4.26)$$

The indices are set as follows

t   Thermal-hydraulic equations
j   Volumetric mixture flux
n   Neutron flux Φ
q   Fission power q'''
f   Fuel temperatures
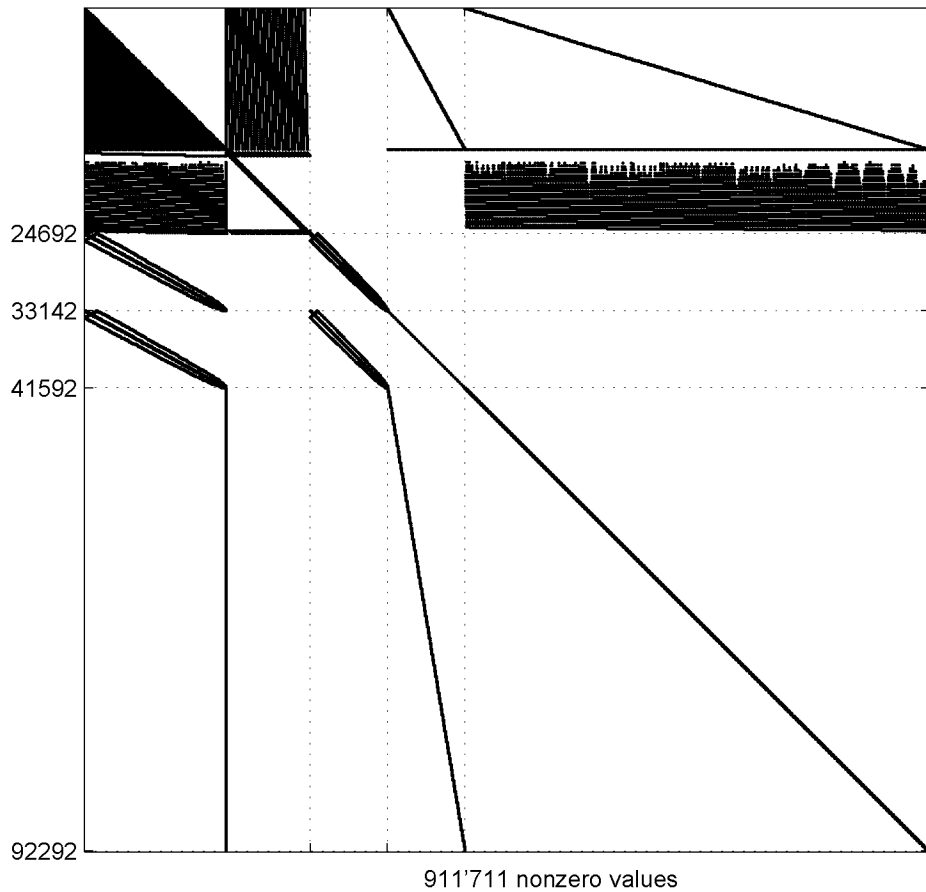
Figure 4.8: The Matrix **A** Divided Into Physical Subspaces

The capital letters N and NT in 4.25 symbolize that the corresponding matrices are complex.

$$\mathbf{A}_N = \mathbf{A}_n + i\mathbf{A}_{nIm} \quad , \mathbf{A}_{NT} = \mathbf{A}_{nt} + i\mathbf{A}_{ntIm} \tag{4.27}$$

The complex part of the neutronics was introduced by A.33.

Figure 4.8 shows the partition of **A** corresponding to 4.25.

Equation 4.28 shows the generalized eigenvalue problem 2.15 as formulated in MATSTAB.

$$\begin{bmatrix} \lambda\mathbf{B}_t\mathbf{e}_t \\ \lambda\mathbf{B}_j\mathbf{e}_j \\ \mathbf{0} \\ \mathbf{0} \\ \lambda\mathbf{B}_f\mathbf{e}_f \end{bmatrix} = \begin{bmatrix} \mathbf{A}_t & \mathbf{A}_{tj} & \mathbf{0} & \mathbf{A}_{tq} & \mathbf{A}_{tf} \\ \mathbf{A}_{jt} & \mathbf{A}_j & \mathbf{0} & \mathbf{0} & \mathbf{A}_{jf} \\ \mathbf{A}_{NT} & \mathbf{0} & \mathbf{A}_N & \mathbf{0} & \mathbf{0} \\ \mathbf{A}_{qt} & \mathbf{0} & \mathbf{A}_{qn} & -\mathbf{I} & \mathbf{0} \\ \mathbf{A}_{ft} & \mathbf{A}_{fj} & \mathbf{0} & \mathbf{A}_{fq} & \mathbf{A}_f \end{bmatrix} \begin{bmatrix} \mathbf{e}_t \\ \mathbf{e}_j \\ \mathbf{e}_n \\ \mathbf{e}_q \\ \mathbf{e}_f \end{bmatrix} \tag{4.28}$$

Equation 4.28 is equivalent to the following set of equations.

$$\lambda \mathbf{B}_t \mathbf{e}_t = \mathbf{A}_t \mathbf{e}_t + \mathbf{A}_{tj} \mathbf{e}_j + \mathbf{A}_{tq} \mathbf{e}_q + \mathbf{A}_{tf} \mathbf{e}_f \tag{4.29}$$

$$\lambda \mathbf{B}_j \mathbf{e}_j = \mathbf{A}_{jt} \mathbf{e}_t + \mathbf{A}_j \mathbf{e}_j + \mathbf{A}_{jf} \mathbf{e}_q \tag{4.30}$$

$$\mathbf{0} = \mathbf{A}_{NT} \mathbf{e}_t + \mathbf{A}_N \mathbf{e}_n \tag{4.31}$$

$$\mathbf{0} = \mathbf{A}_{qt} \mathbf{e}_t + \mathbf{A}_{qn} \mathbf{e}_n - \mathbf{e}_q \tag{4.32}$$

$$\lambda \mathbf{B}_f \mathbf{e}_f = \mathbf{A}_{ft} \mathbf{e}_t + \mathbf{A}_{fj} \mathbf{e}_j + \mathbf{A}_{fq} \mathbf{e}_q + \mathbf{A}_f \mathbf{e}_f \tag{4.33}$$

4.5 The Global Mode

This section explains how Newton's method is applied to the subspace approach introduced above. Since normally the global oscillation mode of the reactor is dominant MATSTAB always starts with calculating this mode. If requested, the eigenvalues/eigenvectors for regional oscillations are calculated afterwards.

4.5.1 The Starting Guesses

Since we use iterative methods, the calculation starts with a guess of the eigenvalue derived from a guess of the decay ratio and from the expected frequency of the oscillation. Equation 2.27 on page 17 is used to transform these values into an eigenvalue.

The starting guess $\mathbf{e}_0$ of the eigenvector is constructed automatically from λ_0 and the starting guess $\mathbf{e}_{n,0}$ for $\mathbf{e}_n$. The vector $\mathbf{e}_{n,0}$ is created from the power distribution of the steady state solution. This implies, that the shape of $\mathbf{e}_n$ is similar to the shape of the power density in the reactor! The equations implemented below, are derived from equations 4.29ff.

$$
\begin{aligned}
\text{Preliminary step:} \quad \mathbf{e}_{q,0} &= \mathbf{A}_{qn} \mathbf{e}_{n,0} \\
\mathbf{e}_{f,0} &= (\lambda_0 \mathbf{B}_f - \mathbf{A}_f) \underset{\text{GE}}{\backslash} (\mathbf{A}_{fq} \mathbf{e}_{q,0}) \\[2ex]
\text{Construction step:} \quad \mathbf{e}_{t,0} &= (\lambda_0 \mathbf{B}_t - \mathbf{A}_t) \underset{\text{LU}}{\backslash} (\mathbf{A}_{tf} \mathbf{e}_{f,0} + \mathbf{A}_{tq} \mathbf{e}_{q,0}) \\
\mathbf{e}_{n,0} &= \mathbf{A}_n \underset{\text{CG}}{\backslash} (\mathbf{A}_{NT} \mathbf{e}_{t,0} + i \mathbf{A}_{nIm} \mathbf{e}_{n,0}) \\
\mathbf{e}_{q,0} &= A_{qn} \mathbf{e}_{n,0} + \mathbf{A}_{qt} \mathbf{e}_{t,0} \\
\mathbf{e}_{f,0} &= (\lambda_0 \mathbf{B}_f - \mathbf{A}_f) \underset{\text{GE}}{\backslash} (\mathbf{A}_{fq} \mathbf{e}_{q,0} + \mathbf{A}_{ft} \mathbf{e}_{t,0})
\end{aligned}
\tag{4.34}
$$

The symbols $\underset{\text{GE}}{\backslash}$, $\underset{\text{LU}}{\backslash}$ and $\underset{\text{CG}}{\backslash}$ are to be understood in the way, that the set of equations is solved either with Gaussian elimination, LU decomposition or conjugate gradient methods.

The construction step improves the guess for $\mathbf{e}_n$ and is therefore repeated three times to improve the overall quality of the starting guess for the eigenvector. There is no sense to do more iterations since λ_0 is not updated and the algorithm produces only a starting guess.

4.5.2 The Main Iteration

The main iteration process is a combination of Newton's method and the iteration over the subspaces.

Newton's method is applied to the thermal-hydraulic part of the problem.

$$\mathbf{f}(\lambda, \mathbf{e}_t) = \mathbf{0} \quad \Leftrightarrow \quad \left| \begin{array}{rcl} \mathbf{u}_{t,1}^T \mathbf{e}_t - 1 & = & 0 \\ (\mathbf{A}_t - \lambda \mathbf{B}_t)\mathbf{e}_t + \mathbf{A}_{tf}\mathbf{e}_f + \mathbf{A}_{tq}\mathbf{e}_q & = & \mathbf{0} \end{array} \right| \tag{4.35}$$

This leads to $\Delta\lambda_{k+1}$ and $\Delta\mathbf{e}_{t,k+1}$ which are then used to create $\mathbf{e}_{n,k+1}, \mathbf{e}_{q,k+1}$, and $\mathbf{e}_{f,k+1}$. The algorithm reads now as follows.

```
Algorithm 4.6: Newton's Method with subspaces
```

1. $\mathbf{e}_{n,0}$ from power distribution
   λ_0 from DR guess and frequency guess

2. $\begin{bmatrix} \Delta\mathbf{e}_{t,k+1} \\ \Delta\lambda_{k+1} \end{bmatrix} = \begin{bmatrix} \mathbf{u}_{t,1}^T & 0 \\ \mathbf{A}_t - \lambda_k\mathbf{B}_t & -\mathbf{B}_t\mathbf{e}_{t,k} \end{bmatrix}_{LU} \setminus \begin{bmatrix} \mathbf{u}_{t,1}^T\mathbf{e}_{t,k} - 1 \\ (\mathbf{A}_t - \lambda_k\mathbf{B}_t)\mathbf{e}_{t,k} + \mathbf{A}_{tf}\mathbf{e}_{f,k} + \mathbf{A}_{tq}\mathbf{e}_{q,k} \end{bmatrix}$

3. $\mathbf{e}_{k+1} = \mathbf{e}_k + \Delta\mathbf{e}_{k+1}$

4. $\lambda_{k+1} = \lambda_k + \Delta\lambda_{k+1}$

5. $\mathbf{e}_{n,k+1} = \mathbf{A}_n \underset{CG}{\setminus} (\mathbf{A}_{NT}\mathbf{e}_{t,k+1} + i\mathbf{A}_{nIm}\mathbf{e}_{n,k})$

6. $\mathbf{e}_{q,k+1} = \mathbf{A}_{qt}\mathbf{e}_{t,k+1} + \mathbf{A}_{qn}\mathbf{e}_{n,k+1}$

7. $\mathbf{e}_{f,k+1} = (\lambda_{k+1}\mathbf{B}_f - \mathbf{A}_f) \underset{GE}{\setminus} (\mathbf{A}_{ft}\mathbf{e}_{t,k+1} + \mathbf{A}_{fq}\mathbf{e}_{q,k+1})$

8. If $||\Delta\mathbf{e}|| > tolerance$ goto step 2

4.6 The Left Eigenvector

As mentioned several times before, the decay ratio describes only one aspect of instability. Most information is stored in the eigenvectors. The right eigenvector is a natural byproduct of the eigenvalue calculation. The left eigenvector, however, has to be calculated separately. The methods used to calculate the left eigenvector are similar to the the methods used for the right eigenvector and the eigenvalue. However, the knowledge of the latter makes the process a bit simpler and faster. The starting point is the generalized left eigenvalue equation corresponding to equation 4.28.

$$
\begin{bmatrix} \lambda \mathbf{B}_t \mathbf{f}_t \\ \lambda \mathbf{B}_j \mathbf{f}_j \\ 0 \\ 0 \\ \lambda \mathbf{B}_f \mathbf{f}_f \end{bmatrix} = \begin{bmatrix} \mathbf{f}_t \\ \mathbf{f}_j \\ \mathbf{f}_n \\ \mathbf{f}_q \\ \mathbf{f}_f \end{bmatrix}^T \begin{bmatrix} \mathbf{A}_t & \mathbf{A}_{tj} & \mathbf{0} & \mathbf{A}_{tq} & \mathbf{A}_{tf} \\ \mathbf{A}_{jt} & \mathbf{A}_j & \mathbf{0} & \mathbf{0} & \mathbf{A}_{jf} \\ \mathbf{A}_{NT} & \mathbf{0} & \mathbf{A}_N & \mathbf{0} & \mathbf{0} \\ \mathbf{A}_{qt} & \mathbf{0} & \mathbf{A}_{qn} & -\mathbf{I} & \mathbf{0} \\ \mathbf{A}_{ft} & \mathbf{A}_{fj} & \mathbf{0} & \mathbf{A}_{fq} & \mathbf{A}_f \end{bmatrix} \tag{4.36}
$$

Transposing the equation leads to a right eigenvector problem.

$$
\begin{bmatrix} \lambda \mathbf{B}_t^T \mathbf{f}_t \\ \lambda \mathbf{B}_j^T \mathbf{f}_j \\ 0 \\ 0 \\ \lambda \mathbf{B}_f^T \mathbf{f}_f \end{bmatrix} = \begin{bmatrix} \mathbf{A}_t^T & \mathbf{A}_{jt}^T & \mathbf{A}_{NT}^T & \mathbf{A}_{qt}^T & \mathbf{A}_{ft}^T \\ \mathbf{A}_{tj}^T & \mathbf{A}_j^T & \mathbf{0} & \mathbf{0} & \mathbf{A}_{fj}^T \\ \mathbf{0} & \mathbf{0} & \mathbf{A}_N^T & \mathbf{A}_{qn}^T & \mathbf{0} \\ \mathbf{A}_{tq}^T & \mathbf{0} & \mathbf{0} & -\mathbf{I} & \mathbf{A}_{fq}^T \\ \mathbf{A}_{tf}^T & \mathbf{A}_{jf}^T & \mathbf{0} & \mathbf{0} & \mathbf{A}_f^T \end{bmatrix} \begin{bmatrix} \mathbf{f}_t \\ \mathbf{f}_j \\ \mathbf{f}_n \\ \mathbf{f}_q \\ \mathbf{f}_f \end{bmatrix} \tag{4.37}
$$

Note, that the structure of the equation system in 4.28 is quite different to that of 4.37 due to the fact, that the matrix $\mathbf{A}$ (see 4.25) is not symmetrical. Since λ is known, the only thing that stops us from solving the system of equations with standard techniques are once more, numerical problems. Nevertheless the number of equations may be reduced to a certain limit, using Gaussian elimination.

The following derivation is by no means trivial. The equations and the order of substitution have to be selected very carefully to maintain sparsity and to keep the computational effort affordable. Even more, some of the intermediate terms appearing below may not be calculated explicitly. It is, however, possible to calculate the product of this term with a vector using the fact that the multiplications of matrices and vectors are associative.

Using equation 4.37 as a starting point, following equations may be derived.

$$
\mathbf{f}_f = (\lambda \mathbf{B}_f^T - \mathbf{A}_f^T) \underset{LU}{\backslash} (\mathbf{A}_{tf}^T \mathbf{f}_t + \mathbf{A}_{jf}^T \mathbf{f}_j) \tag{4.38}
$$

$$
\mathbf{f}_t = (\lambda \mathbf{B}_t^T - \mathbf{A}_t^T) \underset{LU}{\backslash} (\mathbf{A}_{jt}^T \mathbf{f}_j + \mathbf{A}_{NT}^T \mathbf{f}_n + \mathbf{A}_{qt}^T \mathbf{f}_q + \mathbf{A}_{ft}^T \mathbf{f}_f) \tag{4.39}
$$

$$
\mathbf{f}_j = (\lambda \mathbf{B}_j^T - \mathbf{A}_j^T) \underset{GE}{\backslash} (\mathbf{A}_{tj}^T \mathbf{f}_t + \mathbf{A}_{fj}^T \mathbf{f}_f) \tag{4.40}
$$

Inserting 4.38 into 4.39 and 4.40 leads to

$$
\begin{aligned}
\mathbf{f}_t &= (\lambda \mathbf{B}_t^T - \mathbf{A}_t^T) \underset{LU}{\backslash} [\mathbf{A}_{jt}^T \mathbf{f}_j + \mathbf{A}_{NT}^T \mathbf{f}_n + \mathbf{A}_{qt}^T \mathbf{f}_q + \mathbf{A}_{ft}^T (\lambda \mathbf{B}_f^T - \mathbf{A}_f^T) \underset{LU}{\backslash} (\mathbf{A}_{tf}^T \mathbf{f}_t + \mathbf{A}_{jf}^T \mathbf{f}_j)] \\
&= (\lambda \mathbf{B}_t^T - \mathbf{A}_t^T - \mathbf{A}_{fttf}) \underset{LU}{\backslash} [(\mathbf{A}_{jt}^T + \mathbf{A}_{ftjf}) \mathbf{f}_j + \mathbf{A}_{NT}^T \mathbf{f}_n + \mathbf{A}_{qt}^T \mathbf{f}_q] \\
&= \mathbf{A}_{bj} \mathbf{f}_j + \mathbf{A}_{bNT} \mathbf{f}_n + \mathbf{A}_{bq} \mathbf{f}_q \tag{4.41}
\end{aligned}
$$

where

$$\mathbf{A}_{fttf} = \mathbf{A}_{ft}^T (\lambda \mathbf{B}_f^T - \mathbf{A}_f^T) \underset{\text{LU}}{\backslash} \mathbf{A}_{tf}^T$$

$$\mathbf{A}_{ftjf} = \mathbf{A}_{ft}^T (\lambda \mathbf{B}_f^T - \mathbf{A}_f^T) \underset{\text{LU}}{\backslash} \mathbf{A}_{jf}^T$$

$$\mathbf{A}_{bj} = (\lambda \mathbf{B}_t^T - \mathbf{A}_t^T - \mathbf{A}_{fttf}) \underset{\text{LU}}{\backslash} (\mathbf{A}_{jt}^T + \mathbf{A}_{ftjf})$$

$$\mathbf{A}_{bNT} = (\lambda \mathbf{B}_t^T - \mathbf{A}_t^T - \mathbf{A}_{fttf}) \underset{\text{LU}}{\backslash} \mathbf{A}_{NT}^T$$

$$\mathbf{A}_{bq} = (\lambda \mathbf{B}_t^T - \mathbf{A}_t^T - \mathbf{A}_{fttf}) \underset{\text{LU}}{\backslash} \mathbf{A}_{qt}^T$$

and

$$\begin{aligned}
\mathbf{f}_j &= (\lambda \mathbf{B}_j^T - \mathbf{A}_j^T) \underset{\text{GE}}{\backslash} [\mathbf{A}_{fj}^T (\lambda \mathbf{B}_f^T - \mathbf{A}_f^T) \underset{\text{LU}}{\backslash} \mathbf{A}_{tf}^T \mathbf{f}_t + \mathbf{A}_{fj}^T (\lambda \mathbf{B}_f^T - \mathbf{A}_f^T) \underset{\text{LU}}{\backslash} \mathbf{A}_{jf}^T \mathbf{f}_j + \mathbf{A}_{tj}^T \mathbf{f}_t] \\
&= (\lambda \mathbf{B}_j^T - \mathbf{A}_j^T) \underset{\text{GE}}{\backslash} [(\mathbf{A}_{fjtf} + \mathbf{A}_{tj}^T) \mathbf{f}_t + \mathbf{A}_{fjjf} \mathbf{f}_j] \quad (4.42)
\end{aligned}$$

where

$$\mathbf{A}_{fjtf} = \mathbf{A}_{fj}^T (\lambda \mathbf{B}_f^T - \mathbf{A}_f^T) \underset{\text{LU}}{\backslash} \mathbf{A}_{tf}^T$$

$$\mathbf{A}_{fjjf} = \mathbf{A}_{fj}^T (\lambda \mathbf{B}_f^T - \mathbf{A}_f^T) \underset{\text{LU}}{\backslash} \mathbf{A}_{jf}^T$$

Inserting 4.41 into 4.42 leads to

$$\begin{aligned}
\mathbf{f}_j &= (\lambda \mathbf{B}_j^T - \mathbf{A}_j^T - \mathbf{A}_{fjjf}) \underset{\text{GE}}{\backslash} [(\mathbf{A}_{fjtf} + \mathbf{A}_{tj}^T)(\mathbf{A}_{bj} \mathbf{f}_j + \mathbf{A}_{bNT} \mathbf{f}_n + \mathbf{A}_{bq} \mathbf{f}_q)] \\
&= (\lambda \mathbf{B}_j^T - \mathbf{A}_j^T - \mathbf{A}_{fjjf} - (\mathbf{A}_{fjtf} + \mathbf{A}_{tj}^T) \mathbf{A}_{bj}) \underset{\text{GE}}{\backslash} (\mathbf{A}_{fjtf} + \mathbf{A}_{tj}^T)(\mathbf{A}_{bNT} \mathbf{f}_n + \mathbf{A}_{bq} \mathbf{f}_q) \\
&= \mathbf{A}_{Jnq}(\mathbf{A}_{bNT} \mathbf{f}_n + \mathbf{A}_{bq} \mathbf{f}_q) \quad (4.43)
\end{aligned}$$

where

$$\mathbf{A}_{Jnq} = (\lambda \mathbf{B}_j^T - \mathbf{A}_j^T - \mathbf{A}_{fjjf} - (\mathbf{A}_{fjtf} + \mathbf{A}_{tj}^T) \mathbf{A}_{bj}) \underset{\text{GE}}{\backslash} (\mathbf{A}_{fjtf} + \mathbf{A}_{tj}^T)$$

Equation 4.43 expresses $\mathbf{f}_j$ as a function of $\mathbf{f}_q$ and $\mathbf{f}_n$. These vectors depend also on $\mathbf{f}_f$, $\mathbf{f}_t$ and $\mathbf{f}_j$.

$$\mathbf{f}_n = -\mathbf{A}_N^T \underset{\text{PCG}}{\backslash} \mathbf{A}_{qn}^T \mathbf{f}_q \quad (4.44)$$

$$\mathbf{f}_q = \mathbf{A}_{tq}^T \mathbf{f}_t + \mathbf{A}_{fq}^T \mathbf{f}_f \quad (4.45)$$

Inserting 4.38 into 4.45 leads to

$$\begin{aligned}
\mathbf{f}_q &= \mathbf{A}_{tq}^T \mathbf{f}_t + \mathbf{A}_{fq}^T (\lambda \mathbf{B}_f^T - \mathbf{A}_f^T) \underset{\text{LU}}{\backslash} (\mathbf{A}_{tf}^T \mathbf{f}_t + \mathbf{A}_{jf}^T \mathbf{f}_j) \\
&= \mathbf{A}_{tq}^T \mathbf{f}_t + \mathbf{A}_{fqtf} \mathbf{f}_t + \mathbf{A}_{fqjf} \mathbf{f}_j \\
&= (\mathbf{A}_{tq}^T + \mathbf{A}_{fqtf}) \mathbf{f}_t + \mathbf{A}_{fqjf} \mathbf{f}_j \quad (4.46)
\end{aligned}$$

where

$$\mathbf{A}_{fqtf} = \mathbf{A}_{fq}^T (\lambda \mathbf{B}_f^T - \mathbf{A}_f^T) \underset{\text{LU}}{\backslash} \mathbf{A}_{tf}^T$$

$$\mathbf{A}_{fqjf} = \mathbf{A}_{fq}^T (\lambda \mathbf{B}_f^T - \mathbf{A}_f^T) \underset{\text{LU}}{\backslash} \mathbf{A}_{jf}^T$$

Inserting 4.41 into 4.46 leads to

$$\mathbf{f}_q = (\mathbf{A}_{tq}^T + \mathbf{A}_{fqtf})(\mathbf{A}_{bj}\mathbf{f}_j + \mathbf{A}_{bNT}\mathbf{f}_n + \mathbf{A}_{bq}\mathbf{f}_q) + \mathbf{A}_{fqjf}\mathbf{f}_j$$

$$= [(\mathbf{A}_{tq}^T + \mathbf{A}_{fqtf})\mathbf{A}_{bj} + \mathbf{A}_{fqjf}]\mathbf{f}_j + (\mathbf{A}_{tq}^T + \mathbf{A}_{fqtf})(\mathbf{A}_{bNT}\mathbf{f}_n + \mathbf{A}_{bq}\mathbf{f}_q) \qquad (4.47)$$

Inserting 4.43 into 4.47 leads to

$$\mathbf{f}_q = ([(\mathbf{A}_{tq}^T + \mathbf{A}_{fqtf})\mathbf{A}_{bj} + \mathbf{A}_{fqjf}]\mathbf{A}_{Jnq} + (\mathbf{A}_{tq}^T + \mathbf{A}_{fqtf}))(\mathbf{A}_{bNT}\mathbf{f}_n + \mathbf{A}_{bq}\mathbf{f}_q)$$

$$= \mathbf{A}_{QN}\mathbf{f}_n + \mathbf{A}_{QQ}\mathbf{f}_q \qquad (4.48)$$

where

$$\mathbf{A}_{QN} = ([(\mathbf{A}_{tq}^T + \mathbf{A}_{fqtf})\mathbf{A}_{bj} + \mathbf{A}_{fqjf}]\mathbf{A}_{Jnq} + (\mathbf{A}_{tq}^T + \mathbf{A}_{fqtf}))\mathbf{A}_{bNT} \qquad (4.49)$$

$$\mathbf{A}_{QQ} = ([(\mathbf{A}_{tq}^T + \mathbf{A}_{fqtf})\mathbf{A}_{bj} + \mathbf{A}_{fqjf}]\mathbf{A}_{Jnq} + (\mathbf{A}_{tq}^T + \mathbf{A}_{fqtf}))\mathbf{A}_{bq} \qquad (4.50)$$

Equation 4.48 is the base of the calculation of the left eigenvector, since the set of equations 4.48 and 4.44

$$\mathbf{f}_q = (\mathbf{I} - \mathbf{A}_{QQ}) \backslash \mathbf{A}_{QN}\mathbf{f}_n$$

$$\mathbf{f}_n = -\mathbf{A}_N^T \backslash \mathbf{A}_{qn}^T \mathbf{f}_q \qquad (4.51)$$

leads to

$$\mathbf{0} = [\mathbf{A}_N^T + \mathbf{A}_{qn}^T (\mathbf{I} - \mathbf{A}_{QQ}) \backslash \mathbf{A}_{QN}]\mathbf{f}_n \qquad (4.52)$$

which is not yet tractable from a computational point of view. The easily drawn backslash is an unsurmountable obstacle at the time being. Knowing this, it's not at all obvious, that the matrices $\mathbf{A}_{QN}$ and $\mathbf{A}_{QQ}$ in 4.48 may be calculated in a efficient manner. On the contrary, a detailed investigation shows, that the two matrices cannot be calculated with reasonable effort. However, an iterative approach to equation 4.48 does not require the explicit values of $\mathbf{A}_{QN}$ and $\mathbf{A}_{QQ}$. It is much easier to calculate $\mathbf{A}_1 \backslash (\mathbf{A}_2 \mathbf{f})$ which can be reduced to $\mathbf{A}_1 \backslash \tilde{\mathbf{f}}$ instead of $\mathbf{A}_1 \backslash \mathbf{A}_2$. This implies, that some of the above mentioned matrices cannot be given explicitly, but the resulting vector of a matrix/vector multiplication may be calculated nevertheless.

The final algorithm looks as follows.

```
Algorithm 4.7: Left Eigenvector
```

1. $\mathbf{f}_{n,k} = \mathbf{e}_n$ or any starting guess

2. $\mathbf{f}_{q,k} = \mathbf{e}_q$ or any starting guess

3. $\mathbf{f}_{q,k+1} = \mathbf{A}_{QN}\mathbf{f}_{n,k} + \mathbf{A}_{QQ}\mathbf{f}_{q,k}$ $\hspace{2cm}$ (4.48)

4. $\mathbf{f}_{n,k+1} = -\mathbf{A}_N^T \underset{\text{PCG}}{\backslash} \mathbf{A}_{qn}^T\mathbf{f}_{q,k+1}$ $\hspace{2cm}$ (4.44)

5. go back to step 3 until convergence of $\mathbf{f}_q$ and $\mathbf{f}_n$ is reached.

6. $\mathbf{f}_{j,k+1} = \mathbf{A}_{Jnq}(\mathbf{A}_{bNT}\mathbf{f}_n + \mathbf{A}_{bq}\mathbf{f}_q)$ $\hspace{2cm}$ (4.43)

7. $\mathbf{f}_{t,k+1} = \mathbf{A}_{bj}\mathbf{f}_{j,k+1} + \mathbf{A}_{bNT}\mathbf{f}_{n,k+1} + \mathbf{A}_{bq}\mathbf{f}_{q,k+1}$ $\hspace{2cm}$ (4.41)

8. $\mathbf{f}_{f,k+1} = (\lambda\mathbf{B}_f^T - \mathbf{A}_f^T) \underset{\text{LU}}{\backslash} (\mathbf{A}_{tf}^T\mathbf{f}_{t,k+1} + \mathbf{A}_{jf}^T\mathbf{f}_{j,k+1})$ $\hspace{1cm}$ (4.38)

9. $\mathbf{f}_{q,k+2} = (\mathbf{A}_{tq}^T + \mathbf{A}_{fqtf})\mathbf{f}_{t,k+1} + \mathbf{A}_{fqjf}\mathbf{f}_{j,k+1}$ $\hspace{1cm}$ (4.46)

10. go back to step 4 until convergence of $\mathbf{f}_f$, $\mathbf{f}_t$ and $\mathbf{f}_j$ is reached.

The steps 9 and 10 are necessary because the coupling between the equations is not strong enough to give good results after the first iteration. The reason lies in the large variety of matrix sizes involved. $\mathbf{A}_j$ is smaller than 100x100 and $\mathbf{A}_f$ on the other hand is more like 50'000x50'000. These uneven sizes are mandatory to overcome the loss of sparsity during sub-calculations but lead to a weak coupling between some of the equations.

Naturally, the results for the left eigenvector will never be better, than the quality of the eigenvalue taken from the right eigenvector calculation.

4.7 Regional Modes

The algorithm 4.6 is not specific to the calculation of the global mode. The control over the mode calculated lies in the starting guess $[\lambda_0, \mathbf{e}_0]$. Therefore it is possible to find regional oscillations with a corresponding starting guess, i.e. the eigenvector contains the information if an oscillation is global or regional in its shape, the starting guess for regional oscillations must therefore also have the shape of a regional oscillation.

The complex structure of $\mathbf{A}$ prohibits the convergence of the algorithm if the starting guess is not within a relatively close vicinity of the solution. Therefore it is necessary to calculate a starting guess for the regional neutronic eigenvector $\tilde{\mathbf{e}}_{n,0}$ from the higher harmonics of the static nodal equation A.36

$$\bar{\varphi}_{1n} = \frac{\sum_{m=1}^{6}\left(\mathbf{Y}_{1,nm} + \tilde{\beta}\frac{\nu_2\Sigma_{f2}}{\Sigma_{a2}}\mathbf{Y}_{2,nm}\right)\bar{\varphi}_{1m}}{\sum_{m=1}^{6}(\mathbf{X}_{1,nm} + \tilde{\beta}\frac{\nu_2\Sigma_{f2}}{\Sigma_{a2}}\mathbf{X}_{2,nm}) - \Sigma_{a1}(k_\infty - 1)} \equiv \sum_{m=1}^{6}\mathbf{A}_{nm}\bar{\varphi}_{1m} \hspace{1cm} (A.36)$$

where n denotes the number of the node and m stands for the six spatial neighbors. The value k in the matrix $\mathbf{A}_{nm}$ is taken from the steady state core simulator of the NPP.

The starting guesses for the regional calculation are the dominating eigenvectors of $\mathbf{A}_{nm}$. These vectors represent the neutronic modes of the reactor. The eigenvectors of the relatively small matrix $\mathbf{A}_{nm}$ are calculated by the built in functions of MATLAB.

Applying these good starting guesses, it is possible to use algorithm 4.6 as in the global case. To make absolutely sure, that the algorithm converges to a regional solution, the matrices $\mathbf{A}_{jt}, \mathbf{A}_j, \mathbf{A}_{jf}, \mathbf{A}_{fj}, \mathbf{A}_{tj}$ and the vector $\mathbf{e}_j$ are assumed to be zero. Physically this means, that the regional oscillation may not be seen from the outside of the reactor, since the core flow is not oscillating.

The left eigenvector of the regional oscillation is calculated in the same manner as for the global mode. Actually, the calculation comes much cheaper in computer time, since, as stated before, a significant number of matrices may be assumed to be zero.

Chapter 5

Interpretation and Visualization of Results

Contents

5.1   Measurement Database

MATSTAB was validated against a large number of measurements in seven reactors situated at three different sites. While the next chapter describes the results of the validation, this chapter explains how MATSTAB differs from other codes, and how this difference may be used to produce new insights.

As a base for these explanations the measurement series conducted in Leibstadt in 1990 (cycle 7)[12] and 1993 [86] are chosen. These measurements were very thoroughly prepared and covered a wide range of operating points. Even more, the detailed post analysis showed regional oscillations in 1990.

The fifth operating point (45% power, 28% core flow) from the 1993 measurement series (see also Section 6.2.3) showed global oscillations and served as reference case for many of the following plots.

5.2   Displaying Three Dimensional Variables

MATSTAB represents the reactor with a detailed nodalization scheme and a respectable number of equations and variables. In consequence, a huge amount of data results from the calculations and must be presented carefully to give some insight.

All calculated parameters and variables may be stored for later investigations. The power distribution is presented as an example because its axial shape has undoubtedly an important influence to the stability of the reactor.

Figure 5.1 shows a normalized power-density distribution of the Leibstadt reactor measured during the stability test in 1993 [86]. The colors represent the axially averaged values. Each color square represents a fuel assembly. The larger squares, containing 4 fuel assemblies are called super cells, or controlled cells, in case a cross shaped control rod is allocated in between. The numbers plotted within a super cell are therefore the percentage of which a control rod is withdrawn from the core (fully withdrawn rods are not indicated).

To add the valuable information contained in the axial shapes, it is possible to select a couple of channels (indicated with X in Figure 5.1) and plot their axial values (Figure 5.2). The four chosen channels show a very different axial power distribution. The fuel assemblies in the center and at the boundaries of the core show a flat distribution.

The assembly in the outer part of the core is clearly bottom peaked while the controlled assembly is top peaked since the control rod enters from the bottom.

Figure 5.3 shows the radially averaged axial power density distribution of all super cells. This Figure gives a good impression of the calculated power density distribution in the core. Any other physical property may be displayed in the same manner. For example, the void content, liquid flow, neutron flux, fuel temperature and so on.
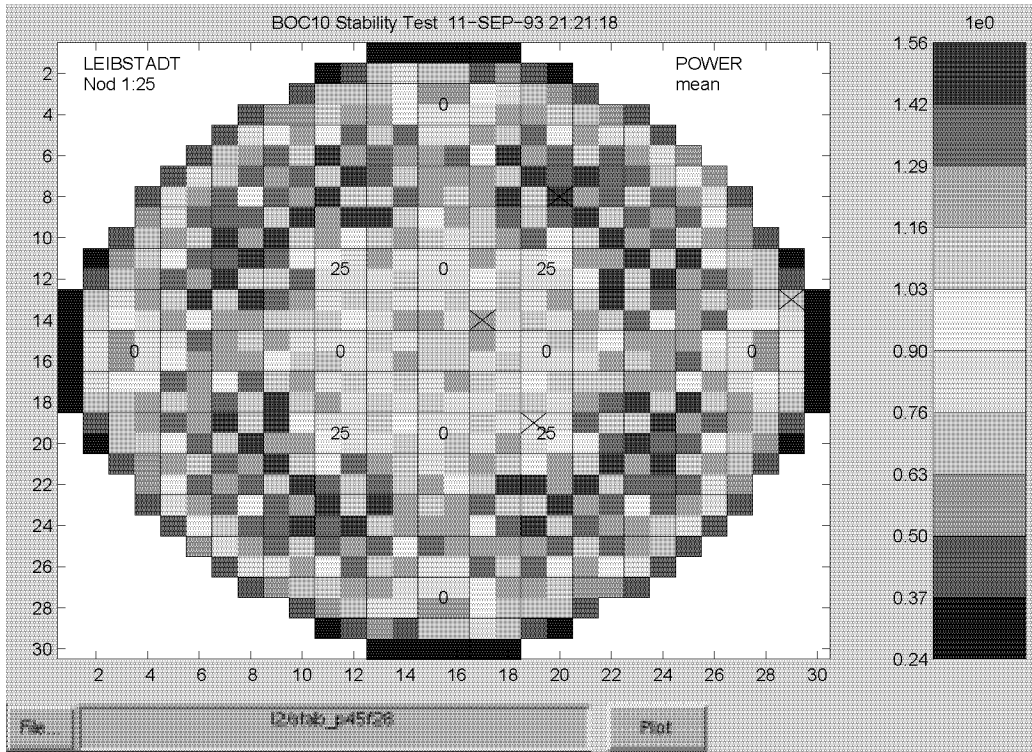
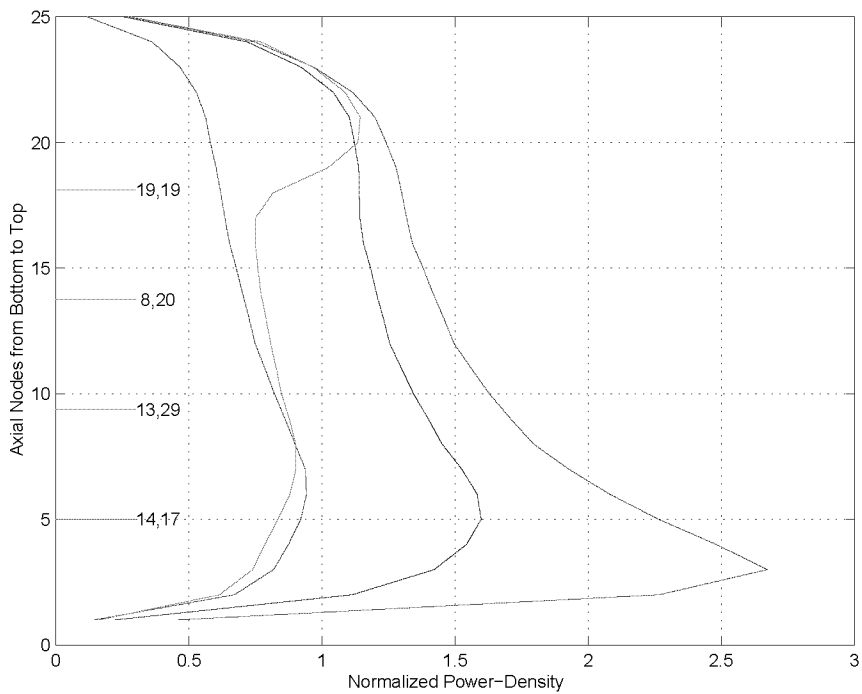Figure 5.1: Axially Averaged Power Density Distribution of the Leibstadt Reactor

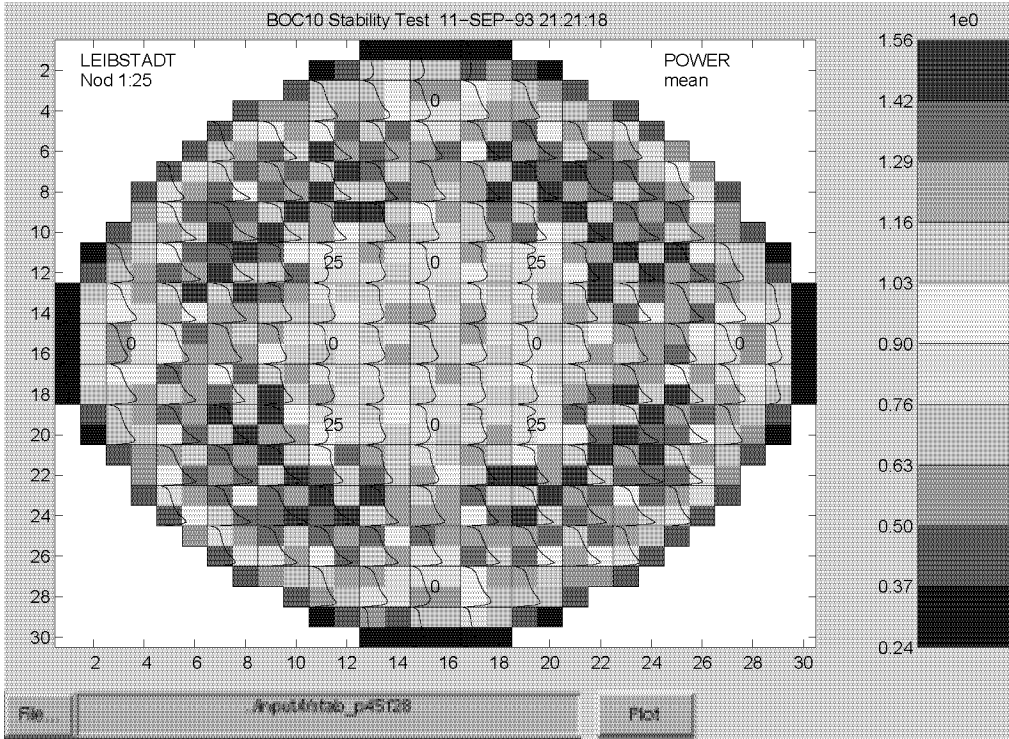Figure 5.2: Axial Power Shapes in Individual Channels of the Leibstadt Reactor

Figure 5.3: Axial Power Shapes in the Leibstadt Reactor

5.3 Eigenvectors

It was stressed several times before that a wealth of information may be gained from an investigation of the left and right eigenvectors of the dominating oscillation modes. The availability of the eigenvectors which come naturally from the calculation of the eigenvalue (see Section 4.3 Equation 4.6), are a major advantage of MATSTAB as will be shown in the following pages.

Equation 2.25 describes the mode j of a chosen variable $\Delta\mathbf{x}_j(\tau)$ in terms of the dominating eigenvalue λ_j, the corresponding left and right eigenvectors $\mathbf{f}_j$ and $\mathbf{e}_j$ and the value at time $\tau = 0$ of the mode considered.

$$\Delta\mathbf{x}_j(\tau) = \mathbf{e}_j e^{\lambda_j \tau} [\mathbf{f}_j^T \Delta\mathbf{x}_j(0)] \tag{2.25}$$

5.3.1 Right Eigenvector

The right eigenvector $\mathbf{e}_j$ describes the relative magnitude and phase of the dominating mode $\Delta\mathbf{x}_j(\tau)$ of the state variable $\mathbf{x}(\tau)$. Since both $e^{\lambda_j \tau}$ and $\mathbf{f}_j^T \Delta\mathbf{x}_j(0)$ are scalars, the shape of the mode $\Delta\mathbf{x}_j(\tau)$ is entirely defined by $\mathbf{e}_j$.
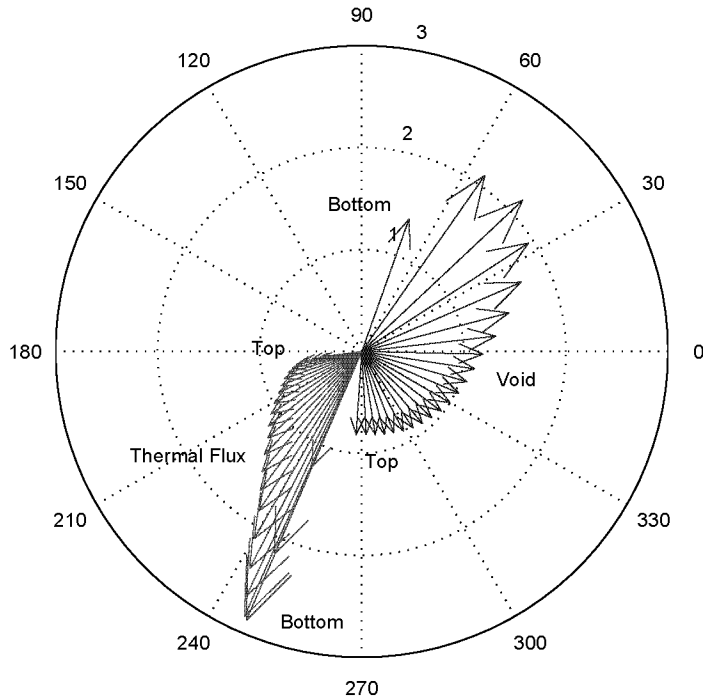
Figure 5.4: Void and Thermal Neutron Flux Phasors in One Channel

The complete eigenvector **e** has a very large number of components, therefore, only its components may be displayed in a reasonable manner.

If just one channel is investigated, it is possible to see the gain as well as the phase shift. The phasors in Figure 5.4 show the phase and gain of the void fraction and of the thermal neutron flux, for all 25 nodes in a specific channel. One can see, that the gain is larger in the bottom part of the reactor and smaller in the upper part. It is also easy to spot, that there is a phase shift of 180 degrees for the void component whereas the phase of the thermal flux component is only shifted by $\approx$ 60 degrees from bottom to top. The channel was selected randomly and represents the normal situation in a channel. Figure 5.5 shows the absolute value of the eigenvector component that corresponds to the thermal flux.

5.3.2 Left Eigenvector

Equation 2.25 also clarifies the role of the left eigenvector $\mathbf{f}_j$. The left eigenvector $\mathbf{f}_j$ determines how the mode is excited by the initial conditions. Note that if $\Delta \mathbf{x}_j(0) = k * \mathbf{e}_j$ for some scalar k, then only the mode j is excited, $\Delta \mathbf{x}(\tau) = \Delta \mathbf{x}_j(\tau)$, since $\mathbf{F}^T \mathbf{E} = \mathbf{I}$ by definition 2.18.
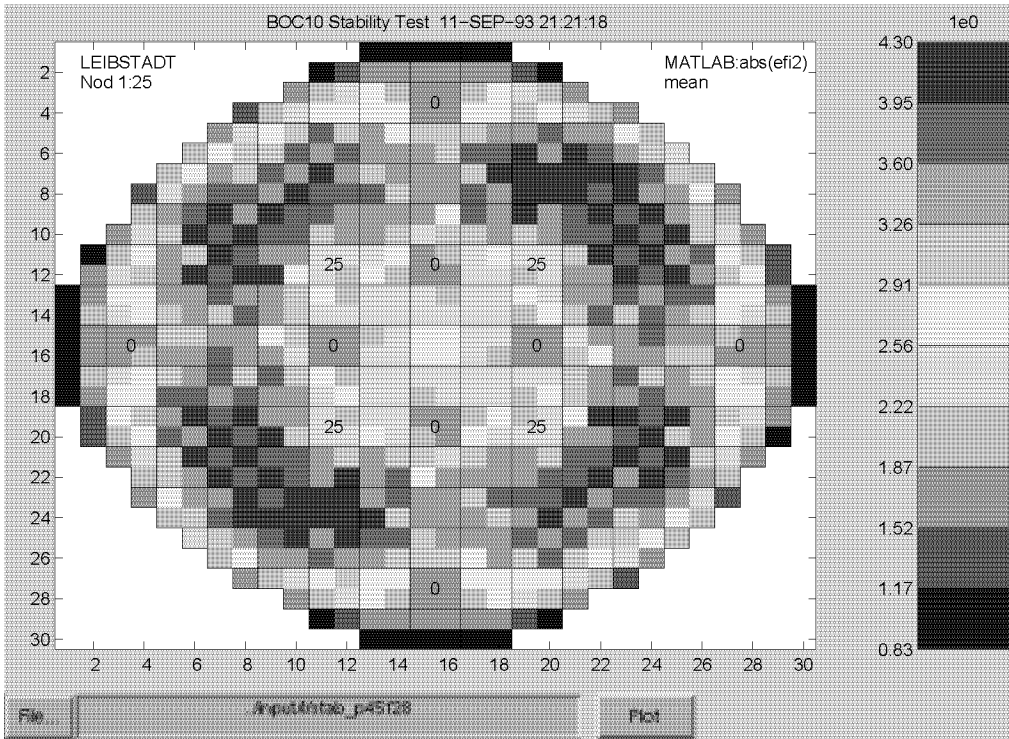
Figure 5.5: Thermal Flux (Absolute Value) of the Right Eigenvector (Axially Averaged)

5.4   The Contributors to the Eigenvalue/Decay Ratio

The real value of the left eigenvector **f** lies in the possibility to broaden the decay ratio concept. The following section outlines a methodology to calculate the contribution of any model component to the eigenvalue/decay ratio and hence to the stability of the system. It is possible to analyze the contribution of any model section, channel, node, equation or parameter to the eigenvalue and hence stability of the system.

The eigenvalue and consequently also the decay ratio, is no longer only one number describing the overall behavior of the coupled system. The number is composed from different components, each of which has its own physical meaning. For example, it is possible to calculate the contribution of each fuel assembly to the eigenvalue or the contribution of a specific equation (e.g. slip) or section (e.g. riser) in the model.

In MATSTAB, the dominating eigenvalue λ is obtained directly during the iterative calculation of the right eigenvector. However, it is instructive to represent the eigenvalue by means of both (left and right) eigenvectors.

Multiplying the basic equation of the generalized eigenvalue problem (Equation 2.15)

$$\mathbf{A}_s\mathbf{e} = \lambda\mathbf{B}\mathbf{e} \tag{2.15}$$

from the left with the left eigenvector, leads to

$$\mathbf{f}^T\mathbf{A}_s\mathbf{e} = \lambda\mathbf{f}^T\mathbf{B}\mathbf{e} \tag{5.1}$$

$$\lambda = \frac{\mathbf{f}^T\mathbf{A}_s\mathbf{e}}{\mathbf{f}^T\mathbf{B}\mathbf{e}} \tag{5.2}$$

$$\lambda = \mathbf{f}^T\mathbf{A}_s\mathbf{e} \tag{5.3}$$

because $\mathbf{f}^T\mathbf{B}\mathbf{e}=1$ due to the scaling of $\mathbf{f}^T$. It is interesting to investigate Equation 5.3 a bit further.

$$\lambda = \mathbf{f}^T\mathbf{A}_s\mathbf{e} \tag{5.4}$$

$$= \sum_{k=1}^{n}\mathrm{f}_k\sum_{l=1}^{n}\mathrm{a}_{k,l}\mathrm{e}_l \tag{5.5}$$

$$= \sum_{k,l}\mathrm{f}_k\mathrm{a}_{k,l}\mathrm{e}_l \tag{5.6}$$

$$\lambda = \begin{bmatrix} 1 & \dots & 1 \end{bmatrix} \begin{bmatrix} \mathrm{f}_1\mathrm{a}_{1,1}\mathrm{e}_1 & \dots & \mathrm{f}_1\mathrm{a}_{1,n}\mathrm{e}_n \\ \vdots & \mathrm{f}_k\mathrm{a}_{k,l}\mathrm{e}_l & \vdots \\ \mathrm{f}_n\mathrm{a}_{n,1}\mathrm{e}_1 & \dots & \mathrm{f}_n\mathrm{a}_{n,n}\mathrm{e}_n \end{bmatrix} \begin{bmatrix} 1 \\ \vdots \\ 1 \end{bmatrix} \tag{5.7}$$

The introduced matrix

$$\mathbf{A}_\lambda = \begin{bmatrix} \mathrm{f}_1\mathrm{a}_{1,1}\mathrm{e}_1 & \dots & \mathrm{f}_1\mathrm{a}_{1,n}\mathrm{e}_n \\ \vdots & \mathrm{f}_k\mathrm{a}_{k,l}\mathrm{e}_l & \vdots \\ \mathrm{f}_n\mathrm{a}_{n,1}\mathrm{e}_1 & \dots & \mathrm{f}_n\mathrm{a}_{n,n}\mathrm{e}_n \end{bmatrix} \tag{5.8}$$

has very interesting properties. The first and most obvious is that the sum of all matrix elements equals the eigenvalue λ.

But furthermore, the entries $\mathrm{f}_k\mathrm{a}_{k,l}\mathrm{e}_l$ of the matrix $\mathbf{A}_\lambda$ represent each a dependency of a certain variable in a certain equation in a certain node. Since the number of these entries is large ($\approx 10^6$) and dependent on the nodalization scheme, it is reasonable to sum up some subsets. For example, one can add all summands within the different model sections; neutronics, thermal-hydraulics or the sections outside the core (steam dome, downcomer, etc.). Since the reactor core is a very interesting section, one should also investigate the contributions of the different fuel channels.

Finally, it is also possible to sum up and analyze the contribution of each model equation (row in the matrix) or each variable (column in the matrix). When summing over a node, a channel or a model section, the contribution of e.g. the void fraction equation differs naturally from the contribution of the void fraction variable. Nevertheless, when summing over the complete model, the contributions of equations and their corresponding variables is the same. The reason lies in the fact that the sum over the row j in the matrix $\mathbf{A}_\lambda$ equals the sum over the column j.

$$\sum_{row\,j} \mathbf{A}_{\lambda} = \sum_{l=1}^{n} \mathrm{f}_j \mathrm{a}_{j,l} \mathrm{e}_l \tag{5.9}$$

$$= \mathrm{f}_j \sum_{l=1}^{n} \mathrm{a}_{j,l} \mathrm{e}_l \tag{5.10}$$

$$= \mathrm{f}_j \mathbf{A}_{s,row\,j} \mathbf{e} \tag{5.11}$$

$$= \mathrm{f}_j \lambda \mathrm{e}_j \tag{5.12}$$

because $\mathbf{e}$ is an eigenvector of $\mathbf{A}_s$ and

$$\sum_{column\,j} \mathbf{A}_{\lambda} = \sum_{k=1}^{n} \mathrm{f}_k \mathrm{a}_{k,j} \mathrm{e}_j \tag{5.13}$$

$$= \mathrm{e}_j \sum_{k=1}^{n} \mathrm{f}_k \mathrm{a}_{k,j} \tag{5.14}$$

$$= \mathrm{e}_j \mathbf{f}^T \mathbf{A}_{s,column\,j} \tag{5.15}$$

$$= \mathrm{e}_j \lambda \mathrm{f}_j \tag{5.16}$$

$$= \sum_{row\,j} \mathbf{A}_{\lambda} \tag{5.17}$$

The expression $\lambda f_j e_j$ is in principle the same as the expression $f_j e_j$ which is well known from control theory as the participation factor. This property of the matrix $\mathbf{A}_{\lambda}$ is very interesting for further investigations, but should not mislead to the conclusion that the matrix is symmetric. As stated before, only the sum over the complete model is the same for equations and variables. When summing over nodes, channels, etc. the results differ.

Representation of the Decay Ratio as a Product of Contributing Factors

The sum in Equation 5.6 is easy to translate into a product which leads to the decay ratio. As shown in Chapter 2, the decay ratio can be written as

$$DR = e^{\frac{2\pi\sigma}{\omega}} \tag{2.27}$$

$$= e^{\left(\frac{2\pi}{\omega} \sum_{k,l} real(\mathrm{f}_k \mathrm{a}_{k,l} \mathrm{e}_l)\right)} \tag{5.18}$$

$$= \prod_{k,l} e^{\frac{2\pi}{\omega} real(f_k a_{k,l} e_l)} \tag{5.19}$$

$$\equiv \prod_{k,l} \mathrm{dr}_{k,l} \tag{5.20}$$

The representation of the eigenvalue as a sum over different contributions seems to be more natural than this representation of the decay ratio as a product of different contributions.

Especially because unimportant objects are 1 in the product representation, which feels a bit strange when speaking about decay ratios. Therefore, the next few sections only deal with the contributions to the eigenvalue where an unimportant object, as expected, contributes with 0.

5.4.1 Contribution of the Model Sections to the Eigenvalue

The Figure 5.6 shows the contribution of the different model sections (outside of the core, thermal-hydraulics, neutronics, flow distribution model, pumps and system pressure) to the real part of the eigenvalue; i.e. the sum of the section contributions equals the real part of the eigenvalue. The four colored bars represent different operating points from the Leibstadt measurement series conducted in 1993 (see Table 6.6 on page 120). For the most stable case, MATSTAB calculated a decay ratio of 0.42 and for the least stable case 1.02.

Unfortunately, Figure 5.6 does not identify a special section as the driving force of instability. The contributions of all sections diminish in a similar way for less stable operating points. The contributions and therefore also the changes in the thermal-hydraulic and neutronic part dominate, however, the behavior of the reactor. In the second plot of Figure 5.6, the contribution of the thermal-hydraulic and neutronic part of the model are added and represented as the contribution of the core. The combined contribution is negative and, therefore, stabilizing. The stabilizing contribution of the thermal-hydraulics over-compensates the destabilizing contribution of the neutronic part. However, the difference becomes smaller for less stable operating points. In other words, when moving from a stable to a less stable operating point, the contributions decrease, but the reduction in the thermal-hydraulic part is larger than the reduction in the neutronic part, hence, the reactor becomes overall less stable.

Figure 5.7 shows this trend. The dashed region, representing the difference between the thermal-hydraulic and neutronic part, diminishes in the less stable region. The interpretation of the absolute value of the contributions is, however, difficult. There are not enough measurements points available to relate the magnitude of a single contribution to the reactor state.

Since in Forsmark always measures the same operating point during start up, it is not possible to generate the corresponding plots for Forsmark. Therefore, some (numerical) studies for different operating points in different power plants are recommended as future work. The necessary steady-state distribution files need, however, to be prepared by the plant, since POLCA is not generally available.

It remains to observe, that the "decay ratio" and "thermal-hydraulics" lines in Figure 5.7 are roughly parallel. This simple relationship between the decay ratio and the contribution of the thermal-dynamics may very well be a coincidence, since only four operating points are involved, but further investigations when more operating points are available are recommended.
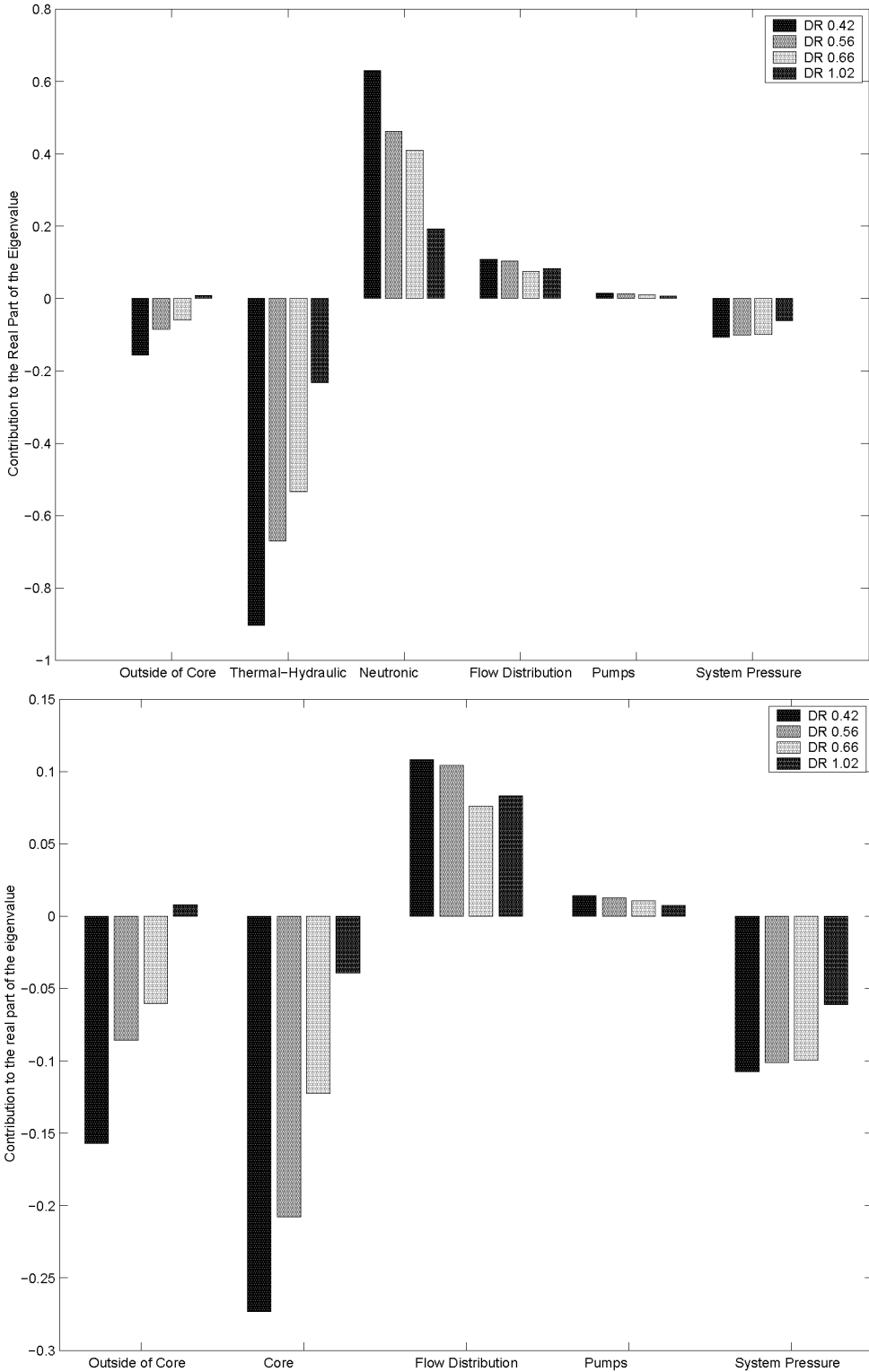
Figure 5.6: Contribution of Each Model Section of the Reactor for Different Operating Points (for 5 and 6 Model Sections)
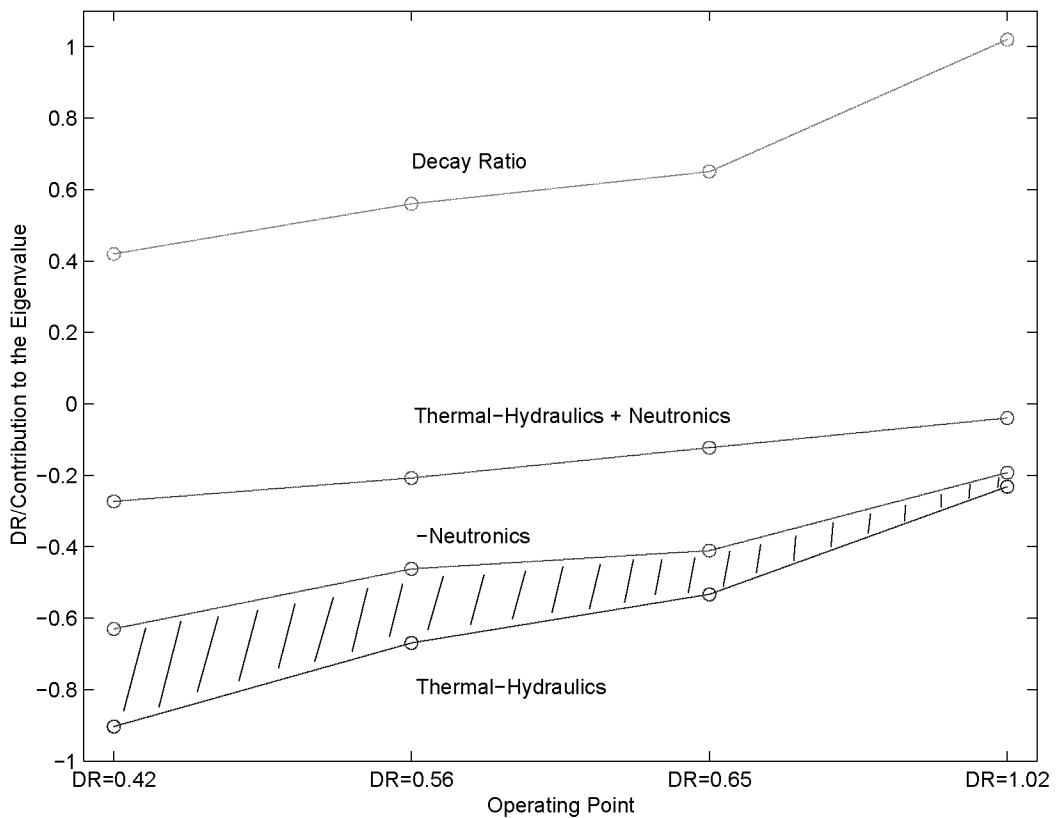
Figure 5.7: Comparison Between the Decay Ratio and the Contributions of the Reactor Core

5.4.2 Contribution of the Fuel Assemblies to the Eigenvalue during an Approach to Instability

In addition to the analysis of the contributions of different model sections, it is also interesting to investigate the contributions to the eigenvalue of the different fuel assemblies in the core. This is done in this section by examining a series of operating points in order of decreasing stability.

Figure 5.8 shows the power density of the Leibstadt reactor for a very stable operating point (DR $\approx$ 0.1). The corresponding plot with the contribution to the real part of the eigenvalue of the different fuel assemblies is shown in Figure 5.9. The colors represent the axially averaged value in each channel. Note that the sum of all channel values (times 25 nodes) added to the values in each node outside of the core, equal the real part of the eigenvalue of the dominating mode. Negative values have a stabilizing influence, whereas positive values have a destabilizing influence.
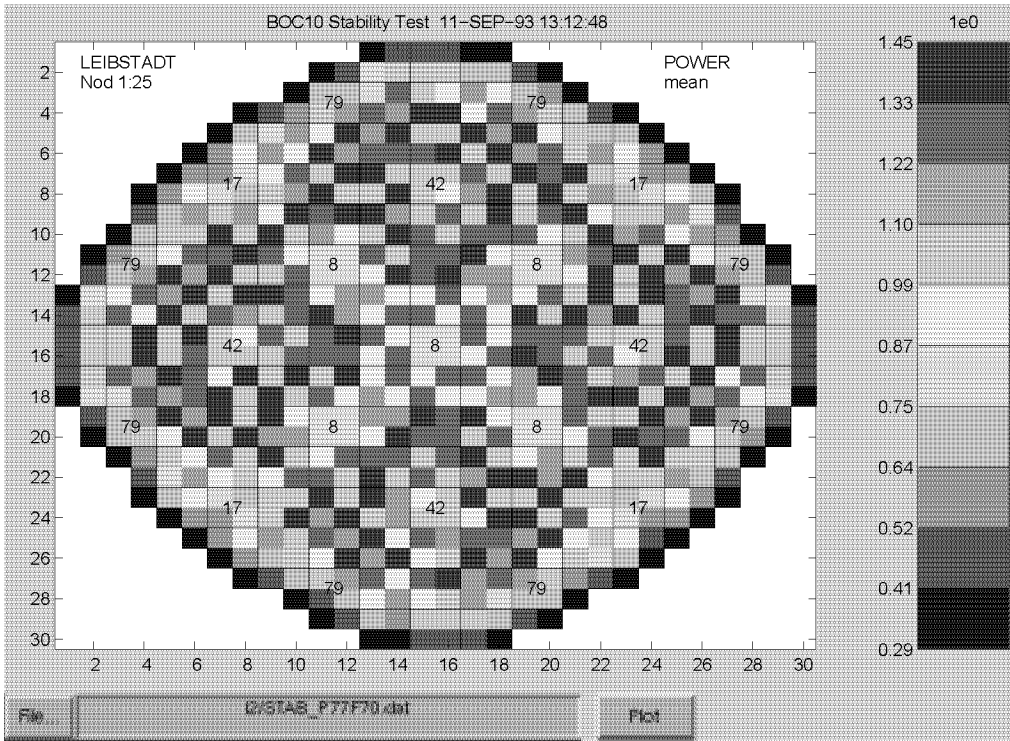
Figure 5.8: Power-Density Distribution for 77% Power and 70% Core Flow in Leibstadt
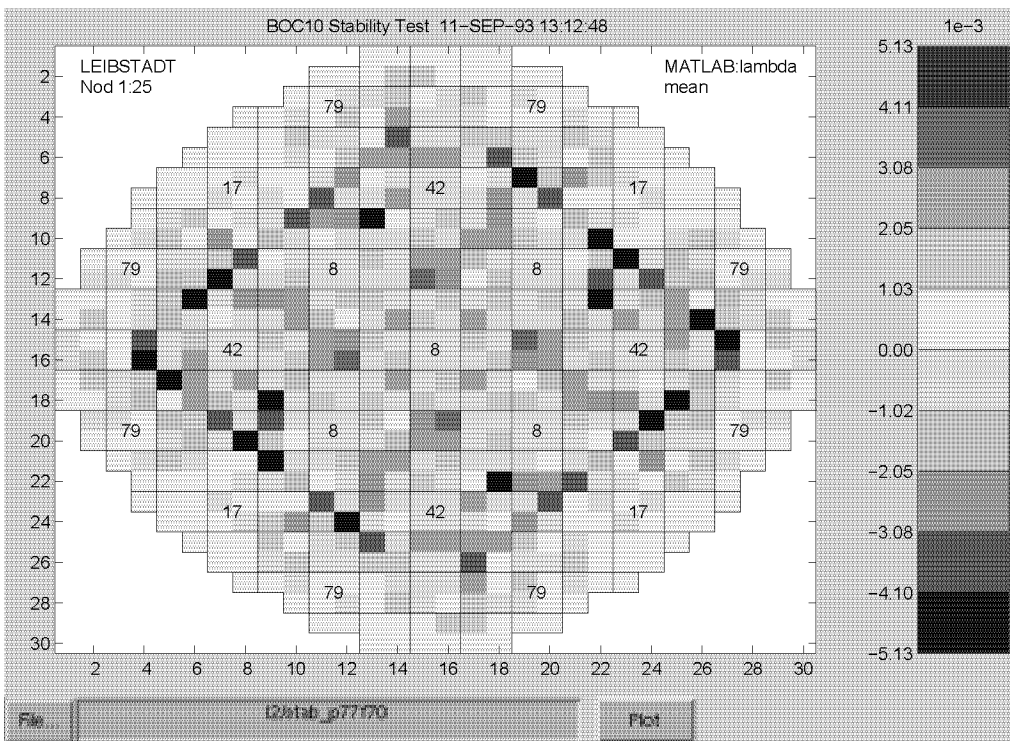

Figure 5.9: Contribution of Each Channel to the Eigenvalue for 77% Power and 70% Core Flow in Leibstadt
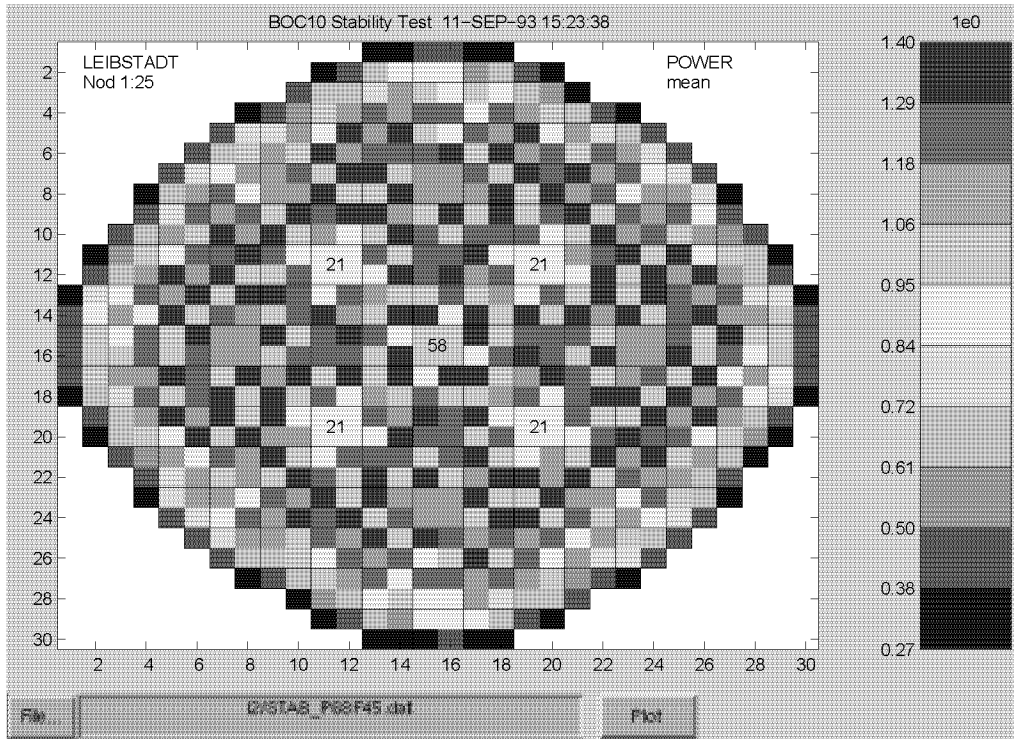
Figure 5.10: Power-Density Distribution for 68% Power and 45% Core Flow in Leibstadt
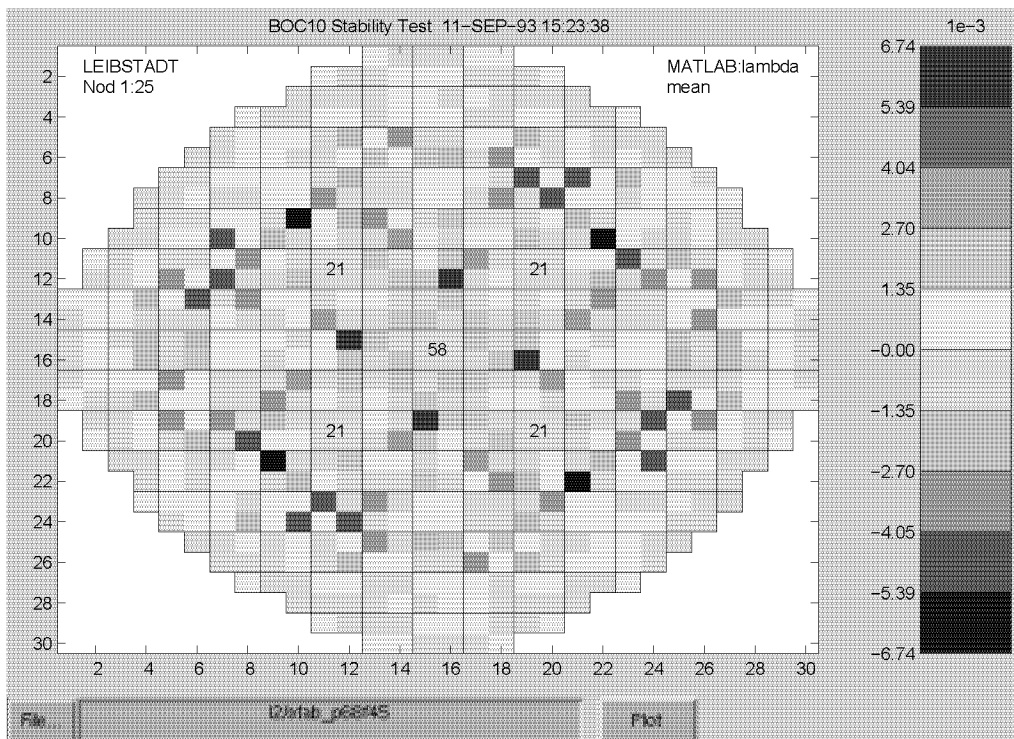

Figure 5.11: Contribution of Each Channel to the Eigenvalue for 68% Power and 45% Core Flow in Leibstadt

While the outer ring of fuel assemblies in the core are more or less neutral (low leakage strat-
egy and ,therefore, low power density), there exists a ring of high-power-density assemblies
with a large stabilizing effect (dark blue). These are the assemblies with a relative flat power
density distribution. The strongly bottom-peaked assemblies with a high power density in
the center of the core are destabilizing but largely outnumbered. As a result, the core is very
stable.

The Figures 5.10 and 5.11 show the same information (power density, contribution to the
real part of the eigenvector respectively) for the next operating point in the Leibstadt mea-
surement series from 1993. The operating point is a bit less stable (DR $\approx$ 0.42) and it may
be observed, that the radial distribution of the eigenvalue contributions became flatter. The
above mentioned ring of stabilizing assemblies breaks up, and the destabilizing assemblies
are found closer to the center of the core. The assemblies at the border of the core remain
close to zero but move from a slightly destabilizing tendency to a slightly stabilizing ten-
dency.

Figures 5.12 and 5.13 represent the next operating point (DR $\approx$ 0.56) in the measurement se-
ries. The break up of the "stabilizing ring" advances further, but the destabilizing assemblies
in the center become less distinct. However, the latter effect is overshadowed by the former,
since overall, the reactor is less stable. The contributions from the model section outside the
core, remained roughly the same, as may be checked in Figure 5.6.

Figures 5.14 and 5.15 represent again the next operating point (DR $\approx$ 0.65) in the measure-
ment series. The tendency is the same as in the figures before, with the exception, that the
destabilizing assemblies in the center decreased in number but not in scale of the contribu-
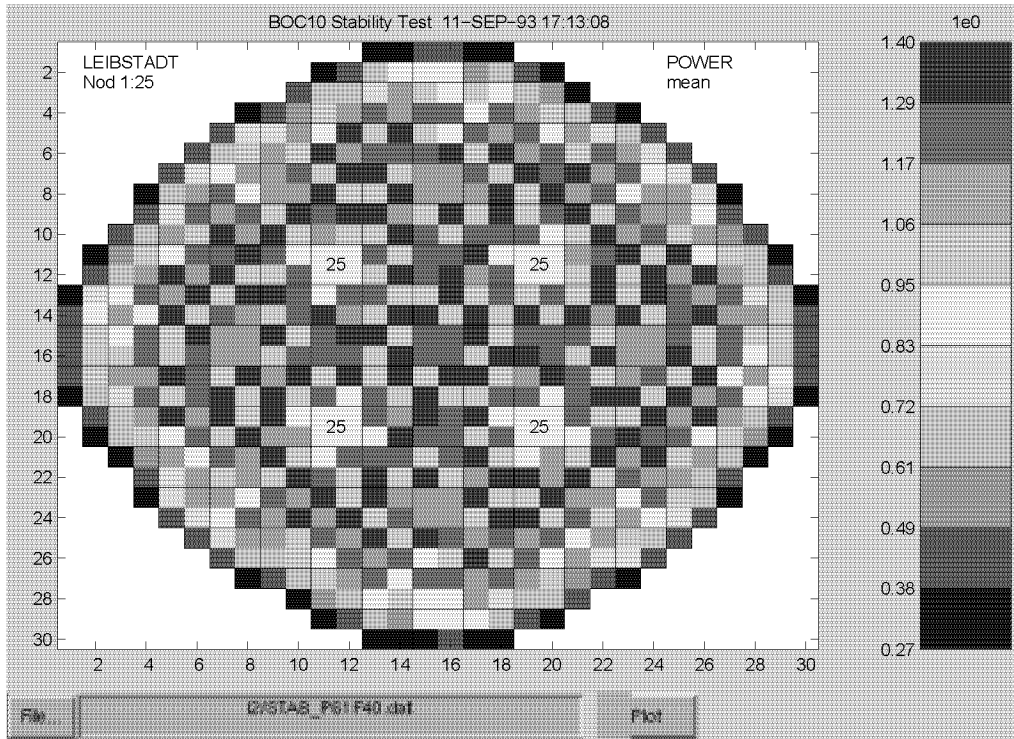tion.

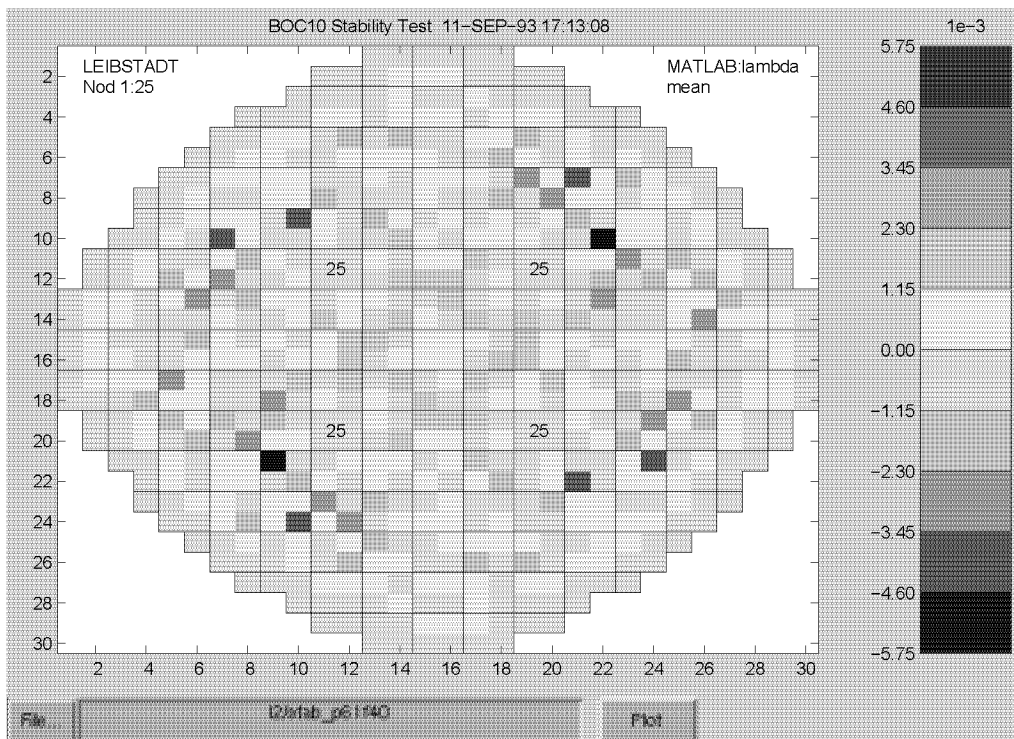Figure 5.12: Power-Density Distribution for 61% Power and 40% Core Flow in Leibstadt

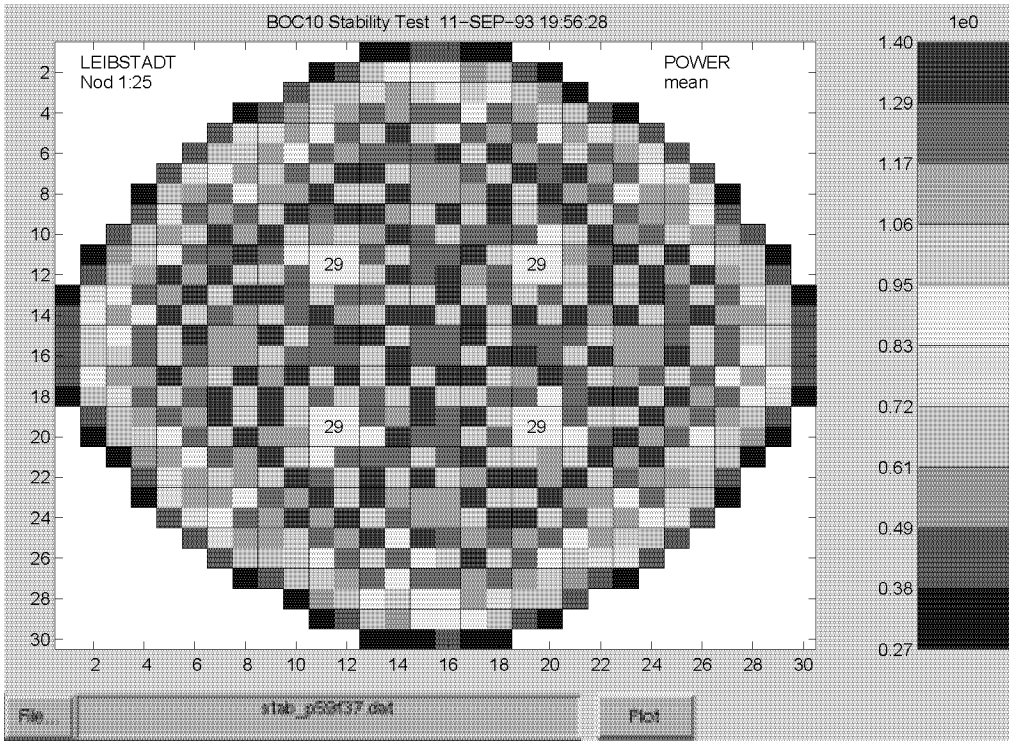Figure 5.13: Contribution of Each Channel to the Eigenvalue for 61% Power and 40% Core Flow in Leibstadt

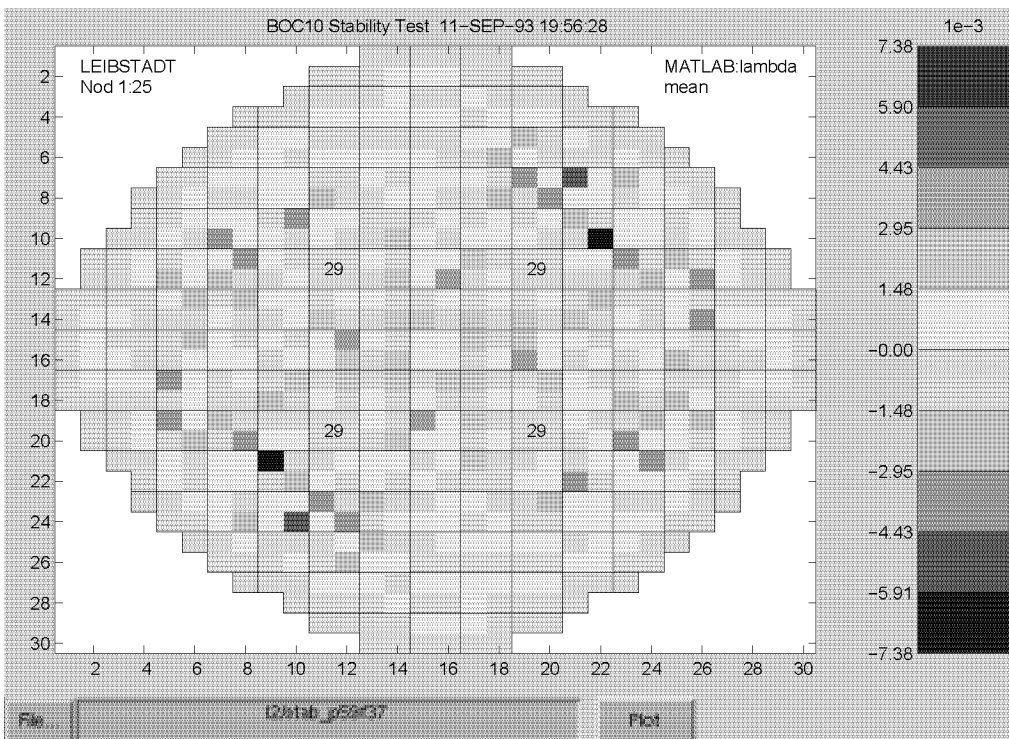Figure 5.14: Power-Density Distribution for 59% Power and 37% Core Flow in Leibstadt

Figure 5.15: Contribution of Each Channel to the Eigenvalue for 59% Power and 37% Core Flow in Leibstadt

5.4.3 The Core of an Unstable Operating Point

Finally, Figures 5.16 and 5.17 show an unstable operating point (DR $\approx$ 1.0). The new aspect is, that the destabilizing center vanished completely, but two point-symmetric areas with a destabilizing effect appeared (orange). The radial shape of the distributions became reasonably flat with the exception of the two stabilizing areas (dark blue). It needs not much fantasy, to imagine a half core oscillation with the symmetry line from top left to bottom right, or from bottom left to top right. Even so, no regional oscillations were observed, this is in agreement with the high decay ratios for regional oscillations predicted by MATSTAB for the very same measurement series (see Table 6.6 on page 120).

One more interesting detail is that in contrast to the section-wise representation, in the assembly-wise representation not all contributions decrease (absolute value), the less stable an operating point is. The contribution of some fuel assemblies actually grows. The most extreme fuel assemblies (dark blue) in Figure 5.17 have a very large negative (stabilizing) contribution to the eigenvalue. Nevertheless, these assemblies are at the place where the regional oscillations reach their maxima and minima.

Figure 5.18 shows the part of the right eigenvector that represents the neutron flux for the dominating (global) mode at unstable operating conditions. According to Equation 2.25, this is also the driving force behind the time development. The arrows in the plot represent the phase and amplitude of the oscillation for some selected nodes. The black arrows are calculated by MATSTAB whereas the white arrows are measured with the LPRMs (Local Power Range Monitor for neutron flux). A detailed description on how the black and white arrows are calculated may be found in Section 6.1.2. In this representation, the absolute values of phase and amplitude have no physical meaning, only relative values are of interest.

Figure 5.19 shows the same information for the first regional mode. The plot shows that the amplitudes close to the symmetry line and close to the border of the core are, as expected, very small. The white arrows represent again the same measurement information as in the figure above. However, the scaling is different. For these two pictures, the scaling is done in such a way, that the first calculated phasor looks exactly to the right.

Since the calculations for this case predict a similar decay ratio for the global as well as for the regional case, it may be assumed, that the measured phasors contain a substantial regional component. It would therefore be prudent to add the calculated contributions from the global and regional modes. A comparison of these compound phasors should give even better agreement with the measurement data which naturally contains the superposition of all modes. It would also be interesting to compare the difference in amplitude of the global and regional component. Unfortunately, this cannot be achieved in a simple way, because MATSTAB has no information on how to scale the vectors. The basic problem is, that the eigenvectors may be multiplied with any complex number, and still stay the same eigenvectors. If the initial condition of the modes were known, Equation 2.25 could have been used. However, this is not the case.
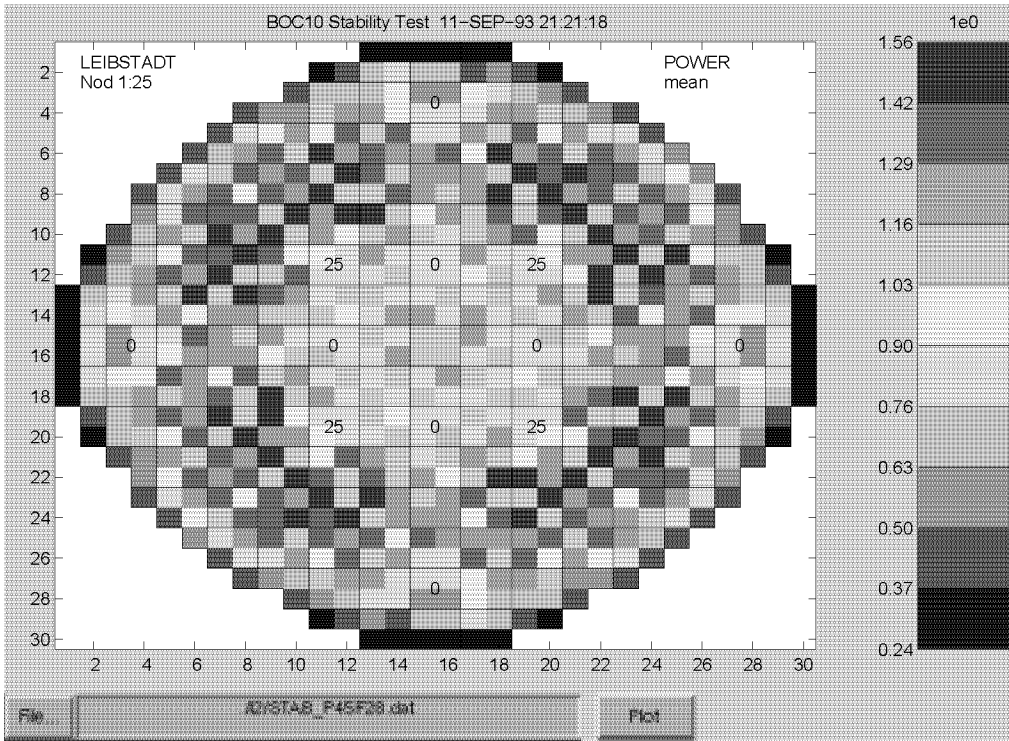
Figure 5.16: Power-Density Distribution for 45% Power and 28% Core Flow in Leibstadt, Reference Case
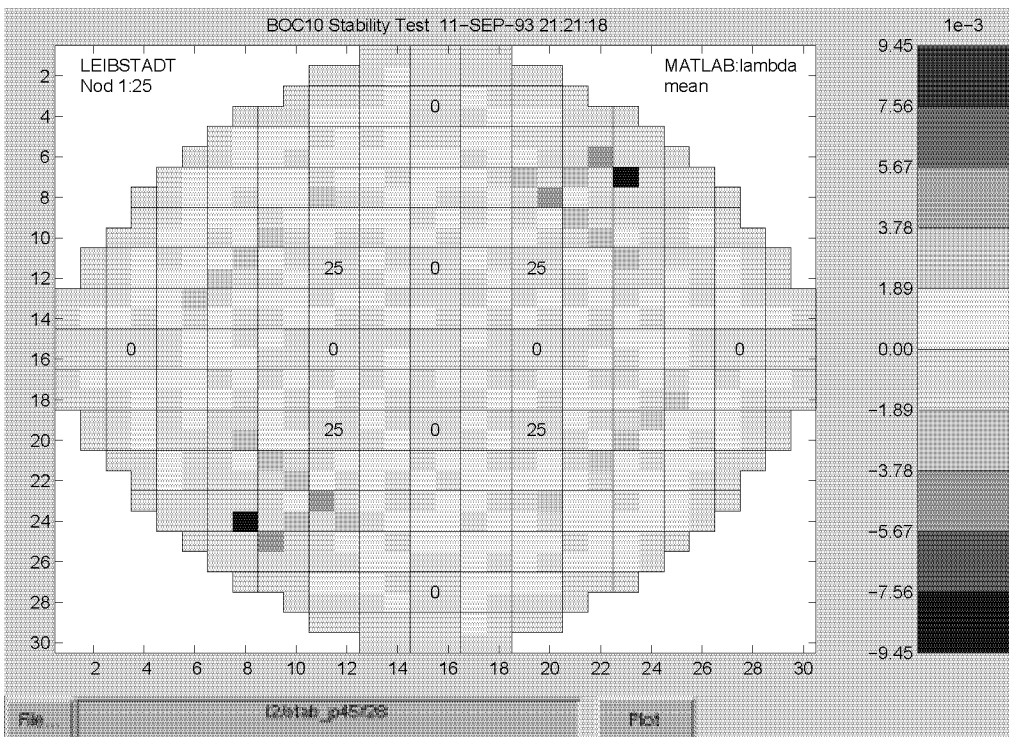

Figure 5.17: Contribution of Each Channel to the Eigenvalue for 45% Power and 28% Core Flow in Leibstadt, Reference Case
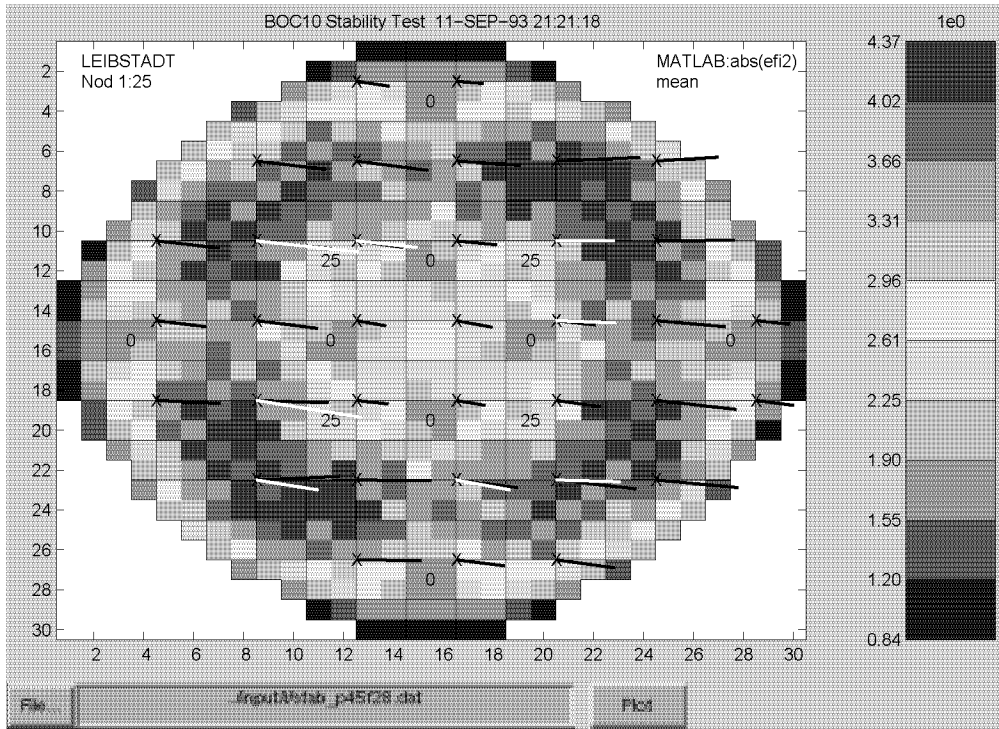
Figure 5.18: Comparison of MATSTAB and Measurement Point P45F28 in Leibstadt, Global Case
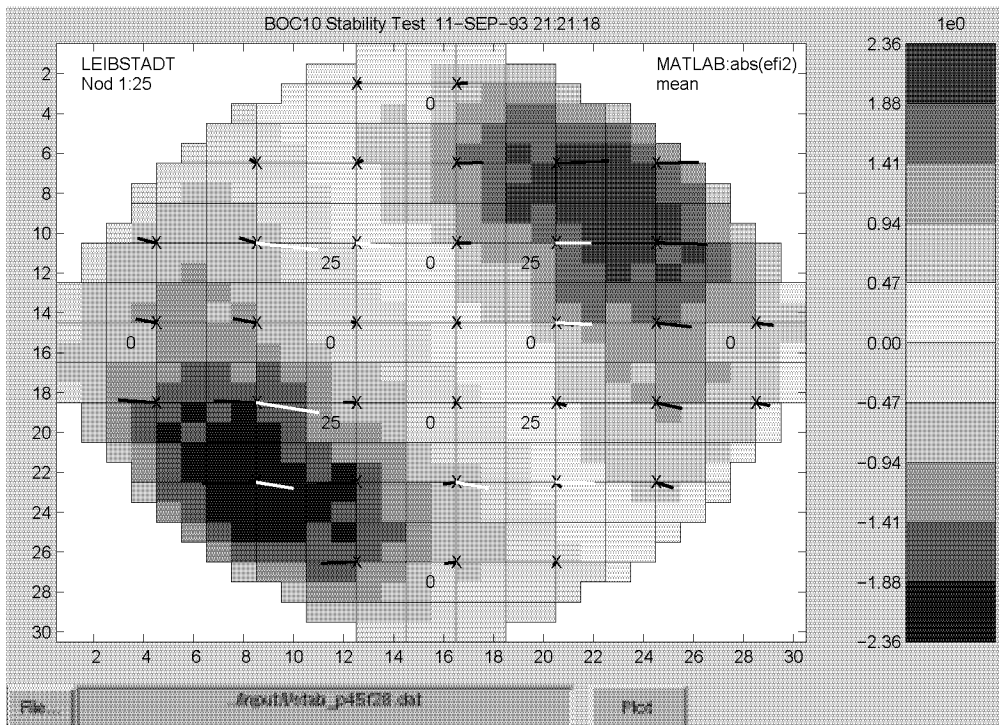

Figure 5.19: Comparison of MATSTAB and Measurement Point P45F28 in Leibstadt, Regional Case

In principle, the amplitudes could be approximately calculated if one does a least-squares fitting and solves the following equation set for C_1 and C_2.

$$C_1 * MATSTAB_{global} + C_2 * MATSTAB_{regional} = MEASUREMENT_{LPRM} \qquad (5.21)$$

The uncertainty in the measurement itself, and the small number of LPRMs make this approach too unreliable to be of use.

A comparison between calculated and measured inlet flow data was done, but again the large uncertainty in the measurement data made a meaningful comparison impossible. For example, the relevant frequency of the oscillation could not be detected from Forsmark's inlet flow measurements.

5.4.4 Further Analysis Around an Unstable Operating Point

The Figures 5.20-5.25 show a brief analysis of the unstable operating point P45F28 shown in Figure 5.16 on page 74. While the reference case corresponds with an operating point measured in 1993 in Leibstadt, the other operating points are just a numerical investigation and were not realized with the reactor. All decay ratios and frequencies are listed in Table 5.1.

Case Description	DR Global	DR Regional	FR Global	FR Regional
Reference Case: Power 45% Core Flow 28%	1.02	1.03	0.42	0.45
Moderate Swap of the Control Rods	0.94	0.94	0.41	0.43
Extreme Swap of the Control Rods	1.23	0.78	0.44	0.43
Power Increase of 5%	1.13	1.18	0.42	0.45

Table 5.1: Investigation Around the Operating Point P45F28 with Power 45% and Core Flow 28% in Leibstadt

Figures 5.20 and 5.21 show the reactor after a moderate swap of control rods i. e. a moderate change in the power density distribution. The core power and the core flow were kept constant. One can observe that in comparison to the reference state (Figure 5.16) the extreme assemblies became fewer, but even more negative (down to -0.035 compared to -0.00945). Both the global and regional oscillation were stabilized, since in each quarter of the core, a control rod was inserted 25 percent. These control rods changed the radial power-shape just enough to make the core stable by a narrow margin.

Figures 5.22 and 5.23 show the reactor after a major swap of control rods. The rods are now inserted in the periphery rather than the center. The concentration of the high power assemblies in the center leads to a very unstable reactor (DR=1.23). The dominant fuel assemblies
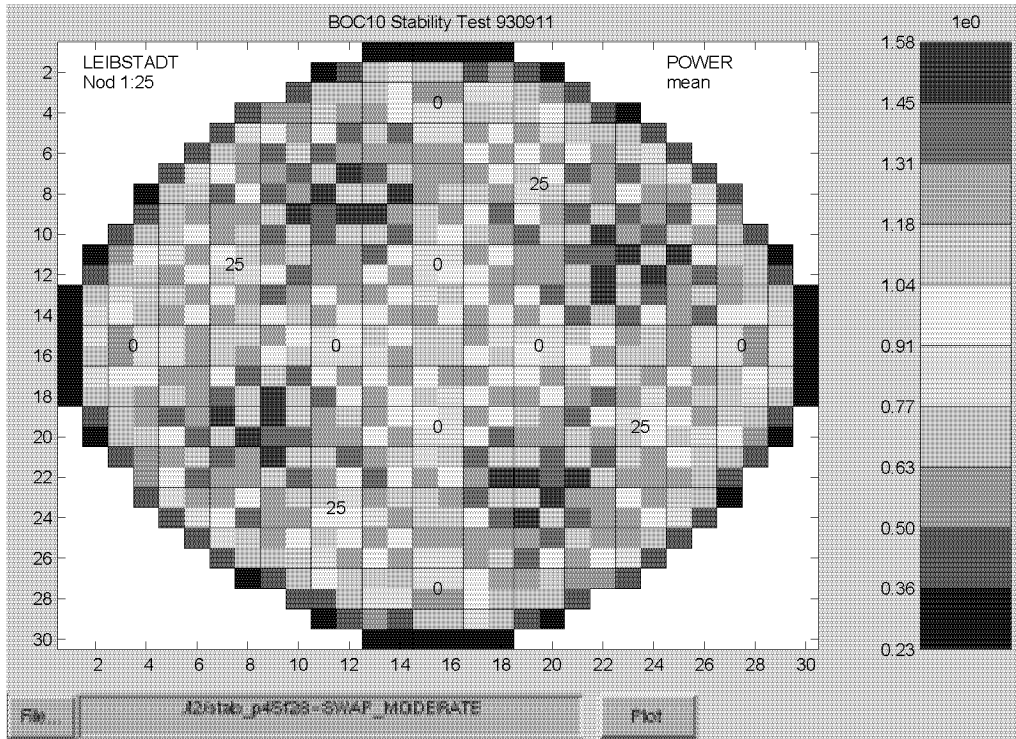
Figure 5.20: Power-Density Distribution After a Swap of Control Rods
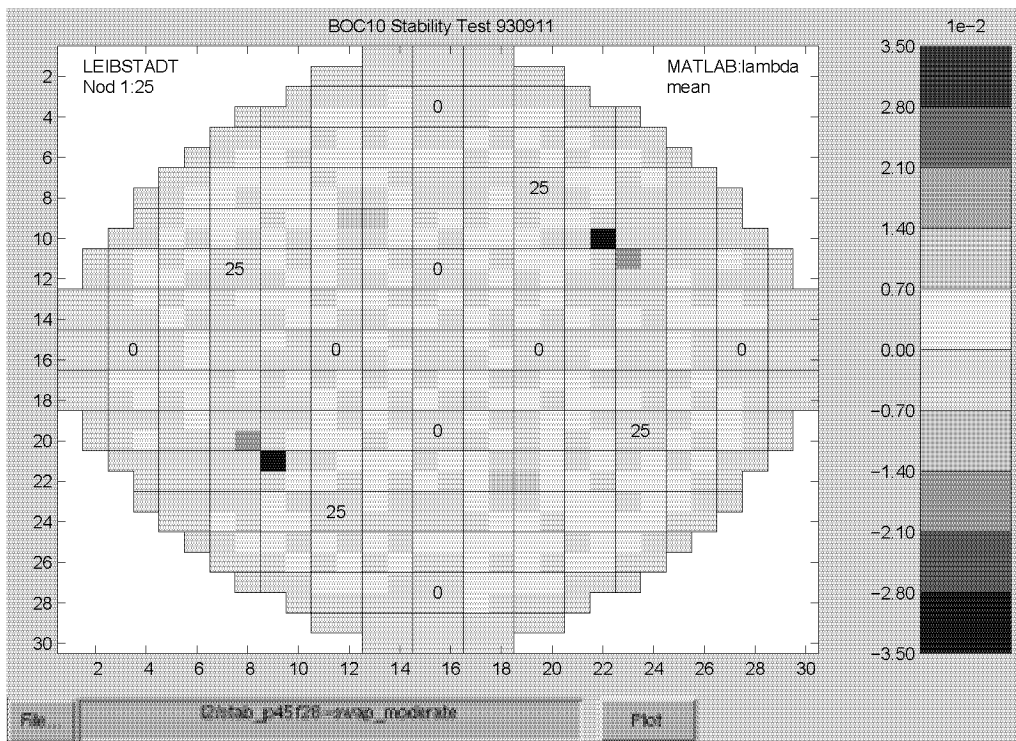
Figure 5.21: Contribution of Each Channel to the Eigenvalue After a Swap of Control Rods

Figure 5.22: Power-Density Distribution After a Major Change in Control Rod Pattern

Figure 5.23: Contribution of Each Channel to the Eigenvalue After a Major Change in Control Rod Pattern
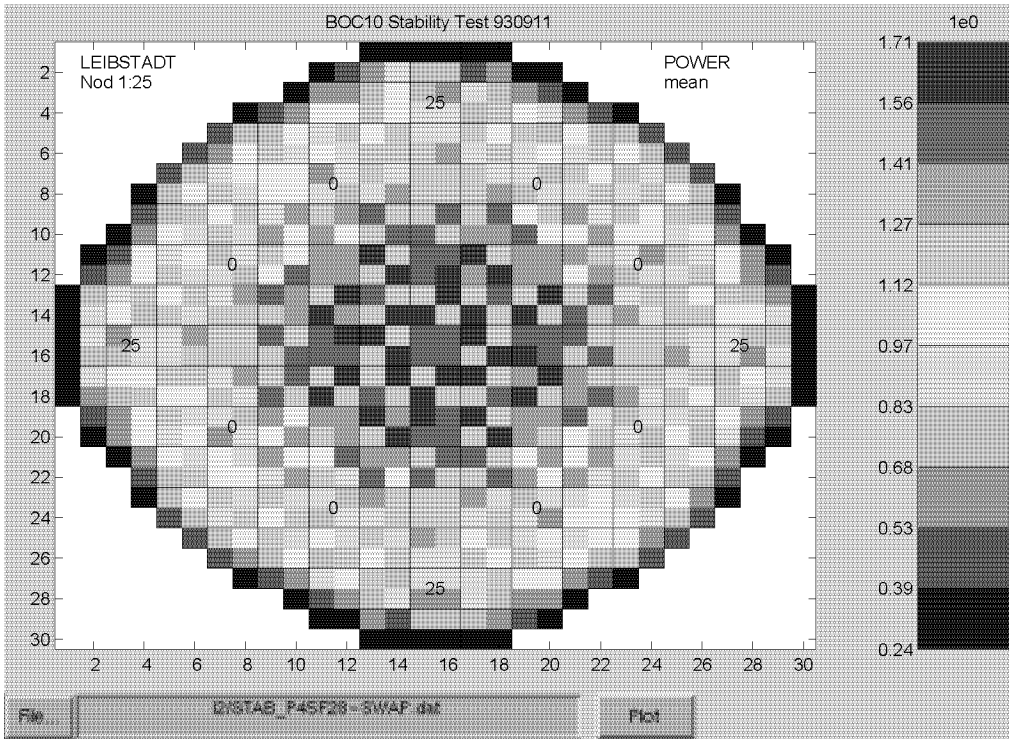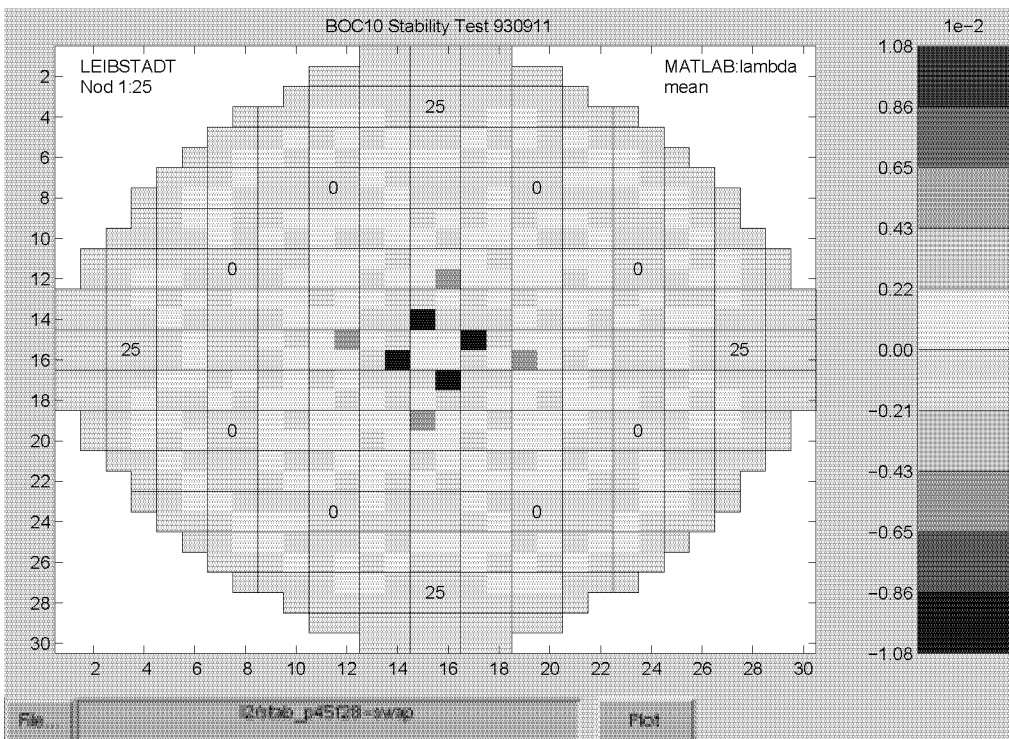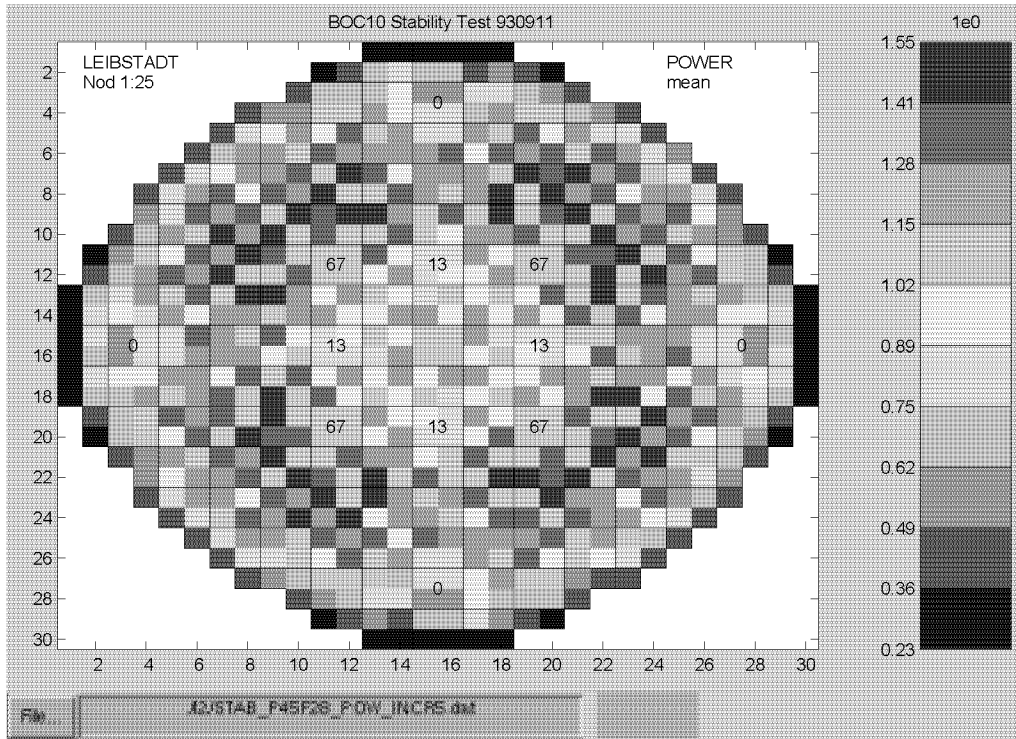
Figure 5.24: Power-Density Distribution After a Positive Change in Power
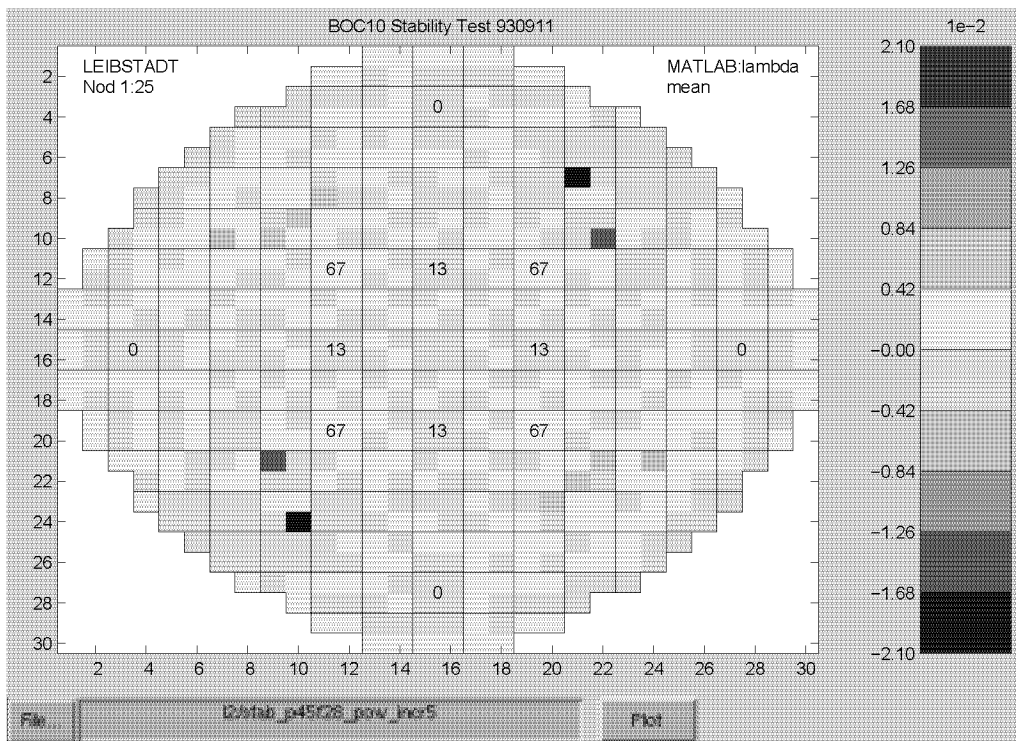

Figure 5.25: Contribution of Each Channel to the Eigenvalue After a Positive Change in Power

are larger in number, but smaller in their contribution (up to -0.0108 compared with -0.035 for the moderate swap). It is easy to spot that the high power density in the center of the reactor suppresses regional behavior, and that the global mode dominates. The numbers in Table 5.1 also give a clear verdict. DR global = 1.23 and DR regional = 0.78.

Figures 5.24 and 5.25 show the reactor after a power increase of five percent above the base case. Pulling the control rods while keeping the core flow constant, shifts the operating point of the reactor to a less favorable part of the power-flow map. Consequently, the decay ratio grew from 1.02 (reference case) to 1.13. In agreement with the measurement series shown in Figures 5.8-5.17, the stabilizing assemblies tend to become smaller in number but larger in scale for a less stable operating point.

Figures 5.26 and 5.27 show a comparison of the axial distribution of the eigenvalue contributions for the stable operating point (Figure 5.8) and the unstable reference case (Figure 5.16), respectively. The interesting information is that the first few nodes from the bottom normally give a positive contribution regardless whether the overall contribution of the fuel assemblies is positive or negative. This is expected, since the boiling boundary is around node four or five.

Figures 5.28 and 5.29 show the contribution to the eigenvalue from the same four fuel assemblies for the two operating points and confirm this observation. The four assemblies are chosen to be extreme cases in both plots. The location (coordinates) of the assemblies is plotted on the left side of the figures.

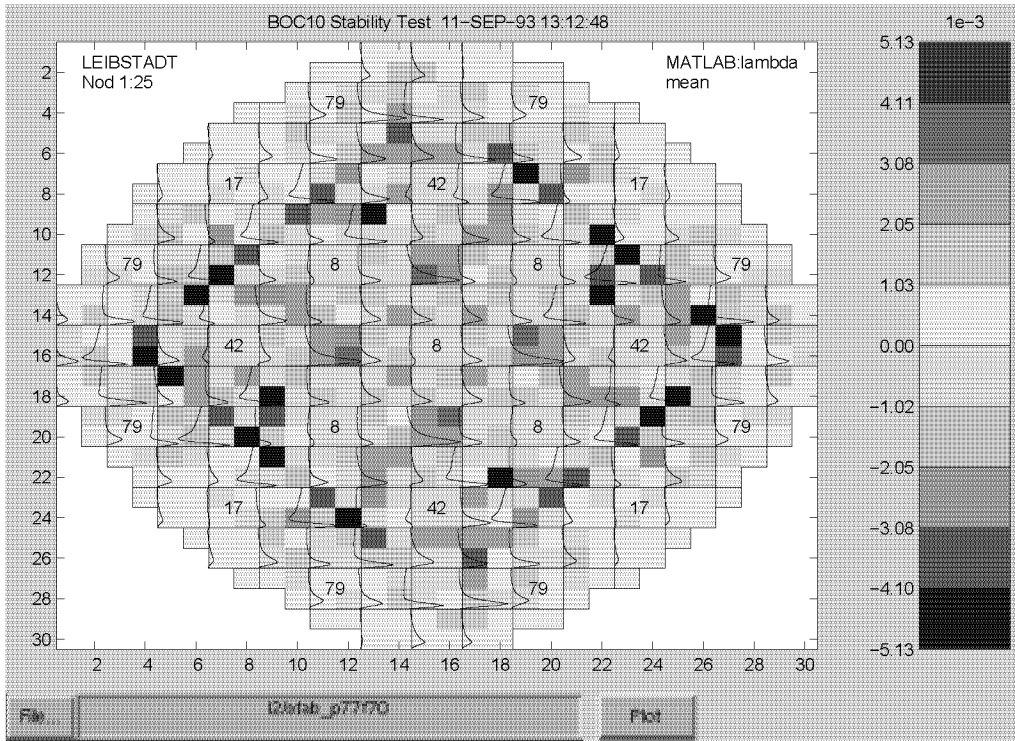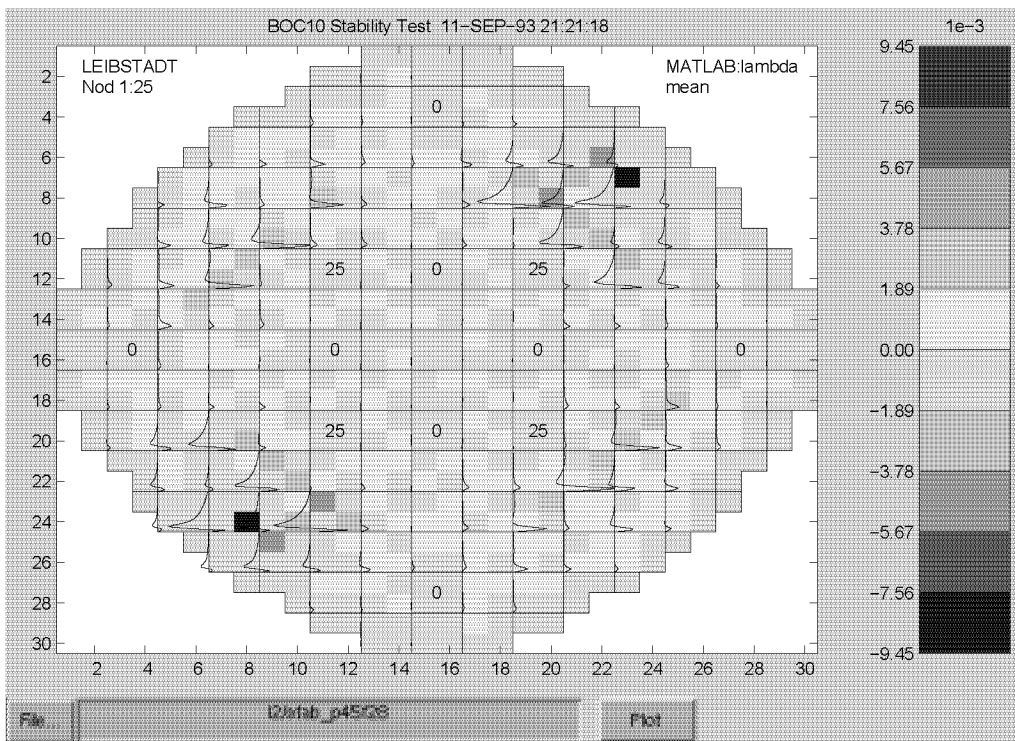Figure 5.26: Contribution of Each Axial Node to the Eigenvalue (Stable Case)

Figure 5.27: Contribution of Each Axial Node to the Eigenvalue (Unstable Case)
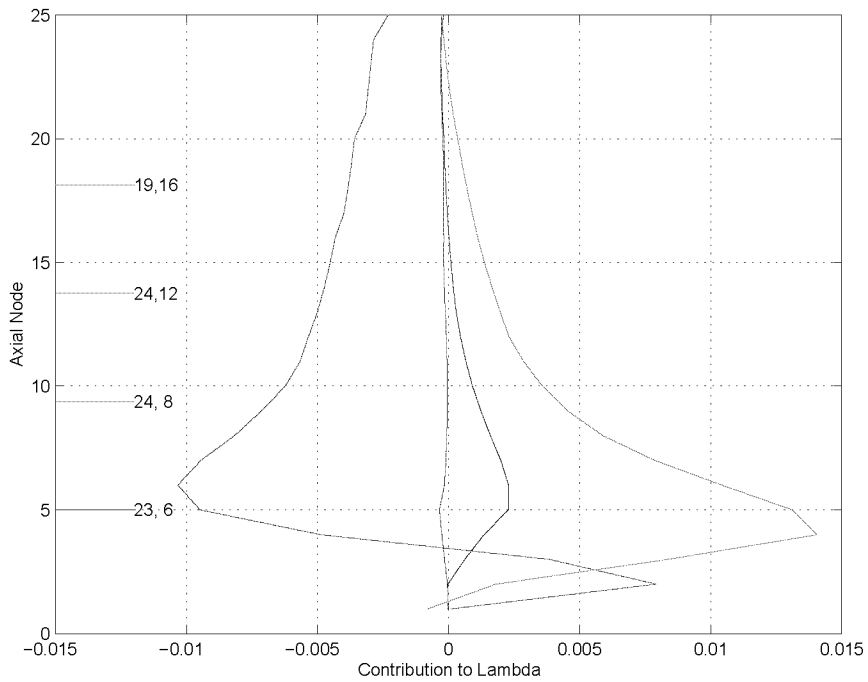
Figure 5.28: Axial Distribution of Contributions to the Eigenvalue for Extreme and Average Fuel Assemblies, Stable Case
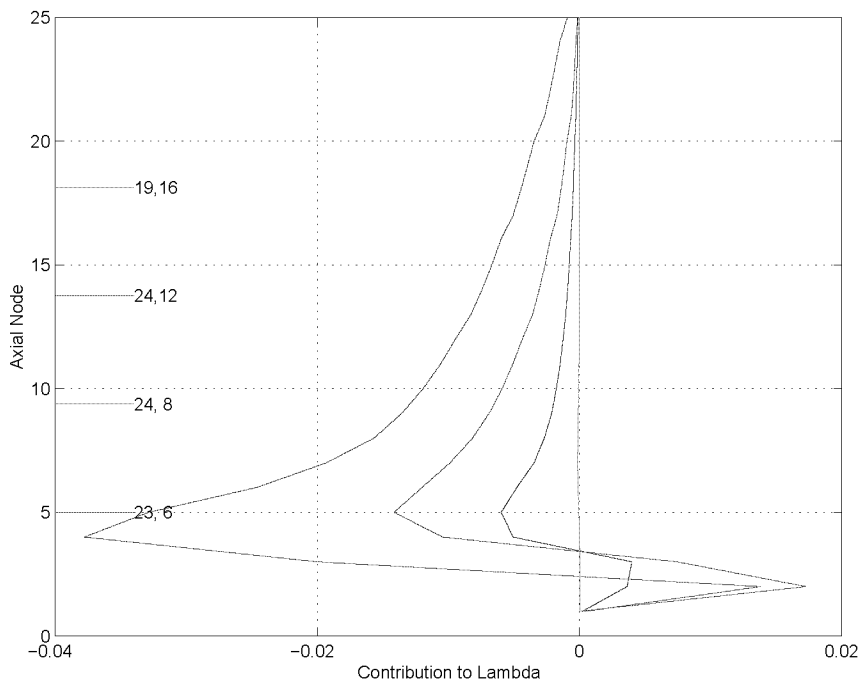

Figure 5.29: Axial Distribution of Contributions to the Eigenvalue for Extreme and Average Fuel Assemblies, Unstable Case

5.4.5 Contribution of Selected Equations and Variables to the Eigenvalue

Taking the level analysis one step further, it is possible to show for each equation or variable its contribution to the real part of the eigenvalue. The difference between the equation-wise and the variable-wise representation is, that in the former case, the rows of the matrix $\mathbf{A}_\lambda$ (Equation 5.7) are summed up, and in the latter case, the columns are summed up.

For example, the contribution of the void fraction equation shows how the void fraction gets affected by the other variables. Figure 5.30 shows, how much the void fraction equation in contributes to the real part of the eigenvalue.
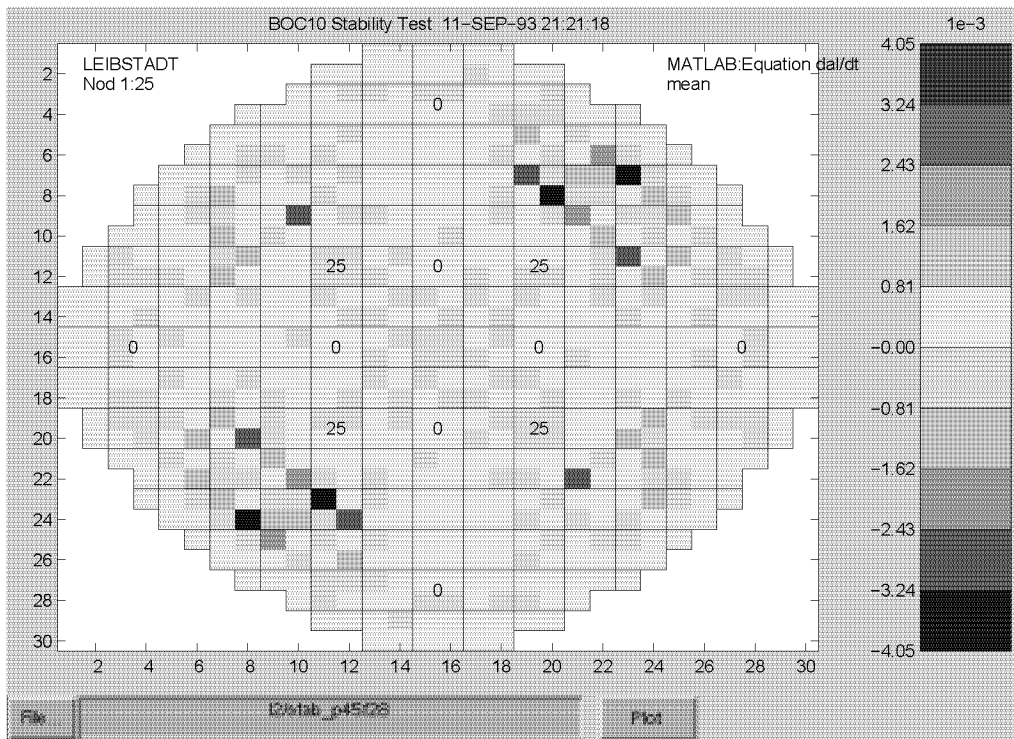
Figure 5.30: Contribution of the Equation for the Void Fraction to the Eigenvalue

The contribution of the void fraction variable shows, how the void fraction affects the other variables. This is shown in Figure 5.31 where the void fraction variable contributions to the real part of the eigenvalue are plotted.

As mentioned in the comment to Equation 5.8, it makes sense to distinguish between equations and variables when looking at a section of the model (e.g. fuel channel). When looking at the full model, equations and variables contribute both with $f_j \lambda e_j$ to the eigenvalue.

The similar information was generated for all equations and variables. The analysis of the data was, however, not fruitful. It was not obvious how to interpret the plots. An unexpected observation was, that the absolute value of the contribution of some equations (e.g. vapor generation rate and liquid temperature) was by several orders of magnitude smaller than the
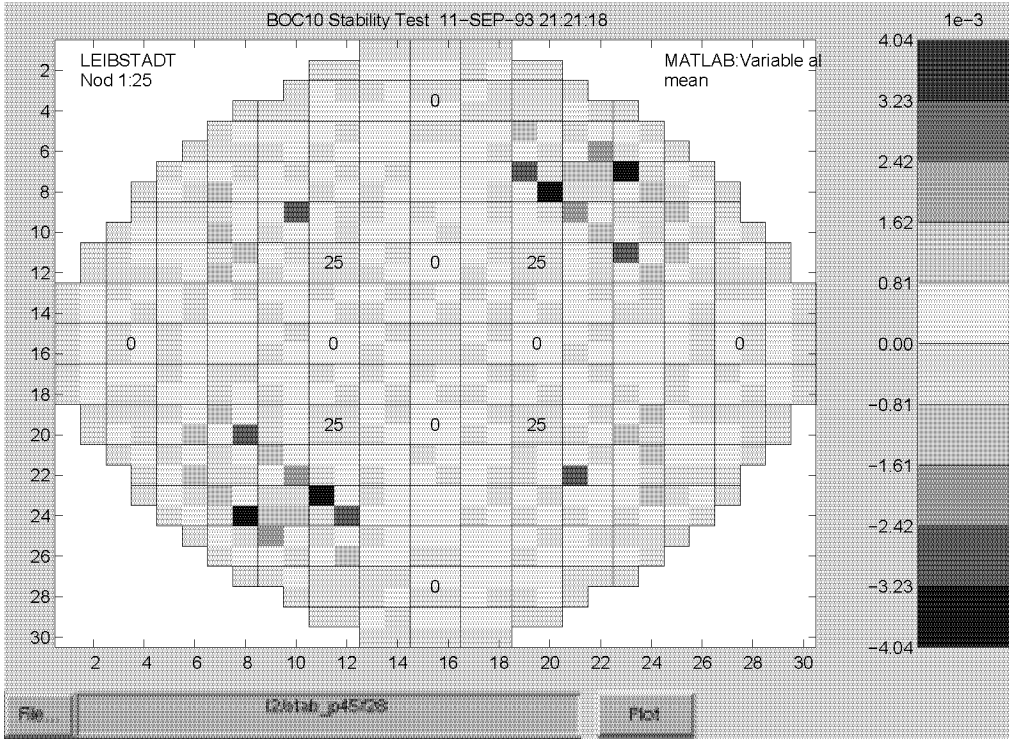
Figure 5.31: Contribution of the Variable Void Fraction to the Eigenvalue

contribution of other equations. This would actually imply, that the information present in these equations is not needed in the model. Further investigations are necessary to support this conclusion.

5.4.6   Analysis of Operating Points based on Eigenvalue Contribution Plots

To overcome the difficulties in interpreting the many thousands of contributions to the real part of the eigenvalue, as encountered in the previous sections of this chapter, the matrix A_λ from Equation 5.7

$$A_\lambda = \begin{bmatrix} f_1 a_{1,1} e_1 & \ldots & f_1 a_{1,n} e_n \\ \vdots & f_k a_{k,l} e_l & \vdots \\ f_n a_{n,1} e_1 & \ldots & f_n a_{n,n} e_n \end{bmatrix} \tag{5.22}$$

is examined a bit further. To start width, two MATSTAB calculations with nearly identical operating points are compared. The only difference between the two calculations, is the pressure drop in the riser (input parameter VHO of MATSTAB). The reference calculation is the Leibstadt case presented in Figure 5.14 where the pressure drop over the riser is set to its default value (VHO=-7.0). The resulting decay ratio is 0.6475. The second case is exactly the same, but VHO=-20.0 and the resulting decay ratio is 0.6397.

Figure 5.32 shows the contribution of all equations in all nodes to the real part of the eigen-value. The x-axis represents the equation number, and the y-axis represents the contribution to the eigenvalue. The ordering of the equations is the same as in the matrix $\mathbf{A}_\lambda$. A detailed description can be found in Table B.4 on page 161. The total number of equations is around 200'000. Since the difference in the two cases is very small, the red and the blue line in the plot can only be distinguished at a few places.
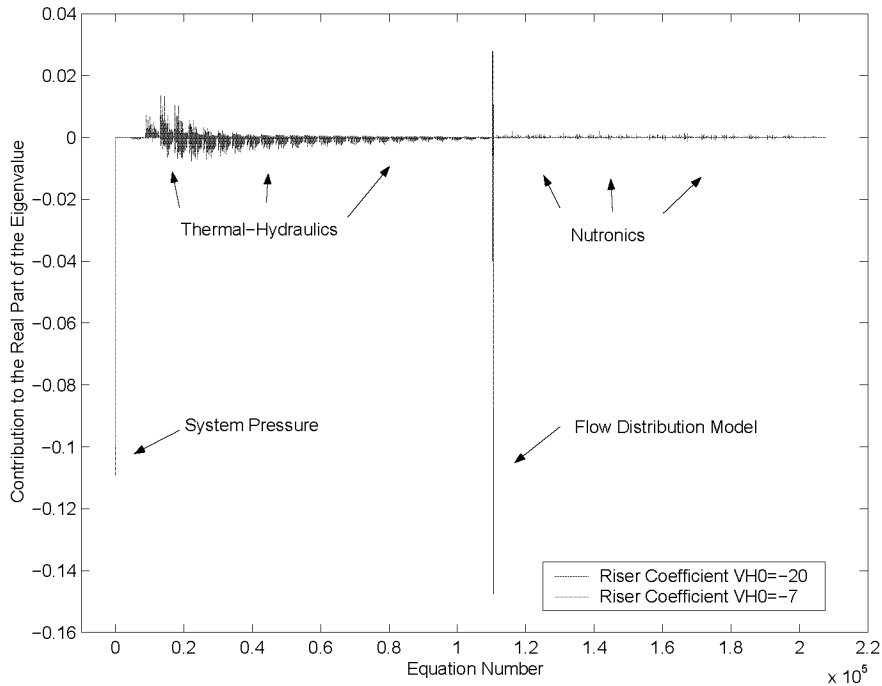
Figure 5.32: Contribution to the Real Part of the Eigenvalue: Equations

The first equation in the matrix, the system pressure, leads to two clearly different values in the two compared calculations. This is not surprising, since the pressure drop over the riser has changed. The second large deviation in the two calculations is the very sharp peak around equation 110'000. The extrema in the reference calculations are smaller than for the second case. After a quick check in Table B.4 on page 161 one can identify the peak as the flow distribution model. A more detailed analysis of this deviation follows later.

The Figure 5.33 shows the cumulative contribution to the eigenvalues previously plotted in Figures 5.32. The cumulative sum of, for example, 1, 2, 3, 4 is defined as 1, 1+2, 1+2+3, 1+2+3+4. Since the curve plotted in Figure 5.32 represents the sum of all elements in $\mathbf{A}_\lambda$, the last point in the graph equals the real part of the eigenvalue.

As mentioned in the comment to Figure 5.26-5.29, the three nodes closest to the bottom in a fuel assembly tend to have a positive contribution to the eigenvalue whereas the remaining nodes have a negative contribution. This observation is very easy to spot in the cumula-tive plots. It can also be easily observed, that the change in the pressure drop stabilizes the thermal-hydraulics (the blue line becomes more negative at the beginning) and destabilizes

Figure 5.33: Cumulative Contribution: Equations
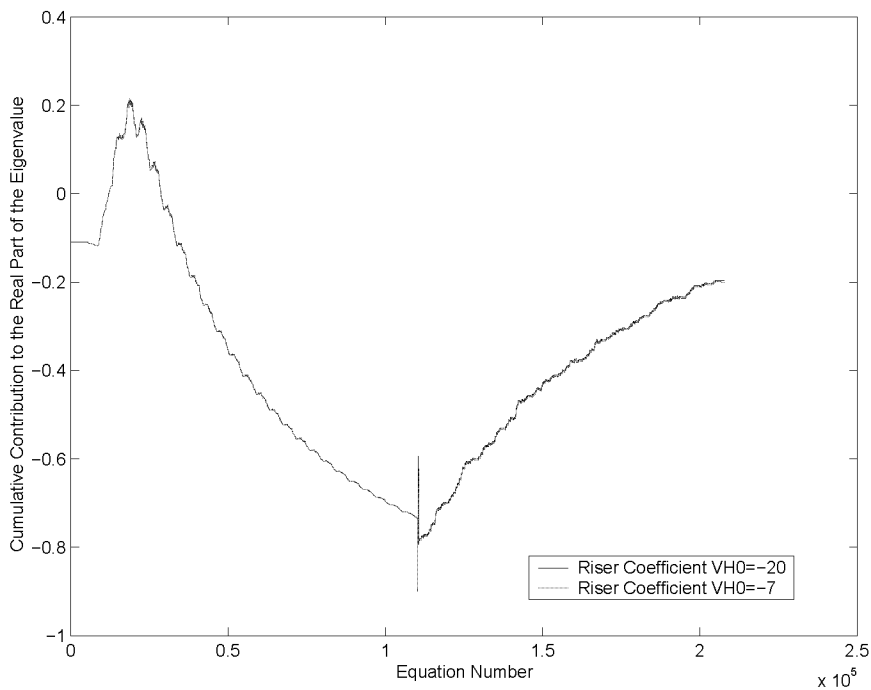
Figure 5.34: Cumulative Contribution: Equations (Using the Same Eigenvector)
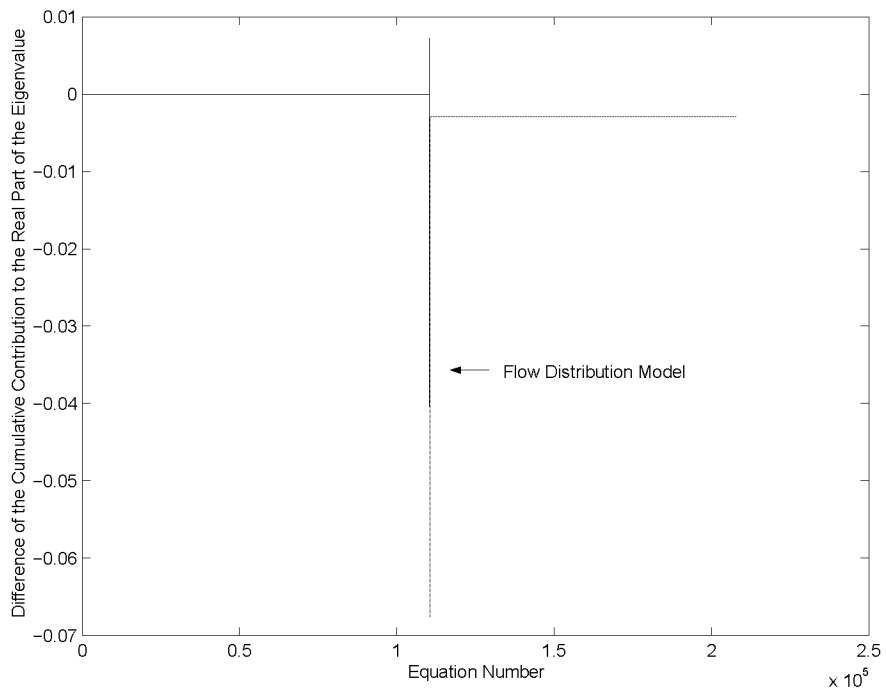
Figure 5.35: Difference of the Cumulative Contribution: Equations
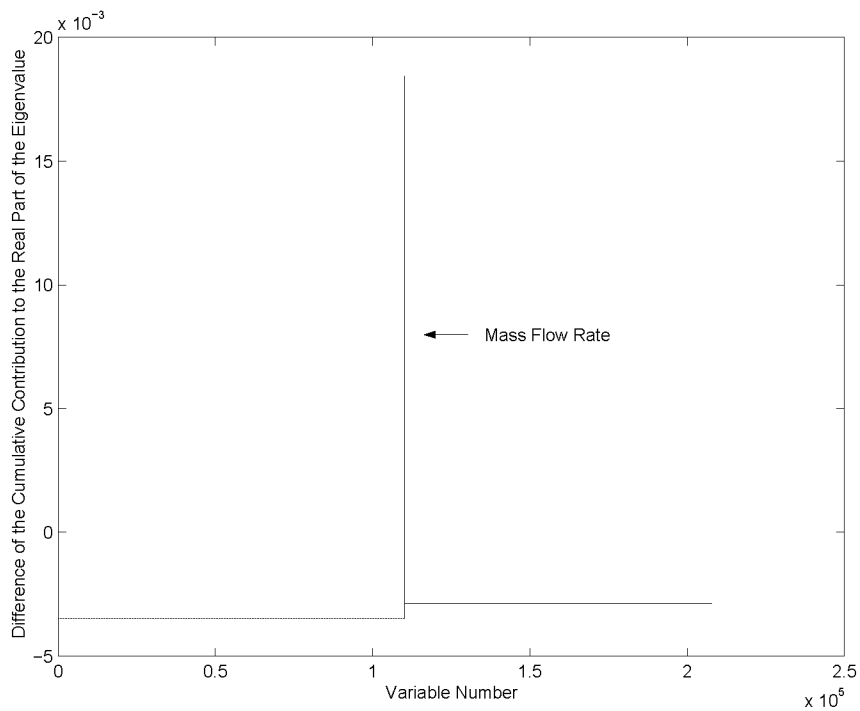
Figure 5.36: Difference of the Cumulative Contribution: Variables

the neutronics (larger positive contribution of the blue line in the second half of the plot). All together, both graphs end with a very similar eigenvalue.

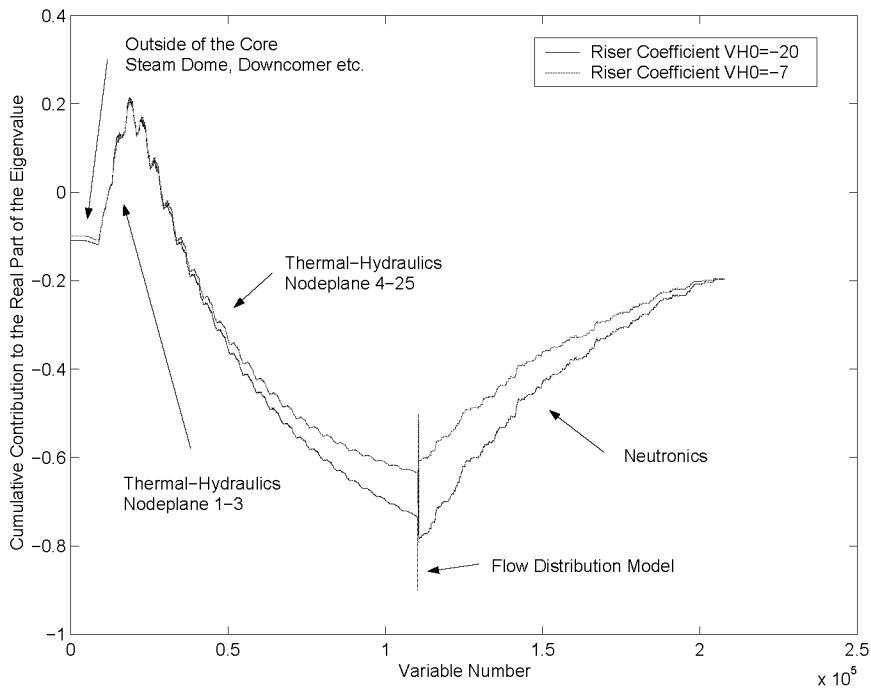A good impression of the real differences between the two cases can be achieved, if the eigenvectors from one of the two cases is used to calculate $\mathbf{A}_\lambda^{VHO=-7}$ and $\mathbf{A}_\lambda^{VHO=-20}$. In this case, the difference between the eigenvectors is neglected, and only the difference between the matrices is analyzed. The result is shown in Figure 5.34. The read and the blue graphs are now so close, that only a plot which shows the difference of the graphs may give more information. Figures 5.35 and 5.36 hence show the difference of the red and the blue graph in Figure 5.34. The plots confirm the observation that the two MATSTAB calculations differ mainly in the equations/variables around 110'000.
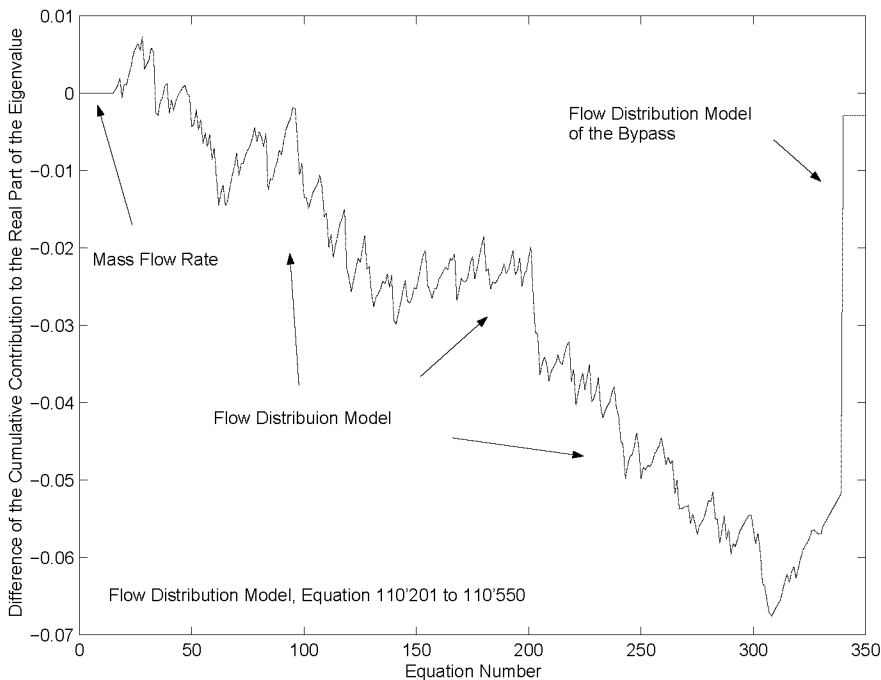
Figure 5.37: Difference of the Cumulative Contribution: Flow Distribution Model

Figure 5.37 shows the same information as Figure 5.35, but focuses on the interesting region between equation 110'201 and 110'550. The difference is situated between equations 110'216 and 110'240 which represent the flow distribution model in the reactor. This is in perfect agreement with the fact that the pressure drop over the riser was changed.

Figure 5.38 shows the same information as Figure 5.36, but focuses on the interesting region between variable 110'201 and 110'215. The difference lies in only two variables. The mass flow rate of the liquid and the mass flow rate of the gas in the last riser node. This is again in agreement with the fact that the pressure drop over the riser is modeled in the last riser node.

Figure 5.39 shows the 324 differences (flow distribution model) from Figure 5.37 in channel-wise representation. As could be expected, the distribution looks pretty similar to the power distribution (Figure 5.14)
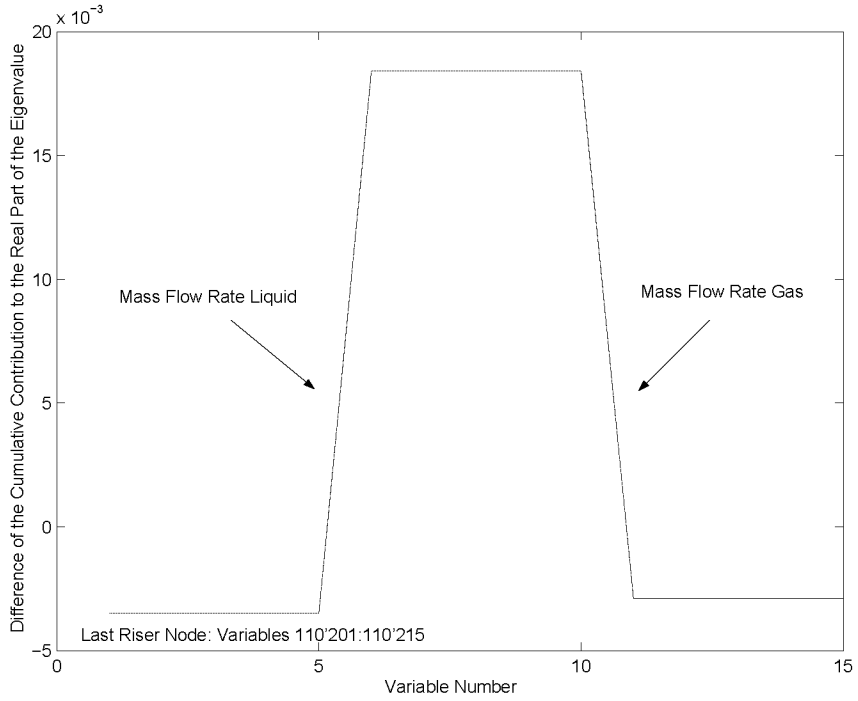
Figure 5.38: Difference of the Cumulative Contribution: Mass Flow Rate
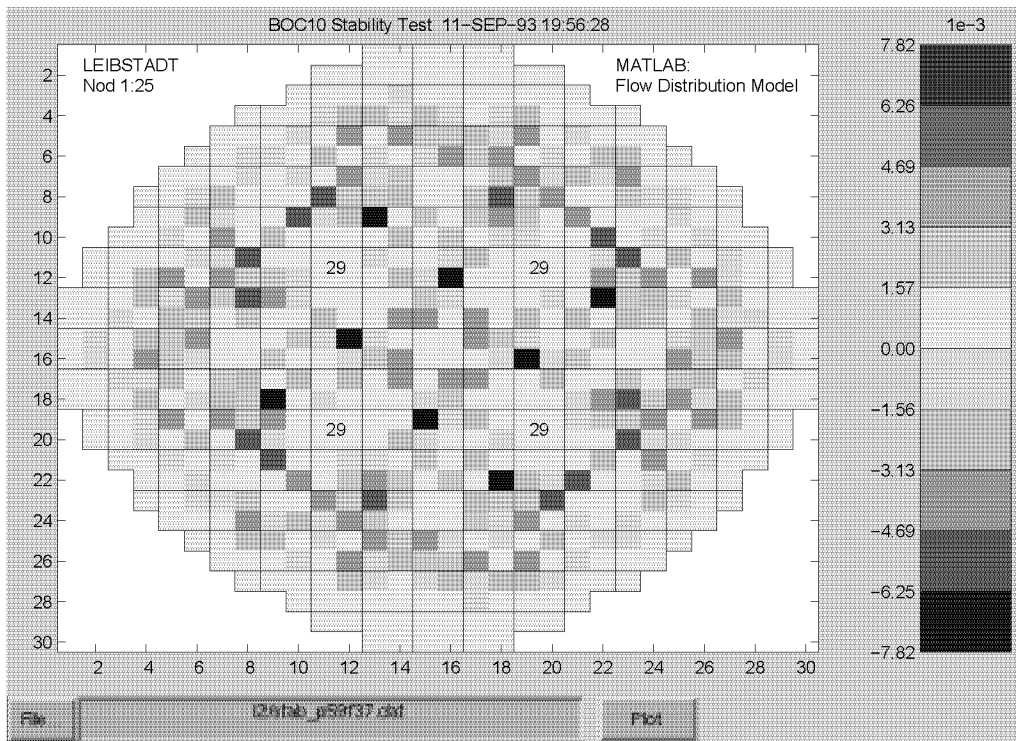
Figure 5.39: Difference of the Cumulative Contribution: Flow Distribution Model, Channel Wise

In concluding, it may be said, that the approach outlined above based on the cumulative contributions is an interesting new way to analyze the stability behavior of the reactor and pinpoints to sources of instability. The simple displays used identified correctly the sources causing changes in the eigenvalue/decay ratio and affecting stability.

5.4.7 Comparison of Different Operating Points in Leibstadt

Figure 5.40 shows the cumulative sums of the rows of the matrix $\mathbf{A}_\lambda$ for the Leibstadt measurement series from 1993. It can be seen very clearly that the stabilizing thermal-hydraulic contribution (left side of the plot) diminishes for a less stable operating point; the destabilizing contribution of the neutronics (right side of the plot) also diminishes. However, the overall effect is destabilizing since the reduction of the stabilizing thermal-hydraulics is larger. This observation is identical with the conclusion drawn from Figure 5.6.

Figure 5.41 shows the similar plot for the measurement series conducted in 1990. The contribution of the thermal-hydraulics to the eigenvalue behaves relatively systematic. The more stable an operating point is, the more negative (stable) is the thermal-hydraulic contribution. A bit more complex is the contribution of the neutronic part. Some of the graphs are convex, while other graphs are concave. The explanation is, however, pretty simple. The shape of the graph changes with the power density distribution. The change of control rods in the numerical experiment changed also the power density distribution, and therefore the contributions of the different fuel assemblies. Since the ordering of the equations is connected with the location of an assembly in the core, shift from the contributions from the center to the periphery, also changes the shape of the graph.

Concluding may be said, that the methods outlined in this chapter give a new angle to the stability investigations. The results show good agreement with measurements and experiences and seem to be promising. The proof, that completely new insights may be gained is, however, still missing.

Figure 5.40: Comparisons of Different Operating Points: Cycle 10

Figure 5.41: Comparisons of Different Operating Points: Cycle 7

5.5 Sensitivity Analysis

Even though the decay ratio and the frequency of the oscillation are a direct and obvious description of the state of the reactor, the contained information is by far not complete. It is by no means obvious or true, why the connection between the decay ratio and a change in variable i.e. flow or power should be linear. 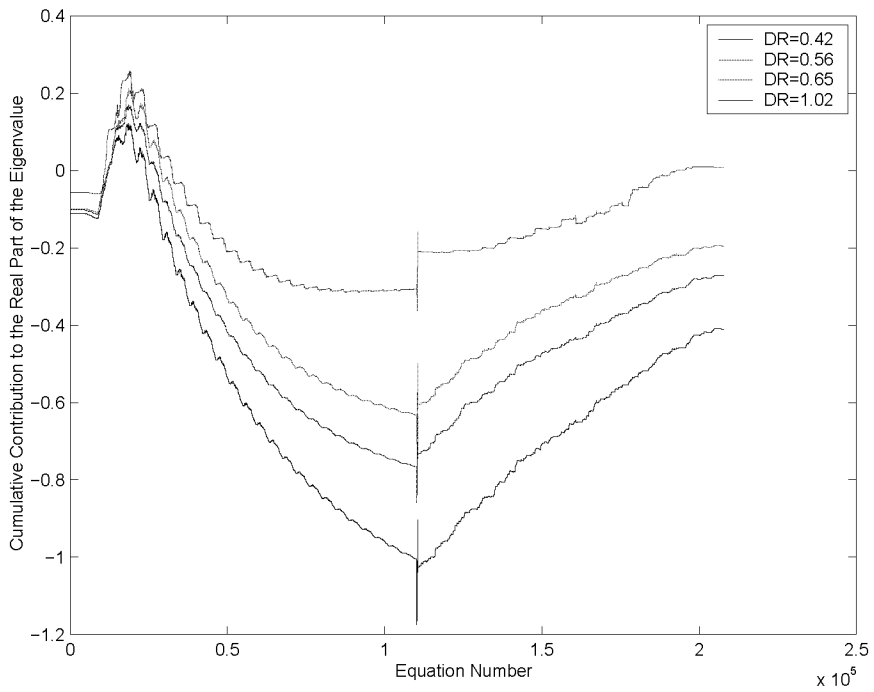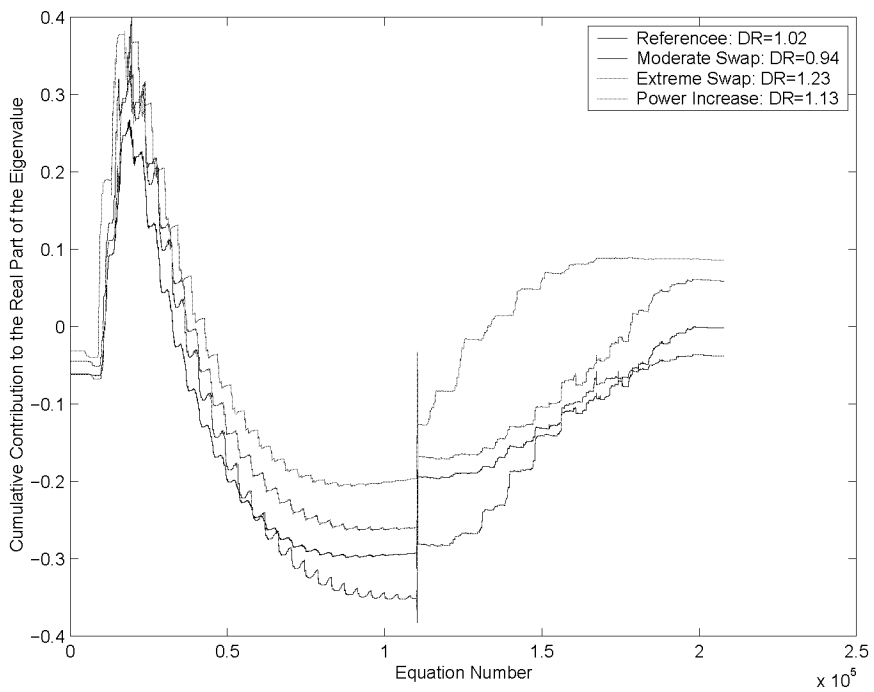Therefore, the decay ratio describes the stability of the investigated state, but does not give the distance (margin) to instability in a practical, "operational" manner.

One way to investigate the influence of a parameter p to stability is to evaluate many cases with slightly different values of p. This approach is normally limited by the computer time available. The MATSTAB model allows a much more efficient approach. The known eigenvalue $\lambda(p)$ is used to calculate the unknown eigenvalue $\lambda(p + \delta p)$.

Consider the matrix $\mathbf{A}$ with the eigenvalues $\lambda_1, \lambda_2, \ldots, \lambda_n$, right eigenvectors $\mathbf{e}_1, \mathbf{e}_2, \ldots, \mathbf{e_n}$ and left eigenvectors $\mathbf{f}_1, \mathbf{f}_2, \ldots, \mathbf{f_n}$ scaled in the way that $\mathbf{EF} = \mathbf{I}$.

Differentiation of the generalized eigenvalue Equation 2.15

$$\mathbf{A}\mathbf{e}_i = \lambda_i \mathbf{B}\mathbf{e}_i \tag{2.15}$$

with respect to any parameter p yields

$$\frac{\partial \mathbf{A}}{\partial p}\mathbf{e}_i + \mathbf{A}\frac{\partial \mathbf{e}_i}{\partial p} = \frac{\partial \lambda_i}{\partial p}\mathbf{B}\mathbf{e}_i + \lambda_i \mathbf{B}\frac{\partial \mathbf{e}_i}{\partial p} \tag{5.23}$$

Multiplying by $\mathbf{f_i^T}$ from the left

$$\mathbf{f}_i^T \frac{\partial \mathbf{A}}{\partial p}\mathbf{e}_i + \lambda_i \mathbf{f}_i^T \mathbf{B}\frac{\partial \mathbf{e}_i}{\partial p} = \frac{\partial \lambda_i}{\partial p}\mathbf{f}_i^T \mathbf{B}\mathbf{e}_i + \lambda_i \mathbf{f}_i^T \mathbf{B}\frac{\partial \mathbf{e}_i}{\partial p} \tag{5.24}$$

and solving for the derivative of the eigenvalue leads to the important relation

$$\frac{\partial \lambda_i}{\partial p} = \frac{\mathbf{f}_i^T \frac{\partial \mathbf{A}}{\partial p}\mathbf{e}_i}{\mathbf{f}_i^T \mathbf{B}\mathbf{e}_i} \tag{5.25}$$

From a calculated state with parameter p, the eigenvalue for the slightly different state with the parameter $p+\delta p$ can be deduced as follows.

$$\lambda_i(p + \Delta p) = \lambda_i(p) + \left(\frac{\mathbf{f}_i^T(p)\frac{\partial \mathbf{A}(p)}{\partial p}\mathbf{e}_i(p)}{\mathbf{f}_i^T(p)\mathbf{B}\mathbf{e}_i(p)}\right) \cdot \Delta p \tag{5.26}$$

This result is useful, because the stability margin of the new state is obtained without calculating its eigenvalue from scratch. It is also one additional way to understand that the information about the stability behavior of the reactor is contained in the eigenvectors.

Example: Slip

One obvious application of Equation 5.26 would be for a small change in power. However, a change in power would also affect many other variables, e.g. the void fractions. Therefore, a new steady-state file from POLCA would be necessary and the effects of all other implied changes would be superimposed upon those of the initial power change.

The Bankoff-Malnes correlation

$$w_g = Sw_l + w^0 \tag{A.95}$$

relates the vapor velocity w_g to the liquid velocity w_l, using a slip factor S. This factor is not expected to change in time. However, its value is not so easy to measure directly in a real NPP. Therefore the uncertainty in the slip is very often used to fit the power-shapes of the modeling code to the measured data.
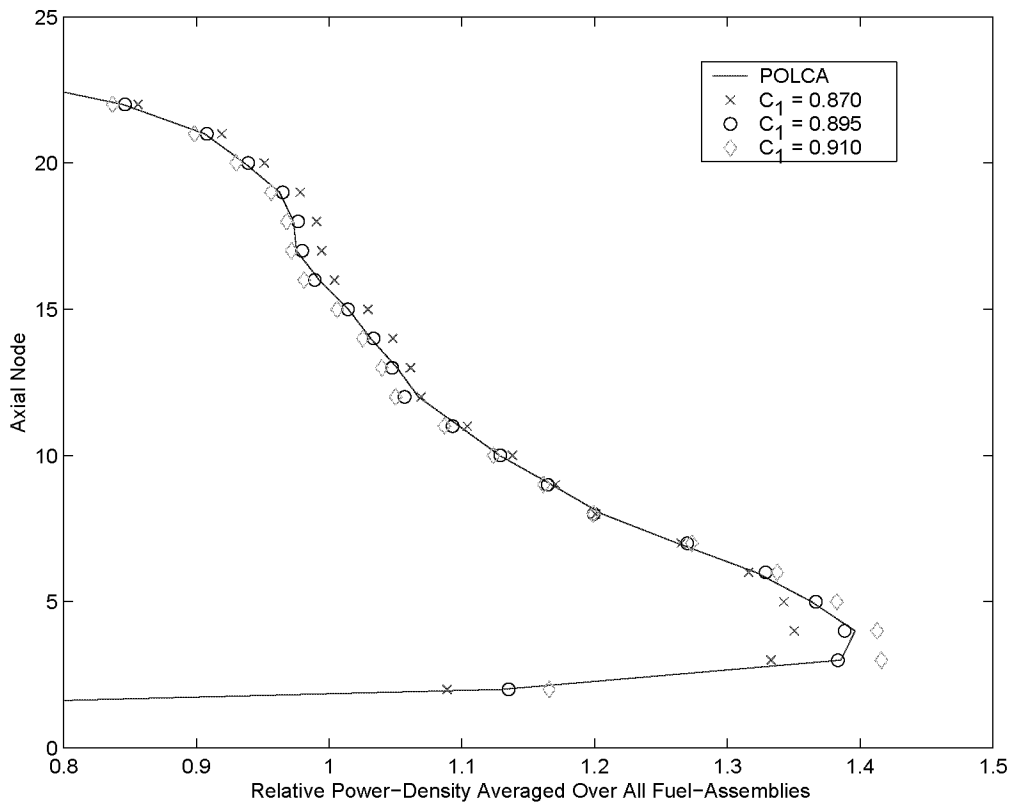
Figure 5.42: Influence of the Slip Parameter c_1 S to the Radially Averaged Power-Density Distribution

Figure 5.42 shows the radially averaged relative power-density distribution for the operating point considered (calculated by POLCA) compared to MATSTAB calculations using different values for c_1 in the slip correlation A.96.

$$S = \frac{1 - \alpha}{c_1 - \alpha} \tag{A.96}$$

The influence of S (respectively c_1) can be seen as clearly as the rather optimal value of 0.895 which is used normally by MATSTAB.

Equation 5.26 is now used to study the effect of a change in S (c_1) on stability. The base of the investigation is the operating point with 59% power and 4010 kg/s core flow from the Leibstadt Cycle-ten measurement. The measured decay ratio was 0.65 and its frequency was 0.50. Table 5.2 shows the influence of the slip parameter S upon the decay ratio and frequency. All values from the sensitivity calculation were derived using $C_1 = 0.895$ as base and $\Delta C_1 = 0.005$ as deviation.

	Full Calculation		Sensitivity Anal.	
Slip (c_1)	DR	FR	DR	FR
0.885	0.6362	0.4321	0.6350	0.4323
0.890	0.6421	0.4340	0.6432	0.4339
0.895	0.6514	0.4356		
0.900	0.6599	0.4373	0.6596	0.4372
0.905	0.6695	0.4387	0.6679	0.4389
0.910	0.6742	0.4402	0.6762	0.4405

Table 5.2: Decay Ratio and Frequency for Different Slip Values

The predictions of the sensitivity analysis show good agreement and lie within the accuracy of the MATSTAB calculation itself. Even though this method is not usable for large steps, it is possible to make a very quick judgment on how the change of a parameter may influence the result.

Chapter 6

Verification/Validation

Contents

6.1   Analysis of the Measurement Data

MATSTAB was validated against numerous stability measurements. Most measurements available are from the Forsmark site, since Forsmark does routinely measure stability during startup to check the newly loaded core. These operating points are very close to each other in power and core flow. Nevertheless, the data spans over ten years, during which period the fuel design changed dramatically. With very few exceptions, the results from MATSTAB compared very well with the measurements and/or RAMONA. Therefore, one conclusion is, that for the used fuel from ABB, Siemens and GE good model parameters are available and that the fuel type has no influence on the prediction quality of MATSTAB.

The people at Leibstadt handle things very differently. Stability tests are only conducted before or after major changes in the NPP, e.g. a power upgrade. In 1990 and 1993 very extensive stability measurements were conducted. These tests covered a wide range of operating points and global as well as regional oscillations were experienced.

As explained in Chapter 3.1.1 on page 25, the main difference between Leibstadt and Forsmark are the recirculation pumps. Leibstadt uses jet pumps driven by external pumps while Forsmark has internal pumps. Due to this difference and the occurrence of out-of-phase oscillations, the Leibstadt data is an important extension to the validation done for Forsmark.

After the successful application of MATSTAB for the above mentioned NPPs, the responsible people at Oskarshamn decided to compare MATSTAB results with their own stability investigations. The validation was conducted by Oskarshamn [19], therefore, we cannot present the results in the same detailed manner as for the other plants. Only decay ratios were compared. It is noteworthy, that the engineers at Oskarshamn were able to use MATSTAB efficiently after a short introduction to the program. The time needed to prepare the input data was short as well, since the POLCA distribution files and some RAMONA input files were available.

Table 6.1 gives a brief overview over the physical data of the different nuclear power plants involved in the validation of MATSTAB.

Naturally, the three above mentioned sites are not the only power plants conducting stability measurements. Due to restrictions in time, it was not possible to widen the validation basis, even though a validation against Ringhals measurements would have been very interesting. Nevertheless, the validation presented covers a large number of measurements and contains some of the most extreme measurements ever done for a commercial NPP (natural circulation in Leibstadt 1990). It remains to say, that the Leibstadt reactor is among the plants with the highest core power-density in the world.

One should always bear in mind, that the measurements have an uncertainty in decay ratio itself. Especially for well damped systems, different analysis tools lead to slightly different results. Even though there is a lot of instrumentation inside the plant, the state of the reactor is only known to a certain degree. Hence, the input to the computer codes is not precisely defined.

Plant	Power [MW]	Core Flow [kg/s]	Fuel Assemblies	Recirc. Pumps	Manufacturer
Forsmark 1	2700	11000	676	internal	ABB
Forsmark 2	2700	11000	676	internal	ABB
Forsmark 3	3020	11400	700	internal	ABB
Leibstadt	3138	11151	648	jet pumps	GE
Oskarshamn 1	1375	4600	448	external	ABB
Oskarshamn 2	1800	5100	444	external	ABB
Oskarshamn 3	3300	12000	700	internal	ABB

Table 6.1: Key Parameters of the NPPs Involved in Validating MATSTAB

Different people that attempt to predict the same measurement data may use a slightly different input and may obtain different decay ratios even if they use the same computer code (e.g. RAMONA 3.9 calculations from ABB, Forsmark, Vattenfall and Studsvik Scandpower). However, the differences lie more or less within +/- 0.05 in decay ratio. An OECD benchmark [34] for Ringhals showed calculation uncertainties that support this observation.

The frequency on the other side, is much less dependent on the state of the reactor and can be derived from the measurements with good accuracy. The predictions are normally very accurate and pose no problem, neither for the analysis of the measurements nor for the predictions of RAMONA and MATSTAB.

Not all signals from the many detectors within a NPP are normally recorded. Usually there are also capacity limits on how many non-standard signals may be recorded digitally with high resolution. For stability purposes LPRM (low power range monitor) detector signals are of high interest. The core of a normal BWR contains about 35 LPRM strings each containing four neutron detectors at four different axial heights. Normally about ten strings are selected and only one or two detector per string are recorded.

The frequency and the decay ratio of each operating point are commonly calculated from the measurements with an ARMA model [88], [35].

6.1.1   ARMA and ARMAX Models

The ARMAX (AutoRegressive Moving Average) technique interprets the fluctuations encountered in one signal $y(\tau)$ in terms of parameters of a linear model

$$y(\tau) = -\Sigma_{i=1}^{n_a} a_i * y(\tau - i) + \Sigma_{i=1}^{n_b} b_i * u(\tau - i) + \Sigma_{i=0}^{n_c} c_i * e(\tau - i) \qquad (6.1)$$

which views $y(\tau)$ as responses to

- the fluctuations experienced in another signal $u(\tau)$, assumed to act as a systematic "driving source", plus

- an extra unknown disturbance $e(\tau)$ of an assumed "white" nature.

The model "parameters" in the vectors a, b and c are normally determined via a least-squares fitting procedure. The vectors obtained from the fitting can be interpreted in terms of a transfer function from the disturbing input $u(\tau)$ to the process $y(\tau)$.

The ARMA technique assumes that there is no systematic driving source; i.e. $u(\tau)$ is set to zero. The process fluctuations $y(\tau)$ are evaluated as though they were excited by the white noise $e(\tau)$ only.

For our purpose, the model orders (n_a, n_b) vary from 2 to 10 and the model which predicts the highest decay ratio in the frequency window of 0.3Hz - 0.7Hz is chosen.

Comprehensive functions to generate and use ARMAX models are provided by the system identification tool-box of MATLAB.

A recommendable textbook about system identification and the modeling of dynamic systems was written by Ljung [47].

6.1.2   Comparing LPRM Signals With MATSTAB

In addition to validate against decay ratio and frequency, the MATSTAB calculation may also be compared directly with a LPRM detector signal. A possibly existing linear trend is first removed from the time series of the detector, so that the signal is oscillating around the zero axis. As described above, the dominating frequency in the range of 2-4 rad/s is calculated. Using this frequency and a reference signal (e.g. APRM A), an ARMAX model is used to calculate the relative phase and amplitude of the original signal. This procedure is repeated for all the LPRM detector signals available. The same physical properties are taken directly from the right eigenvector of the MATSTAB solution. Since the detector position may be somewhere between the center of two core nodes, the values are linearly interpolated between the neighboring core nodes.

In the Figures (6.5-6.10) the phases and amplitudes from the measurement and the calculation are compared with each other. The measurements are represented by white vectors, the

calculations are represented by black vectors. Since the phase and amplitude of the MAT-STAB vectors are only defined relatively to each other, the largest amplitude of the MAT-STAB vectors is used to scale the LPRM signal vectors (the other way round would be more logical, but this way round the size of the vectors fits better into the plot). Hence one white and one black vector is always in perfect agreement. As a result, one vector would not be visible on the plot. This is slightly disturbing for the impression of the plot and therefore the vector is shown with a slight deviation to be visible nevertheless.

6.2 Global Oscillations

Since most of the measurements were done during normal start up, the measured decay ratios are quite small and relate to global oscillations. Some comparisons with regional oscillations follow in the next section, where the Leibstadt data from 1990 is investigated.

6.2.1 Forsmark

MATSTAB was validated against 42 stability measurements conducted in the cycles 8-19 at the Forsmark NPP in Sweden [109],[110],[111]. The range of operating points lay between 3800 and 5000 kg/s of core flow and 59% to 68% power (see Tables 6.2, 6.3 and 6.4).

Forsmark 1

MATSTAB was validated against 18 stability measurements Forsmark 1 conducted in the cycles 10-19. The range of operating points lay between 3800 and 4400 kg/s of core flow and 59% to 66% power. Table 6.2 summarizes the results and shows a good agreement between MATSTAB and the measurement. The abbreviation boc/moc/eoc are used to describe beginning/middle/end of cycle, whereas aug stands for august.

Only three calculated decay ratios differ more than 0.1 from the measurement, and most of them are much closer (Figures 6.1, 6.2). The standard deviation for all cases is 0.06 for the decay ratio and 0.02 for the frequency.

The available RAMONA 3.9 calculations [105], [33] are included in the table to show that MATSTAB and RAMONA are of comparable accuracy, despite the linearized equations used in MATSTAB (Figure 6.3, 6.4). The standard deviation of the RAMOMA runs is also 0.05 for the decay ratio. However, if only the measurements where RAMONA runs are available are evaluated, MATSTAB reaches a standard deviation of 0.05 as well.

The content of Figures 6.5-6.10 are explained in Section 6.1.2 and Chapter 5. They basically show the part of the right eigenvector which relates to the thermal neutron flux (colors) and the comparison between the measured and the calculated LPRM oscillation (arrows). The agreement between the white (measurement) and black (calculation) arrows is reasonably well. Especially the angle (phase-shift) between the arrows is predicted correctly.

Operating point			Decay Ratio			Frequency [Hz]		
Cycle	Power [%]	Core Flow [Kg/s]	Measurement	MATSTAB	RAMONA 3.9	Measurement	MATSTAB	RAMONA 3.9
c10 boc	65.5	4100	0.49	0.60		0.47	0.45	
c11 boc	65.2	3966	0.46	0.45		0.44	0.41	
c12 boc	64.5	4183	0.53	0.51		0.49	0.45	
c13 boc 1	59.6	3987	0.40	0.38	0.43	0.45	0.42	0.44
c13 boc 2	59.9	4317	0.30	0.28	0.30	0.46	0.42	0.45
c13 boc 3	64.3	4385	0.49	0.43	0.38	0.48	0.45	0.48
c13 boc 4	65.1	4044	0.68	0.52		0.47	0.44	
c14 boc 1	59.9	4383	0.44	0.36	0.38	0.49	0.44	0.45
c14 moc 2	64.3	4092	0.60	0.48	0.58	0.48	0.43	0.47
c14 boc 3	64.8	4313	0.56	0.51	0.53	0.51	0.46	0.48
c14 boc 4	64.7	4014	0.64	0.56	0.66	0.51	0.46	0.47
c15 boc	64.4	4057	0.63	0.57	0.56	0.53	0.48	0.46
c15 aug	64.1	4027	0.38	0.37		0.45	0.42	
c17 boc	65.0	3940	0.40	0.41	0.34	0.45	0.45	
c17 eoc	64.5	3823	0.58	0.52		0.45	0.45	
c18 boc	64.7	4043	0.56	0.62	0.42	0.55	0.52	
c18 moc	62.6	4045	0.44	0.45	0.46	0.46	0.46	
c19 boc	63.7	3884	0.61	0.59		0.52	0.50	

Table 6.2: Comparison Between MATSTAB and Measurements in Forsmark 1

Figure 6.1: Validation of the Decay Ratio for Forsmark 1

Figure 6.2: Validation of the Frequency for Forsmark 1
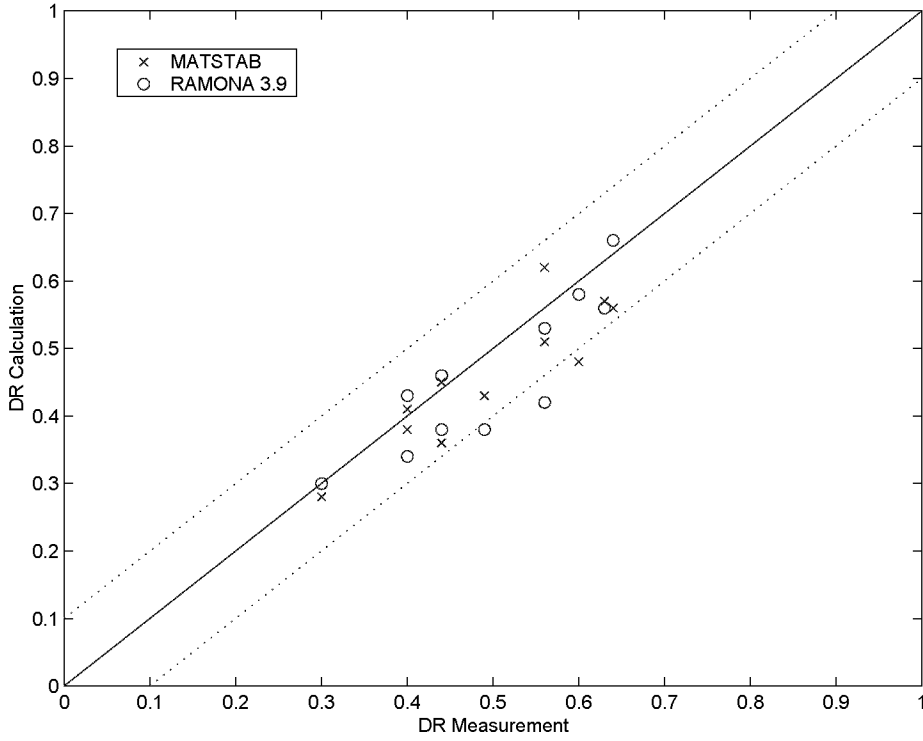
Figure 6.3: Comparison Measurement/MATSTAB/RAMONA 3.9 for Forsmark 1

Figure 6.4: Comparison of MATSTAB and RAMONA 3.9 for Forsmark 1

Figure 6.5: Comparison of MATSTAB and Measurement C11 boc in Forsmark 1

Figure 6.6: Comparison of MATSTAB and Measurement C12 boc in Forsmark 1

Figure 6.7: Comparison of MATSTAB and Measurement C13-1 boc in Forsmark 1

Figure 6.8: Comparison of MATSTAB and Measurement C13-2 boc in Forsmark 1

Figure 6.9: Comparison of MATSTAB and Measurement C13-3 boc in Forsmark 1

Figure 6.10: Comparison of MATSTAB and Measurement C14-1 boc in Forsmark 1

Forsmark 2

MATSTAB was validated against 11 stability measurements Forsmark 2, conducted in the cycles 12-17. The range of operating points lay between 3800 and 4200 kg/s of core flow and 60% to 70% power (see Table 6.3). The standard deviation for all cases is 0.09 for the decay ratio and 0.03 for the frequency. The newly released code RAMONA 5 was validated against some of the Forsmark 2 measurements [44]. The results are also printed in Table 6.3 to show that even the improved RAMONA code does not deliver better results than MATSTAB. Actually, RAMONA 5 shows at the moment worse results than RAMONA 3.9. The standard deviation for the decay ratio is 0.13.

Operating point			Decay Ratio			Frequency [Hz]	
Cycle	Power [%]	Core Flow [Kg/s]	Measurement	MATSTAB	RAMONA 5	Measurement	MATSTAB
c12 boc	65.0%	4083	0.46	0.48		0.44	0.42
c13 moc	64.3%	3940	0.52	0.51		0.40	0.41
c14 startup	65.1%	4028	0.52	0.55	0.56	0.43	0.43
c14 boc	65.0%	4026	0.46	0.50		0.47	0.44
c14 moc	63.3%	3850	0.73	0.47	0.60	0.47	0.37
c15 startup	64.0%	3791	0.49	0.40	0.64	0.40	0.36
c15 moc	67.3%	4234	0.68	0.69	0.57	0.49	0.49
c16 boc	64.0%	4127	0.69	0.66	0.56	0.48	0.48
c17 boc	64.4%	3948	0.30	0.38	0.53	0.41	0.41
c17 2300	64.3%	3896	0.60	0.52	0.61	0.46	0.43
c17 moc	62.6%	3980	0.68	0.66	0.71	0.45	0.46

Table 6.3: Comparison Between MATSTAB and Measurements in Forsmark 2

Figure 6.11 and 6.12 compare the MATSTAB calculations with the values obtained from the measurements.

If the measurement of cycle 14 moc is omitted, the deviation of MATSTAB is only 0.05 for the decay ratio respectively 0.02 for the frequency. The RAMONA 5 results, however, do not benefit in the same way from the omission of 14 moc. The standard deviation stays the same.

Figure 6.15 shows, that the difference between the measurement and the calculations of MATSTAB is larger for low core flows than it is for high flows. The reason lies in the model for the recirculation pumps. This effect is studied in [108].
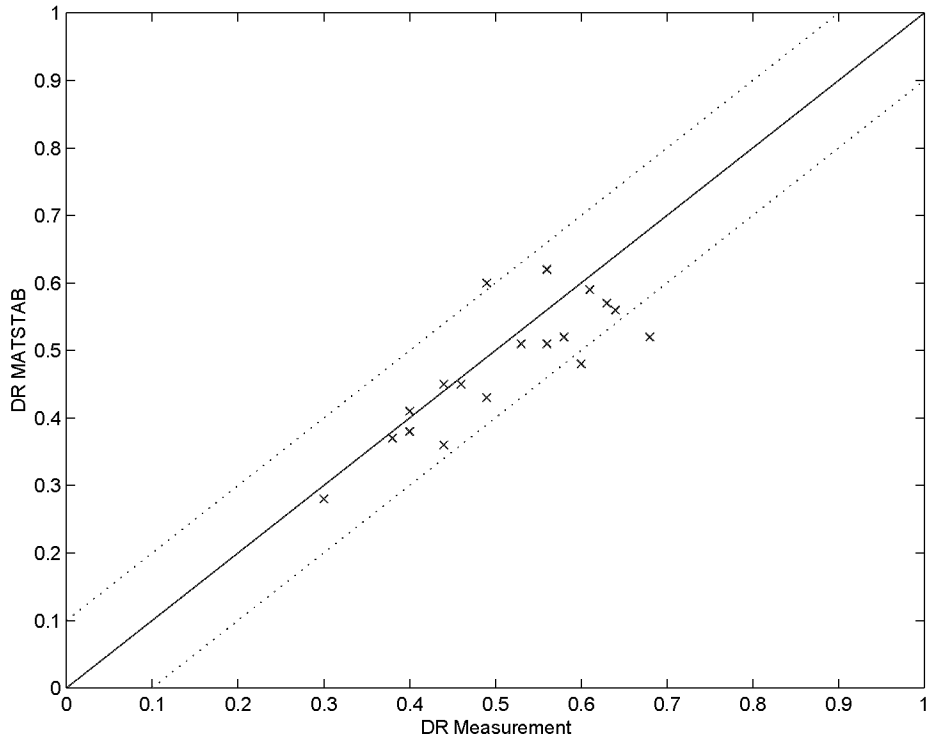
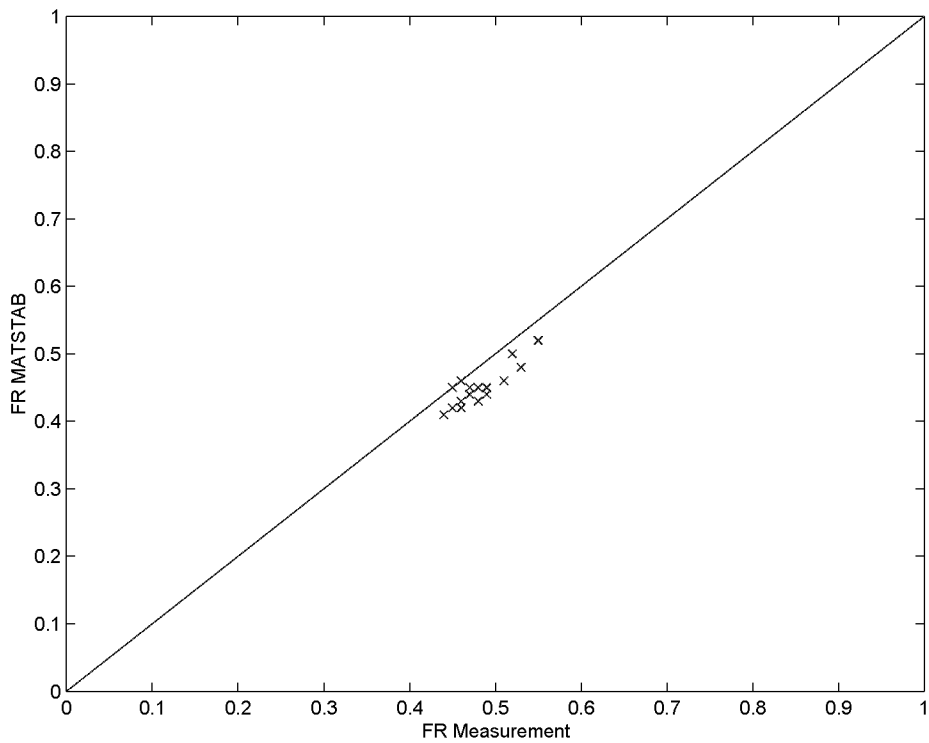Figure 6.11: Validation of the Decay Ratio for Forsmark 2
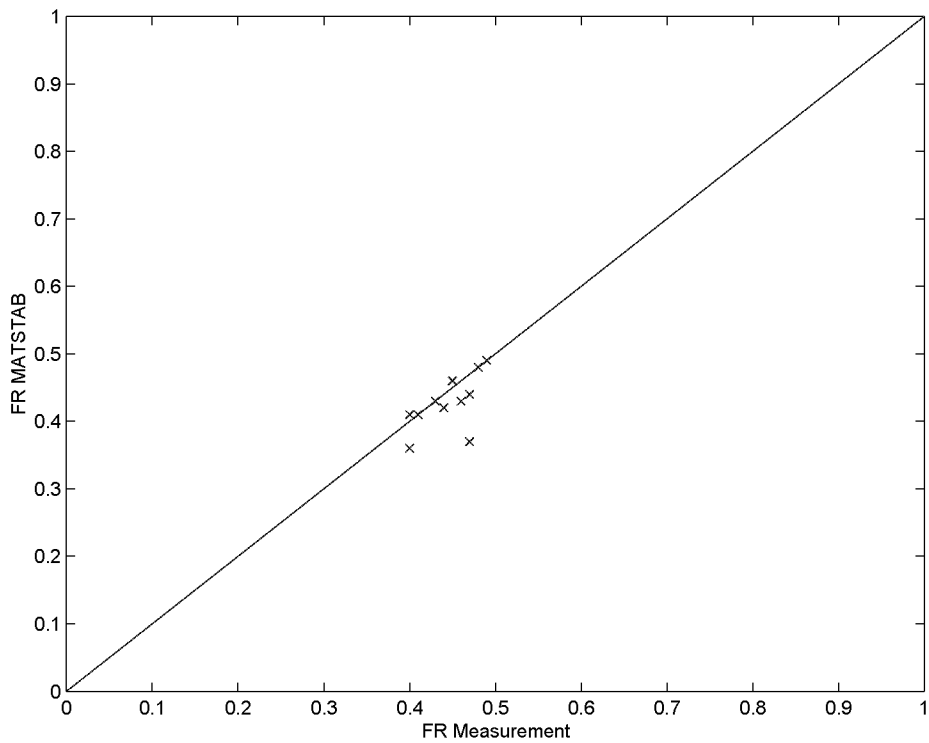
Figure 6.12: Validation of the Frequency for Forsmark 2
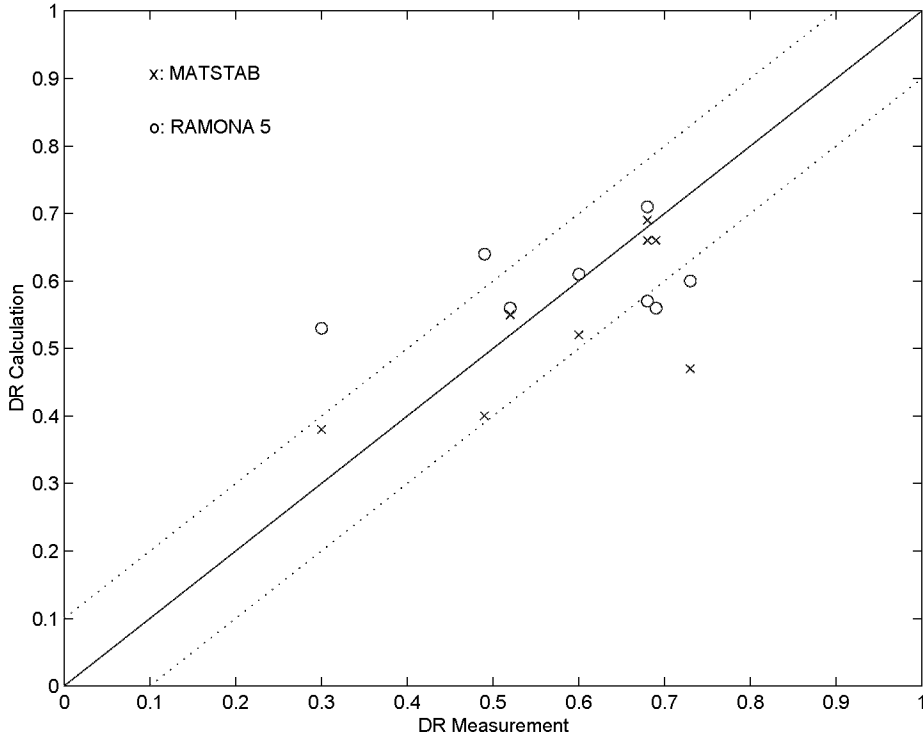
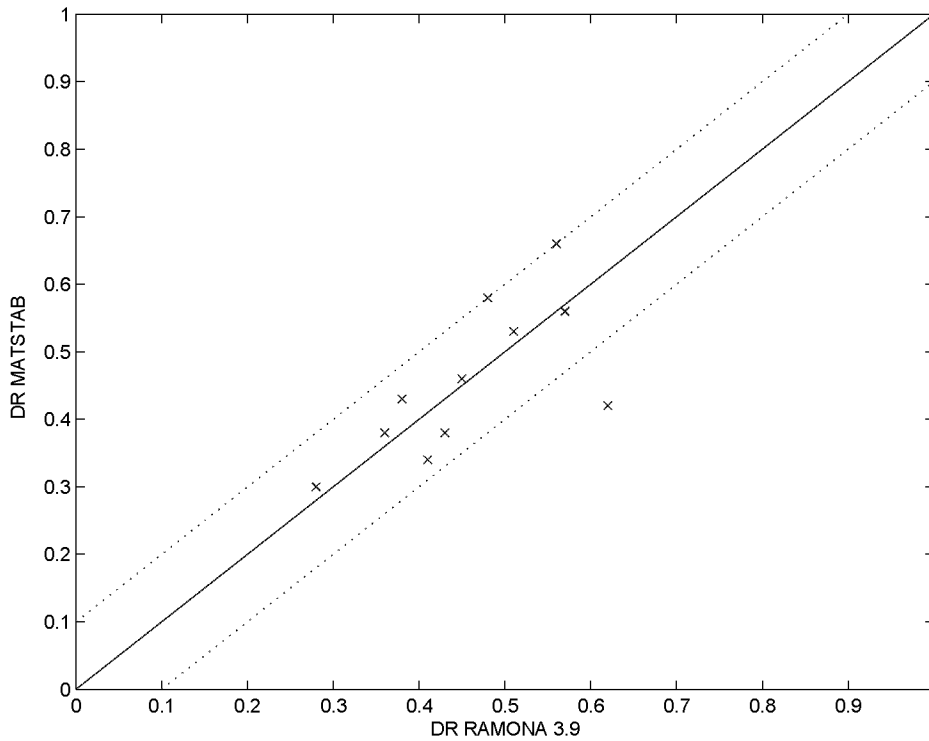Figure 6.13: Comparison Measurement/MATSTAB/RAMONA 5 for Forsmark 2
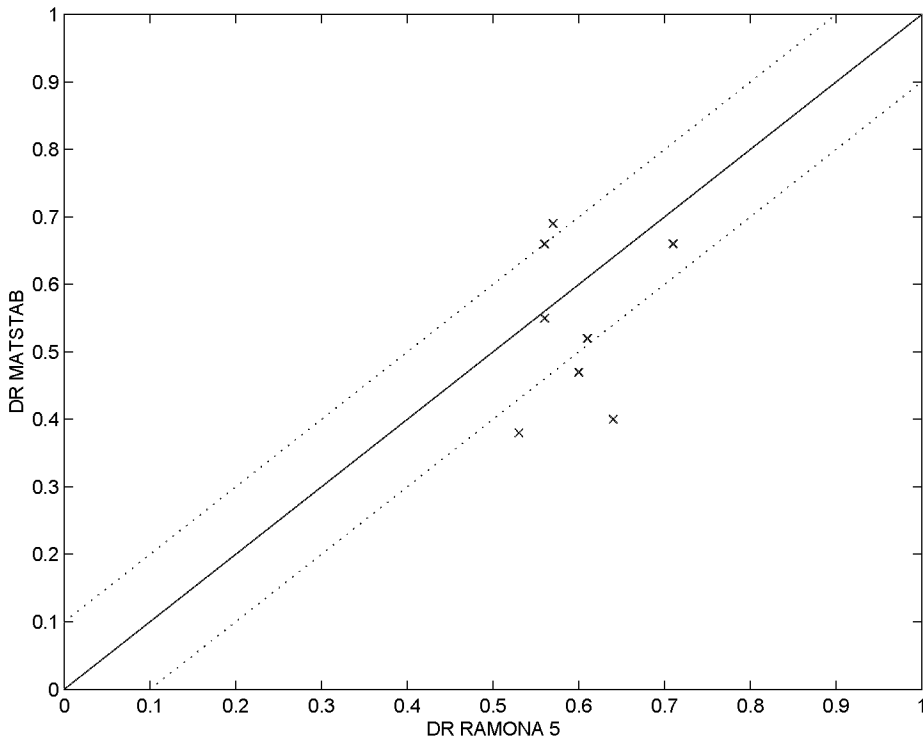
Figure 6.14: Comparison of MATSTAB and RAMONA 5 for Forsmark 2
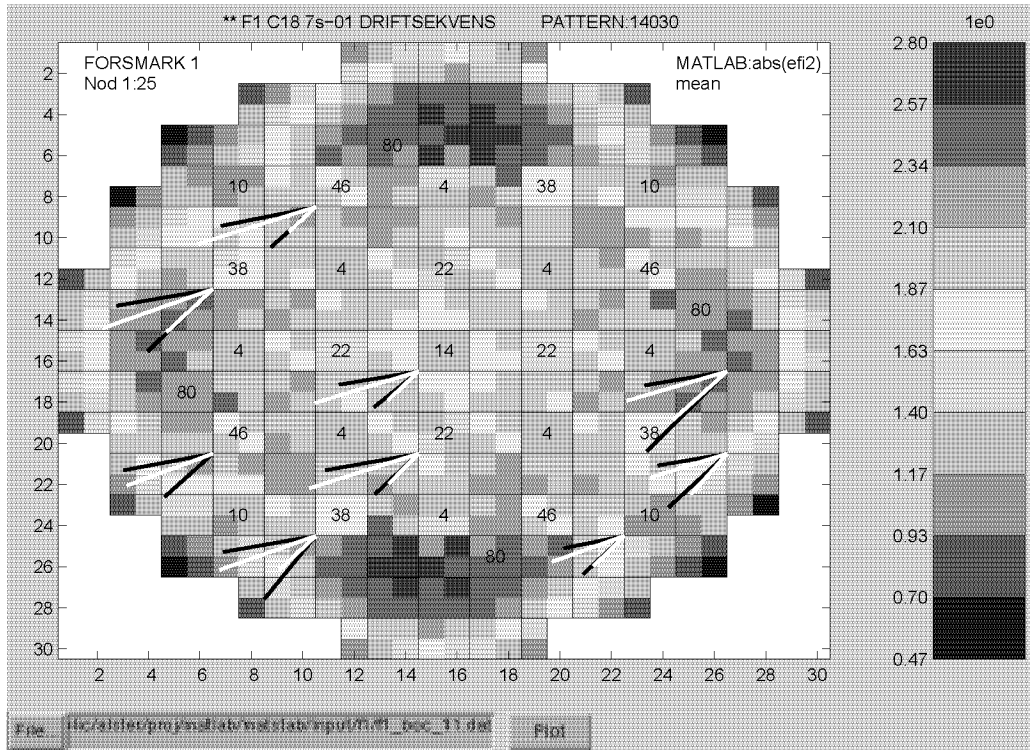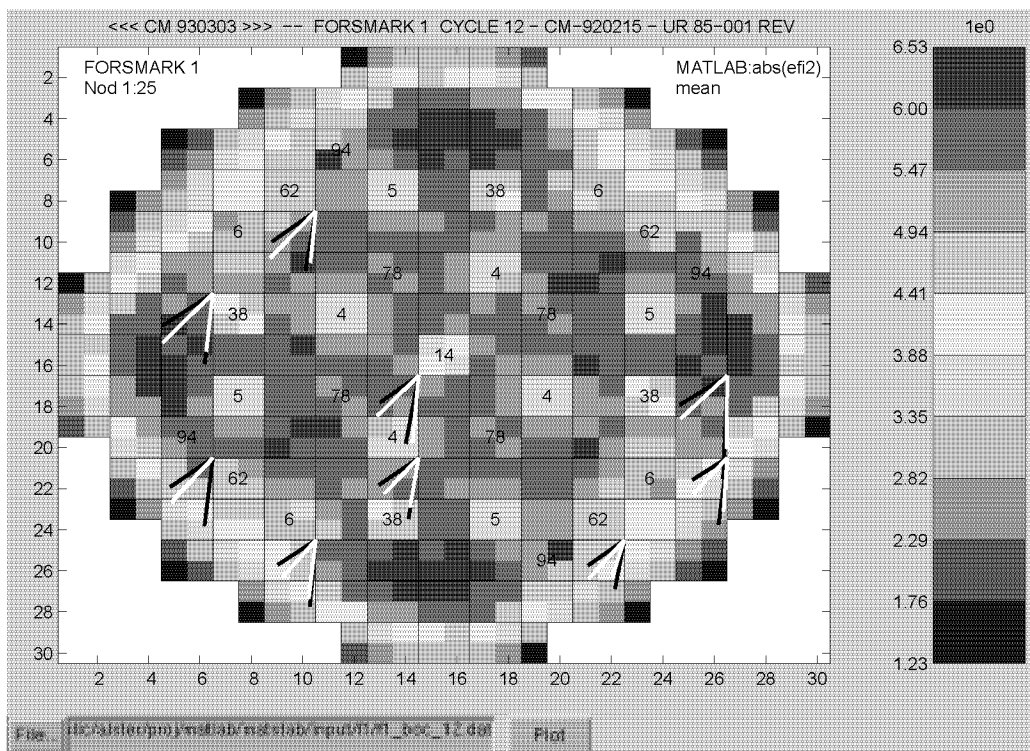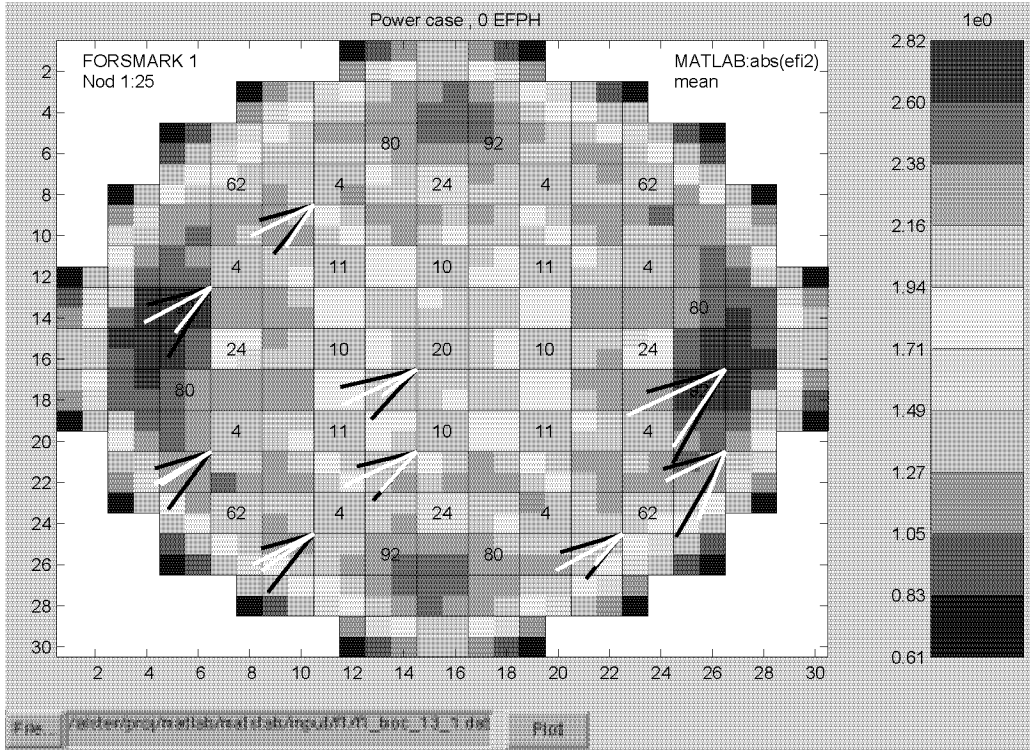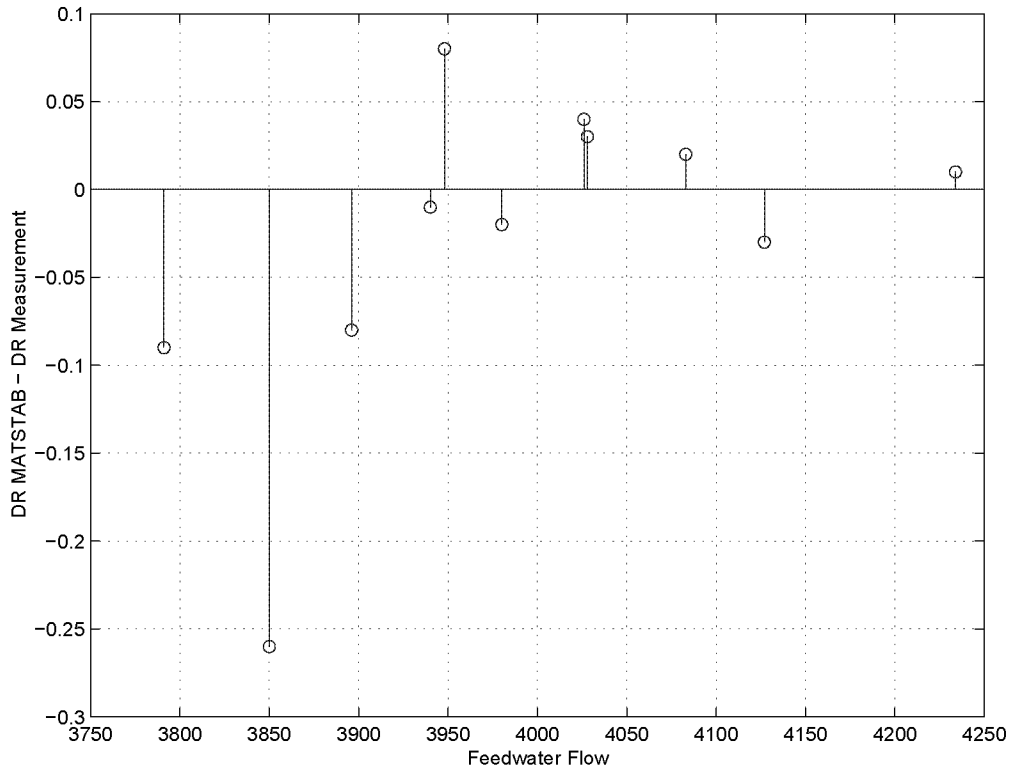
Figure 6.15: Comparison Measurement/MATSTAB with Respect to the Core Flow
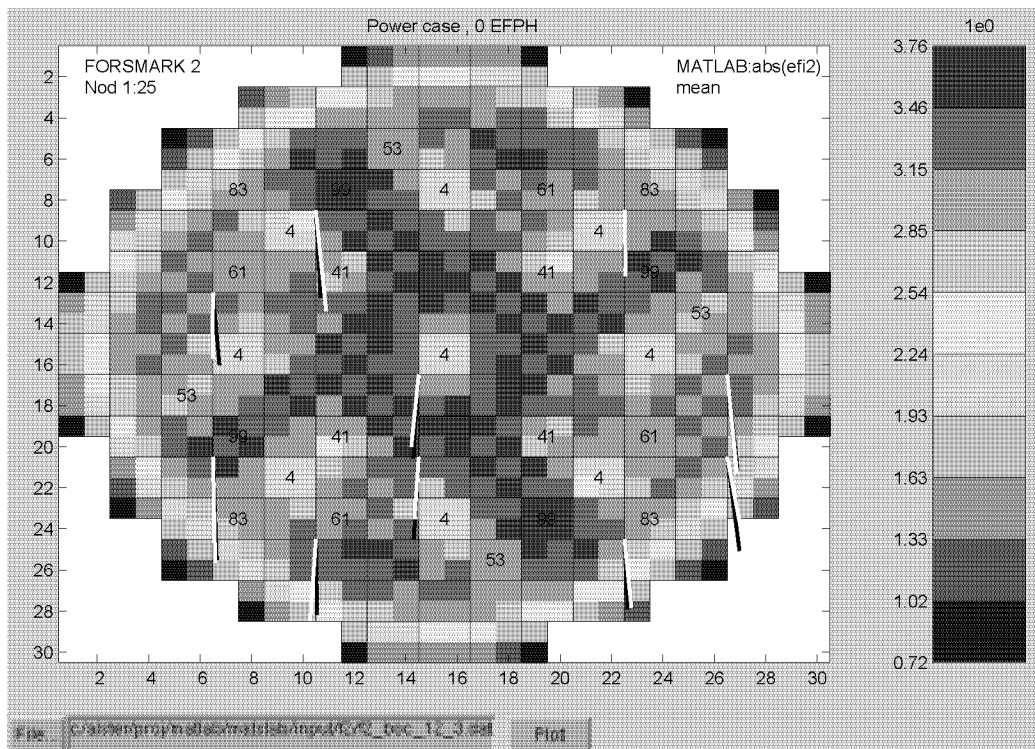
Figure 6.16: Comparison of MATSTAB and Measurement C12 boc in Forsmark 2
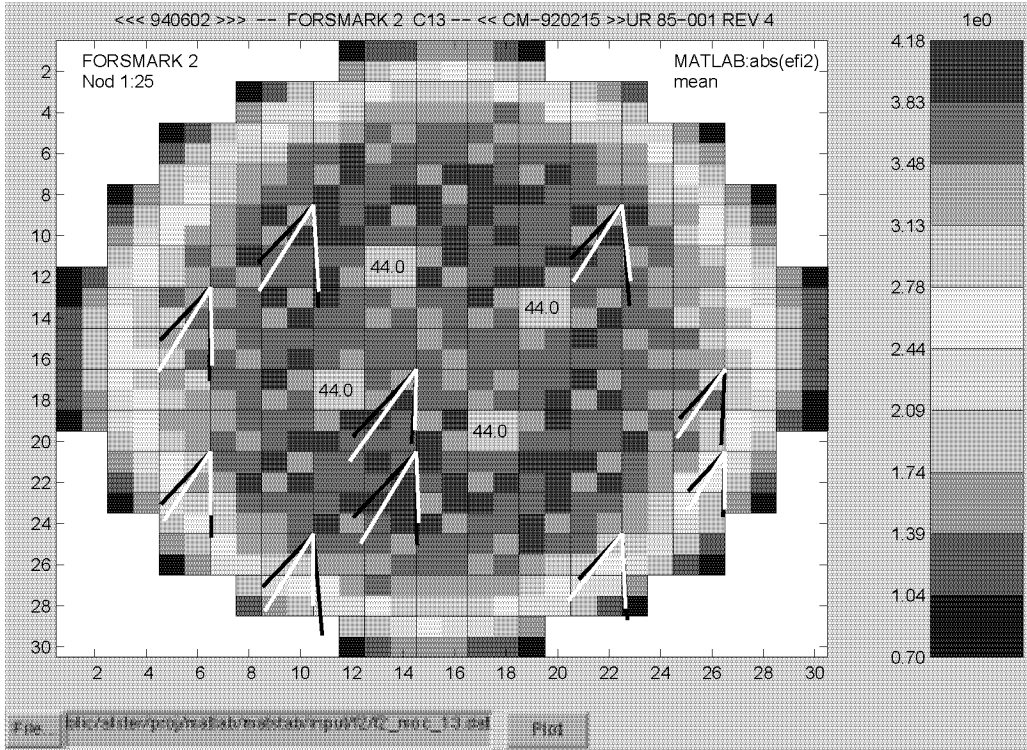
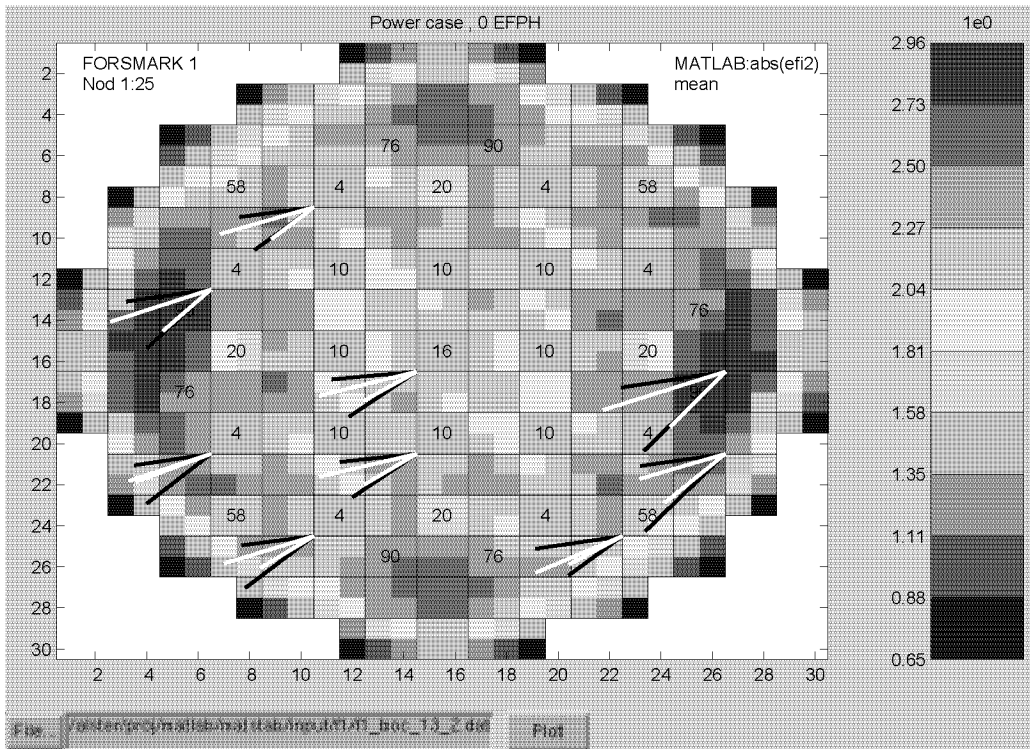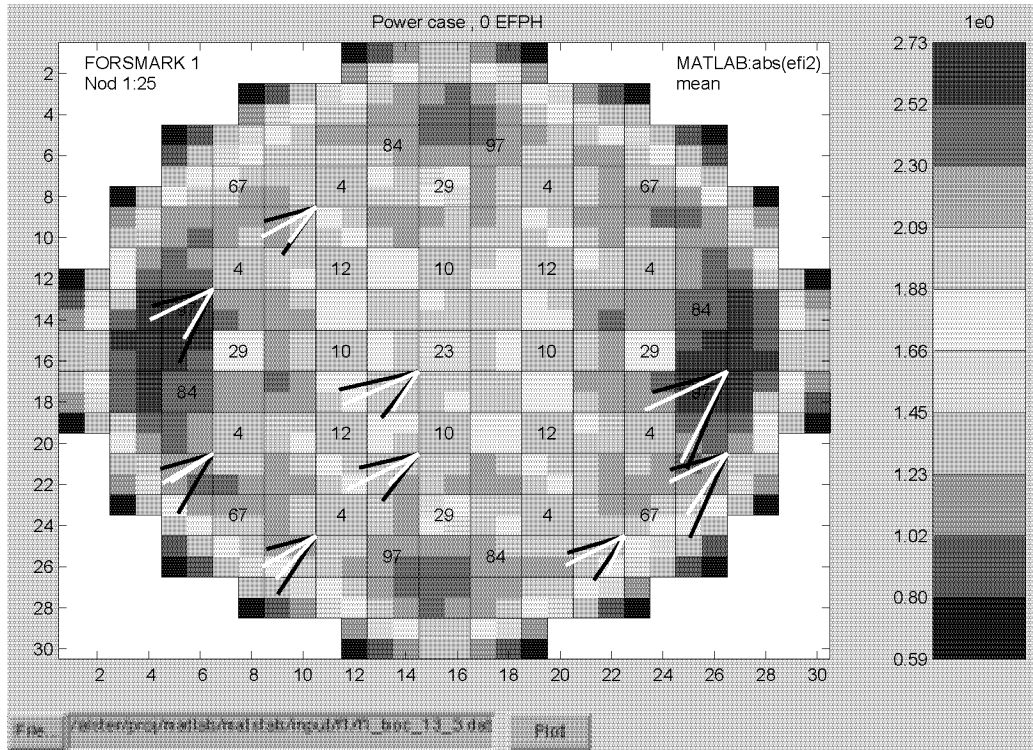Figure 6.17: Comparison of MATSTAB and Measurement C13 moc in Forsmark 2
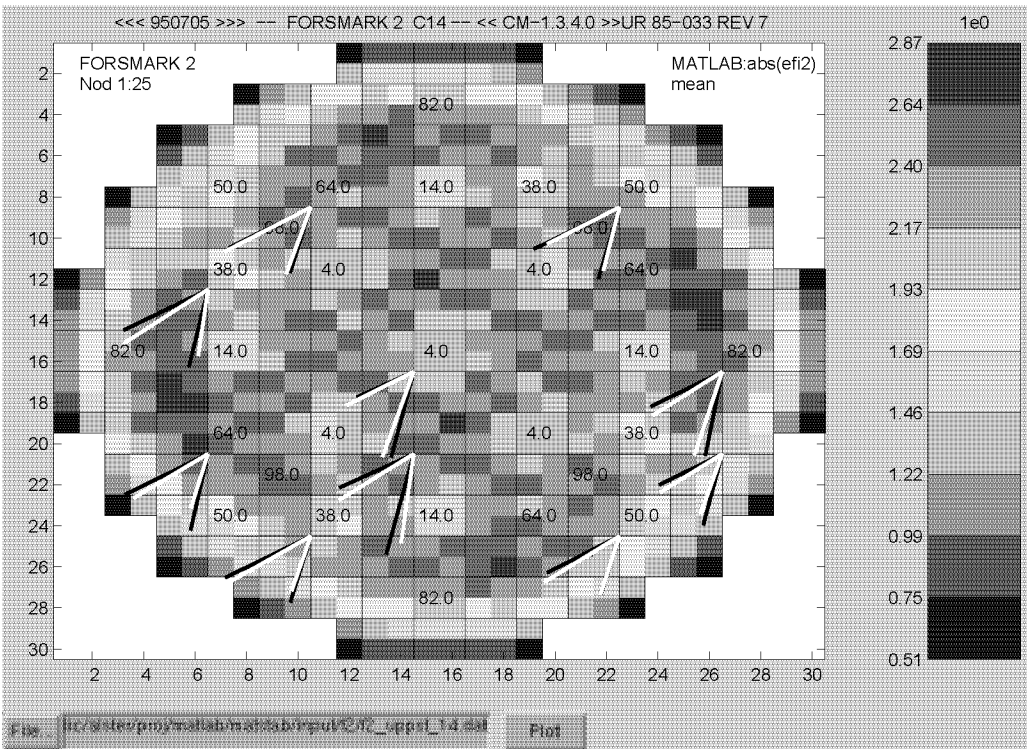
Figure 6.18: Comparison of MATSTAB and Measurement C14 Startup in Forsmark 2
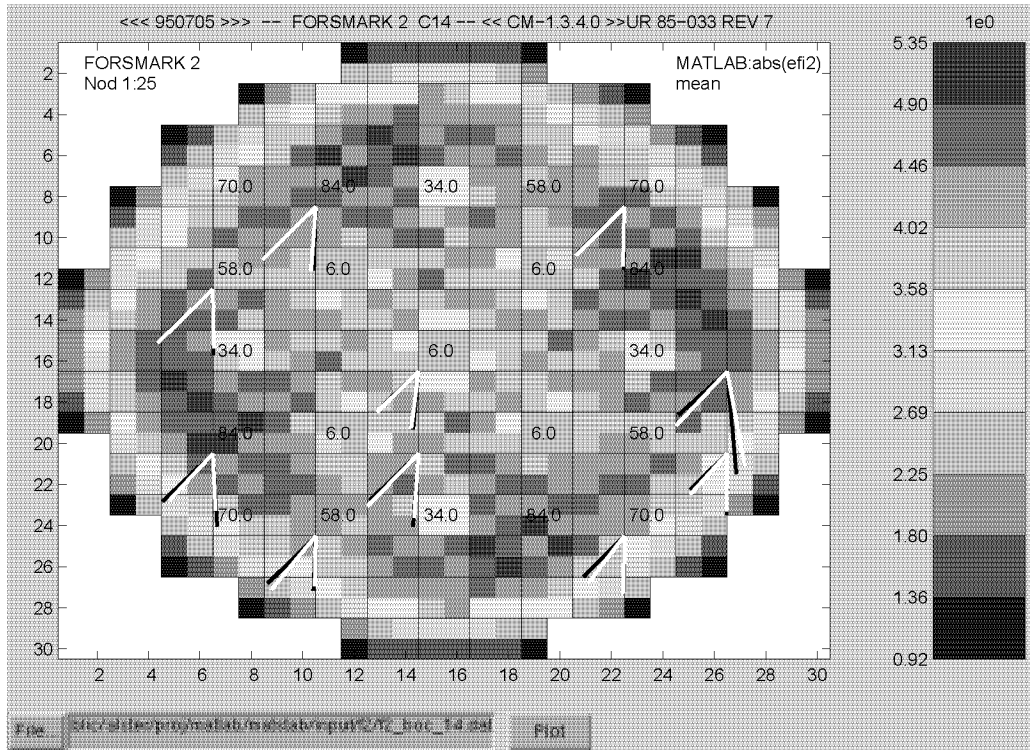
Figure 6.19: Comparison of MATSTAB and Measurement C14 boc in Forsmark 2
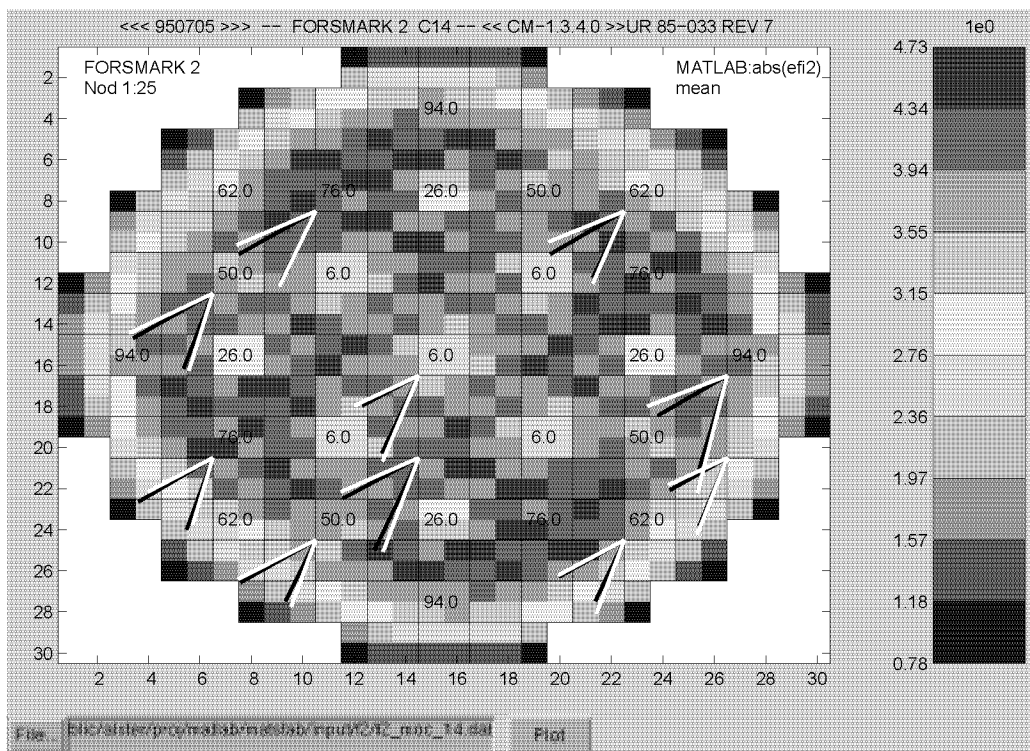
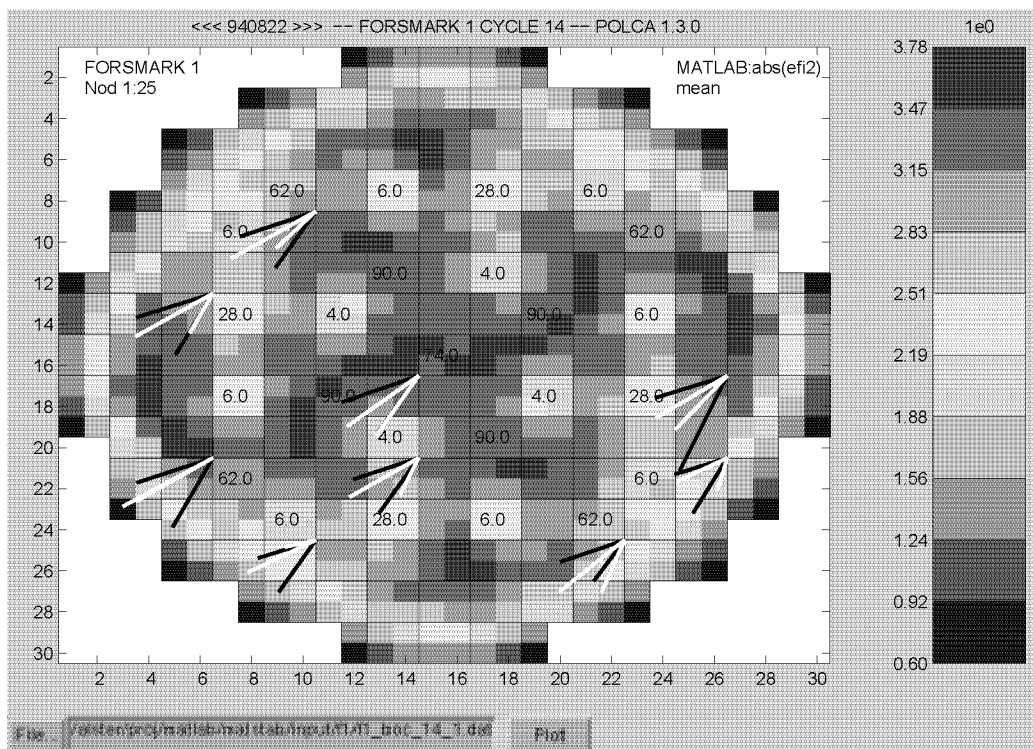Figure 6.20: Comparison of MATSTAB and Measurement C14 moc in Forsmark 2

The content of Figures 6.16-6.20 are explained in Section 6.1.2 and Chapter 5. The agreement between measured and calculated LPRM signal oscillations for Forsmark 2 is even better than the agreement for Forsmark 1, especially cycle 14 yields very good results.

Forsmark 3

MATSTAB was validated against 13 stability measurements Forsmark 3 conducted in the cycles 8-14. The range of operating points lay between 4200 and 5000 kg/s of core flow and 63% to 66% power (see Table 6.3).

Operating point			Decay Ratio		Frequency [Hz]	
Cycle	Power [%]	Core Flow [Kg/s]	Measurement	MATSTAB	Measurement	MATSTAB
C8 boc	63.0	4218	0.48	0.47	0.48	0.44
C8 moc	65.0	4533	0.70	0.69	0.50	0.49
C9 boc	65.0	4300	0.58	0.48	0.48	0.46
C9 moc	65.0	4240	0.76	0.75	0.54	0.51
C10 boc	64.9	4275	0.52	0.55	0.47	0.51
C10 moc	63.6	4756	0.50	0.56	0.52	0.52
C12 boc	64.6	4644	0.50	0.51	0.47	0.50
C12 moc	63.2	4965	0.44	0.51	0.51	0.54
C13 boc	64.0	4600	0.45	0.44	0.44	0.46
C13 moc	63.8	4535	0.55	0.62	0.51	0.52
C14 boc	63.7	4168	0.51	0.52	0.46	0.45
C14 nov	62.2	4799	0.52	0.47	0.49	0.49
C14 jan	65.1	4820	0.52	0.58	0.50	0.49

Table 6.4: Comparison Between MATSTAB and Measurements in Forsmark 3

Figure 6.21 and 6.22 compare the MATSTAB calculation with the values obtained from the measurement. The standard deviation for all cases is 0.05 for the decay ratio and 0.02 for the frequency.

Figures 6.23 - 6.28 show again good agreement between calculated and measured LPRM signal oscillations. Even for detector strings with four LPRM detectors, the phase-shift is predicted well.
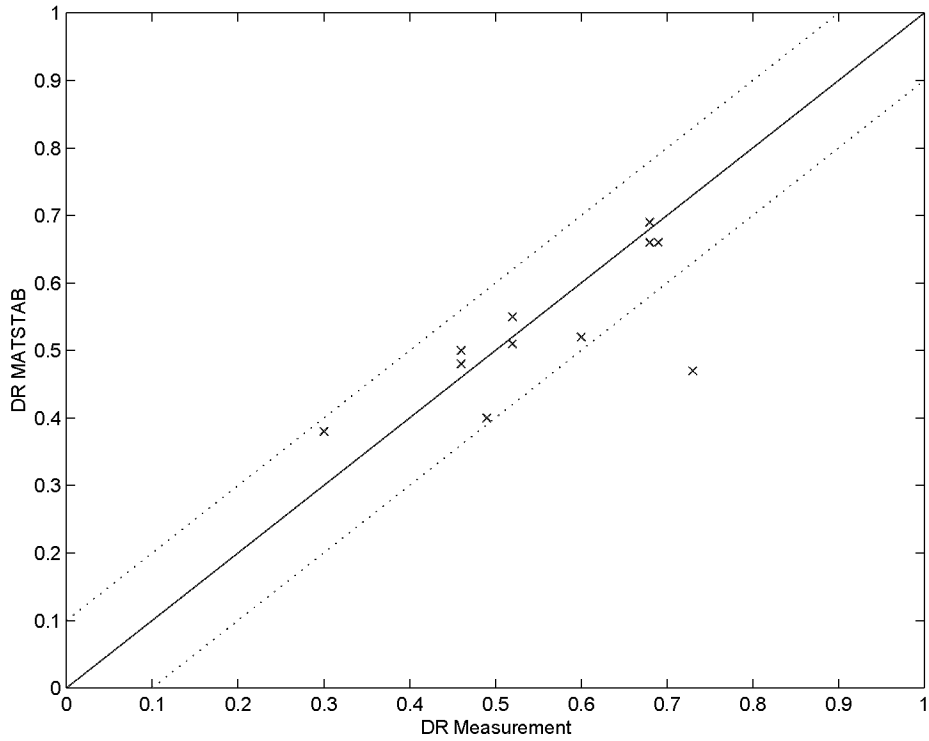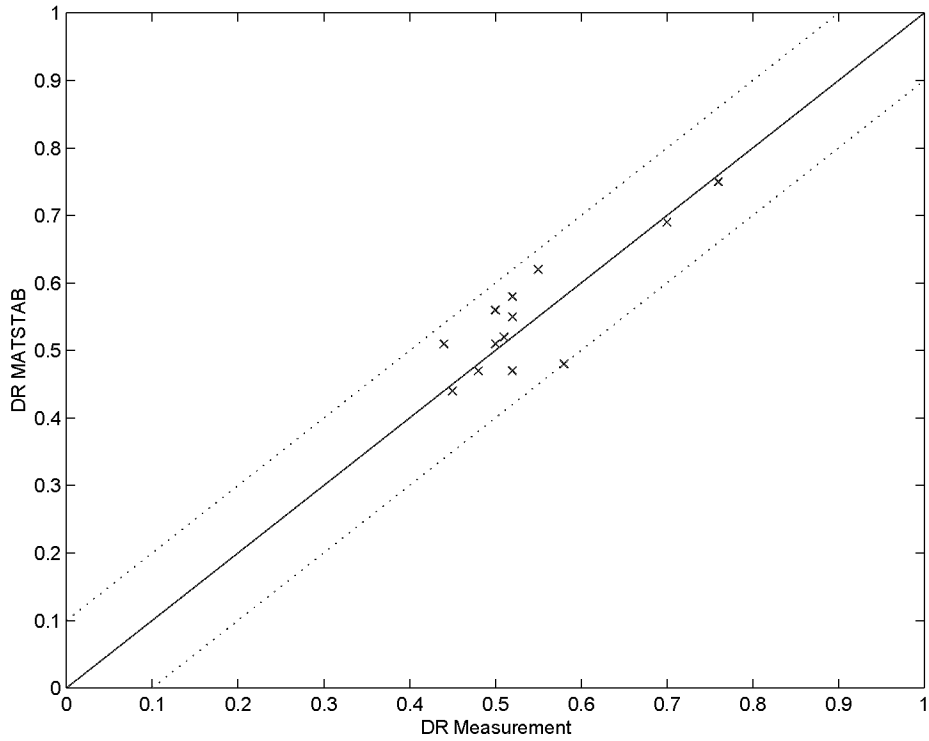
Figure 6.21: Validation of the Decay Ratio for Forsmark 3
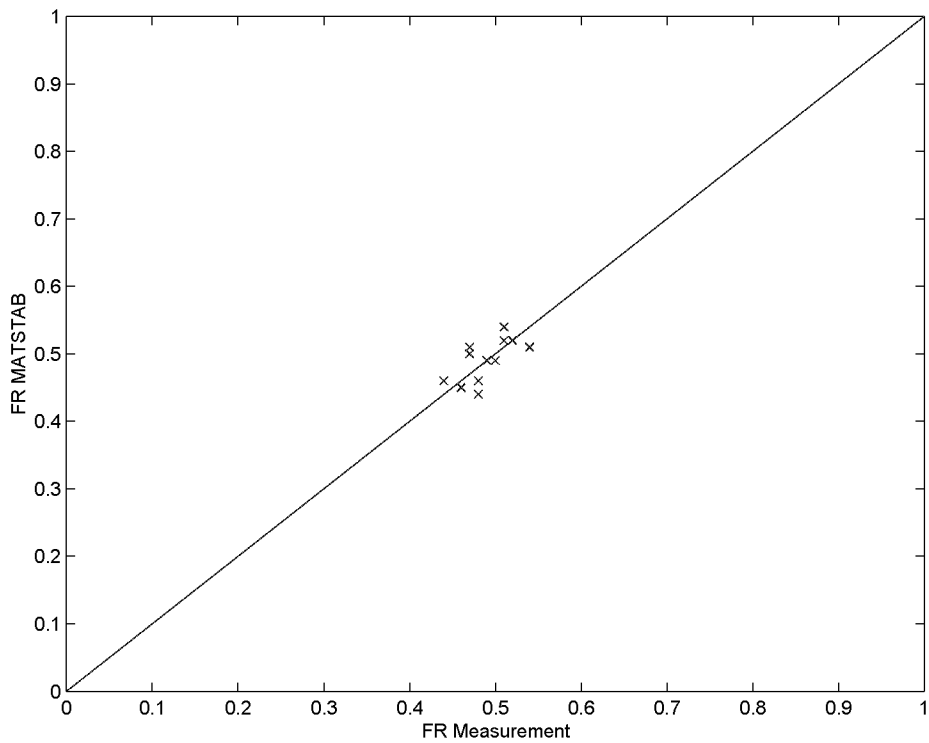

Figure 6.22: Validation of the Frequency for Forsmark 3
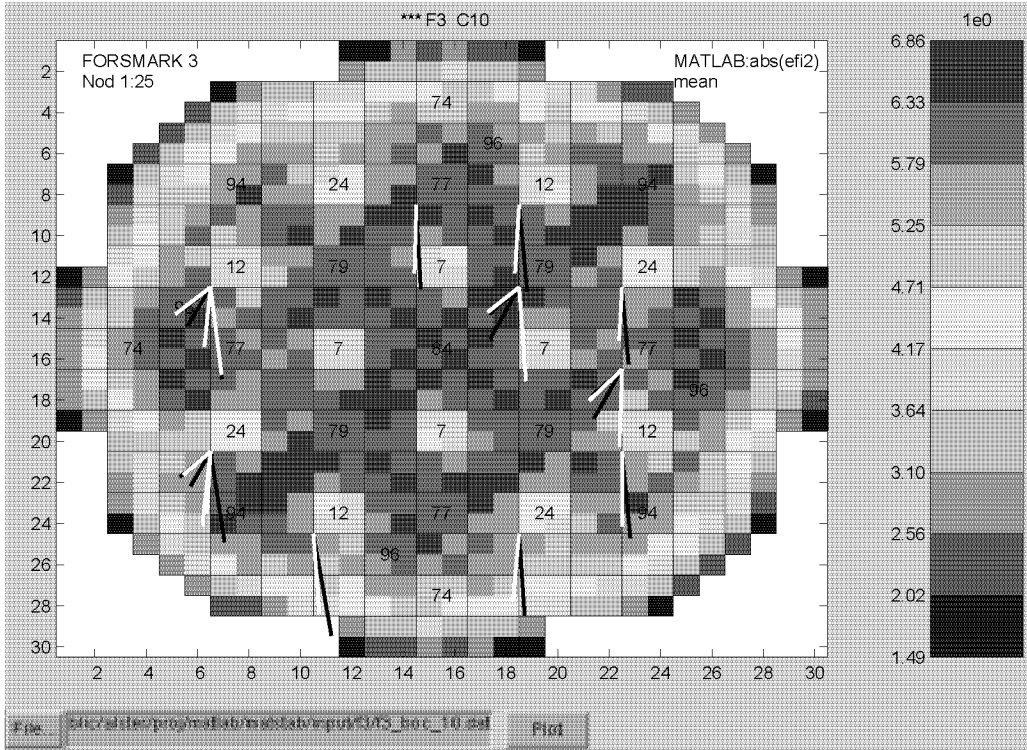
Figure 6.23: Comparison of MATSTAB and Measurement C10 boc in Forsmark 3
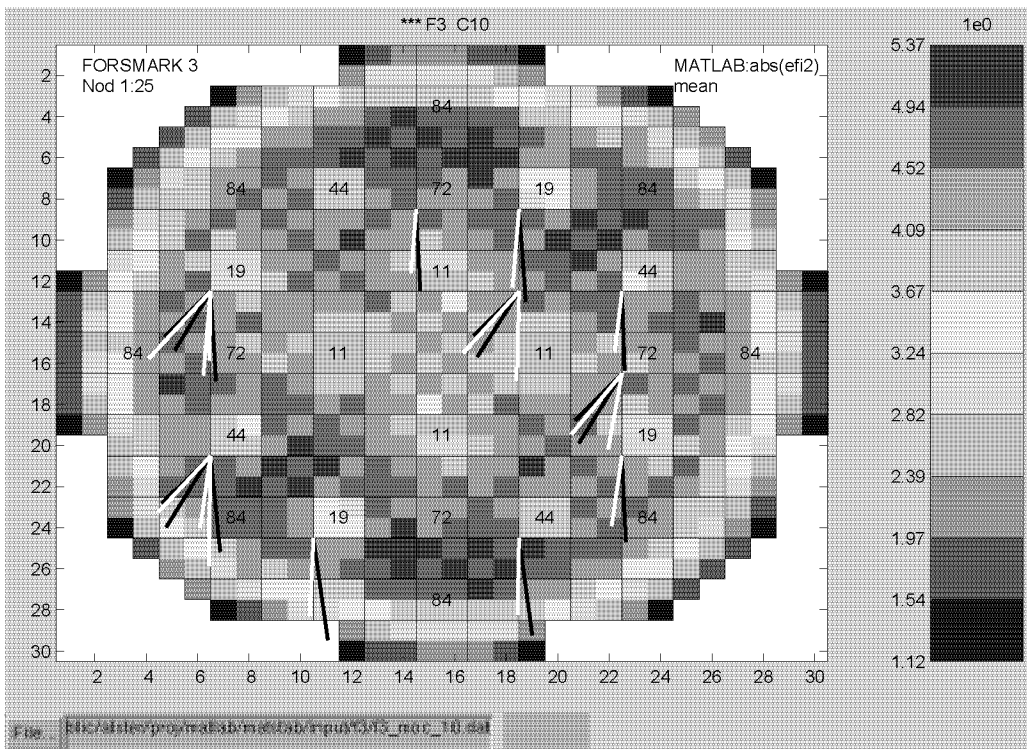
Figure 6.24: Comparison of MATSTAB and Measurement C10 moc in Forsmark 3
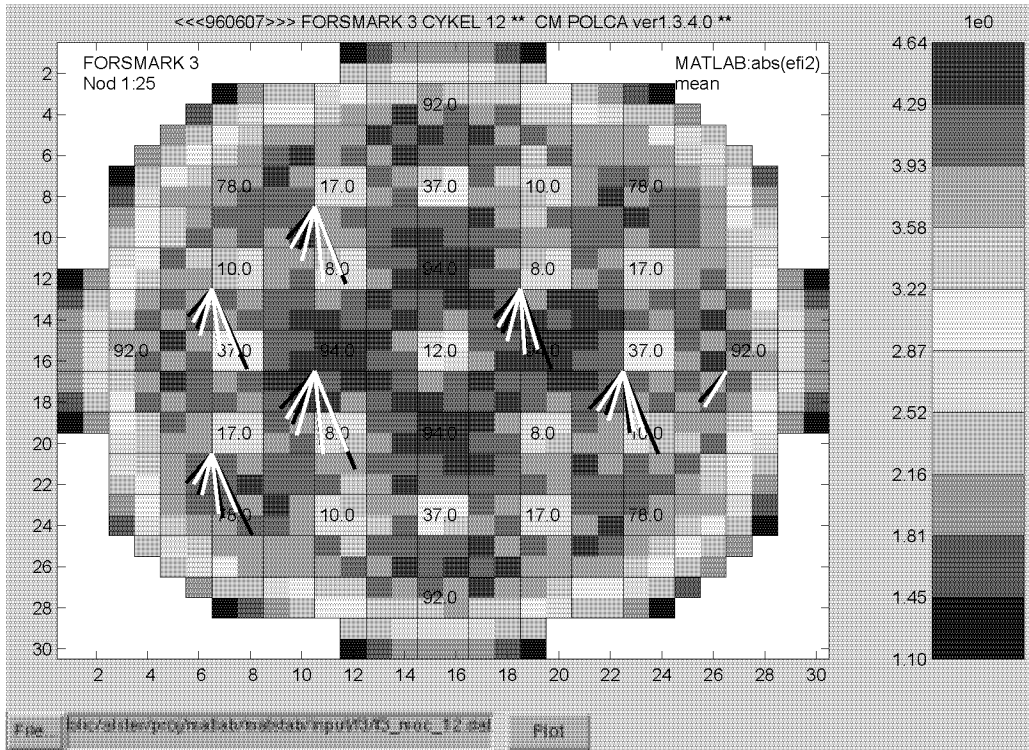
Figure 6.25: Comparison of MATSTAB and Measurement in C12 moc Forsmark 3
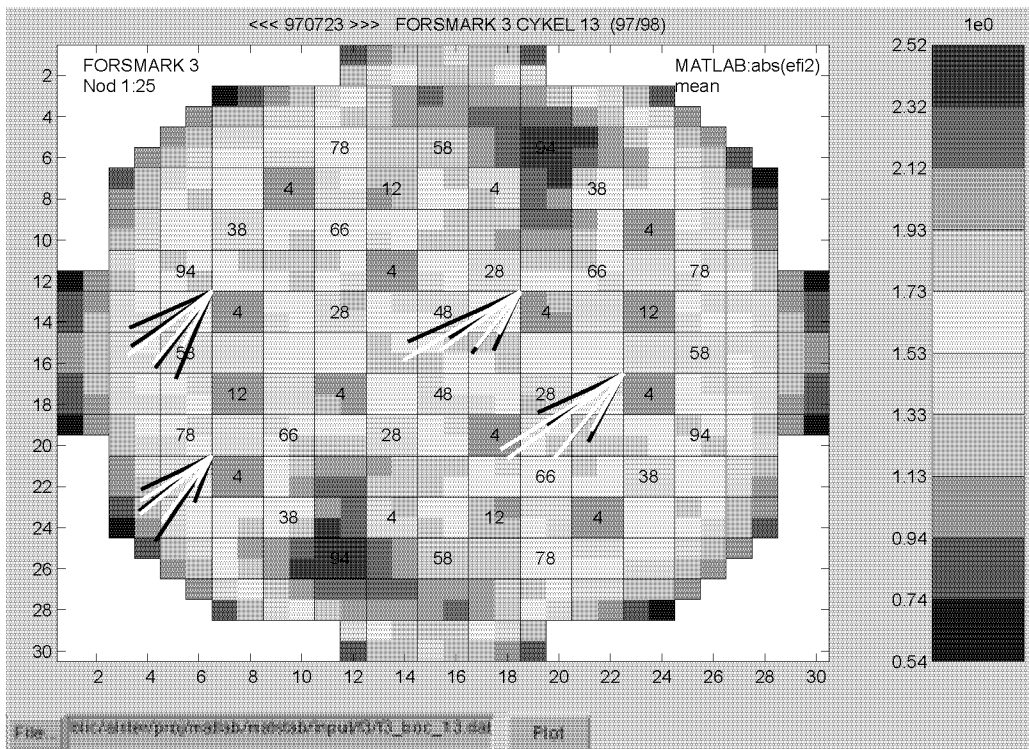
Figure 6.26: Comparison of MATSTAB and Measurement in C13 boc Forsmark 3
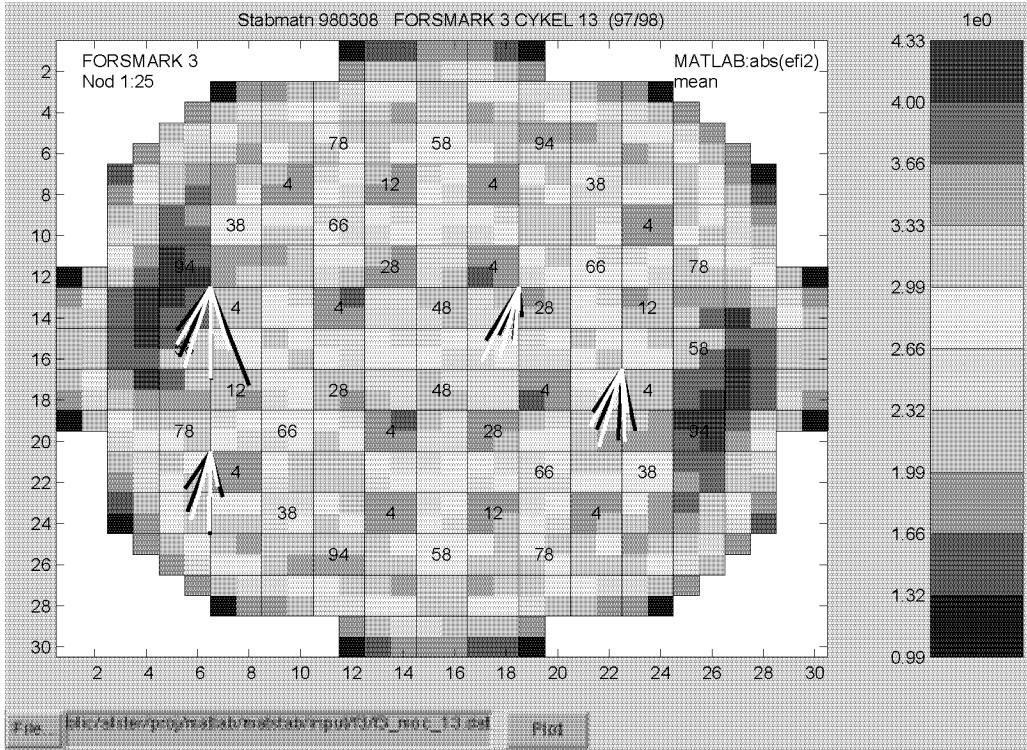
Figure 6.27: Comparison of MATSTAB and Measurement C13 moc in Forsmark 3
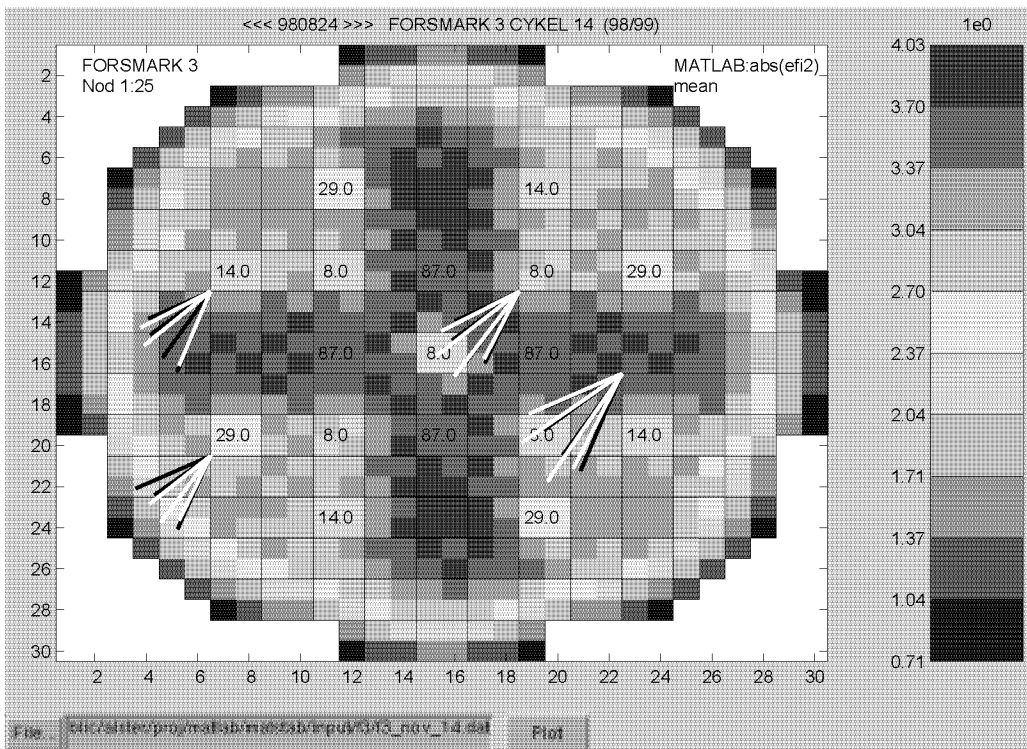
Figure 6.28: Comparison of MATSTAB and Measurement C14 nov in Forsmark 3

6.2.2 Oskarshamn

All the following results are taken from the MATSTAB validation report [19] prepared by Oskarshamn. The information is added to show that MATSTAB gives good results for NPPs which it was not tested against during the development phase. It is also noteworthy, that the Oskarshamn people had no problems with generating the input desks for MATSTAB or using the code in general.

Operating point			Decay Ratio			Operating point			Decay Ratio	
Cycle	Power [%]	Core Flow [Kg/s]	Measurement	MATSTAB		Cycle	Power [%]	Core Flow [Kg/s]	Measurement	MATSTAB
Oskarshamn 1						Oskarshamn 3				
C21	75.1	2767	0.35	0.37		C10	74.7	6399	0.31	0.46
C21	75.1	2889	0.32	0.29		C10	59.8	4384	0.67	0.70
C22	74.0	2776	0.27	0.35		C10	56.4	4090	0.71	0.66
C23	74.3	2797	0.24	0.32		C10	60.2	4354	0.77	0.75
C24	75.4	2747	0.44	0.46		C11	63.4	4425	0.72	0.76
C24	74.5	2724	0.48	0.42		C11	60.5	4380	0.70	0.76
						C12	62.7	4360	0.68	0.74
Oskarshamn 2						C12	62.5	4360	0.83	0.75
C19	85.0	3175	0.60	0.69		C13	65.3	4796	0.69	0.70
C19	82.4	2966	0.64	0.74		C13	60.5	4177	> 1	1.00
C19	78.9	2949	0.69	0.64		C13	65.0	5100	0.63	0.50
C19	83.6	3172	0.73	0.65		C14	50.0	4978	0.32	0.26
C19	80.8	3003	0.60	0.69		C14	50.0	5344	0.30	0.22
C19	78.8	2995	0.67	0.63		C14	66.2	5083	0.60-0.63	0.54
C20	80.1	2966	0.58	0.53		C14	66.0	5000	0.56-0.63	0.57
C20	81.5	3005	0.62	0.67		C14	66.8	5400	0.47	0.43
C20	79.1	3052	0.58	0.61		C14	66.2	5122	0.67	0.54
C21	91.3	2993	0.62	0.57		C14	67.0	5375	0.67	0.52
C21	78.3	3036	0.47	0.53		C15	75.0	6240	0.54	0.35
C22	82.8	3024	0.57	0.50		C15	71.0	6040	0.45	0.35
C23	70.8	2630	0.38	0.45						
C23	83.7	3186	0.50	0.46						
C24	85.1	3180	0.53	0.43						
C25	73.3	2991	0.42	0.50						

Table 6.5: Comparison Between MATSTAB and Measurements in Oskarshamn

Oskarshamn 1

MATSTAB shows good agreement with the measurements of Oskarshamn 1 (Figure 6.29) even though the decay ratios in general are very small. The standard deviation for all cases is 0.06 for the decay ratio.

Oskarshamn 2

MATSTAB shows good agreement with the measurements of Oskarshamn 2 (Figure 6.30). In cycle 19-20 the core contained only SVEA-64 fuel assemblies. In cycle 21-24 Atrium-9 fuel was introduced, in cycle 24 and 25 Atrium-10B. The partial length rods introduced with the new fuel types lead to no problems for the 3D neutronics of MATSTAB. The measurement data from Oskarshamn 2 is taken from the online stability monitor and not from a thorough investigation of the LPRM data. This may be a reason for the slightly higher deviations when compared with Oskarshamn 1. The standard deviation is 0.07 in decay ratio.

Oskarshamn 3

MATSTAB shows good agreement with the measurements of Oskarshamn 3 up till cycle 13 (Figure 6.31). In cycle 14 the deviation is large and in cycle 15 the deviation is unreasonably large. The reason for the large error in the latest two cycles is not yet understood. The standard deviation of all measurements is 0.08 for the decay ratio.
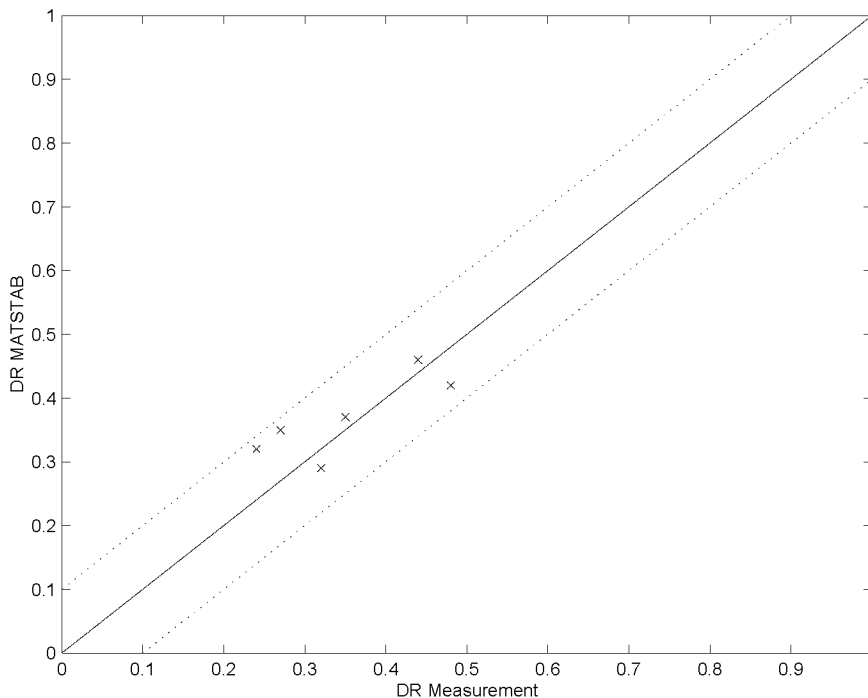
Figure 6.29: Validation of the Decay Ratio for Oskarshamn 1
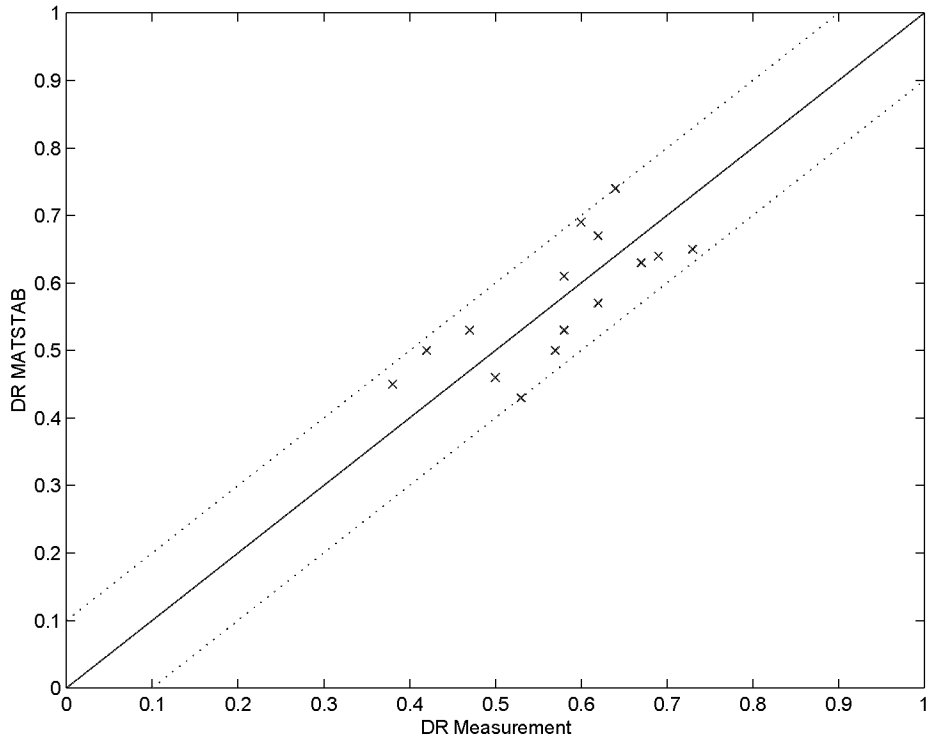
Figure 6.30: Validation of the Decay Ratio for Oskarshamn 2
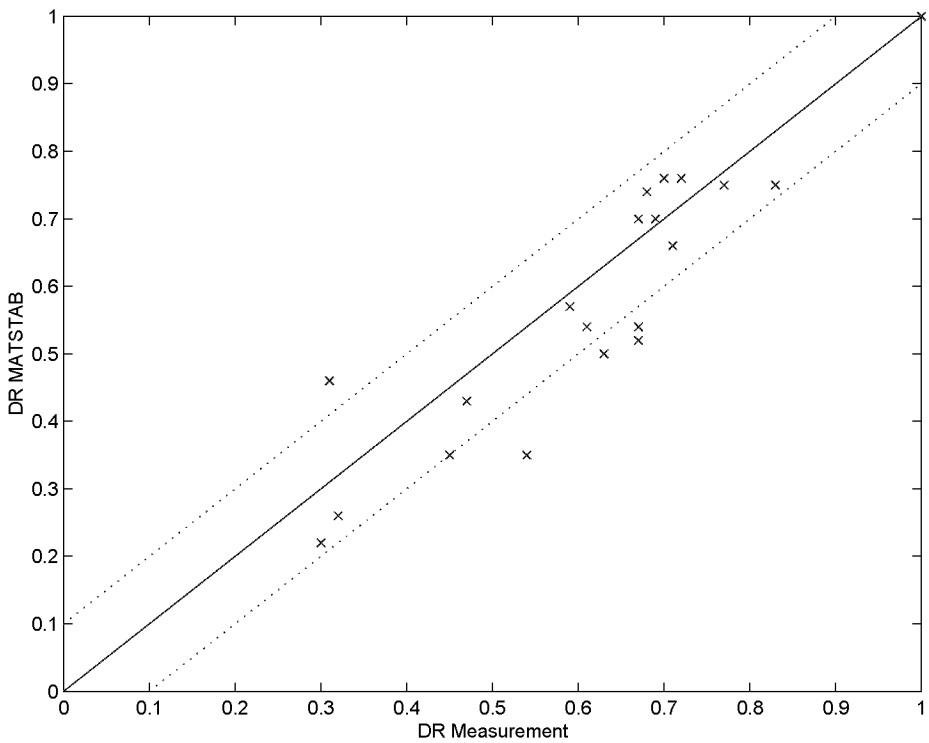
Figure 6.31: Validation of the Decay Ratio for Oskarshamn 3

6.2.3 Leibstadt

A core stability test was conducted in KKL shortly after the beginning of cycle ten (see [86] or Chapter 5 for an extensive analysis). The core contained about 51% of 10x10 lattice SVEA-96 fuel. The remainder consisted chiefly of 8x8 lattice GE-8 and GE-10 fuel. The range of operating points lay between 3050 and 7784 kg/s of core flow and 45% to 77% power (see Table 6.6). As for the Forsmark and Oskarshamn cases, MATSTAB is able to predict the decay ratios and frequencies with reasonable accuracy. The standard deviation for all cases is 0.08 for the decay ratio and 0.02 for the frequency.

Operating point			Decay Ratio			Frequency [Hz]		
Cycle	Power [%]	Core Flow [Kg/s]	Measurement	MATSTAB global	MATSTAB regional	Measurement	MATSTAB global	MATSTAB regional
C10	77	7784	0.22	0.07	0.09	0.63	0.60	0.66
C10	68	5078	0.44	0.42	0.46	0.60	0.52	0.57
C10	61	4464	0.53	0.56	0.57	0.54	0.47	0.52
C10	59	4010	0.65	0.65	0.65	0.50	0.44	0.48
C10	45	3050	0.97	1.02	1.03	0.47	0.42	0.45

Table 6.6: Comparison Between MATSTAB and Measurements in Leibstadt

Figures 6.32 and 6.33 compare the global mode of the MATSTAB calculation with the values obtained from the measurements. If the first operating point is omitted (the DR of very stable points is extremely hard to predict though not important for the analysis), the standard deviation is 0.03 for the decay ratio and 0.02 for the frequency.

In contrast to the measurement series in cycle seven, which is discussed later, neither the online monitoring system nor the post analysis indicated the appearance of regional oscillations. However, MATSTAB predicts a significant possibility for regional oscillations in the cycle ten measurements series. The global and the regional modes have decay ratios of similar size and correspond to the decay ratios measured during the experiment. Actually, the regional decay ratios are slightly larger than the global ones (see Table 6.6). Interestingly, the frequencies of the regional oscillations are in general closer to the measurement than the frequencies from the global oscillations. Assuming that the MATSTAB calculations are correct, it is astonishing, that in none of the five operating points the slightest indication for regional oscillation were seen. One explanation is, that the signal amplitude of the regional oscillation was much smaller than the signal amplitude of the global oscillation. This would make it difficult to detect the regional oscillation. This problem is discussed in a paper from Van der Hagen et al. [112] using data from a Ringhals 1 measurement in 1990.

If one compares the phases and amplitudes of the global MATSTAB solutions with the mea-

surements (Figures 6.34-6.38), the good agreement supports the assumption, that the reactor was oscillating in the global mode. As in the Forsmark cases, the phase is predicted more accurate than the amplitude.
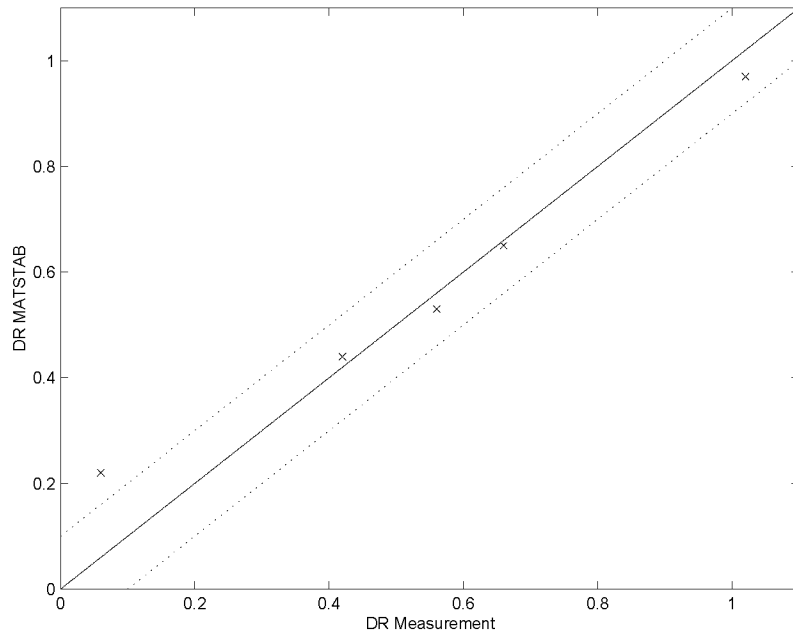
Figure 6.32: Validation of the Decay Ratio for Leibstadt Cycle 10
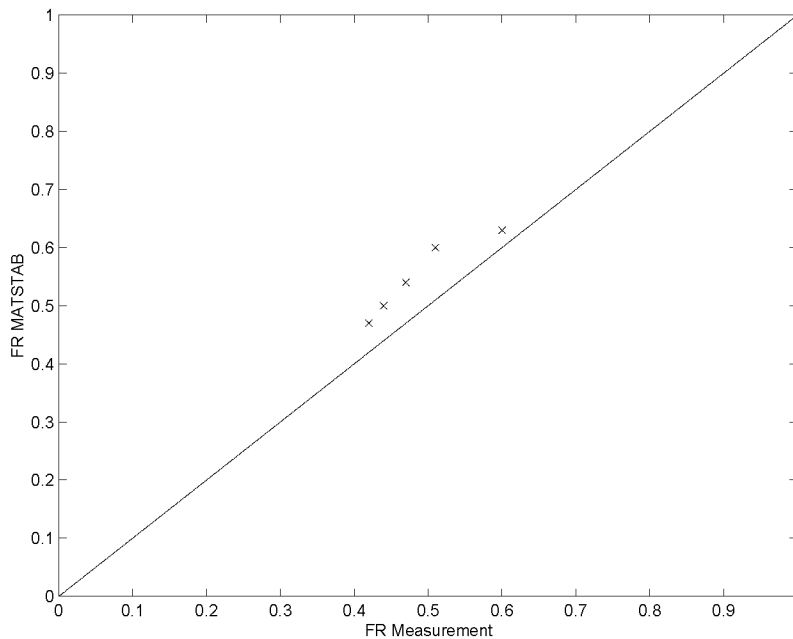
Figure 6.33: Validation of the Frequency for Leibstadt Cycle 10
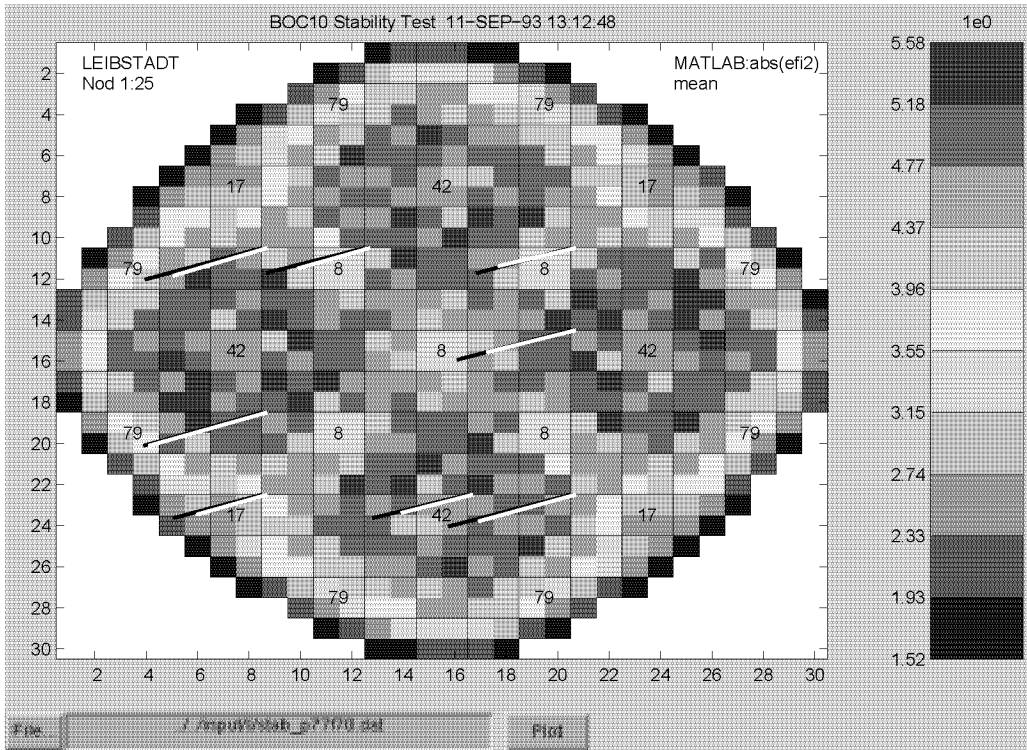
Figure 6.34: Comparison of MATSTAB and Measurement Point P77F70 in Leibstadt

Figure 6.35: Comparison of MATSTAB and Measurement Point P68F45 in Leibstadt

Figure 6.36: Comparison of MATSTAB and Measurement Point P61F40 in Leibstadt

Figure 6.37: Comparison of MATSTAB and Measurement Point P59F37 in Leibstadt

Figure 6.38: Comparison of MATSTAB and Measurement Point P45F28 in Leibstadt

6.3   Regional Oscillations

The ability to foresee regional oscillations, despite all the simplifications needed for a fast frequency-domain code, is one of MATSTABs big advantages. However, the MATSTAB module that deals with regional oscillations is not tested and validated as thoroughly as the global module. In addition, there are not many measurement cases available with dominating regional oscillations. A further problem is, that MATSTAB, as all linear codes, is not able to predict amplitudes.

MATSTAB only analyzes one operating point, therefore, the input data concerning the actual plant status is absolutely crucial for the results of the calculation. After a stability measurement, several hundred POLCA calculations are done to follow the operating points from startup to the measurement. This assures, that the xenon density and other time dependent quantities are taken correctly into consideration. The measurement itself, should be performed at a fixed operating point, which can be described by a POLCA steady state calculation.

If dominating regional oscillations occur, they can also interact with the global mode. For example, it is possible that within a few minutes, or even seconds, the oscillation pattern changes from global to regional and back again. To complicate things even further, the axis of

the regional oscillation may rotate in time. This behavior may take place while the operating point does not change significantly in power and core flow.

Therefore, MATSTAB cannot describe what happened during a measurement. However, MATSTAB can predict for a special operating point if regional oscillations are to be expected. MATSTAB is able to calculate not only the eigenvalue and hence the decay ratio for the global case, but also for as many regional oscillations modes as specified. If the decay ratio of a regional case is close to or even larger than the global one, regional oscillations are to be expected.

This simple and obvious rule was verified for all the Forsmark measurements, where the decay ratio of the regional case was always clearly smaller than for the global case.

6.3.1 Leibstadt

Things were very different in the case of Leibstadt during the measurements conducted in 1990 (cycle seven). The operating conditions were much less stable than in any Forsmark measurement. During the measurements of cycle seven, regional oscillations were actually observed, and a comprehensive report about the measurements series was written by J. Blomstrand [12].

Operating point			Decay Ratio			Frequency [Hz]		
Cycle	Power [%]	Core Flow [Kg/s]	Measurement	MATSTAB Global	MATSTAB Regional	Measurement	MATSTAB Global	MATSTAB Regional
C7	61.4	8466	0.20			0.53		
C7	55.2	4071	0.60/0.65	0.24	0.31	0.38/0.49	0.33	0.41
C7	56.9	4077	0.92-0.99	0.36	0.58	0.58	0.43	0.48
C7	58.6	4092	0.94-0.99	0.35	0.59	0.58	0.43	0.48
C7	58.6	4087	0.99-1.01	0.44	0.61	0.58	0.47	0.48
C7	58.6	4082	1.01-1.04	0.46	0.69	0.58	0.47	0.52
C7	58.0	4066	0.96-0.99	0.44	0.61	0.58	0.47	0.48

Table 6.7: Comparison Between MATSTAB and Measurements for Leibstadt Cycle 7

For the last five operating points, MATSTAB correctly predicts the domination of the regional oscillation (55.2/4071 was actually in phase). The decay ratio of the first regional mode is clearly larger than the decay ratio of the global mode (see table 6.7). The specific values of the decay ratios are, however, completely wrong for the global as well as for the regional case. The MATSTAB model of Leibstadt must be more or less correct, since it predicts good results for cycle 10. A mistake in the regional module would explain the small

values for the corresponding decay ratios, but could not explain the small values in the global case, because the global module is independent from the regional module.

The most likely cause for the large deviation between calculation and measurement is a mistake in the POLCA steady state. This assumption is supported by the fact, that not only the decay ratio, but also the frequency of the oscillation differs from the measurement. Since on one hand, the frequency is easy to predict, and on the other hand, the frequency is related to the transport time of the coolant through the core, POLCA most probably calculated a wrong steady state.

The mistake is systematically repeated in all operating points, as may be seen from the Figures 6.39 and 6.40.

There is no big surprise in the fact, that the phasor plots in Figure 6.41ff show also a large disagreement between calculation and measurement.

The only way to clarify the situation, as well as the reliability of MATSTAB for regional oscillations, will be the analysis of some regional measurements from another plant.
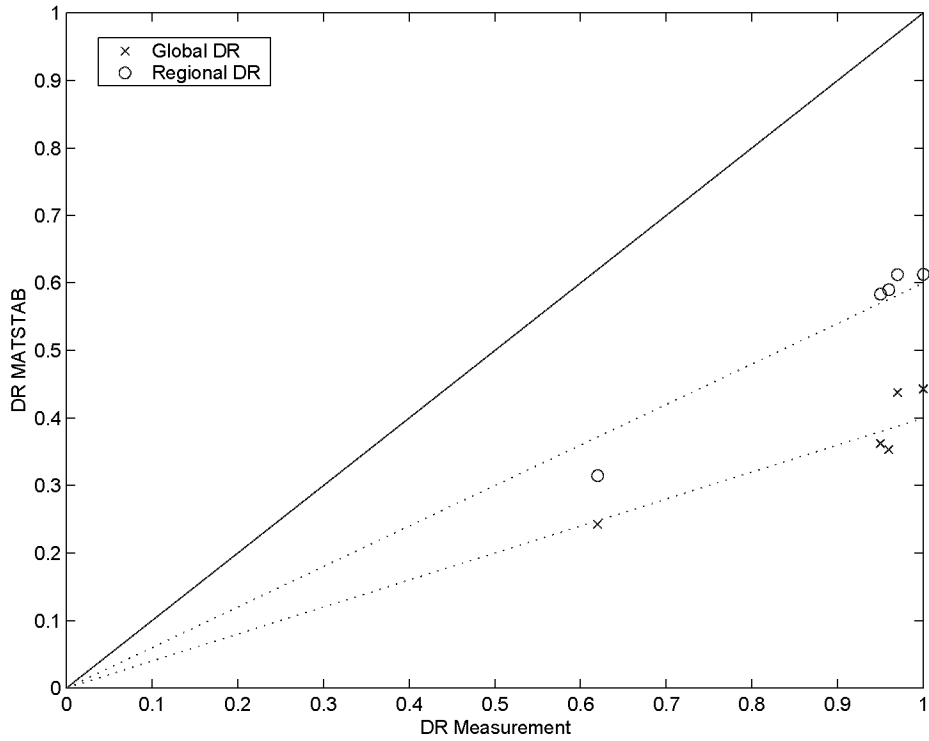
Figure 6.39: Validation of the Decay Ratio for Leibstadt Cycle 7
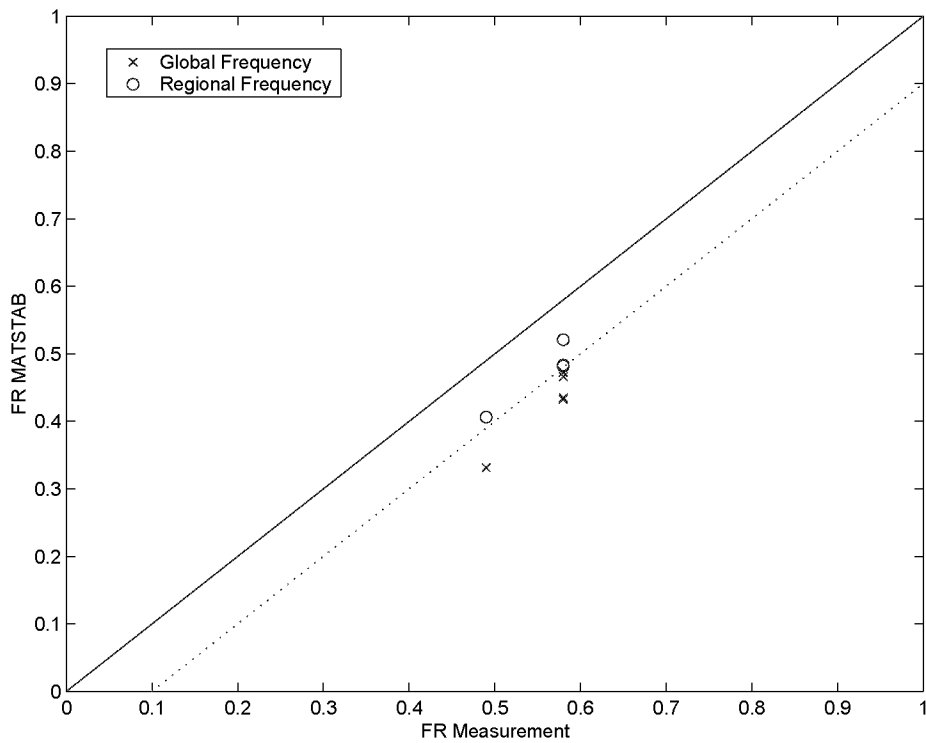
Figure 6.40: Validation of the Frequency for Leibstadt Cycle 7
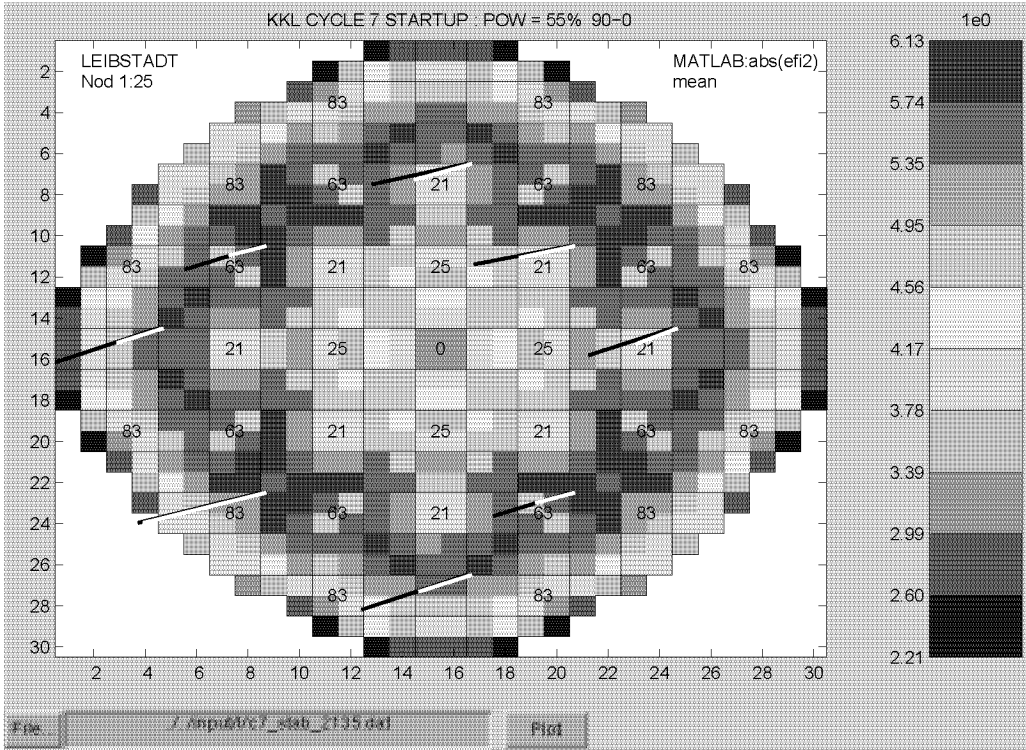
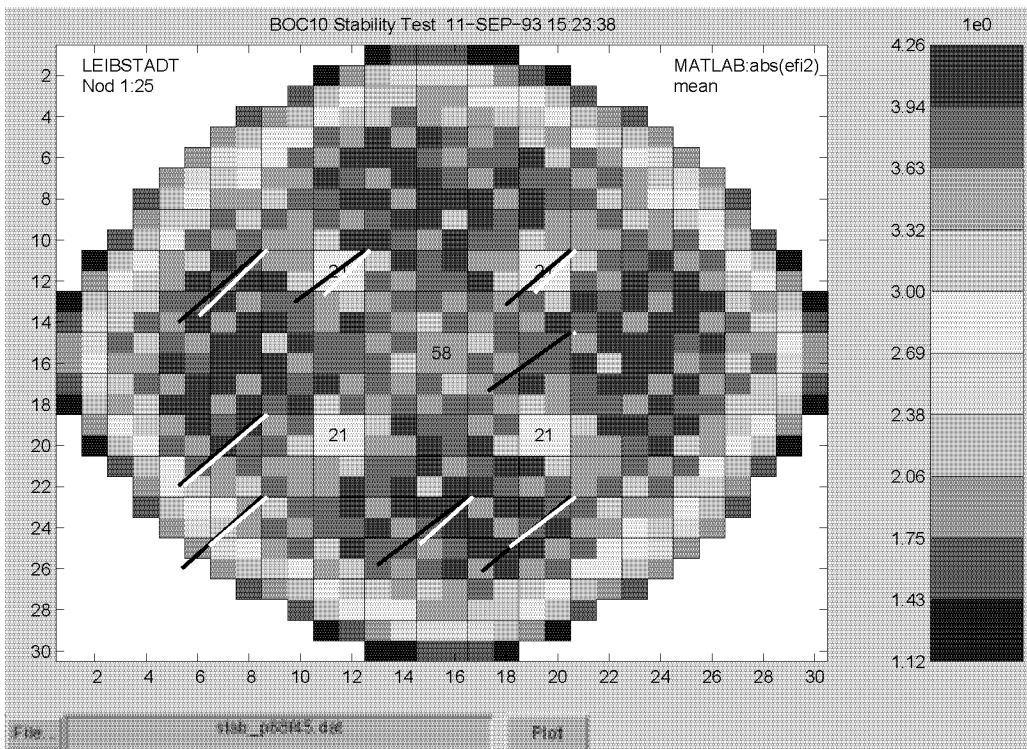Figure 6.41: Comparison of MATSTAB and Measurement Point 21:35 in Leibstadt
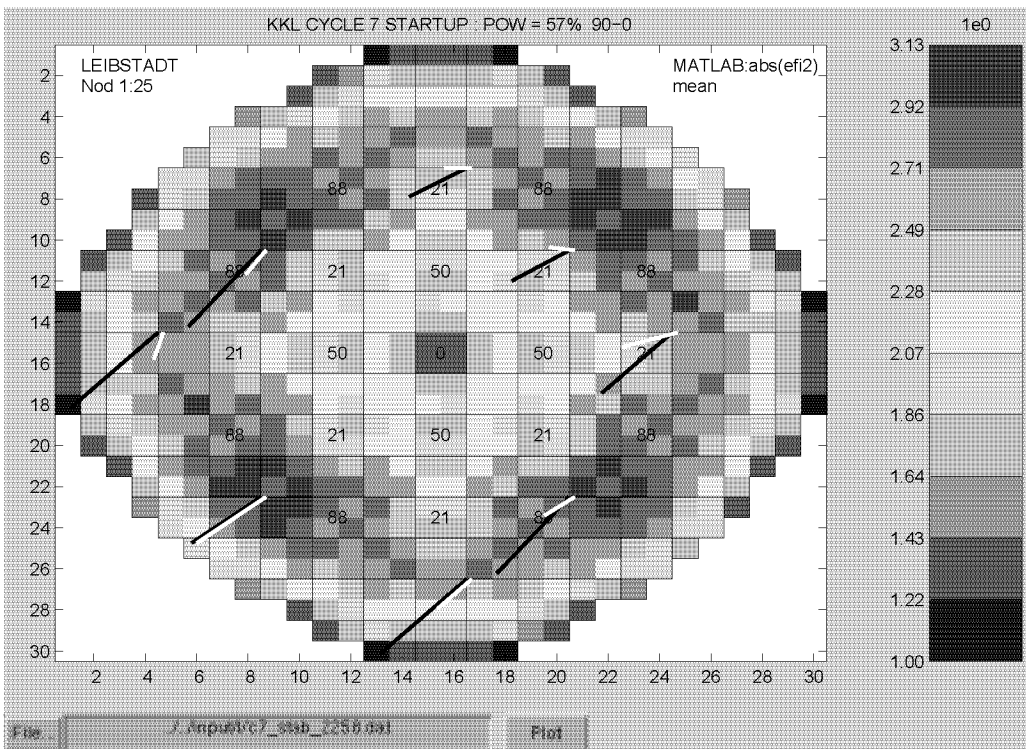
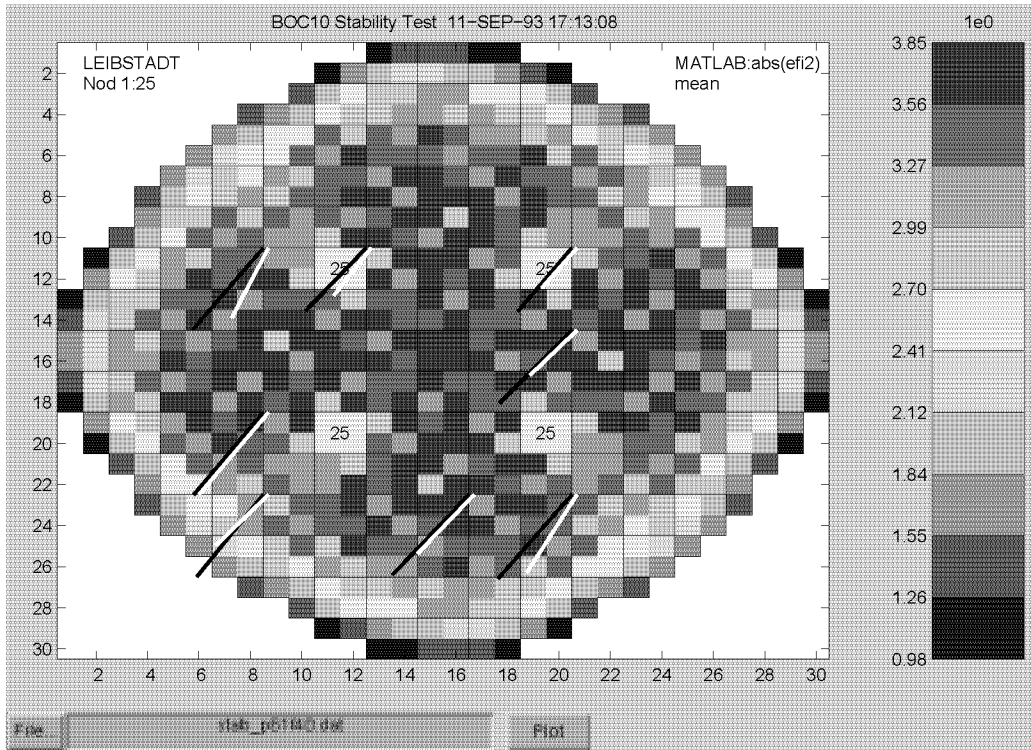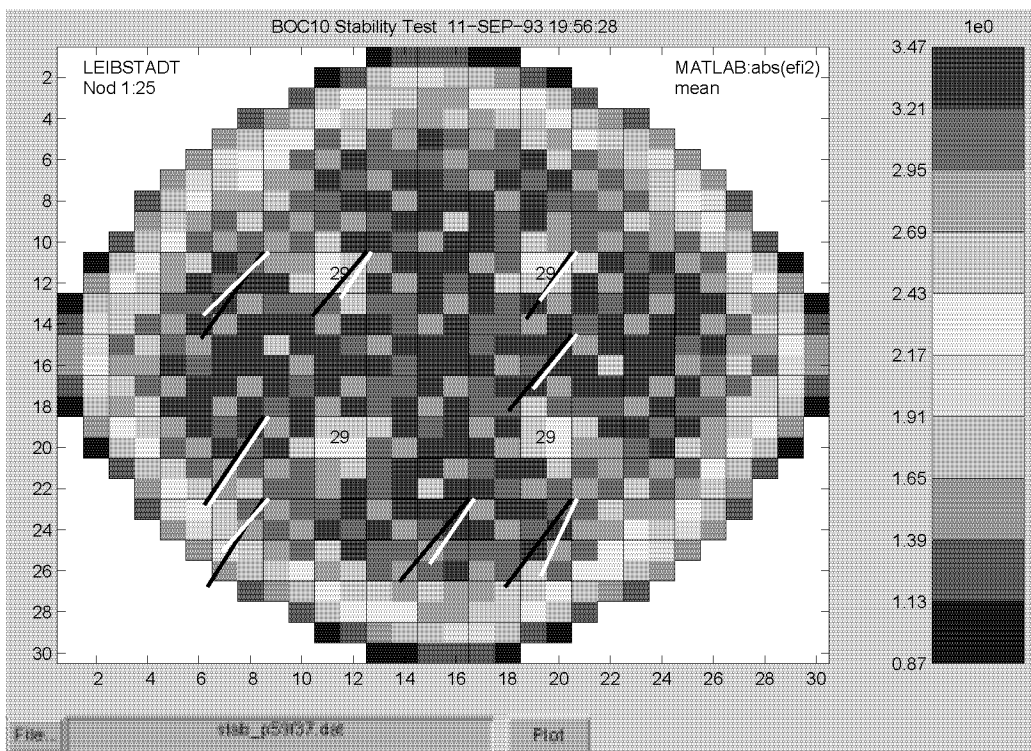Figure 6.42: Comparison of MATSTAB and Measurement Point 22:58 in Leibstadt
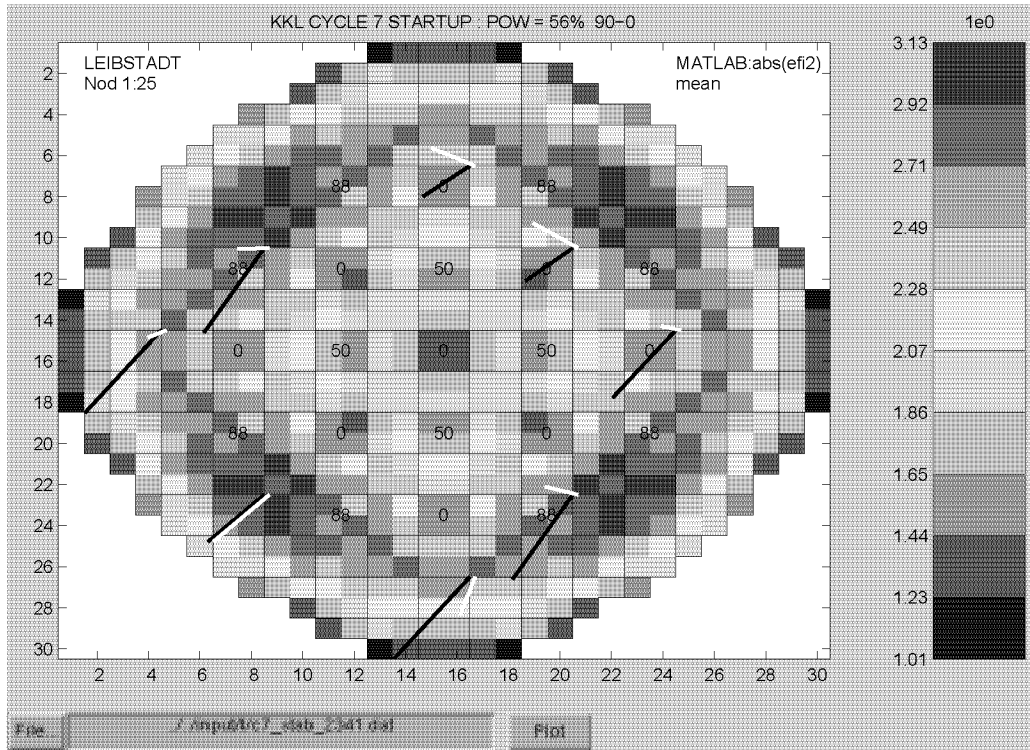
Figure 6.43: Comparison of MATSTAB and Measurement Point 23:41 in Leibstadt

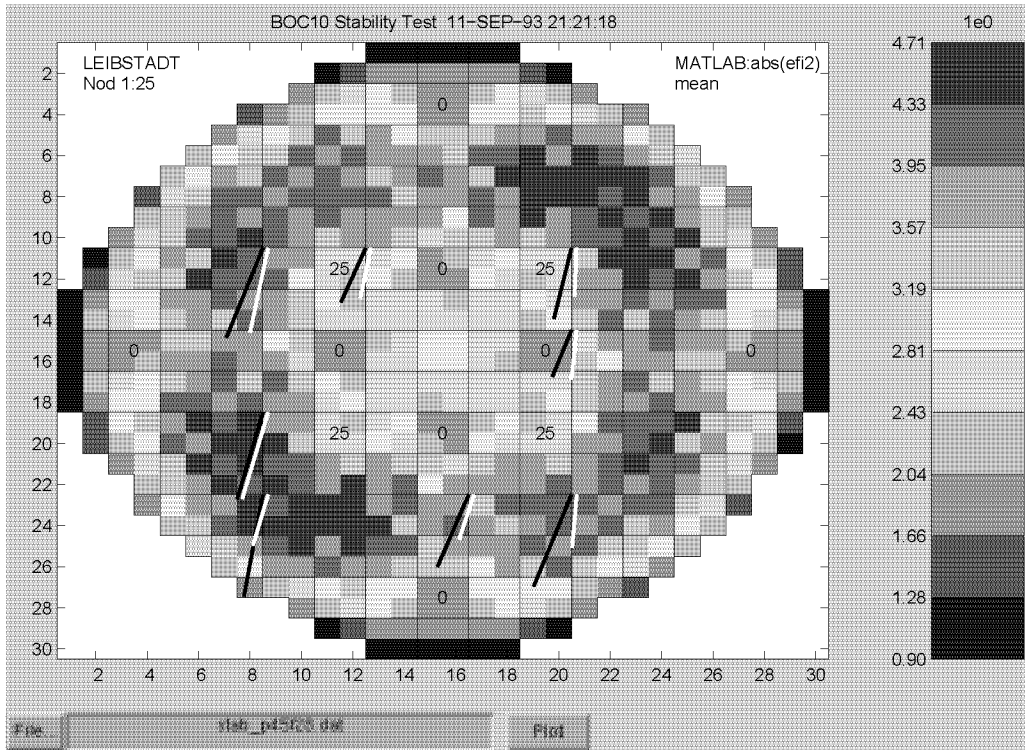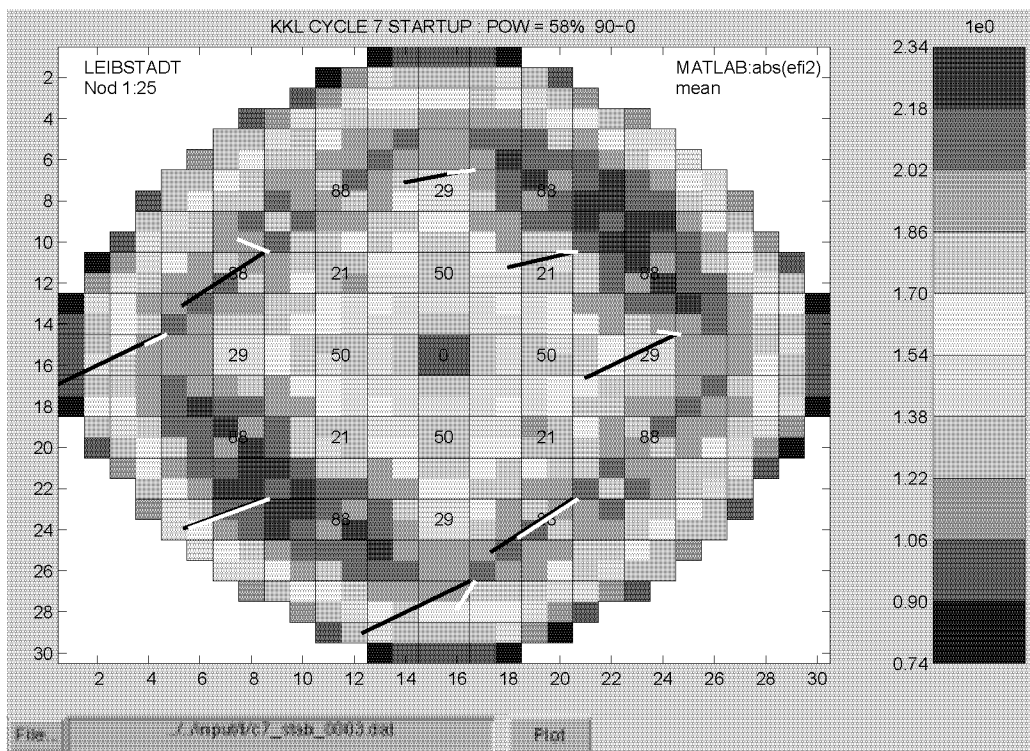Figure 6.44: Comparison of MATSTAB and Measurement Point 00:03 in Leibstadt

Chapter 7

Conclusions

MATSTAB is a new computer code, able to predict global and regional power-void oscillations in a boiling water reactor. The predictions of the code are validated against stability measurements in all three reactors in Forsmark and in Oskarshamn as well as against the Leibstadt reactor in Switzerland. The predictions are normally very accurate for global oscillations and are comparable with the results of state-of-the art transient codes.

The MATSTAB model is based on RAMONA 3B (thermal-hydraulics, thermal conduction) and POLCA 4 (neutronics). The thermal-hydraulic part is one dimensional but multi-channel, with full radial resolution (each fuel assembly is modeled independently). The neutronic part is three dimensional with 25 nodes for each fuel assembly. The good agreement between prediction and measurement justify the chosen model. However, it seems that the model is more complex than necessary. Most thermal-hydraulic equations were copied from RAMONA in a one-to-one manner. Since RAMONA was designed for general transient calculations, several equations could be simplified for stability calculations. The same is true for the thermal conduction model. Especially the nodalization of the pellet and cladding could be replaced by an analytical approach. This would reduce the number of equations in the system matrix substantially. At the moment, nearly half of the equations originate from the nodalization of the fuel. Nevertheless, the gain for the solution algorithm would be only moderate, since the structure of the fuel equations is simple and allows a fast numerical solution despite its size.

MATSTAB linearizes the set of equations and takes full advantage of sparse matrix technology and frequency-domain methods. With this combination, it is possible to overcome the high memory and CPU requirements of the detailed model. Within ten minutes (with a standard PC), it is possible to predict global oscillations and in another five minutes the decay ratio of the regional oscillation can be predicted. The fast solution of MATSTAB is certainly an advantage in the daily use, but also other codes like RAMONA-5 improved significantly in speed since the development of MATSTAB. Therefore, the real benefit lies in the fact, that MATSTAB calculates more information about the stability behavior of a BWR reactor than just the plain decay ratio. Especially the decay ratio of the regional oscillation and the information available from the eigenvectors are of big interest.

Using the information available from the right and left eigenvectors, a new method is introduced to analyze the contribution of specific model sections, fuel assemblies, variables or equations to the eigenvalue (decay ratio). The method is promising and some first, simple examples are explored. An in-depth analysis of the numerous possibilities remains to be done.

Putting all pieces together, the new approach chosen in MATSTAB proved to be successful. The goals for accuracy, ease of use and speed could be met, while new ways to explore BWR stability have been opened.

Proposals for Future Work

The following topics are good candidates for future work:

- Further development of the new method to analyze the contributions of different parts of the model to the eigenvalue.

- Regional analysis for Ringhals

- Two-group model for the neutronics

- Simplification of the fuel model

Appendix A

The RAMONA/POLCA Model

A.1 Neutron Kinetics and Power Generation

The most rigorous description of the neutron flux behavior is given by the Boltzmann transport equation. A numerical solution of this fully three dimensional problem is prohibitively expensive in computer time and memory. Therefore the following simplifications are standard in 3D numerical reactor models and proven to be acceptable.

- The energy dependence is characterized by two energy groups.

  The border between thermal and fast neutrons is set at 1 eV such that neutrons in the thermal group do not scatter up into the fast group.

- Using Fick's law, the transport equation is simplified into a diffusion equation.

  The solution of the core neutronics requires the definition of average cross sections. The complex geometry of a fuel assembly cannot be modeled precisely with the Diffusion equation and the coarse mesh used to calculate reactor wide data. A homogenization is carried out by first obtaining a fine-mesh (2-D), multi group transport code theory solution for the fuel cell using zero current boundary conditions. Then, flux weighting of the multi group cross sections is performed to obtain the equivalent two-group parameters for the homogenized fuel cell. For example, the node averaged total cross section for energy group g is

$$\overline{\Sigma_{t,g}} = \frac{\int\limits_{fuelcell} dV \int\limits_{\Delta E_g} dE \cdot \Sigma_t\,(r,E)\,\varphi\,(r,E)}{\int\limits_{fuelcell} dV \int\limits_{\Delta E_g} dE \cdot \varphi\,(r,E)} \tag{A.1}$$

  where $\varphi(r,E)$ is the fine mesh, multi-group flux solution for the fuel cell obtained from detailed auxiliary calculations performed e.g. with the lattice physics code PHOENIX [2]. ΔE_g is the energy width of the group g. The first integration is the homogenization procedure and the second integration is the energy averaging procedure known as

group collapsing. All lattice code calculations are conducted in this work by the steady state core simulators PRESTO or POLCA. MATSTAB reads the required data from the master files generated by these steady state codes (see Figure 2.2 on page 19).

- The time dependence of the delayed neutrons is characterized by 6 delayed groups.

A.1.1   Governing Equations for Neutron Kinetics

The general diffusion theory equation is derived from the equation of continuity which states, that the rate of change in number of neutrons is equal to the rate of production minus the rate of absorption minus the rate of leakage of neutrons within a volume of interest. See any reactor physics textbook for an in-depth explanation, e.g. [48].

$$\frac{1}{V}\frac{\partial \varphi}{\partial \tau} = source - \Sigma_{absorption}\varphi - \text{div}\mathbf{J} \tag{A.2}$$

The neutron leakage term is obtained by applying Fick's Law.

$$\mathbf{J} = -D\nabla\varphi \tag{A.3}$$

Inserting $\mathbf{J}$ in the equation of continuity, assuming that D is not a function of position gives

$$\frac{1}{V}\frac{\partial \varphi}{\partial \tau} = D\nabla^2\varphi - \Sigma_{absorption}\varphi + source \tag{A.4}$$

The two-group equations with more detailed absorption and production terms are:

Diffusion equation for the fast neutron flux

$$\frac{1}{V_1}\frac{\partial \varphi_1}{\partial \tau} = D_1\nabla^2\varphi_1 - (\Sigma_{a1} + \Sigma_r)\varphi_1 + (1-\beta)(\nu_1\Sigma_{f1}\varphi_1 + \nu_2\Sigma_{f2}\varphi_2) + \sum_d \lambda_d C_d \tag{A.5}$$

$$\tag{A.6}$$

Diffusion equation for the thermal neutron flux

$$\frac{1}{V_2}\frac{\partial \varphi_2}{\partial \tau} = D_2\nabla^2\varphi_2 - \Sigma_{a2}\varphi_2 + \Sigma_r\varphi_1 \tag{A.7}$$

Precursors of delayed neutrons for group d

$$\frac{\partial C_d}{\partial \tau} = \beta_d(\nu_1\Sigma_{f1}\varphi_1 + \nu_2\Sigma_{f2}\varphi_2) - \lambda_d C_d \tag{A.8}$$

A.1.2 Boundary Conditions

The core of a BWR is surrounded by the coolant which acts as a reflector for both fast and thermal neutrons. A reflector can significantly affect the characteristics of the neutron population within the core. It is therefore important to represent correctly the effects produced by a reflector. Fick's Law is not valid in the immediate vicinity of the surface of the core, so another approach has to be found. It would be possible to simply include the reflector as a part of the overall reactor. However, this way is computationally costly since fine meshes are required to represent the reflector in a finite-difference approximation. MATSTAB uses another common approach which overcomes this problem by excluding the reflector but, instead, applying appropriate boundary conditions at the core-reflector interfaces. The most general approach for the two-group approximation is to use a matrix albedo $\mathbf{a}$ defined at the surface of the core. The following equations originate from the model used in POLCA and are described in detail in [52].

$$\mathbf{J}^{return} = \mathbf{a} \cdot \mathbf{J}^{out} \tag{A.9}$$

$$\mathbf{a} = \begin{bmatrix} a_{11} & 0 \\ a_{21} & a_{22} \end{bmatrix}, \quad \mathbf{J} = \begin{bmatrix} J_1 \\ J_2 \end{bmatrix} \tag{A.10}$$

The values of $\mathbf{a_{ij}}$ are taken from the master file of the steady state code.

A.1.3 Node Integrated Balance Equations

The nodalization of the core leads to node averaged quantities, denoted with a bar.

$$\bar{\varphi}_1 = \frac{1}{h_x h_y h_z} \int_{\substack{volume \\ ofnode}} \varphi_1 dr \tag{A.11}$$

and

$$\frac{1}{V_1} \frac{\partial \bar{\varphi}_{1n}}{\partial \tau} = \frac{1}{h_x h_y h_z} \int_{\substack{volume \\ ofnode}} \nabla D_1 \nabla \varphi_1 dr - (\Sigma_{a1} + \Sigma_r) \bar{\varphi}_{1n}$$
$$+ (1 - \beta) (\nu_1 \Sigma_{f1} \bar{\varphi}_{1n} + \nu_2 \Sigma_{f2} \bar{\varphi}_{2n}) + \sum_d \lambda_d \bar{C}_d \tag{A.12}$$

for the fast neutron flux. By means of the divergence theorem, we can rewrite the volume integral as a surface integral

$$\frac{1}{h_x h_y h_z} \int_{\substack{volume \\ ofnode}} \nabla D_1 \nabla \varphi_1 dr = \frac{1}{h_x h_y h_z} \int_{\substack{surface \\ ofnode}} D_1 \nabla \varphi_1 dA = - \sum_{m=1}^{6} \frac{1}{h_{nm}} \mathbf{J}_{1,nm} \tag{A.13}$$

Where n is the number of the node and m is one of its neighbors. The node integrated balance equations for the node n therefore look as follows.

$$\frac{1}{V_1}\frac{d\bar{\varphi}_{1n}}{d\tau} = -\sum_{m=1}^{6}\frac{1}{h_{nm}}\mathbf{J}_{1,nm} - (\Sigma_{a1} + \Sigma_r)\bar{\varphi}_{1n} + (1-\beta)\left(\nu_1\Sigma_{f1}\bar{\varphi}_{1n} + \nu_2\Sigma_{f2}\bar{\varphi}_{2n}\right)$$
$$+ \sum_d \lambda_d\bar{C}_d \tag{A.14}$$

$$\frac{1}{V_2}\frac{d\bar{\varphi}_{2n}}{d\tau} = -\sum_{m=1}^{6}\frac{1}{h_{nm}}\mathbf{J}_{2,nm} - \Sigma_{a2}\bar{\varphi}_{2n} + \Sigma_r\bar{\varphi}_{1n} \tag{A.15}$$

$$\frac{d\bar{C}_{dn}}{d\tau} = \beta_d\left(\nu_1\Sigma_{f1}\bar{\varphi}_{1n} + \nu_2\Sigma_{f2}\bar{\varphi}_{2n}\right) - \lambda_d\bar{C}_{dn} \tag{A.16}$$

The expression relating the node interface net currents to the average fluxes of the adjacent nodes is

$$\frac{1}{h_{nm}}\mathbf{J}_{g,nm} = \mathbf{X}_{g,nm}\bar{\varphi}_{1,n} - \mathbf{Y}_{g,nm}\bar{\varphi}_{1,m} \tag{A.17}$$

where h_{nm} is the extension of node n in the nm direction. The complete derivation is found in [52],[48]. The coupling coefficients are given by

$$\mathbf{X}_{1,nm} = \frac{R_{nm}}{h_x^2}\sqrt{\tilde{D}_{1n}}\sqrt{\tilde{D}_{1m}}\,q_n\,s_n \tag{A.18}$$

$$\mathbf{Y}_{1,nm} = \frac{R_{nm}}{h_x^2}\sqrt{\tilde{D}_{1n}}\sqrt{\tilde{D}_{1m}}\,q_m\,s_m \tag{A.19}$$

$$\mathbf{X}_{2,nm} = \frac{R_{nm}}{h_x^2}\sqrt{\tilde{D}_{2n}}\sqrt{\tilde{D}_{2m}}\,q_n\,s_n\,r_{\infty n} \tag{A.20}$$

$$\mathbf{Y}_{2,nm} = \frac{R_{nm}}{h_x^2}\sqrt{\tilde{D}_{2n}}\sqrt{\tilde{D}_{2m}}\,q_m\,s_m\,r_{\infty m} \tag{A.21}$$

$$\mathbf{X}_{1,nr} = \frac{2}{h_{nr}^2}\frac{\tilde{D}_{1n}\tilde{D}_{1r}}{\tilde{D}_{1n}+\tilde{D}_{1r}}q_n s_n \tag{A.22}$$

$$\mathbf{Y}_{1,nr} = 0 \tag{A.23}$$

$$\mathbf{X}_{2,nr} = \frac{2}{h_{nr}^2}\left[\frac{\tilde{D}_{2n}\tilde{D}_{2r}}{\tilde{D}_{2n}+\tilde{D}_{2r}} - \frac{\frac{C_{21}}{r_{\infty n}}}{\left(\frac{1}{\tilde{D}_{1n}}+\frac{1}{\tilde{D}_{1r}}\right)\left(\frac{1}{\tilde{D}_{2n}}+\frac{1}{\tilde{D}_{2r}}\right)}\right]q_n s_n r_{\infty n} \tag{A.24}$$

$$\mathbf{Y}_{2,nr} = 0 \tag{A.25}$$

where

Node size ratios

$R_{nm} = 1$		, m points in x,y-direction
$R_{nm} = \frac{h_x^2}{h_z^2}$		, m points in z-direction
$R_{nr} = 0$		, m points to reflector
$r_\infty = \frac{\Sigma_r}{\Sigma_{a2}}$		

Infinite multiplication factor $k_\infty = \tilde{\beta}\frac{\nu_1\Sigma_{f1}+r_\infty\nu_2\Sigma_{f2}}{\Sigma_{a1}}$

$\tilde{\beta} = 1 - \beta + \Sigma_d\frac{\beta_d\lambda_d}{\lambda+\lambda_d}$

$\Lambda = \frac{D_1}{\Sigma_{a1}}$

Thermal diffusion length $L^2 = \frac{D_2}{\Sigma_{a2}}$

$\chi = \frac{L^2}{\Lambda}$

$l^2 = \frac{h_x^2}{2+\frac{h_x^2}{h_z^2}}$

$b_1^2 = \frac{1}{4}l^2\frac{k_\infty-1}{L^2+\Lambda}$

$b_2^2 = \frac{3}{4}l^2\frac{1+\chi}{L^2}$

$t_1 = 1 - \frac{1}{3}b_1^2$

$s_n = 1 + \frac{2}{3}b_1^2$

$t_2 = b_2 - c_p(b_2 - t_1)$

$\tilde{D}_g = D_g t_g$

$\tilde{D}_{1r} = \frac{h_{nr}}{4}\frac{1-a_{11}}{1+a_{11}}$

$\tilde{D}_{2r} = \frac{h_{nr}}{4}\frac{1-a_{22}}{1+a_{22}}$

$C_{21} = \frac{8}{h_{nr}}\frac{a21}{(1-a_{11})(1-a_{22})}$

$r_n = \frac{\phi_2}{\phi_1}$

$q_n = 1 + \frac{\chi}{1+\chi}\left(\frac{r}{r_\infty}-1\right)$

A.1.4   Prompt Jump Approximation

The time derivative of the fast and the thermal flux are both set to zero, which means that the left hand side of A.14 and A.15 are set to zero.

$$0 = -\left[\sum_{m=1}^{6}\mathbf{X}_{1,nm}+\Sigma_{a1}+\Sigma_r\right]\bar{\phi}_{1n}+\sum_{m=1}^{6}\mathbf{Y}_{1,nm}\bar{\phi}_{1m}$$
$$+ (1-\beta)(\nu_1\Sigma_{f1}\bar{\phi}_{1n}+\nu_2\Sigma_{f2}\bar{\phi}_{2n})-\sum_d\lambda_d\bar{C}_{dn} \tag{A.26}$$

$$0 = -\left[\sum_{m=1}^{6}\mathbf{X}_{2,nm}-\Sigma_r\right]\bar{\phi}_{1n}+\sum_{m=1}^{6}\mathbf{Y}_{2,nm}\bar{\phi}_{1m}-\Sigma_{a2}\bar{\phi}_{2n} \tag{A.27}$$

The prompt jump approximation is valid, if the life time of a neutron is much smaller than the studied phenomena. Physically it is an immediate adaption of the neutron flux to perturbations.

The life time of some precursors is much closer to the time a density wave needs to pass the reactor than the neutron life time and, therefore, significant. The time derivative of the precursors may not be set to zero. Nevertheless it is possible to simplify equation A.16 without much loss in accuracy.

Equation 2.25 describes the time dependence of a state variable. For the variable $\bar{C}_d(\tau)$ it reads as follows.

$$\bar{C}_{dn}(\tau) = \bar{c}_{dn}e^{\lambda\tau} \quad ,d = 1,\dots,6 \tag{A.28}$$

Where $\bar{c}_{dn}$ is a scalar and not time dependent. Equation A.16 may now be written as follows.

$$\frac{d\bar{c}_{dn}e^{\lambda\tau}}{d\tau} = \beta_d(\nu_1\Sigma_{f1}\bar{\varphi}_{1n} + \nu_2\Sigma_{f2}\bar{\varphi}_{2n}) - \lambda_d\bar{C}_{dn} \tag{A.29}$$

It is now possible to carry out the derivation with respect to time. This transforms the differential equation into a algebraic equation.

$$\lambda\bar{C}_{dn} = \beta_d(\nu_1\Sigma_{f1}\bar{\varphi}_{1n} + \nu_2\Sigma_{f2}\bar{\varphi}_{2n}) - \lambda_d\bar{C}_{dn} \tag{A.30}$$

$\bar{C}_{dn}$ is depending on λ which actually is unknown. Therefore the starting guess of λ is used to calculate $\bar{C}_{dn}$. This simplification is good enough, as long as the starting guess for λ is reasonable. The draw back is however, that λ is complex and therefore the matrix **A** becomes complex too. It remains to mention that this equation is used for the POLCA model as well as for the RAMONA model.

Inserting A.31 into A.26 yields

$$\bar{C}_{dn} = \frac{\beta_d}{\lambda - \lambda_d}(\nu_1\Sigma_{f1}\bar{\varphi}_{1n} + \nu_2\Sigma_{f2}\bar{\varphi}_{2n}) \tag{A.31}$$

Inserting A.31 into A.26 yields

$$0 = -\left[\sum_{m=1}^{6} \mathbf{X}_{1,nm} + \Sigma_{a1} + \Sigma_r\right]\bar{\varphi}_{1n} + \sum_{m=1}^{6} \mathbf{Y}_{1,nm}\bar{\varphi}_{1m} \\ + \tilde{\beta}(\nu_1\Sigma_{f1}\bar{\varphi}_{1n} + \nu_2\Sigma_{f2}\bar{\varphi}_{2n}) \tag{A.32}$$

where

$$\tilde{\beta} = 1 - \beta + \sum_d \frac{\beta_d\lambda_d}{\lambda + \lambda_d} \tag{A.33}$$

Solving A.27 for $\overline{\varphi}_{2n}$ yields

$$\overline{\varphi}_{2n} = \frac{\left[\Sigma_r - \sum_{m=1}^{6} \mathbf{X}_{2,nm}\right]}{\Sigma_{a2}} \overline{\varphi}_{1n} + \frac{\sum_{m=1}^{6} \mathbf{Y}_{2,nm}}{\Sigma_{a2}} \overline{\varphi}_{1m}. \tag{A.34}$$

Inserting the solution into A.32 leads to

$$0 = -\left[\sum_{m=1}^{6} \mathbf{X}_{1,nm} + \Sigma_{a1} + \Sigma_r - \tilde{\beta} \nu_1 \Sigma_{f1} - \tilde{\beta} \nu_2 \Sigma_{f2} \frac{\left[\Sigma_r - \sum_{m=1}^{6} \mathbf{X}_{2,nm}\right]}{\Sigma_{a2}}\right] \overline{\varphi}_{1n}$$
$$+ \left[\sum_{m=1}^{6} \mathbf{Y}_{1,nm} + \tilde{\beta} \nu_2 \Sigma_{f2} \frac{\sum_{m=1}^{6} \mathbf{Y}_{2,nm}}{\Sigma_{a2}}\right] \overline{\varphi}_{1m} \tag{A.35}$$

and

$$\overline{\varphi}_{1n} = \frac{\sum_{m=1}^{6} \left(\mathbf{Y}_{1,nm} + \tilde{\beta} \frac{\nu_2 \Sigma_{f2}}{\Sigma_{a2}} \mathbf{Y}_{2,nm}\right) \overline{\varphi}_{1m}}{\sum_{m=1}^{6} \left(\mathbf{X}_{1,nm} + \tilde{\beta} \frac{\nu_2 \Sigma_{f2}}{\Sigma_{a2}} \mathbf{X}_{2,nm}\right) - \Sigma_{a1} (k_\infty - 1)} \equiv \sum_{m=1}^{6} \mathbf{A}_{nm} \overline{\varphi}_{1m} \tag{A.36}$$

A.1.5   Linearization

Linearizing the neutronics means to linearize A.36.

$$\Delta \overline{\varphi}_{1n} = \frac{\partial \overline{\varphi}_{1n}}{\partial \overline{\varphi}_{1m}} \Delta \overline{\varphi}_{1m} + \frac{\partial \overline{\varphi}_{1n}}{\partial \alpha} \Delta \alpha + \frac{\partial \overline{\varphi}_{1n}}{\partial t} \Delta t$$
$$= \sum_{m=1}^{6} \mathbf{A}_{nm} \Delta \overline{\varphi}_{1m} + \sum_{m=1}^{6} \frac{[\mathbf{A}_{nm}(\alpha + \Delta \alpha) - \mathbf{A}_{nm}(\alpha)] \overline{\varphi}_{1m}}{\Delta \alpha} \Delta \alpha \tag{A.37}$$
$$+ \sum_{m=1}^{6} \frac{[\mathbf{A}_{nm}(t + \Delta t) - \mathbf{A}_{nm}(t)] \overline{\varphi}_{1m}}{\Delta t} \Delta t$$

To calculate A.37 one needs to know $D_1, D_2, \Sigma_{a1}, \Sigma_{a2}, \Sigma_r, \nu_1 \Sigma_{f1}, \nu_2 \Sigma_{f2}, \nu_1$ and ν_2 for $\alpha, \alpha + \Delta \alpha, t$ and for $t + \Delta t$. These values are calculated with the help of the tables generated for the steady state core simulator. The tables are stored in the master file, and therefore available without problems. Therefore the linearization with respect to the void and temperature dependence is done numerically.

A.1.6   Power Generation

MATSTAB takes into account the fact, that the fission energy is deposited as thermal energy both inside the fuel pellet where the fission takes place and outside the pellet due to neutron slowing down and gamma ray attenuation.

The total power generation rate in the fuel is

$$\overline{q}''' = K \left(1 - H \left(0, \infty\right)\right) \left(\Sigma_{f1} \overline{\varphi}_{1n} + \Sigma_{f2} \overline{\varphi}_{2n}\right) \tag{A.38}$$

where $H(0, \infty) = 0.07$ and $K = 3.2 \cdot 10^{11}$ Joule/Fission.

The thermal flux in A.38 is eliminated with the help of A.34.

$$\bar{q}''' = K(1 - H(0, \infty)) \left(\left[\Sigma_{f1} + \frac{\Sigma_{f2}}{\Sigma_{a2}} \left(\Sigma_r - \sum_{m=1}^{6} \mathbf{X}_{2,nm} \right) \right] \bar{\varphi}_{1n} + \frac{\Sigma_{f2}}{\Sigma_{a2}} \sum_{m=1}^{6} \mathbf{Y}_{2,nm} \bar{\varphi}_{1m} \right)$$

$$\equiv \mathbf{A}_{qn} \bar{\varphi}_{1n} + \mathbf{A}_{qm} \bar{\varphi}_{1m} \tag{A.39}$$

A.1.7   Linearization

The linearization of A.39 reads as follows.

$$\Delta \bar{q}''' = \frac{\partial \bar{q}'''}{\partial \bar{\varphi}_{1n}} \Delta \bar{\varphi}_{1n} + \frac{\partial \bar{q}'''}{\partial \bar{\varphi}_{1m}} \Delta \bar{\varphi}_{1m} + \frac{\partial \bar{q}'''}{\partial \alpha} \Delta \alpha + \frac{\partial \bar{q}'''}{\partial t} \Delta t$$

$$\approx \mathbf{A}_{qn} \Delta \bar{\varphi}_{1n} + \mathbf{A}_{qm} \Delta \bar{\varphi}_{1m}$$

$$+ \frac{\mathbf{A}_{qn}(\alpha + \delta \alpha) - \mathbf{A}_{qn}(\alpha)}{\delta \alpha} \bar{\varphi}_{1n} \Delta \alpha$$

$$+ \frac{\mathbf{A}_{qm}(\alpha + \delta \alpha) - \mathbf{A}_{qm}(\alpha)}{\delta \alpha} \bar{\varphi}_{1m} \Delta \alpha \tag{A.40}$$

$$+ \frac{\mathbf{A}_{qn}(t + \delta t) - \mathbf{A}_{qn}(t)}{\delta t} \bar{\varphi}_{1n} \Delta t$$

$$+ \frac{\mathbf{A}_{qm}(t + \delta t) - \mathbf{A}_{qm}(t)}{\delta t} \bar{\varphi}_{1m} \Delta t$$

A.2   Modeling of Thermal Conduction

Associated with each neutronic node is an average fuel pin for which the thermal energy source and heat conduction are calculated. The calculated average fuel temperature feeds back into the neutronics (Doppler effect) and the calculated heat flux from the cladding surface enters the hydraulics calculations.

A.2.1   Field Equation of Thermal Conduction

The thermal energy storage and conduction in the fuel pins, consisting of the fuel pellets, of the gas gap between pellet and cladding and of the fuel cladding is modeled with the following assumptions.

- Fuel and cladding are rigid, retaining their cylindrical geometries. Possible variations in time of the gas gap width can be taken into account by a temperature dependent gap conductance.

- The volumetric heat generation q_f''' is uniformly distributed over the fuel pellet cross section. Gamma heat generation in the gas gap and the cladding is ignored.

- Axial and azimuthal conduction is negligible

- The thermal properties like heat capacity, conductivity etc. can be represented with the correlations stated below.

The general form of the heat conduction equation

$$\rho c \frac{\partial t}{\partial \tau} = \nabla\left(k\nabla t\right) + q''' \tag{A.41}$$

is formulated for the fuel and for the cladding separately. After neglecting axial and azimuthal conduction the equation looks as follows.

Pellet:

$$(\rho c)_f \frac{\partial t_f}{\partial \tau} = \frac{1}{r}\frac{\partial}{\partial r}\left(r k_f \frac{\partial t_f}{\partial r}\right) + q_f''' \quad ,0 \leq r < R_f \quad ,\tau > 0 \tag{A.42}$$

with the boundary conditions:

$$\left.\frac{\partial t_f}{\partial r}\right|_{r=0} = 0 \qquad\qquad\qquad \text{,for all } \tau$$

$$\left. k_f \frac{\partial t_f}{\partial r}\right|_{r=R_f} = \frac{k_{gp}}{\delta}\left[t_c\left(R_{ci}\right) - t_f\left(R_f\right)\right] \qquad \text{,for all } \tau \tag{A.43}$$

Cladding:

$$(\rho c)_c \frac{\partial t_c}{\partial \tau} = \frac{\partial}{\partial r}\left(k_c \frac{\partial t_c}{\partial r}\right) \quad , r = R_{ci} < r < R_{co}, \tau > 0 \qquad (A.44)$$

with the boundary conditions:

$$
\begin{aligned}
k_c \frac{\partial t_c}{\partial r} &= \frac{k_{gp}}{\delta}\left[t_c\left(R_{ci}\right) - t_f\left(R_f\right)\right] \quad , r = R_{ci}, \quad \text{for all } \tau \\
-k_c \frac{\partial t_c}{\partial r} &= \overline{h}_c\left[t_c\left(R_{co}\right) - t_{fl}\right] \qquad , r = R_{co} \quad \text{for all } \tau
\end{aligned}
\qquad (A.45)
$$

Following correlations are implemented:

volumetric heat capacity of the fuel

$$(\rho c)_f = c_1 + c_2 t_f + c_3 t_f^2 + c_4 t_f^3 + c_5 t_f^4 \qquad (A.46)$$

volumetric heat capacity of the cladding

$$(\rho c)_c = c_7 \qquad (A.47)$$

thermal conductivity for the fuel

$$k_f = \frac{c_8}{1 + c_9 \cdot t_f} \qquad (A.48)$$

thermal conductivity for the cladding

$$k_c = c_{10} \qquad (A.49)$$

thermal conductance of the gas gap

$$\frac{k_{gp}}{\delta} = \min\left\{c_{11} + c_{12} \cdot \overline{t}_f + c_{13} \cdot \overline{t}_f^2, c_{14}\right\} \qquad (A.50)$$

$$\text{with} \quad \overline{t}_f = \frac{1}{M_f}\sum_{i=1}^{M_f} t_{f,i} \qquad (A.51)$$

convective heat transfer for forced convection (Dittus Boelter)

$$\overline{h}_{c,forced\ convection} = \frac{k_l}{d_h} N_{Nu} \qquad (A.52)$$

convective heat transfer for nucleate boiling (Jens-Lotte)

$$\overline{h}_{c,nucleate\ boiling} = \frac{q''_{NB}}{t_W - t_{sat}} \qquad (A.53)$$
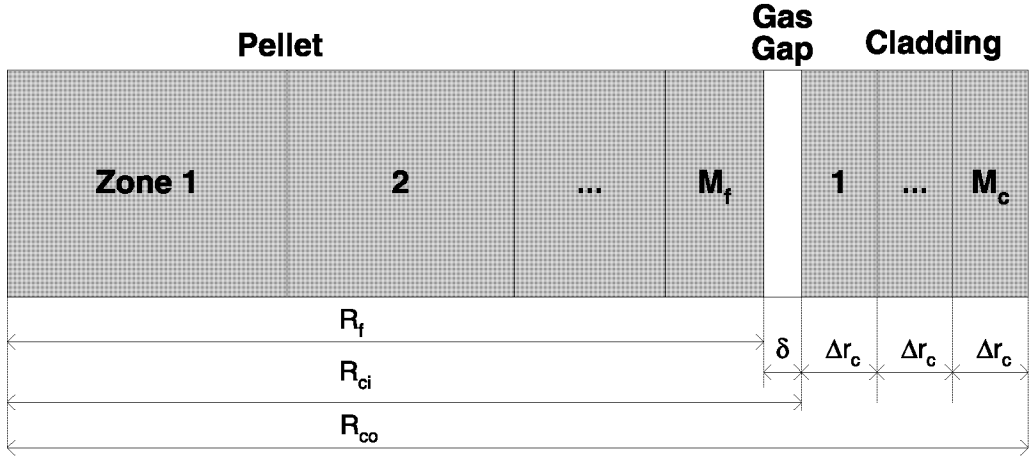
Figure A.1: Nodalization Scheme for the Heat Conduction in the Fuel Rod

A.2.2   Discretization

The fuel pin is radially divided into M_f fuel zones, a gas gap and M_c cladding zones. Fuel zones have the same volume, cladding zones the same thickness.

After long calculations (done explicitly in [114]) one derives

Pellet:

$$\frac{d\bar{t}_{f,1}}{d\tau} = \frac{4M_f}{R_f^2(\rho c)_f} k_f(t_{f,2}) \frac{\bar{t}_{f,2} - \bar{t}_{f,1}}{\sqrt{2}} + \frac{\bar{q}_f'''}{(\rho c)_f} \tag{A.54}$$

$$\frac{d\bar{t}_{f,i}}{d\tau} = \frac{4M_f}{R_f^2(\rho c)_f} \left[k_f(t_{f,i}) \frac{\bar{t}_{f,i-1} - \bar{t}_{f,i}}{\sqrt{\frac{i}{i-1}} - \sqrt{\frac{i-2}{i-1}}} \right.$$
$$\left. - k_f(t_{f,i+1}) \frac{\bar{t}_{f,i} - \bar{t}_{f,i+1}}{\sqrt{\frac{i+1}{i}} - \sqrt{\frac{i-1}{i}}} \right] + \frac{\bar{q}_f'''}{(\rho c)_f} \tag{A.55}$$

$$i = 2, \ldots, M_f - 1$$

$$\frac{d\bar{t}_{f,M_f}}{d\tau} = \frac{4M_f}{R_f^2(\rho c)_f} \left[k_f(t_{f,M_f}) \frac{\bar{t}_{f,M_f-1} - \bar{t}_{f,M_f}}{\sqrt{\frac{M_f}{M_f-1}} - \sqrt{\frac{M_f-2}{M_f-1}}} \right.$$
$$\left. - \frac{R_f(\bar{t}_{f,M_f} - \bar{t}_{c,1})}{\frac{R_f(1-\sqrt{1-\frac{1}{M_f}})}{k_f(t_f(R_f))} + \frac{2\delta}{k_{gp}} + \frac{\Delta r_c}{k_c}} \right] + \frac{\bar{q}_f'''}{(\rho c)_f} \tag{A.56}$$

with the pellet surface temperature

$$t_f(R_f) = \frac{\frac{R_f\left(1-\sqrt{1-\frac{1}{M_f}}\right)}{k_f(t_f(R_f))}\left(\bar{t}_{c,1}-\bar{t}_{f,M_f}\right)}{\frac{R_f\left(1-\sqrt{1-\frac{1}{M_f}}\right)}{k_f(t_f(R_f))}+\frac{2\delta}{k_{gp}}+\frac{\Delta r_c}{k_c}}+\bar{t}_{f,M_f} \qquad (A.57)$$

Cladding:

$$\frac{dt_{c,1}}{d\tau} = k_c\frac{\bar{t}_{c,2}-\bar{t}_{c,1}}{(\rho c)_c(\Delta r_c)^2}+\frac{\frac{\bar{t}_{f,M_f}-\bar{t}_{c,1}}{(\rho c)_c\Delta r_c}}{\frac{R_f\left(1-\sqrt{1-\frac{1}{M_f}}\right)}{k_f(t_f(R_f))}+\frac{\delta}{k_{gp}}+\frac{\Delta r_c}{2k_c}} \qquad (A.58)$$

$$\frac{d\bar{t}_{c,j}}{d\tau} = k_c\frac{\bar{t}_{c,j+1}-2\bar{t}_{c,j}+\bar{t}_{c,j-1}}{(\Delta r_c)^2(\rho c)_c} \qquad (A.59)$$

$$j = 2,\dots,M_c-1$$

$$\frac{d\bar{t}_{c,M_c}}{d\tau} = -\frac{\bar{h}_c(t_w-t_{fl})}{(\rho c)_c\Delta r_c}-k_c\frac{\bar{t}_{c,M_c}-\bar{t}_{c,M_c-1}}{(\rho c)_c(\Delta r_c)^2} \qquad (A.60)$$

A.2.3   Linearization

The effort to linearize equations A.54-A.56, A.58 -A.60 analytically is not worth the benefit in time. Therefore the equations are linearized numerically with respect to $t_{f,i}, t_{c,i}, q'''$ and the system pressure P. However, these equations are much more detailed than effectively necessary. They are part of the legacy of RAMONA. A simpler set of equations as used in other codes as NUFREQ [79] could be solved analytically and would tidy up this part of MATSTAB. Even though the six differential equations for the fuel contribute quite a large number of equations the system matrix $\mathbf{A}_s$, they do not lead to any numerical difficulties because of their weak spatial coupling.

The implemented equations read as follows.

$$\Delta t_{f,i} = \sum_{j=1}^{M_f}\frac{\partial t_{f,i}}{\partial t_{f,j}}\Delta t_{f,j} + \sum_{j=1}^{M_c}\frac{\partial t_{f,i}}{\partial t_{c,j}}\Delta t_{c,j} + \frac{\partial t_{f,i}}{\partial \bar{q}_f'''}\Delta\bar{q}_f''' + \frac{\partial t_{f,i}}{\partial P}\Delta P \qquad (A.61)$$

$$\Delta t_{c,i} = \sum_{j=1}^{M_f}\frac{\partial t_{c,i}}{\partial t_{f,j}}\Delta t_{f,j} + \sum_{j=1}^{M_c}\frac{\partial t_{c,i}}{\partial t_{c,j}}\Delta t_{c,j} + \frac{\partial t_{c,i}}{\partial \bar{q}_f'''}\Delta\bar{q}_f''' + \frac{\partial t_{c,i}}{\partial P}\Delta P \qquad (A.62)$$

A.3 Modeling of Thermal-Hydraulics

The thermal-hydraulic model of MATSTAB (RAMONA) is a

- four-equation
- non-homogeneous
- non-equilibrium
- one-dimensional
- two-phase flow

model with constitutive equations for thermodynamic state variables. Thermal non-equilibrium between the phases is accounted for by allowing the liquid in a two-phase mixture to depart from saturated conditions, while the vapor is assumed to be at saturation. Hydrodynamic non-equilibrium, i.e. un-equal velocities of the two phases, is introduced via a slip correlation.

The following assumptions are made

- MATSTAB describes the coolant flows in the pressure vessel, using a single recirculation loop and a single steam line representative for all steam lines and recirculation loops respectively.

- The models allow for the liquid phase to be sub-cooled or saturated, but they restrict the vapor to saturation conditions.

- The flow parameters are assumed to be uniform over a cross section

- Averages of products are set equal to products of averages

- The spatial variation of pressure P is ignored for all thermo-physical property calculations and in the mass and energy balances, but in the momentum balance the axial pressure variation is accounted for.

- Flow channels in the core, downcomer and recirculation loop are of constant cross-section A_c.

Thermodynamic variables are determined at the saturated state corresponding to the system pressure (except the properties of sub-cooled water), and they are calculated as rational functions of pressure A.71 through A.80. The compressibility and thermal expansion of the liquid are approximated by that of saturated liquid. The following description of the TH-model is very brief, because no major changes to the RAMONA model are introduced. The interested user may consult [114] for a complete derivation.

A.3.1   Governing Equations for the Thermal-Hydraulics

The thermal-hydraulic models in MATSTAB are based on the following four conservation equations [45] for mixture momentum, vapor mass, liquid mass and mixture energy.

Mixture momentum balance

The one-dimensional, area-averaged mixture momentum balance is

$$\frac{\partial G_m}{\partial \tau} + \frac{\partial}{\partial z}\left[\alpha\rho_g w_g^2 + (1-\alpha)\rho_l w_l^2\right] = -\frac{\partial P}{\partial z} - g_z\rho_m - f_l\Phi_l^2\frac{G_m\left|G_m\right|}{2\rho_l d_h} \qquad \text{(A.63)}$$

where the mixture mass flux G_m in the axial direction is

$$G_m = \langle\alpha\rho_g w_g + (1-\alpha)\rho_l w_l\rangle \qquad \text{(A.64)}$$

The symbols f_l, Φ_l^2 and d_h designate the single-phase Darcy friction factor, computed as if the mixture were flowing as a liquid, the two phase flow friction multiplier and the hydraulic diameter of the channel, wetted by the fluid. The symbol g_z is the gravitational acceleration component in the negative z-direction.

Phasic mass balances for saturated vapor and liquid

The phasic mass balances

$$\frac{\partial}{\partial \tau}(\alpha\rho_g) + \nabla(\rho_g j_g) = \Gamma_V \qquad \text{(A.65)}$$

$$\frac{\partial}{\partial \tau}[(1-\alpha)\rho_l] + \nabla(\rho_l j_l) = -\Gamma_V \qquad \text{(A.66)}$$

are used in the form of the mixture volumetric flux divergence.

$$\begin{aligned}
\nabla j_m = \nabla j_g + \nabla j_l &= \nabla(\alpha w_g) + \nabla((1-\alpha)w_l) \\
&= \frac{\rho_l - \rho_g}{\rho_l\rho_g}\Gamma_V - \left[\frac{\alpha}{\rho_g}\frac{D_g\rho_g}{D\tau} + \frac{1-\alpha}{\rho_l}\frac{D_l\rho_l}{D\tau}\right]
\end{aligned} \qquad \text{(A.67)}$$

where $\frac{D_k}{D\tau}$ is the substantial derivative $\frac{\partial}{\partial \tau} + w_k\frac{\partial}{\partial z}$, k = l,g

Mixture energy conservation

$$\frac{\partial}{\partial \tau}\left[\alpha\rho_g u_g + (1-\alpha)\rho_l u_l\right] + \frac{\partial}{\partial z}\left[\alpha\rho_g h_g w_g + (1-\alpha)\rho_l h_l w_l\right] = \frac{q_w'}{A} + (1-\alpha)q_l''' \qquad \text{(A.68)}$$

A.3.2 Differential Equations

Pressure

As stated in the assumptions above, local pressure differences and acoustical effects are disregarded. A single system pressure P_{syst} is defined

$$\langle P \rangle_{syst} = \frac{1}{V_1 + V_2} \int_{V_1 + V_2} P \, dV \tag{A.69}$$

as the pressure, averaged over the volume V_1 of liquid and the volume V_2 of two phase mixture and pure vapor, as shown in figure A.2.

The time rate of change of $\langle P \rangle_{syst}$ is computed by integrating the liquid part of A.67 over V_1 and the two phase part of A.67 over V_2. In the resultant equations, one replaces the volume integrals of ∇j_m by surface integrals and recognizes the continuity of the volumetric flux j at all locations of flow discontinuity and at moving interfaces. By adding up the two equations and solving for the time-derivative $d \frac{\langle P \rangle_{syst}}{d\tau}$, one reaches after tedious calculations, done explicitly in [114] pages 125ff.

$$\frac{d \langle P \rangle_{syst}}{d\tau} = \frac{(Aj)_{FW} + (Aj)_{SL} + \int_{V_2} \frac{\rho_l - \rho_g}{\rho_l \rho_g} \Gamma_V dV}{\int_{V_1+V_2} \left[\alpha \frac{\rho_g'}{\rho_g} + (1 - \alpha) \frac{\rho_l'}{\rho_l} \right]} \tag{A.70}$$

where $\rho_l' = \frac{\partial}{\partial P} \rho_l$ and $(Aj)_{FW}$ is the contribution to pressure rise from the feed-water injection. $(Aj)_{SL}$ is the vapor volumetric flow rate entering the steam line, tending thereby to reduce the pressure change rate. The last term accounts for the effects of phase change.

The thermal properties of the coolant $t_{sat}, \rho_f, \rho_l, \rho_g, \rho_m, h_{fg}, c_{p,l}, u_g, u_l, h_g$ and h_l are fitted as functions in $\langle P \rangle_{syst}$.

$$t_{sat}(P) = \sum_{i=0}^{i=5} a_i P^i \Big/ \sum_{i=0}^{i=5} b_i P^i \tag{A.71}$$

$$\rho_f(P) = \sum_{i=0}^{i=4} a_i t_{sat}^i \Big/ \sum_{i=0}^{i=3} b_i t_{sat}^i \tag{A.72}$$

$$\rho_l(P) = \rho_f + \sum_{i=0}^{i=2} a_i P^i (t_l - t_{sat}) \tag{A.73}$$

$$\rho_g(P) = \sum_{i=0}^{i=5} a_i t_{sat}^i \Big/ \sum_{i=0}^{i=3} b_i t_{sat}^i \tag{A.74}$$

$$\rho_m(P) = \alpha \rho_g + (1 - \alpha) \rho_l \tag{A.75}$$

$$h_{fg}(P) = \sum_{i=0}^{i=3} a_i t_{sat}^i \Big/ \sum_{i=0}^{i=4} b_i t_{sat}^i \tag{A.76}$$
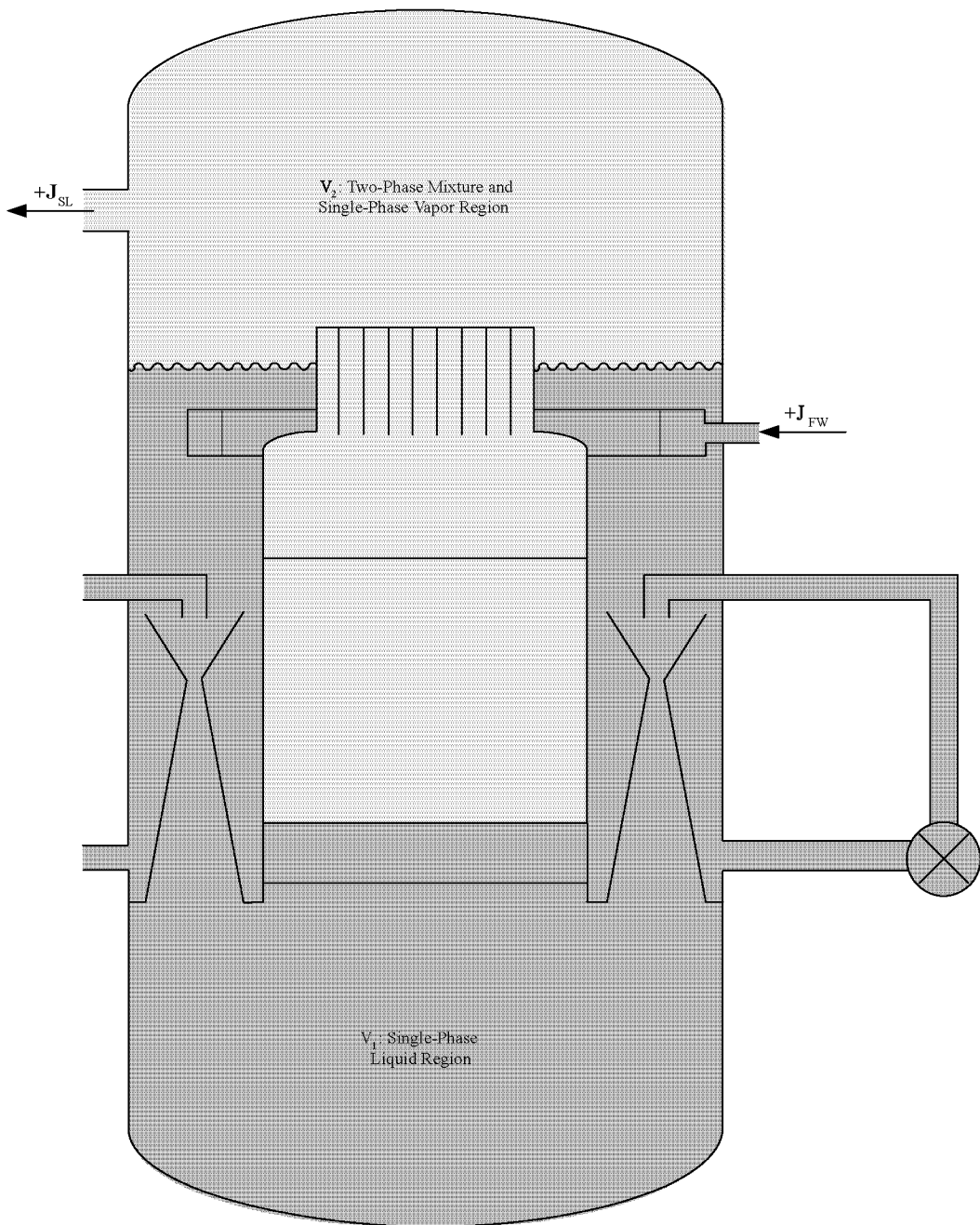
Figure A.2: Integration Regions for System Pressure

$$c_{p,l}(\text{P}) = \sum_{i=0}^{i=4} a_i t_{sat}^i \bigg/ \sum_{i=0}^{i=3} b_i t_{sat}^i \tag{A.77}$$

$$u_g(\text{P}) = h_{fg} + \text{P}(1/\rho_f - 1/\rho_g) + c_{p,l}(t_{sat} - t_{sat}^0) \tag{A.78}$$

$$u_l(\text{P}) = c_{p,l}(t_l - t_{sat}^0)h_g \qquad\qquad = u_g + \text{P}/\rho_g \tag{A.79}$$

$$h_l = u_l + \text{P}/\rho_l \tag{A.80}$$

As a result one can eliminate the implicit pressure dependence stemming from the properties in the momentum balance A.63 and decouple it form the mass and energy balances.

Closed-Contour Momentum Balance

To obtain the closed contour momentum balance for a typical contour ζ_1 in figure 3.3 on page 27 through the j-th core flow channel, MATSTAB divides the contour into N_s straight segments of constant flow cross section A_i and length L_i. We denote the segment average of the ith segment by

$$< \cdot >_i = \frac{1}{\text{L}_i} \int_0^{\text{L}_i} \cdot \, dz \tag{A.81}$$

A typical segment is shown in figure A.3
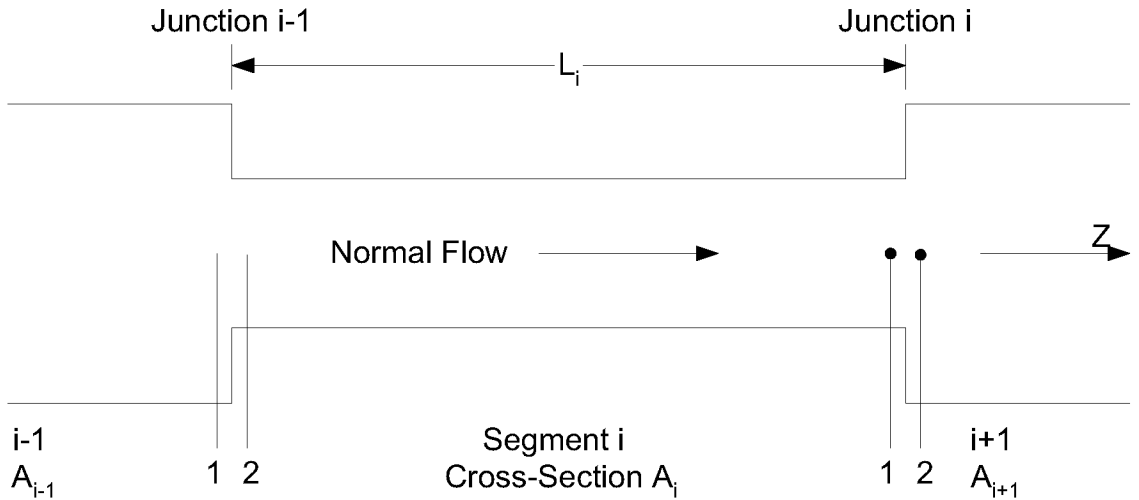
Figure A.3: Notations for Contour Integration of the Momentum Balance

By integrating the momentum balance equation A.63 separately for each one of the N_s segments in the jth contour through the jth core channel, one obtains N_s segment-averaged momentum balances.

$$L_i \frac{d <G_m>_i}{d\tau} = \left\{ P + \left[\alpha \rho_g w_g^2 + (1-\alpha) \rho_l w_l^2 \right] \right\}_{i-1,2} - \left\{ P + \left[\alpha \rho_g w_g^2 + (1-\alpha) \rho_l w_l^2 \right] \right\}_{i,1}$$
$$- g_{z,i} L_i < \rho_m >_i - \frac{1}{2 d_{h,i}} \int_0^{L_i} \frac{f_l \Phi_l^2}{\rho_l} G_m |G_m| dz$$

(A.82)

Next, one adds up the N_s equations for the jth flow contour to obtain a single, ordinary differential equation for the time rate of change of momentum along the closed contour with index j.

$$\frac{d}{d\tau} M_j \equiv \frac{d}{d\tau} \sum_{i=1}^{N_s} L_i \langle G_m \rangle = \sum_{i=1}^{N_s} \Delta \left\{ P + w_g G_g + w_l G_l \right\}_j$$
$$- \left\{ \sum_{i=1}^{N_s} g_{z,i} \langle \rho_m \rangle_i L_i + \frac{1}{2} \sum_{i=1}^{N_s} + \frac{1}{d_{h,i}} \int_0^{L_i} \frac{f_l \Phi_l^2}{\rho_l} G_m |G_m| dz \right\}_j$$

(A.83)

The pressure differences across the junction with index i (Figure. A.3) are eliminated with the aid of the jump condition given by

$$P_{i,1} + \frac{1}{2} \left[G_l w_l + G_g w_g \right]_1 = P_{i,2} + \frac{1}{2} \left[G_l w_l + G_g w_g \right]_2 + \xi_{12} \frac{1}{2} \left[G_l w_l + G_g w_g \right]_{A_{\min}}$$ (A.84)

and therefore

$$\left\{ P + w_g G_g + w_l G_l \right\}_j = \frac{1}{2} \left\{ \left[w_g G_g + w_l G_l \right]_2 \right.$$
$$\left. - \left[w_g G_g + w_l G_l \right]_1 - \xi_{12} \left[w_g G_g + w_l G_l \right]_{A_{min}} \right\}_j$$

(A.85)

A.85 applies to all junctions, except across the mixing throat in the jet pump designated by i=JT, there

$$\Delta \left\{ P + w_l G_l \right\}_{JT} = \Delta P_{JT}$$ (A.86)

A.83 can now be written as

$$\frac{d M_j}{d\tau} = \Delta P_{JT} - \sum_{i=1}^{N_s} \left\{ g_{z,i} \langle \rho_m \rangle L_i + \frac{1}{2 d_{h,i}} \int_0^{L_i} \frac{f_l \Phi_l^2}{\rho_l} G_m |G_m| dz \right\}_j$$
$$+ \frac{1}{2} \sum_{\substack{i=1 \\ i \neq JT}}^{N_s} \left\{ \left[w_g G_g + w_l G_l \right]_2 - \left[w_g G_g + w_l G_l \right]_1 \left[1 + \left(\frac{A_1}{A_{\min}} \right)^2 \xi_{12} \right] \right\}_j$$

(A.87)

The four summands are the pump head, the gravitational head, the frictional pressure loss and the sum of the singular pressure losses (area changes, spacers) along the path.

Mixture Energy

Integrating A.68 over the cell volume V_k and introducing

$$u_m \rho_m = (1 - \alpha) \rho_l u_l + \alpha \rho_g u_g \tag{A.88}$$

leads to

$$
\begin{aligned}
\frac{d \langle u_m \rho_m \rangle_k}{d\tau} &= (h_g W_g + h_l W_l)_{k-1} - (h_g W_g + h_l W_l)_k \\
&\quad + \left[\langle q'_w \rangle_k + \langle A (1 - \alpha) q'''_l \rangle_k \right] \frac{V_k}{A_k}
\end{aligned} \tag{A.89}
$$

Steam Mass

By integrating A.65 over the k-th computational cell, assuming a uniform vapor density and using the divergence theorem one obtains

$$\frac{d (m_g)_k}{d\tau} = \langle \Gamma_V \rangle_k \Delta V + (W_g)_{k-1} - (W_g)_k \tag{A.90}$$

A.3.3 Algebraic Equations

Mixture Volumetric Flow

The integral of A.67 over the coolant volume in the vessel yields

$$A_j (z) \, j_{m,j} (z) = A \left(z^+_{core\ inlet} \right) j_{m,j} \left(z^+_{core\ inlet} \right) + \Phi_j (z) \tag{A.91}$$

with

$$z^+_{core\ inlet} = \lim_{\varepsilon \to 0} (z_{core\ inlet} + \varepsilon) \tag{A.92}$$

and the volume expansion

$$\Phi_j (z) = \int\limits_{z_{core\ inlet}}^{z} A_j \left[\frac{\rho_l - \rho_g}{\rho_l \rho_g} \Gamma_V - \frac{\alpha}{\rho_g} \frac{D_g \rho_g}{D_\tau} - \frac{(1 - \alpha)}{\rho_l} \frac{D_l \rho_l}{D_\tau} \right]_j dz \tag{A.93}$$

and in the finite difference approximation

$$\Phi_j = V_j \Gamma_v \frac{\rho_l - \rho_g}{\rho_l \rho_g} + W_{g,k-1} \left(\frac{1}{\rho_{g,k}} - \frac{1}{\rho_{g,k-1}} \right) + W_{l,k-1} \left(\frac{1}{\rho_{l,k}} - \frac{1}{\rho_{l,k-1}} \right) \tag{A.94}$$

Slip

MATSTAB treats non-homogeneous two-phase flow, i.e. unequal velocities of the phases with a slip correlation.

$$w_g = S w_l + w^0 \tag{A.95}$$

This relates the vapor velocity w_g with the liquid velocity w_l, using the Bankoff-Malnes correlation.

$$
\begin{aligned}
S &= \frac{1-\alpha}{c_1 - \alpha} & \alpha \leq c_1 - c_{cut} \\
S &= c_2 - c_3(\alpha - c_4) & c_{max} > \alpha > c_1 - c_{cut} \\
S &= c_{max} & \alpha \geq c_{max}
\end{aligned}
\tag{A.96}
$$

with the vapor void fraction

$$\alpha = \frac{m_g}{\rho_g \left(\langle P \rangle_{syst} \right) \Delta V} \tag{A.97}$$

Phasic Velocity

From A.67 and A.95 one derives the phasic velocities

$$w_g = \frac{S j_m + (1-\alpha) w^0}{1 + \alpha (S-1)} \tag{A.98}$$

$$w_l = \frac{j_m - \alpha w^0}{1 + \alpha (S-1)} \tag{A.99}$$

Mass Flow Rate

$$W_g = A \rho_g \alpha_g w_g \tag{A.100}$$

$$W_l = A (1-\alpha) \rho_l w_l \tag{A.101}$$

Vapor Generation Rate

The vapor generation rate is computed in two parts

$$\Gamma_V = \Gamma_W + \Gamma_{ph} \tag{A.102}$$

The first part accounts for evaporation due to heat transfer from the wall to the liquid phase. The second part accounts for mass transfer (evaporation or condensation) due to heat transfer between the phases.

$$\Gamma_W = \frac{q'_W / A}{h_{fg} + c_{p,l} \left[(t_{sat} - t_l) \frac{\rho_l}{\rho_g} + \frac{1}{2} (t_w - t_{sat}) \left(\frac{\rho_l}{\rho_g} - 1 \right) \right]} \qquad (A.103)$$

The three terms in the denominator correspond to the heat of evaporation, necessary heating of sub-cooled liquid and removal of energy by the liquid which is returned from the boundary layer to the bulk of liquid.

$$\Gamma_{ph} = \frac{c_1 + c_2 \alpha (1 - \alpha)}{h_{fg}} \left[(t_l - t_{sat}) + c_3 |t_l - t_{sat}| \right] \qquad (A.104)$$

The three state variables q'_w, t_l and t_w introduced in A.103 are given in their final form. A detailed derivation can again be found in [114]

Linear Heat Generation Rate:

$$q'_W = \left(\xi \overline{h_c} \right) \left(t_w - t_{fl} \right) - \left(\xi \overline{U} \right)_{lb} \left(t_{fl} - t_{lb} \right) \qquad (A.105)$$

where ξ is the heated perimeter. The second term in A.105 accounts for the bypass.

Liquid Temperature:

$$t_l = t_{sat} + \frac{\rho_m u_m - \alpha \rho_g u_g}{(1 - \alpha) \rho_l c_{p,l}} \qquad (A.106)$$

Equation A.106 is an implicit definition of the liquid temperature because ρ_l and u_g dependent themselves on t_l.

Wall Temperature:

$$t_w = t_c \left(R_{co} \right) = t_{fl} + \frac{t_{c,MC} - t_{fl}}{1 + \frac{h_c \Delta r_c}{2 k_c}} \qquad (A.107)$$

A.3.4   Linearization

Pressure

The linearization of the system pressure A.70 becomes

$$
\begin{aligned}
\Delta\langle P\rangle_{\text{syst}} &= \frac{\partial\langle P\rangle_{\text{syst}}}{\partial P}\Delta\langle P\rangle_{\text{syst}} + \frac{\partial\langle P\rangle_{\text{syst}}}{\partial\Gamma_v}\Delta\Gamma_v + \frac{\partial\langle P\rangle_{\text{syst}}}{\partial t_l}\Delta t_l \\
&= \frac{\partial\langle P\rangle_{\text{syst}}}{\partial P}\Delta\langle P\rangle_{\text{syst}} + \frac{\frac{\rho_l-\rho_g}{\rho_l\rho_g V_{k_1}}}{\alpha\frac{\rho_g'}{\rho_g} + (1-\alpha)\frac{\rho_l'}{\rho_l}V_{k_{1,2}}}\Delta\Gamma_v \\
&\quad + \frac{\Gamma_v V_{k_1}}{\rho_g}\left(\frac{\left[\alpha\frac{\rho_g'}{\rho_g}\rho_l + (1-\alpha)\rho_l'\right] - \left(\frac{\rho_l}{\rho_g}-1\right)\alpha\rho_g'}{\left[\alpha\frac{\rho_g'}{\rho_g}\rho_l + (1-\alpha)\rho_l'\right]^2 V_{k_{1,2}}}\right)\frac{\partial\rho_l}{\partial t_l}\Delta t_l
\end{aligned}
\tag{A.108}
$$

The value of $\frac{\partial\langle P\rangle_{\text{syst}}}{\partial P}\Delta\langle P\rangle_{\text{syst}}$ is derived numerically while $\frac{\partial\rho_l}{\partial t_l}$ comes easily from A.73

Momentum Balance

The linearization of the momentum balance A.83 becomes

$$
\Delta M = \frac{\partial M}{\partial P}\Delta P + \frac{\partial M}{\partial\alpha}\Delta\alpha + \frac{\partial M}{\partial t_l}\Delta t_l + \frac{\partial M}{\partial W_1}\Delta W_1 + \frac{\partial M}{\partial W_g}\Delta W_g
\tag{A.109}
$$

This linearization is done numerically due to the complexity of A.83.

Mixture Energy

The linearization of the mixture energy A.89 becomes

$$
\begin{aligned}
\Delta u_m\rho_m &= \frac{\partial u_m\rho_m}{\partial P}\Delta P + \frac{\partial u_m\rho_m}{\partial t_l}\Delta t_l + \frac{\partial u_m\rho_m}{\partial W_{1,k}}\Delta W_{1,k} + \frac{\partial u_m\rho_m}{\partial W_{1,k-1}}\Delta W_{1,k-1} \\
&\quad + \frac{\partial u_m\rho_m}{\partial W_{l,g}}\Delta W_{l,g} + \frac{\partial u_m\rho_m}{\partial W_{l,g-1}}\Delta W_{l,g-1} + \frac{\partial u_m\rho_m}{\partial q_w'}\Delta q_w' + \frac{\partial u_m\rho_m}{\partial q_l'''}\Delta q_l''' + \frac{\partial u_m\rho_m}{\partial\alpha}\Delta\alpha \\
&= -h_{l,k}\Delta W_{l,k} + h_{l,k-1}\Delta W_{l,k-1} - h_{g,k}\Delta W_{g,k} + h_{g,k-1}\Delta W_{g,k-1} \\
&\quad + \frac{V_k}{A_k}\Delta q_w' + V_k(1-\alpha)\Delta q_w' - V_k q_l'''\Delta\alpha
\end{aligned}
\tag{A.110}
$$

$\frac{\partial u_m\rho_m}{\partial P}$ and $\frac{\partial u_m\rho_m}{\partial t_l}$ is neglected.

Steam Mass

The linearization of the steam mass A.90 becomes

$$
\begin{aligned}
\Delta m_{g,k} &= \frac{\partial m_{g,k}}{\partial \Gamma_{v,k}} \Delta \Gamma_{v,k} + \frac{\partial m_{g,k}}{\partial W_{g,k}} \Delta W_{g,k} + \frac{\partial m_{g,k}}{\partial W_{g,k-1}} \Delta W_{g,k-1} \\
&= V_k \Delta \Gamma_v - \Delta W_{g,k} + \Delta W_{g,k-1}
\end{aligned}
\tag{A.111}
$$

Mixture Volumetric Flux

The linearization of the volumetric mixture flux A.67 becomes

$$
\begin{aligned}
A \Delta j_m &= A(z_{coreinlet}^+) \Delta j_m(z_{coreinlet}^+) \\
&\quad + \frac{\partial \Phi}{\partial \Gamma_v} \Delta \Gamma_v + \frac{\partial \Phi}{\partial W_{g,k-1}} \Delta W_{g,k-1} + \frac{\partial \Phi}{\partial W_{l,k-1}} \Delta W_{l,k-1} \\
&= V_k \frac{\rho_l - \rho_g}{\rho_l \rho_g} \Delta \Gamma_v + \left(\frac{1}{\rho_{l,k}} - \frac{1}{\rho_{l,k-1}} \right) \Delta W_{l,k-1} + \left(\frac{1}{\rho_{g,k}} - \frac{1}{\rho_{g,k-1}} \right) \Delta W_{g,k-1}
\end{aligned}
\tag{A.112}
$$

$\frac{\partial \Phi}{\partial P}$ and $\frac{\partial \Phi}{\partial t_l}$ is neglected.

Slip

The linearization of the slip A.96 becomes

$$
\begin{aligned}
\Delta S \quad &= \frac{\partial S}{\partial \alpha} \Delta \alpha \\
&= \frac{1 - c_1}{(c_1 - \alpha)^2} \Delta \alpha & \alpha \leq c_1 - c_{cut} \\
&= -c_3 \Delta \alpha & c_{max} > \alpha > c_1 - c_{cut} \\
&= 0 & \alpha \geq c_{max}
\end{aligned}
\tag{A.113}
$$

Phasic Velocity

The linearization of the gas velocity A.98 becomes

$$
\begin{aligned}
\Delta w_g &= \frac{\partial w_g}{\partial \alpha} \Delta \alpha + \frac{\partial w_g}{\partial j_m} \Delta j_m + \frac{\partial w_g}{\partial S} \Delta S \\
&= \frac{w_g(1 - S) - w^0}{1 + \alpha(S - 1)} \Delta \alpha + \frac{S}{1 + \alpha(S - 1)} \Delta j_m + \frac{j_m - w_g \alpha}{1 + \alpha(S - 1)} \Delta S
\end{aligned}
\tag{A.114}
$$

Mass Flow Rate

The linearization of the liquid mass flow rate A.101 becomes

$$
\begin{aligned}
\Delta W_l &= \frac{\partial W_l}{\partial P}\Delta P + \frac{\partial W_1}{\partial \alpha}\Delta\alpha + \frac{\partial W_1}{\partial S}\Delta S + \frac{\partial W_1}{\partial t_1}\Delta t_1 + \frac{\partial W_1}{\partial j_m}\Delta j_m \\
&= A(1-\alpha)w_l\frac{\partial \rho_l}{\partial P}\Delta P \\
&\quad - \rho_l A\frac{-[1+\alpha(S-1)]w^0 - (j_m - \alpha w^0)(S-1)}{[1+\alpha(S-1)]^2}\Delta\alpha \\
&\quad - A(1-\alpha)\rho_l\frac{(j_m - \alpha w^0)\alpha}{[1+\alpha(S-1)]^2}\Delta S \\
&\quad + A(1-\alpha)w_l\frac{\partial \rho_l}{\partial t_l}\Delta t_l \\
&\quad + \frac{A(1-\alpha)\rho_l}{1+\alpha(S-1)}\Delta j_m
\end{aligned}
\tag{A.115}
$$

The linearization of the gas mass flow rate A.100 becomes

$$
\begin{aligned}
\Delta W_g &= \frac{\partial W_g}{\partial P}\Delta P + \frac{\partial W_g}{\partial \alpha}\Delta\alpha + \frac{\partial W_g}{\partial w_g}\Delta w_g \\
&= A\alpha w_g\frac{\partial \rho_g}{\partial P}\Delta P + A\rho_g w_g\Delta\alpha + A\alpha\rho_g\Delta w_g
\end{aligned}
\tag{A.116}
$$

Vapor Generation Rate

The linearization of the vapor generation rate A.102 becomes

$$
\Delta\Gamma_v = \frac{\partial \Gamma_v}{\partial P}\Delta P + \frac{\partial \Gamma_v}{\partial \alpha}\Delta\alpha + \frac{\partial \Gamma_v}{\partial t_1}\Delta t_1 + \frac{\partial \Gamma_v}{\partial t_w}\Delta t_w + \frac{\partial \Gamma_v}{\partial q'_w}\Delta q'_w
\tag{A.117}
$$

This linearization is done numerically due to the complexity of A.102.

Linear Heat Generation Rate

The linearization of the linear heat generation rate A.105 becomes

$$
\begin{aligned}
\Delta q'_w &= \frac{\partial q'_w}{\partial P}\Delta P + \frac{\partial q'_w}{\partial t_w}\Delta t_w + \frac{\partial q'_w}{\partial t_1}\Delta t_1 \\
&= \frac{\partial q'_w}{\partial P}\Delta P + \frac{\partial q'_w}{\partial W_1}\Delta W_1 \\
&\quad + (4\xi\bar{h}_{c,boil} + \xi\bar{h}_{c,nonboil})\Delta t_w - \xi\bar{h}_{c,nonboil}\Delta t_l
\end{aligned}
\tag{A.118}
$$

The first term is linearized numerically due to the manyfold dependence on P.

Liquid Temperature

The linearization of the liquid temperature A.106 becomes

$$\Delta t_l = \frac{\partial t_l}{\partial t_{l,0}} \Delta t_{l,0} + \frac{\partial t_l}{\partial P} \Delta P + \frac{\partial t_l}{\partial \alpha} \Delta \alpha + \frac{\partial t_l}{\partial u_m \rho_m} \Delta u_m \rho_m \qquad (A.119)$$

This linearization is done numerically for all parts. The work of doing this by hand does not correspond to the benefits.

Wall Temperature

The linearization of the wall temperature A.107 becomes

$$\Delta t_w = \frac{\partial t_w}{\partial t_{0,w}} \Delta t_{0,w} + \frac{\partial t_w}{\partial P} \Delta P + \frac{\partial t_w}{\partial t_{c,MC}} \Delta t_{c,MC} + \frac{\partial t_w}{\partial t_l} \Delta t_l \qquad (A.120)$$

Also this linearization is done numerically for all parts due to the same reasons as above.

A.4   The Numerical Linearization

The implemented numerical scheme to linearize numerically is very simple. The equation is evaluated once for the steady state and once with one parameter slightly disturbed. The linearization of $g(\alpha)$ with respect to α is therefore

$$\Delta g(\alpha) = \frac{g(\alpha + \delta \alpha) - g(\alpha)}{\delta \alpha} \qquad (A.121)$$

The size of $\delta \alpha$ is chosen so small, that a small change in $\delta \alpha$ would not change $\Delta g(\alpha)$. Using A.121 is very fast, though not elegant.

Appendix B

Detailed Structure of the Matrix A_S

MATSTAB uses vectors to store thermal-hydraulic or neutronic properties. Each entry in a given vector represents the property in a corresponding node. Vectors that contain thermal-hydraulic properties are larger than vectors that contain neutronic properties since the nodes outside of the core are also included. The total number of nodes is dependent on the size of the reactor and on the number of nodes used to describe the outer part of the core (e.g. steam dome, downcomer, etc.). The number of nodes outside the core are chosen as explained in Figure 3.4. For the sake of simplicity real numbers for the Leibstadt NPP with half core case symmetry are used. The GE-6 reactor of Leibstadt uses 648 fuel assemblies. The channels are numbered according to Table B.1.

1	2	3	4	5	6	7	8	9	10	11	12	13		30
31	32	33	34	35	36	37	38	39	40	41	42	43	...	60
61	62	63	64	65	66	67	68	69	70	71	72	73	...	90
	91	92	93	94	95	96	97	98	99	100	101	102	...	118
	119	120	121	122	123	124	125	126	127	128	129	130	...	146
		147	148	149	150	151	152	153	154	155	156	157	...	172
			173	174	175	176	177	178	179	180	181	182	...	196
			197	198	199	200	201	202	203	204	205	206	...	220
				221	222	223	224	225	226	227	228	229	...	242
					243	244	245	246	247	248	249	250	...	262
						263	264	265	266	267	268	269	...	280
							281	282	283	284	285	286	...	296
									297	298	299	300	...	308
										309	310	311	...	318
												319	...	324

Table B.1: MATSTAB Numbering Scheme for the Channels in a Half-Core Case

Table B.2 and B.3 describe the structure and numbering scheme for neutronic as well as thermal-hydraulics vectors.

Section	First Node	Last Node	Number of Nodes
Node 1-25 of Channel 1	1	25	25
Node 1-25 of Channel 2	26	50	25
...			
Node 1-25 of Channel 324	8076	8100	25

Table B.2: MATSTAB Numbering Scheme for the Neutronic Representation of the Core

Section	First Node	Last Node	Number of Nodes
Steam Dome	1	1	1
Entry Node DC 1	2	2	1
Downcomer 1	3	8	6
Entry Node DC 2	9	9	1
Downcomer 2	10	15	6
Entry Node LP 1	16	16	1
Lower Plenum 1	17	18	2
Entry Node LP 2	19	19	1
Lower Plenum 2	20	22	3
Entry Nodes CH 1-324	23	346	324
Entry Node Bypass	347	347	1
Node 1 CH 1-324	348	671	324
Node 1 Bypass	672	672	1
Node 2 CH 1-324	673	996	324
Node 2 Bypass	997	997	1
...			
Node 25 CH 1-324	8148	8471	324
Node 25 Bypass	8472	8472	1
Entry Node Riser	8473	8473	1
Riser	8474	8478	5

Table B.3: MATSTAB Numbering Scheme for the Thermal-Hydraulic Representation of the Reactor

Besides the structure of the vectors, it is also necessary to know how many thermal-hydraulic and neutronic state variables are foreseen to be implemented. The quantity of these variables defines the number of equations used in each node. The matrix was originally designed for 13 thermal-hydraulic and 12 neutronic variables. Even though some of these variables are no longer necessary, the matrix structure was never changed. During the construction phase of the matrix, the corresponding rows and columns are filled with zeros. During the iterative solution phase however, the empty rows and columns are omitted. In addition to the 13 times 8478 and 12 times 8100 equations there is one equation for the system pressure, two equations for the pump dynamics and 325 equations for the distribution of the core

flow into 324 channels an the bypass. This adds up to 13x8478+12x8100+1+2+325=207742 equations.

Table B.4 shows the ordering of the equations in the matrix $\mathbf{A}_s$.

Section	First Row	Last Row	Number of Rows
TH Section			
System Pressure	1	1	1
Steam Dome	2	14	13
Entry Node DC 1	15	27	13
Downcomer 1	28	105	78
Entry Node DC 2	106	118	13
Downcomer 2	119	196	78
Entry Node LP 1	197	209	13
Lower Plenum 1	210	235	26
Entry Node LP 2	236	248	13
Lower Plenum 2	249	287	39
Entry Nodes CH 1-324	288	4499	4212
Entry Node Bypass	4500	4512	13
Node 1 CH 1-324	4513	8724	4212
Node 1 Bypass	8725	8737	13
Node 2 CH 1-324	8738	12945	4212
Node 2 Bypass	12946	12958	13
...			
Node 25 CH 1-324	105913	110124	4212
Node 25 Bypass	110125	110137	13
Entry Node Riser	110138	110150	13
Riser	110151	110215	65
Flow Distribution Model Core	110216	110539	324
Flow Distribution Model Bypass	110540	110540	1
Pump (driving flow)	110541	110541	1
Pump (pressure drop)	110542	110542	1
Neutronic Section			
Node 1-25 of Channel 1	110543	110842	300
Node 1-25 of Channel 2	110843	111142	300
...			
Node 1-25 of Channel 324	207443	207742	300

Table B.4: MATSTAB Numbering Scheme in the Matrix $\mathbf{A}_s$ for the Leibstadt Reactor

Section	First Row	Last Row	Number of Rows
TH Section			
System Pressure	1	1	1
Steam Dome	2	14	13
Entry Node DC 1	15	27	13
Downcomer 1	28	79	52
Entry Node DC 2	80	92	13
Downcomer 2	93	196	104
Entry Node LP 1	197	209	13
Lower Plenum 1	210	235	26
Entry Node LP 2	236	248	13
Lower Plenum 2	249	313	65
Entry Nodes CH 1-338	314	4707	4394
Entry Node Bypass	4708	4720	13
Node 1 CH 1-338	4721	9114	4394
Node 1 Bypass	9115	9127	13
Node 2 CH 1-338	9128	13521	4394
Node 2 Bypass	13522	13534	13
...			
Node 25 CH 1-338	110489	114882	4394
Node 25 Bypass	114883	114895	13
Entry Node Riser	114896	114908	13
Riser	114909	114960	52
Flow Distribution Model Core	114961	115298	338
Flow Distribution Model Bypass	115299	115299	1
Pump (driving flow)	115300	115300	1
Pump (pressure drop)	115301	115301	1
Neutronic Section			
Node 1-25 of Channel 1	115302	115601	300
Node 1-25 of Channel 2	115602	115901	300
...			
Node 1-25 of Channel 338	216402	216701	300

Table B.5: MATSTAB Numbering Scheme in the Matrix $\mathbf{A}_s$ for Forsmark 1 and 2

Section	First Row	Last Row	Number of Rows
TH Section			
System Pressure	1	1	1
Steam Dome	2	14	13
Entry Node DC 1	15	27	13
Downcomer 1	28	66	39
Entry Node DC 2	67	79	13
Downcomer 2	80	144	65
Entry Node LP 1	145	157	13
Lower Plenum 1	258	183	26
Entry Node LP 2	184	196	13
Lower Plenum 2	197	222	26
Entry Nodes CH 1-350	223	4772	4550
Entry Node Bypass	4773	4785	13
Node 1 CH 1-350	4786	9335	4550
Node 1 Bypass	9336	9348	13
Node 2 CH 1-350	9349	13898	4550
Node 2 Bypass	13899	13911	13
...			
Node 25 CH 1-350	114298	118847	4550
Node 25 Bypass	118848	118860	13
Entry Node Riser	118861	118873	13
Riser	118878	118925	52
Flow Distribution Model Core	118926	119275	350
Flow Distribution Model Bypass	119276	119276	1
Pump (driving flow)	119277	119277	1
Pump (pressure drop)	119278	119278	1
Neutronic Section			
Node 1-25 of Channel 1	119279	119578	300
Node 1-25 of Channel 2	119579	119878	300
...			
Node 1-25 of Channel 350	223979	224278	300

Table B.6: MATSTAB Numbering Scheme in the Matrix $\mathbf{A}_s$ for Forsmark 3

Appendix C

Input / Output of MATSTAB

C.1   Screen Output of MATSTAB

```
Command:
MATALAB>> matstab f2/f2_moc_14.dat

Output:
Plant: f2  File:  /matlab/matstab/input/f2/f2_moc_14.dat
Ramona file:      /matlab/matstab/input/f2/parameter.inp
Power-Void Iteration:
It. nr    Rel. Err. neu    Rel. Err. th      Keff
-------+---------------+--------------+-------------
   1        -0.06152        -0.99974      0.99875
   2         0.04869        -0.10821      0.99959
   3        -0.00960         0.01933      0.99954
   4         0.00376        -0.00392      0.99956
keff:    0.99956

Input preparation  CPU-time: 134.09 s
Input preparation Real time: 145.2023 s

  It.#     dr      freq.       tol
-------+--------+---------+-------------
        0.5416   0.4319  2.29477e-10
        0.5314   0.4251  6.52154e-12
        0.5388   0.4249  3.72006e-12
   1    0.5388   0.4249  3.72006e-12
        0.5405   0.4253  1.93813e-11
   2    0.5405   0.4253  1.93813e-11
```

```
Eigenvalue calculation for Harmonics no. 1:

  It.#      dr      freq.       tol
-------+--------+---------+-------------
        0.4292   0.4009  1.06655e-09
        0.4352   0.3948  9.05887e-10
        0.4645   0.3952  8.22336e-10
   1    0.4645   0.3952  8.22336e-10
        0.4798   0.3979  2.37738e-10
        0.4777   0.3996  1.01786e-10
        0.4728   0.4000  5.57586e-11
   2    0.4728   0.4000  5.57586e-11


Total CPU-time:  656.98 s
Total Real time: 670.9491 s
```

C.2   MATSTAB Input Desk for Leibstadt

```
************************************************************
*            MATSTAB MODEL OF LEIBSTADT                   *
*            BWR CORE STABILITY ANALYSIS                  *
************************************************************

DEFAULT CALCULATION OPTIONS

save_all = 1;        Controls whether everything is saved or not
left_eig = 1;        Calcualting the left eigenvector
Harmonics= 2;        Controls the nr of harmonics calculated
lam      =-0.1+2.8i; Eigenvalue
tol_pv   = 1e-2;     Tolerance on power-void iteration
tol_th   = 5e-3;     Tolerance on T/H steady-state solution
tol_neu  = 1e-3;     Tolerance on neutronic steady-state solution
tolnewt  = 1e-10;    Tolerance on eigenvalue calculation
opt      = 'short';  Printing option for eigenvalue calculation
no_core  = 0;        No ex_core components

CONTROL PARAMETERS
110000              17   3 0 0  0 0 0  2 0 0  2 3 0  0 0 1 0 1

GEOMETRY            N      A       H      DH   VHI/VHO

DOWNCOMER1
210000              6    10.33    5.073   1.16   -0.0
```

```
DOWNCOMER2
220000              6    0.72    4.384    0.128  -0.0


LOWER PLENUM 1
230000              2    9.26    6.0      6.1    -0.0


LOWER PLENUM 2
240000              3    10.51   1.79     0.30   -0.0


RISER
260000              5    7.4     3.4      0.154  -7.0


STEAM  DOME              A       H        DH      WLEV
270000                   20.96   8.46     5.17    0.567


FW AND PUMP LOCATION     NFW1    NFW2     NP1     NP2
290000                   5       1        7       2


ASSEMBLY IDENTIFIER
332000     1 "A84"
332000     2 "B84"
332000     3 "B85"
332000     4 "C84"
332000     5 "C85"
332000     6 "D85"
332000     7 "E85"
332000     8 "E86"
332000     9 "F86"
332000    10 "G86"
332000    11 "H87"
332000    12 "I87"
332000    13 "J88"
332000    14 "J89"
332000    15 "K88"
332000    16 "K90"
332000    17 "L90"
332000    18 "M90"
332000    19 "N90"
332000    20 "N90R"
332000    21 "N90A"
332000    22 "L91"
332000    23 "M91"
332000    24 "O91"
332000    25 "O91R"
332000    26 "R91"
```

```
332000     27 "O92"
332000     28 "P92"
332000     29 "R92"
332000     30 "S92"
332000     31 "S92R"
332000     32 "S92A"
332000     33 "T92"
332000     34 "T92R"
332000     35 "T92A"
332000     36 "W92"
332000     37 "W92R"
332000     38 "P93"
332000     39 "S93"
332000     40 "T93"
332000     41 "T93R"
332000     42 "U93"
332000     43 "U93R"
332000     44 "X93"
332000     45 "X93R"
332000     46 "U94"
332000     47 "X94"
332000     48 "Y94"
332000     49 "Y94R"
332000     50 "Z94"
332000     51 "B95"
332000     52 "C95"
332000     53 "A95"
332000     54 "Y95"
332000     55 "D95"
332000     56 "B96"
332000     57 "D96"
332000     58 "E96"
332000     59 "F96"


**************************************************
*************** NUCLEAR DATA *********************
**************************************************


                  CRITK  BG21  BG22  AB1   AB2   DREF
400000             1.0    0     0     0     0     1.6
                  CREF    DAVER
401000            -0.0667  1.597


410000            -0.1132 -0.4704 24.57   25.04
       (BL (I) , I=1, NBE)
```

```
420000    0.1408  0.0889  0.0830  0.0902  0.0938  0.1551  0.1452
420000    0.0704  0.0113  0.0098  0.0770  0.1635  0.1223  0.0137
420000   -0.0106  0.1310  0.1554  0.0668  0.0019  0.0151  0.0655
420000    0.1551  0.1287  0.0071  0.0068  0.1279  0.1325  0.0074
420000    0.0068  0.1325  0.1279  0.0068  0.0074  0.1287  0.1551
420000    0.0068  0.0071  0.1554  0.0655  0.0668  0.1310  0.0151
420000    0.0019  0.1223  0.1635 -0.0106  0.0137  0.1452  0.0770
420000    0.0704  0.1551  0.0098  0.0113  0.1408  0.0938  0.0889
420000    0.0902  0.0830

          (BE(I),I=1,NBE)
430000    0.0306  0.0220  0.0247  0.0246  0.0214  0.0298  0.0269
430000    0.0291 -0.0130 -0.0319  0.0276  0.0283  0.0318  0.0155
430000    0.0814  0.0324  0.0273  0.0321 -0.0566  0.0134  0.0320
430000    0.0269  0.0306 -0.0412 -0.0369  0.0303  0.0300 -0.0252
430000   -0.0389  0.0300  0.0303 -0.0389 -0.0252  0.0360  0.0269
430000   -0.0369 -0.0412  0.0273  0.0320  0.0320  0.0324  0.0134
430000   -0.0566  0.0318  0.0283  0.0814  0.0155  0.0269  0.0276
430000    0.0291  0.0298 -0.0319 -0.0130  0.0306  0.0214  0.0220
430000    0.0246  0.0247

KINETIC PARAMETERS

  cycl 7              NG   VEL1      VEL2
490000                6    1.7457E+7  3.9401E+05

      (B(I),I=1,NG)

491000 0.1555E-3 1.1825E-3 1.0573E-3
       2.1438E-3 0.7703E-3 0.2674E-3

      (AL(I),I=1,NG)
492000 0.0124 0.0305 0.111 0.301 1.14 3.01

499000 2.835181e-03  -4.514440e-05  4.783549e-07
       5.814993e-05  -6.998074e-05


*************************************************
********** THERMAL HYDRAULIC MODEL **************
*************************************************


                 (CSS(I),I=1,4)
500000    1.9    0.25    0.9    0.147
```

```
BOILING MODEL
        (CPB(I),I=1,3)          CRT(1)
        (Martinelli-Nelson)
501000  5.0E+6 4.0E+7 0.0        2400


FUEL PIN MODEL
        NRODS     RCA        DRCA
520001  62        0.006135   8.1E-4
520002  62        0.006135   8.1E-4
520003  62        0.006135   8.1E-4
520004  62        0.006135   8.1E-4
520005  62        0.006135   8.1E-4
520006  62        0.006135   8.1E-4
520007  62        0.006135   8.1E-4
520008  62        0.006135   8.1E-4
520009  62        0.006135   8.1E-4
520010  62        0.006135   8.1E-4
520011  62        0.006135   8.1E-4
520012  72        0.006135   8.1E-4
520013  62        0.006135   8.1E-4
520014  62        0.006135   8.1E-4
520015  62        0.006135   8.1E-4
520016  62        0.006135   8.1E-4
520017  60        0.006135   8.1E-4
520018  60        0.006135   8.1E-4
520019  60        0.006135   8.1E-4
520020  60        0.006135   8.1E-4
520021  60        0.006135   8.1E-4
520022  60        0.006135   8.1E-4
520023  60        0.006135   8.1E-4
520024  96        0.004810   6.3E-4
520025  96        0.004810   6.3E-4
520026  96        0.004810   6.3E-4
520027  96        0.004810   6.3E-4
520028  96        0.004810   6.3E-4
520029  96        0.004810   6.3E-4
520030  96        0.004810   6.3E-4
520031  96        0.004810   6.3E-4
520032  96        0.004810   6.3E-4
520033  96        0.004810   6.3E-4
520034  96        0.004810   6.3E-4
520035  96        0.004810   6.3E-4
520036  96        0.004810   6.3E-4
520037  96        0.004810   6.3E-4
520038  96        0.004810   6.3E-4
```

```
520039   96       0.004810   6.3E-4
520040   96       0.004810   6.3E-4
520041   96       0.004810   6.3E-4
520042   96       0.004810   6.3E-4
520043   96       0.004810   6.3E-4
520044   96       0.004810   6.3E-4
520045   96       0.004810   6.3E-4
520046   96       0.004810   6.3E-4
520047   96       0.004810   6.3E-4
520048   96       0.004810   6.3E-4
520049   96       0.004810   6.3E-4
520050   96       0.004810   6.3E-4
520051   96       0.004810   6.3E-4
520052   96       0.004810   6.3E-4
520053   96       0.004810   6.3E-4
520054   96       0.004810   6.3E-4
520055   96       0.004810   6.3E-4
520056   96       0.004810   6.3E-4
520057   96       0.004810   6.3E-4
520058   96       0.004810   6.3E-4
520059   96       0.004810   6.3E-4


Data from ABB Report NTD 94-350


          E1      E2     RLCA GCAMAX   GC40     GC41     GC42
521001 10.0507 2.1196E-3 16.0 21000 3.8489E+3 -3.1009 5.7648E-3
521002 10.0507 2.1196E-3 16.0 21000 3.8489E+3 -3.1009 5.7648E-3
521003 10.0507 2.1196E-3 16.0 21000 3.8489E+3 -3.1009 5.7648E-3
521004 10.0507 2.1196E-3 16.0 21000 3.8489E+3 -3.1009 5.7648E-3
521005 10.0507 2.1196E-3 16.0 21000 3.8489E+3 -3.1009 5.7648E-3
521006 10.0507 2.1196E-3 16.0 21000 3.8489E+3 -3.1009 5.7648E-3
521007 10.0507 2.1196E-3 16.0 21000 3.8489E+3 -3.1009 5.7648E-3
521008 10.0507 2.1196E-3 16.0 21000 3.8489E+3 -3.1009 5.7648E-3
521009 10.0507 2.1196E-3 16.0 21000 3.8489E+3 -3.1009 5.7648E-3
521010 10.0507 2.1196E-3 16.0 21000 3.8489E+3 -3.1009 5.7648E-3
521011 10.0507 2.1196E-3 16.0 21000 3.8489E+3 -3.1009 5.7648E-3
521012 10.0507 2.1196E-3 16.0 21000 3.8489E+3 -3.1009 5.7648E-3
521013 10.0507 2.1196E-3 16.0 21000 3.8489E+3 -3.1009 5.7648E-3
521014 10.0507 2.1196E-3 16.0 21000 3.8489E+3 -3.1009 5.7648E-3
521015 10.0507 2.1196E-3 16.0 21000 3.8489E+3 -3.1009 5.7648E-3
521016 10.0507 2.1196E-3 16.0 21000 3.8489E+3 -3.1009 5.7648E-3
521017 10.0507 2.1196E-3 16.0 21000 3.8489E+3 -3.1009 5.7648E-3
521018 10.0507 2.1196E-3 16.0 21000 3.8489E+3 -3.1009 5.7648E-3
521019 10.0507 2.1196E-3 16.0 21000 3.8489E+3 -3.1009 5.7648E-3
521020 10.0507 2.1196E-3 16.0 21000 3.8489E+3 -3.1009 5.7648E-3
```

```
521021 10.0507 2.1196E-3 16.0 21000 3.8489E+3 -3.1009 5.7648E-3
521022 10.0507 2.1196E-3 16.0 21000 3.8489E+3 -3.1009 5.7648E-3
521023 10.0507 2.1196E-3 16.0 21000 3.8489E+3 -3.1009 5.7648E-3
521024  9.9802 2.1292E-3 16.0 20000 4.9439E+3 -2.0730 6.2922E-3
521025  9.9802 2.1292E-3 16.0 20000 4.9439E+3 -2.0730 6.2922E-3
521026  9.9802 2.1292E-3 16.0 20000 4.9439E+3 -2.0730 6.2922E-3
521027  9.9802 2.1292E-3 16.0 20000 4.9439E+3 -2.0730 6.2922E-3
521028  9.9802 2.1292E-3 16.0 20000 4.9439E+3 -2.0730 6.2922E-3
521029  9.9802 2.1292E-3 16.0 20000 4.9439E+3 -2.0730 6.2922E-3
521030  9.9802 2.1292E-3 16.0 20000 4.9439E+3 -2.0730 6.2922E-3
521031  9.9802 2.1292E-3 16.0 20000 4.9439E+3 -2.0730 6.2922E-3
521032  9.9802 2.1292E-3 16.0 20000 4.9439E+3 -2.0730 6.2922E-3
521033  9.9802 2.1292E-3 16.0 20000 4.9439E+3 -2.0730 6.2922E-3
521034  9.9802 2.1292E-3 16.0 20000 4.9439E+3 -2.0730 6.2922E-3
521035  9.9802 2.1292E-3 16.0 20000 4.9439E+3 -2.0730 6.2922E-3
521036  9.9802 2.1292E-3 16.0 20000 4.9439E+3 -2.0730 6.2922E-3
521037  9.9802 2.1292E-3 16.0 20000 4.9439E+3 -2.0730 6.2922E-3
521038  9.9802 2.1292E-3 16.0 20000 4.9439E+3 -2.0730 6.2922E-3
521039  9.9802 2.1292E-3 16.0 20000 4.9439E+3 -2.0730 6.2922E-3
521040  9.9802 2.1292E-3 16.0 20000 4.9439E+3 -2.0730 6.2922E-3
521041  9.9802 2.1292E-3 16.0 20000 4.9439E+3 -2.0730 6.2922E-3
521042  9.9802 2.1292E-3 16.0 20000 4.9439E+3 -2.0730 6.2922E-3
521043  9.9802 2.1292E-3 16.0 20000 4.9439E+3 -2.0730 6.2922E-3
521044  9.9802 2.1292E-3 16.0 20000 4.9439E+3 -2.0730 6.2922E-3
521045  9.9802 2.1292E-3 16.0 20000 4.9439E+3 -2.0730 6.2922E-3
521046  9.9802 2.1292E-3 16.0 20000 4.9439E+3 -2.0730 6.2922E-3
521047  9.9802 2.1292E-3 16.0 20000 4.9439E+3 -2.0730 6.2922E-3
521048  9.9802 2.1292E-3 16.0 20000 4.9439E+3 -2.0730 6.2922E-3
521049  9.9802 2.1292E-3 16.0 20000 4.9439E+3 -2.0730 6.2922E-3
521050  9.9802 2.1292E-3 16.0 20000 4.9439E+3 -2.0730 6.2922E-3
521051  9.9802 2.1292E-3 16.0 20000 4.9439E+3 -2.0730 6.2922E-3
521052  9.9802 2.1292E-3 16.0 20000 4.9439E+3 -2.0730 6.2922E-3
521053  9.9802 2.1292E-3 16.0 20000 4.9439E+3 -2.0730 6.2922E-3
521054  9.9802 2.1292E-3 16.0 20000 4.9439E+3 -2.0730 6.2922E-3
521055  9.9802 2.1292E-3 16.0 20000 4.9439E+3 -2.0730 6.2922E-3
521056  9.9802 2.1292E-3 16.0 20000 4.9439E+3 -2.0730 6.2922E-3
521057  9.9802 2.1292E-3 16.0 20000 4.9439E+3 -2.0730 6.2922E-3
521058  9.9802 2.1292E-3 16.0 20000 4.9439E+3 -2.0730 6.2922E-3
521059  9.9802 2.1292E-3 16.0 20000 4.9439E+3 -2.0730 6.2922E-3

522000   0.23709E+7  0.26470E+4 -0.28373E+1
         0.12498E-2 -0.12066E-6  0.20301E+7

        MM   MMC
523000   4    2
```

```
PUMP MODEL
          IPUMP    IJPUMP
540000    3        20


JET PUMP PARAMETERS
          IDRL   ANOZ     ASCT     ATHR     RKDR     RKSCT     RJJP
542000    2      0.00323  0.01764  0.02087  0.0845   0.0006689 639.


          IFLOWP   IDISTP
547000    0        1


          PUMPNR  PINERT  FLOWR  HEADR  DENSR  TORQHR  PDIFFL
547100    155.5   808.6   2.37   192    755    25127   -2.605



HOMOLOGOUS PUMP CURVES (from TRAC input)


          KHS1... XHS1(1,6)...q/w
547211    10 -.480 -.40 -.30  -.20  0.0  0.2  0.4  0.6  0.8 1.0


          KHS1....HEADS1 h/w**2
547212    10   1.37 1.33 1.27 1.24 1.22 1.20 1.17 1.14 1.08 1.0


          KHS2....XHS2(k)...w/q
547213    10  -.40 -.275  -.10  0.0  0.1  0.3  0.4  0.5  0.8  1.0


          KHS2....HEADS2...h/q**2
547214    10 -0.38 -0.40 -0.38 -0.35 -0.32 -0.20 -0.14 0 0.545 1.0


          KTS1    XTS1(K),K=1,KTS1...q/w
547231    9 -0.2  0.0    0.2    0.4  0.6  0.8  0.9  0.95  1.0


          KTS1    TORQS1(K), K=1,KTS1...beta/w**2
547232    9  0.49  0.54  0.59   0.65  0.77 0.95 0.98  0.96 0.87


          KTS2    XTS2(K), K=1,KTS2.....w/q
547233    9  -0.2  0.0  0.2  0.4  0.6  0.8  0.9  0.95  1.0


          KTS2    TORQS2(K), K=1,KTS2....beta/q**2
547234    9 -.31 -.15 -.02 -.220 0.460 0.710 0.810 0.850 0.870


          B1PUMP B2PUMP B3PUMP  OMEG1P  OMEG2P
547300    0.486   8.05   25.6    1.6E-4   4.7
```

```
        PSLIPM   PTORQM
547400  0.07     10000


        RLAD     WDR
548100  57.4     3654


STEAM SEPARATOR
        NSEP     ASEP     HSEP     RLEFF0
550000  261      12.81    2.29     120.


POWER GENERATION  +++ modified from 3.7% to 2%
580000  0.02  0.01  200.27375
581000  0.02  0.02  1.E+11     1.0    0.    0.0
```

Bibliography

[1] ABB Atom AB, Core Master Documentation Vol. 6, POLCA Users Manual, 1994

[2] ABB Atom AB, PHOENIX - User's Guide, UR 85-149 Rev. 5, 1985

[3] ABB Atom AB, POLCA 7 Documentation, User's Manual, 1999

[4] G.Th. Analytis, D. Hennig, J. K.-H. Karlsson, The Physical Mechanism of Core-Wide and Local Instabilities at the Forsmark-1 BWR, NURETH-9 San Francisco, 1999

[5] L.A. Belblidia, L.E. Weaver, and R.W. Carlson, Nodal Analysis of Density-Wave Oscillations in Boiling Water Nuclear Reactors, Ann. Nucl. Energy Vol. 10 No. 10 1983

[6] L.A. Belblidia, KKL RAMONA Stability Benchmark Calculations, ScandPower Report TR1/44.72.02, 1995

[7] B.G. Bergdahl, F. Reisch, R. Oguma, J. Lorenzen, F.Åkerhielm, BWR Stability Investigation at Forsmark 1, Ann. Nucl. Energy Vol. 16 No. 10, 1989

[8] A.E. Bergles, Review of Instabilities in Two-Phase Systems, Two-Phase Flows & Heat Transfer, Proceedings of NATO Advanced Study Institute, Istanbul, 1976

[9] J. Blomstrand, S.Å. Andersson, BWR Core Response to Fluctuations in Coolant Flow and Pressure with Implications on Noise Diagnosis and Stability Monitoring, ANS Meeting, Kiamsha Lake, New York, 1982

[10] J. Blomstrand, Noise Analysis of Core Coolant Flow Signals, Recorded in Swedish and Finnish BWRs, Asea Atom Report UR87-328, 1987

[11] J. Blomstrand, Stability Investigation of SVEA-64 BWR Fuel NURETH-4 Karlsruhe, (ABB Atom Report SVEA 89-61), 1989

[12] J. Blomstrand, The KKL Core Stability Test, Conducted on September 6th 1990, ABB Atom Report, BR 91-245, 1992

[13] J. Blomstrand, Core Stability Monitoring: On-Line Performance Qualification of COSMOS in KKL, Jahrestagung Kerntechnik 93, Köln (ABB Rep. BR 93-416), 1993

[14] J.A. Borkowski, Time Domain Model Sensitivity in Boiling Water Reactor Stability, Analysis Using TRAC/BF1, Nucl. Technol. Vol. 103 July, 1995

[15] K.E. Carlson, R.A. Riemke et al., RELAP5/MOD3 Code Manual. Vol. I: Code Struc-
     ture, System Models, and Solution Methods, NUREG/CR-5545, 1990

[16] K.C. Chan, Thermal-hydraulic Stability of Steam Generators (PhD) University of Cal-
     ifornia, Berkley, 1974

[17] H.-S. Cheng, U.S. Rohatgi, SBWR Stability Investigation Using Ramona-4B Code
     Proceedings of Advanced Reactor Safety, International Topical Meeting, Pittsburgh,
     1994

[18] A. Chevrier, Development of Stability Identification System for Boiling Water Reac-
     tors, PSI, TM 93-41-42, 1993

[19] Th. Christer Netterbrant, Oskarshamn 1, 2 och 3 - Verifeiering av MATSTAB, okg,
     Rapport 2000-03852, 2000

[20] J. Cullum, W. Kerner and R. Willoughby, A Generalized Nonsymmetric Lanczos Pro-
     cedure, Comput. Phys. Comm 53:19-48, 1989

[21] B. Damiano, J. A. March-Leuba, J. A. Euler, Application of Galerkin's Method to
     Calculate the Behavior of BWR, During Limit-Cycle Oscillations, Nucl. Sci. Eng.
     Vol. 113, 1993

[22] F. D'Auria et al., State of the Art Report on Boiling Water Reactor Stability,
     OCDE/GD(97)13, 1997

[23] J.W. Demmel, Applied numerical algebra, SIAM, 1997

[24] Y.M. Farawila, Application of Modal Neutron Kinetics to Boiling Water Reactor Os-
     cillation Problems, Nucl. Sci. & Eng. 129, 1998

[25] L.R. Foulke, E.P. Gyftopoulos, Application of the Natural Mode Approximation to
     Space-Time Reactor Problems, Nucl. Sci. & Eng. 30, 1967

[26] A. Gandini, Higher Order Time-Dependent Generalized Perturbation Theory, Nucl.
     Sci. & Eng. 67, 1977

[27] A. Gandini, Implicit and Explicit Higher Order Perturbation Methods for Nuclear
     Reactor Analysis, Nucl. Sci. & Eng. 67, 1978

[28] A. Gandini, On the Standard Perturbation Theory, Nucl. Sci. & Eng. 79, 1981

[29] F.D. Giust, L. Moberg, B. Melkerson, Out of Phase Oscillations in the Ringhals-1
     BWR Reactor, Measurements, Data Analysis and Qualification of a Predictive Ra-
     mona Model, 28th ASME/AICh/ANS Conference, San Diego, 1992

[30] G.F. Golub, Ch.F. van Loan, Matrix Computations, The Johns Hopkins University
     Press, 1996

[31] W. Hackbusch, Iterative Solution of Large Sparse Systems of Equations, Springer
     Verlag, 1994

[32] Ph. Hänggi, Th. Smed, P. Lansåker, MATSTAB, A Fast Frequency Domain Based Code to Predict Boiling Water Reactor Stability Using a Detailed Three Dimensional Model, NURETH-9 San Francisco, 1999

[33] J. Hanberg, Forsmark 1 - Verifiering av RAMONA 3.9 mot Stabilitetsberäkningar på F1 Cykel 17 och Cykel 18, Vattenfall PB-120/99, 1999

[34] D. Hennig, L. Nechvatal, Results of the OECD / NEA BWR Stability Benchmark Task STARS Kolloquium, PSI, 1995

[35] D. Hennig, Time Series Analysis for BWR Stability Analysis, PSI Report TM-41-97-1, 1997

[36] D. Hennig, A Study on Boiling Water Reactor Stability Behavior, Nucl. Techn. Vol. 126, 1999

[37] Z. Jia, Some Numerical Methods for Large Unsymmetric Eigenproblems, Ph. D. Thesis, Universität Bielefeld, Germany, 1994

[38] C. Jönsson, J. Blomstrand, S. Andersson, Experimental Investigations on BWR Core and Coolant Channel Flow Stability, ABB Atom Report RPA 89-81, 1989

[39] A.A. Karve, Nuclear-Coupled Thermal-Hydraulic Stability Analysis of Boiling Water Reactors, Ph. D. Thesis, University of Virginia, 1998

[40] W.E. Kastenberg, P. L. Chambre, On the Stability of Nonlinear Space Dependent Reactor Kinetics, Nucl. Sci. Eng. 31 67, 1968

[41] W.E. Kastenberg, A Stability Criterion for Space Dependent Nuclear Reactor Systems with Variable Temperature Feedback, Nucl. Sci. Eng. 37 19, 1969

[42] S. Katsenelenbogen, L. Moberg, J. Rea, Ramona Calculations on LaSalle-2 Stability Event, 1991

[43] M. Kosinski, RM1DAY-Interface Program between RAMONA-3B and CORE MASTER I Data Files, Users Manual, ABB Atom Report NTD 94-436, 1994

[44] Z. Koszela, Forsmark 2 - Kvalificering av RAMONA5-Modell med CM2/POLCA7 mot Stabilitestsmätningar under Cykel 14,15,16 och 17, ABB Atom AB, Rapport SPD 99-193 rev 2, 1999

[45] R.T. Lahey Jr., G. Yadigaroglu, A Lagrangian Analysis of Two-Phase Hydrodynamic and Nuclear-Coupled Density-Wave Oscillations, Heat Trans. Tokyo, Vol. IV, paper B5.9, 1974

[46] R.T. Lahey, M.Z. Podowski, For Best Estimate Prediction of Mulitchannel Core Stability Margins, Nucl. Eng. and Design 151, 1994

[47] L.Ljung, T. Glad, Modeling of Dynamic Systems, Prentice Hall, Englewood Cliffs, N.J., 1994

[48] J.R. Lamarsh, Introduction to Nuclear Engineering, Addison-Wesley, Massachusetts, 1983

[49] P. Lansåker, Private Communications 1995-2000

[50] R.B. Lehoucq, D.C. Sorensen and C. Yang, ARPACK User's Guide: Solution of Large-Scale Eigenvalue Problems with Implicitly Restarted Arnoldi Methods, ISBN 0-89871-407-9, 1998, or www.caam.rice.edu/software/ARPACK

[51] S-Ö Lindahl, P. Quaglia, Core Master/BWR - POLCA Data Documentation, ABB Report UR 85-222 Rev. 7, 1985

[52] S-Ö Lindahl, POLCA-Model Description, ABB Report UR 86-192 Rev. 4, 1986

[53] R. Lehoucq, Analysis and Implementation of an Implicitly Restarted Arnoldi Iteration, Ph. D. thesis, Rice University, Houston, TX, 1995

[54] J. March-Leuba, D.G. Cacuci, R.B. Perez, Non-Linear Dynamics and Stability of PWR, Part I - Qualitative Analysis, Nucl. Sci. Eng. 93, 1986

[55] J. March-Leuba, D.G. Cacuci, R.B. Perez, Non-Linear Dynamics and Stability of PWR, Part II - Quantitative Analysis, Nucl. Sci. Eng. 93, 1986

[56] J. March-Leuba, E.D. Blakeman, A Mechanism for Out of Phase Instabilities in BWR, Nucl. Sci. Eng. 107, 1991

[57] J. March-Leuba, J.M. Rey, Coupled Thermal Hydraulic-Neutronic Instabilities in Boiling Water Nuclear Reactors: A Review of the State of the Art, Nucl. Engineering and Design 145, 1993

[58] W. Marquino, S. Fuller, P. Lansåker and S. Abrahamsson, Internal Pump Reactor Stability: Qualification of TRACG Computer Code, ICONE-2 San Francisco, Vol I, 55, 1993

[59] Mathworks Inc., MATLAB Version 5 User's Guide, Prentice Hall, ISBN 0132725509, 1997

[60] R. Miró, D. Ginestar, D. Hennig, G. Verdú, On the Regional Oscillation Phenomenon in BWR's, to be Published, 1999

[61] L. Moberg, S. Katsenelenbogen, Assessment and Application of the RAMONA Three Dimensional Transient Code to BWR Stability, BWR Stability Meeting, Holtzville NY, 1990

[62] M. Mori, K. Tsuda, A. Itami, Benchmarking and Qualification of the NUFREQ-NPT Code for BWR Core Stability Analysis,

[63] J.L. Muñoz-Cobo, G. Verdú, Application to Hopf Bifurcation Theory and Variational Methods to the Study of Limit Cycles in BWR, Ann. Nucl. Energy Vol. 18 No. 5, 1991

[64] J.L. Muñoz-Cobo, G. Verdú, C. Pereira, Dynamic Reconstruction and Lyapunov Exponents From Time Series Data in BWR. Application to BWR Stability Analysis, Ann. Nucl. Energy 19, 1992

[65] J.L. Muñoz-Cobo, R.b. Perez, D. Ginestar, A. Escriva, and G. Verdú, Non Linear Analysis of Out of Phase Oscillations in Boiling Water Reactors, Ann. Nucl. Energy 23, 1996

[66] D. Ribbing, KKL-RAMONA-evaluation of Stability as a Function of Feedwater Temperature, ABB Atom Report NTD 95-425, 1995

[67] OECD et al., Proceedings International Workshop on BWR Stability, OECD-NEA CSNI Report 178, 1990

[68] R. Oguma, B.G. Bergdahl Stability Investigation of Leibstadt BWR, Based on Noise Analysis, Eurosim AB, ES-1-94, 1993

[69] T.C. Oppe, W.D. Joubert, D.R. Kincaid, NSPCG User's Guide, A Package for Solving Large Sparse Linear Systems by Various Iterative Methods, CNA-216, University of Texas, 1988

[70] P. Otaduy, J. March-Leuba, Lapur User's Guide, NUREG/CR-5421, 1989

[71] G. Palmiotti, Use of the Explicit High-Order Perturbation Formulation, Ncul. Sci. & Eng. 83, 1983

[72] J.K. Park, M. Becker, Q.C. Park, Model Analysis for Reactor Kinetics and Stability, NUREG/CR-3377, 1983

[73] G.C. Park, M. Z. Podowski, M. Becker, R. T. Lahey Jr., The Development of NUFREQ-N, an Analytical Model for the Stability Analysis of Nuclear Coupled Density Wave Oscillations in Boiling Water Reactors. NUREG /CR-3375, 1983

[74] I.Pázsit, Determination of Reactor Stability in Case of Dual Oscillations, Ann. Nucl. Energy Vol. 22 No. 6, 1995

[75] B.N. Parlett, D.R. Taylor, and Z.A. Liu, A look-ahead Lanczos Algorithm for Unsymmetric Matrices, Math. Comp. 44:105-124, 1985

[76] M.P. Paulsen, J.H. McFadden, C.E. Peterson, J.A. McLure, G.C. Gose and P.J. Jensen, The RETRAN-03 Computer Code, Nuclear Technology. Vol. 95, pp. 105-115, Jan. 1991

[77] M.P. Paulsen, J.G. Shatford, L.J. Agee, J.L. Westacott, A Nondiffusiove Solution Method for Retran-03 Boiling Water Reactor Stability Analysis, Nucl. Techn. Vol 100, Nov 1992

[78] S.J. Peng, M.Z. Podowski and R.T. Lahey, Jr., M. Becker, NUFREQ-NP: A Computer Code for the Stabillity Analysis of Boiling Water Nuclear Reactors, Nucl. Sci. Eng., 88, 404, 1984

[79] S.J. Peng, M.Z. Podowski and R.T. Lahey, Jr., NUFREQ-NP: A Digital Computer Code for the Linear Stabillity Analysis of Boiling Water Nuclear Reactors, NUREG/CR-4116, 1985

[80] G. Peters, J.H. Wilkinson, Inverse Iteration, Ill-Conditioned Equations and Newton's Method, SIAM Review, Vol. 21, No. 3, July, 1979.

[81] E. Pollmann, J. Schulze, D. Kreuter, Stability Measurements In The German Nuclear Power Plant Wuergassen During Cycle 14, Nucl. Technol. Vol. 108 Dec., 1994

[82] R.O.S. Prasad, J.B. Doshi, K. Iyer, A Numerical Investigation of Nuclear Coupled Density Wave Oscillations, Nuclear Engineering and Design March-April, 1995

[83] Y.F. Rao, K. Fukuda, R. Kaneshima, Analytical Study of Coupled Neutronic and Thermal-Dynamic Instabilities in a Boiling Channel, 1995

[84] Rea, D. Kreuter, F. Wehle, Siemens Experience on Linear and Nonlinear Analysis of Out of Phase BWR Instabilities, Topfuel '95, 1995

[85] U.S. Rohatgi, A.N. Mallen, H.S. Cheng, W. Wulff, Validation of the Engineering Plant Analyzer Methodology with Peach Bottom 2 Stability Tests, Nucl. Eng. and Design 151, 1994

[86] C. Rotander, J. Blomstrand, The KKL Core Stability Test, Conducted on September 11th, 1993, ABB Atom Report, NTD 93-104, 1994

[87] C. Rotander, Operational Experience with Respect to Core Stability, Topfuel 95, 1995

[88] C. Rotander, Methods to Identify Stability Properties for a Thermal-Hydraulic Channel and from Reactor Noise Measurements, ISSN 0347-1071, KTH, 1999

[89] Y. Saad, Numerical Solution of Large Nonsymmetric Eigenvalue Problems, Comput. Phys. Comm, 53:71-90, 1989

[90] Y. Saad, Iterative Methods for Sparse Linear Systems, PWS Publishing Company, 1996

[91] M. Sadkane, Block-Arnoldi-Chebyshev Methods for Unsymmetric Large Eigenvalue Problems, Numer. Math. 64:195-211, 1993

[92] Scandpower A/S, RAMONA-3 User's Manual, 1993

[93] Th. Smed, Interaction Between High Voltage AC and DC Systems, Royal Institute of Technology, 1991

[94] Th. Smed, Private communications, 1995-2000

[95] W.M. Stacey, Jr., General modal Expansion Method, Nucl. Sci. Eng. 28 438, 1967

[96] R.J.J. Stamm'ler, M.J. Abbate, Methods of Steady-State - Reactor Physics in Nuclear Design, Academic Press Inc., ISBN 0-12-663320-7, 1983

[97] Y. Takeuchi, Y. Takigawa, Study on Mechanism for BWR Regional Oscillations, 1993

[98] Y. Takeuchi, Y. Takigawa, H. Uematsu, S. Ebata, J.C. Shaug, B.S. Shiralkar, TRACG Transient Analysis Code, Three Dimensional Kinetics Model Implementation and Applicability or Space Dependent Analysis, Nucl. Technol. Vol. 105 Feb., 1994

[99] R.P. Taleyarkhan, A.F. McFarlane, R.T. Lahey, M.Z. Podowski, Benchmarking and Qualification of the NUFREQ-NPW Code, 1994

[100] L.N. Trefethen, D. Baud, Numerical Linear Algebra, SIAM, 1997

[101] R.C. Torok, T.C. Derbidge, J.M. Healzer, Water Level Measurement Uncertainty during BWR Instability, Nucl. Eng. and Design 151, 1994

[102] Rizwan-Uddin, J. Dorning, Density Wave Instabilities in ABWR, ANS Proceedings, San Diego, 1992

[103] Rizwan-Uddin, On Density-Wave Oscillations In Two-Phase Flows, Int. J. Multiphase Flow Vol. 20. No. 4, 1994

[104] M. Uehrio, Linear Stability Analysis on Instabilities of In-Phase and Out-of-phase Modes in Boiling Water Reactors, Jour. of Nucl. Science and Technol. Vol. 33 No. 8, 1996

[105] K. Vallin, Verifiering av Ramona 3.9 mot Stabilitetsm ätningar i Forsmark 1 från C12 till C15, Vattenfall Br änsle PB-130/96, 1996

[106] K. Valtonen, BWR Stability Analysis, Tech. rep., Finnish Center for Radiation and Nuclear Safety, Helsinki, 1989

[107] D.D.B. Van Bragt, T.H.J.J. Van der Hagen, Stability of Natural Circulation Boiling Water Reactors Part I/II, Nucl. Technol. 121, 1998

[108] G. Van den Bussche, Verifiering av HC-Pumpmodellen i Ramona och MATSTAB, FKA FT 98/231, Forsmark technical report, 1998

[109] G. Van den Bussche, Validering av MATSTAB för Forsmark 1, Forsmark Kraftgrupp, FT-Rapport, to be written,

[110] G. Van den Bussche, Validering av MATSTAB för Forsmark 2, Forsmark Kraftgrupp, FT-Rapport 99/241, 1999

[111] G. Van den Bussche, Validering av MATSTAB för Forsmark 3, Forsmark Kraftgrupp, FT-Rapport 99/242, 1999

[112] T.H.J.J. Van der Hagen, I. Pázsit, O. Thomson, Methods for the Determination of the In Phase and Out of Phase Stability Characteristics of A Boiling water Reactor, Nucl. Technol. 107, 1994

[113] T.H.J.J. Van der Hagen, Exploring the Dodewaard Type-I and Type-II Stability, Ann. Nucl. Energy Vol 24 No 8, 1997

[114] W. Wulff, H.S. Cheng, D.J. Diamond and M. Khatib-Ranbar, A Description and Assessment of RAMONA-3B. A Computer Code with Three Dimensional Neutron Kinetics for BWR System Transients, NUREG/CR-3364, 1984

[115] W. Wulff, H.S. Cheng, A.N. Mallen, and U.S. Rohatgi, BWR Stability Analysis with the BNL Engineering Plant Analyzer, Tech. Rep. BNL-Nureg-52312, Brookhaven National Laboratory, 1992

[116] G. Yadigaroglu, Two-Phase Flow Instabilities and Propagation Phenomena in Industrial Design and Nuclear Engineering, Hemisphere, 1981

[117] G. Yadigaroglu, Instabilities In Two-Phase Flow, Short Course on Multiphase Flow and Heat Transfer, 1994

[118] Y. Yoshioka, H. Tabata, Analytical Study on JSBWR Core Stability, Proceedings of Advanced Reactor Safety, International Topical Meeting, Pittsburgh, 1994

[119] K.W. Zerreßen, D. Kreuter, Post-Calculation of Core Instabilities Measured in the German BWRs KRB-B/C Using the Frequency Domain Code STAIF, International Workshop on Abnormal Transients in Nuclear Power Plants Atlanta, 1987

Nomenclature

General

DR   Decay ratio, see equation (2.26), page 17

λ Eigenvalue, see equation (2.15), page 15

n_u Number of state variables leading to algebraic equations, page 12

n_x Number of state variables leading to differential equations, page 12

ω Imaginary part of the eigenvalue, page 16

σ Real part of the eigenvalue, page 16

τ Time, page 12

u State variable that leads to algebraic equations, see equation (2.3), page 13

x State variable that leads to differential equations, see equation (2.3), page 13

T   Transpose operator, page 52

Matrices

$\mathbf{A}_\lambda$ Stability contribution matrix, page 63

$\mathbf{A_s}$ Matrix describing the linearized system, see equation (2.12), page 14

$\mathbf{B}$ Diagonal matrix, distinguishing differential and algebraic variables, page 36

$\mathbf{E}$ Matrix with the right eigenvectors as columns, page 15

$\mathbf{F}$ Matrix with the left eigenvectors as columns, page 15

$\mathbf{L}$ Lower triangular matrix, page 38

$\mathbf{U}$ Upper triangular matrix, page 38

Neutronics

β Total fraction of delayed neutrons, page 134

C Precursor density, page 134

D_1 Fast diffusion constant, page 134

$H(\tau_1, \tau2)$ Decay heat due between τ_1 and τ_2, page 140

J   Neutron current, page 135

K Total energy released per fission, $3.204e^{-11}j$, page 140

λ_m Decay constant of delayed group d, page 138

v_1, v_2 Number of neutrons generated per fission, page 135

$\overline{\varphi}_1 \overline{\varphi}_2$ Cell averaged neutron flux, page 134

q''' Volumetric heat generation rate (from nuclear fission and decay), page 139

Σ_{a1}, Σ_{a2} Absorption cross sections, page 134

Σ_r Scattering cross section from group 1 to 2, page 134

Σ_{f1}, Σ_{f2} Fission cross sections, page 134

V_1, V_2 Neutron velocity of energy group 1,2, page 134

X   Neutronic coupling coefficient, page 136

Y   Neutronic coupling coefficient, page 136

Subscripts/Superscripts

c   Cladding, page 141

f   Fuel, page 141

fl   Fluid, page 153

FW   Feedwater, page 147

g   Saturated vapour, page 146

gp   Gap between pellet and cladding, page 141

j   Channel number, page 150

JT   Jet pump, page 150

l   Liquid, page 146

lb   Liquid in bypass, page 153

m   Two phase mixture, page 146

sat   Saturation, page 147

SL   Steam line, page 147

w   Wall, page 146

Thermal Conduction

c Specific heat capacity, page 141

M_c Number of cladding zones, page 142

M_f Number of fuel zones, page 142

R_f Fuel radius, page 141

$\bar{t}$ Node averaged temperature, page 142

$t_{f,i}$ Temperature of the fuel in zone i, page 141

Thermal-Hydraulics

α Vapor void fraction, page 152

A   Cross sectional area, page 146

A_c Cross sectional area of flow channel c, page 145

c_I User defined coefficient, page 152

$c_{p,l}$ Specific heat capacity (of the liquid) at constant pressure, page 149

d_h Hydraulic diameter, page 146

f_l Single phase Darcy friction factor, page 146

Γ Vapor generation rate, page 153

G_m Mass flux, page 146

g_z Gravity constant, page 146

$\bar{h}_c$ Convective heat transfer coefficient, page 153

h_{fg} Enthalpy of evaporation, page 149

h_g Enthalpy of vapor, page 149

h_l Enthalpy of liquid, page 149

j_m Mixture volumetric flux, page 146

L_i Length of segment i , page 149

M Momentum of coolant along a closed contour, page 150

m Mass, page 151

Φ	Two phase friction multiplier, page 151
P	Pressure, page 147
P_{syst}	System pressure, page 147
q'_w	Linear heat generation rate, page 153
ρ_f	Density of saturated liquid, page 147
ρ_g	Density of saturated vapor, page 147
ρ_l	Density of subcooled and super-heated liquid, page 147
ρ_m	Mixture density, page 147
t_{sat}	Saturation temperature, page 147
S	Slip, page 152
t_l	Temperature of the liquid, page 153
t_w	Temperature of the cladding surface, page 153
u_g	Specific internal energy of saturated vapor, page 149
u_l	Specific internal energy of liquid, page 149
V	Volume of the node, page 151
W_g	Mass flow rate of the gas, page 152
w_g	Phasic velocity of the gas, page 152
W_l	Mass flow rate of the liquid, page 152
w_l	Phasic velocity of the liquid, page 152
ξ	Heated perimeter, page 150
$\zeta_{1,2}$	Form loss coefficient, page 149

Vectors

e	Right eigenvector, page 15
f	Left eigenvector, page 15
f	System function of state variables **x**, see equation (2.1), page 12
g	System function of state variables **u**, see equation (2.2), page 12
u	State variables that lead to algebraic equations, see equation (2.1), page 12
x	State variables that lead to differential equations, see equation (2.1), page 12

Index

Acknowledgments

As any major work, this thesis could not have been written, without the help and support of numerous people. This is especially true, since this work was carried out at three different locations (NPP Leibstadt, NPP Forsmark, Federal Institute of Technology Zürich [ETH]) and combining different fields of research.

I sincerely thank all my colleagues and advisors at Leibstadt, Forsmark and ETH for the practically unlimited support and the friendly working at(o)mosphere. During my year(s) in Sweden, I learned a lot about engineering physics, programming, team-work and hospitality.

I am particularly grateful to:

- **Dr. Hans-Urs Zwicky** and **Clas-Göran Wiktor**, both former employees of the Leibstadt nuclear power plant. When confronted with my wish to obtain Leibstadt as sponsor for my Ph.D. thesis, they agreed spontaneously and were full of help and good ideas.

- **Prof. Dr. George Yadigaroglu**, the head of the nuclear engineering laboratory at ETH and my thesis director. He deserves a lot of thanks for his steady support and advice. He gave me a lot of room to go an unusual way and to develop my own ideas. Nevertheless, he was always there when needed.

- **Dr. Thomas Smed** and **Pär Lansåker** from the Forsmark nuclear power plant. They started the original MATSTAB project and invited me to join. They answered a virtually unlimited number of questions and objections and contributed therefore very much to my education.

- **Prof. Dr. Jan Blomstrand**, the head of the division of nuclear reactor engineering at the Royal Swedish Institute of Technology (KTH) in Stockholm. He became a co-referee of the thesis and adviced me in the field of BWR stability.

- **PD Dr. Jürgen Halin**, Privatdozent at ETH. He became a co-referee of the thesis and advised me in the field of numerical algorithms and methods.

- **Prof. Dr. Göran Andersson**, head of the Power Systems group at the Laboratory for Electrical Power Transmission and High Voltage Technology at ETH. He advised me in the field of power systems and control theory.

Curriculum Vitae

Personalia

Name:	Philipp Hänggi
Address:	Leberngasse 19, 4600 Olten
Telephone:	Residence: +41 (0)62 213 98 97
	Office: +41 (0)62 286 75 15
E-mail:	philipp@haenggi.net
Homepage:	www.haenggi.net
Date of Birth:	December 19th, 1968
Place of Birth:	Horgen, Switzerland

Education

Spring 76 - Spring 82	Primary school in Olten
Spring 82 - Spring 84	Secondary school in Hägendorf
Spring 84 - Autumn 88	Scientific college in Olten
Autumn 88 - Autumn 94	Study of physics at the Swiss Federal Institute of Technology (ETH)
	Main study direction: Nuclear Physics
	Extension study: Information-Security and Cryptology
June 91 - June 92	Military service and officer school
Winter 94 - Spring 95	Guest scientist at Hahn Meitner Institute in Berlin
Spring 95 - June 99	Doctoral work at NPP Leibstadt/NPP Forsmark/ETH
	thereof one year (1996) guest in Sweden
July 99 -	Starting work as a nuclear engineer at Atel Ltd in Olten

Practical Training

Spring 92 (8 Weeks)	NPP Gösgen
	Fuel-Rod Corrosion / Fuel Assembly-Service
Spring 93 (8 Weeks)	Paul Scherrer Institute, Würenlingen
	Axial Modeling of the Neutron Flux of the Pool Reactor SAPHIR
Autumn 94 (16 Weeks)	Paul Scherrer Institute, Würenlingen (diploma work)
	3-D Modeling of the Pool Reactor SAPHIR

Awards

1986,1987,1988	Winner of the college math-contests in Olten